The Interstellar Medium and Star Formation of Nearby, Low-Mass Galaxies

A DISSERTATION
SUBMITTED TO THE FACULTY OF THE GRADUATE SCHOOL
OF THE UNIVERSITY OF MINNESOTA
BY

Steven Ray Warren

IN PARTIAL FULFILLMENT OF THE REQUIREMENTS
FOR THE DEGREE OF
Doctor of Philosophy

Dr. Evan D. Skillman, Advisor

August, 2012

Acknowledgements

Graduate school is a journey in which you meet and ultimately rely upon many people. My time as a graduate student was no different and many people need to be acknowledged and thanked for their contributions.

First and foremost I must give my appreciation to my wife, Jessica. You have sacrificed too much for me over the past six years, commonly absorbing my stressors. The completion of this thesis was only made possible by your hard work and commitment. It is as much yours as it is mine. Thank you for all of your love and support. You truly are my hero.

I do not think I could have succeeded without the guidance of my advisor, Evan Skillman. Evan has been more than an academic advisor to me. He has been a financial advisor, medical advisor, life advisor, and most importantly, Evan has been exactly what I needed him to be, understanding. Thank you very much for the support over the years and for pushing my limits in order to make me the best astrophysicist I can be, no matter how much I resisted. You always have my best interests in mind.

My collaborators have been very beneficial to my development as a scientist. Andrew Cole was tasked with training me right out of the gate. The main VLA-ANGST team, Jürgen Ott, Adrienne Stilp, Julianne Dalcanton, and Fabian Walter, all play a major role in this thesis.

The faculty and staff of the University of Minnesota Institute for Astrophysics deserve a lot of credit. I am indebted to Terry Thibeault. She made sure I got paid and always solved any issues I threw her way. Terry is the glue that holds the department together. Corinne Komor is a connoisseur of the fine things in life and a great friend. I am grateful for my preliminary and final oral exam committee members: Evan Skillman, Terry Jones, Tom Jones, Larry Rudnick, and Yong-Zhong Qian. Thank you to

Liliya Williams for allowing me to teach a few lab courses. Bob Gehrz is my hockey inspiration. Thanks for lacing up with me.

It is very difficult to earn a PhD without the help from your fellow graduate students. I want to thank each and every one of them for the good times. Peter Mendygral and Daniel Polsgrove were instrumental in my course work as study partners. Pete is my go-to person for anything computer related (and I probably abuse this...sorry!). Dan was useful for humbling me at any sport/competition as he seems to be a professional at everything. Damon Farnsworth suffered with me through learning radio astronomy and will one day be on the PGA tour with me. Karl Isensee's "skillz" only helped his cribbage game so much.

A special thanks goes out to my past and current officemates. Shea Brown helped teach me the fundamentals of radio astronomy and remains one of the smartest people I have ever met. Kristen McQuinn has been a great source for life experiences and we share many common interests, good and bad. Danielle Berg always entertained me with her unique vocabulary and constant drama. Jake Simones and Kyle Neary instituted Friday beers, which is never a bad thing.

I would also like to thank my undergraduate advisors at San Diego State University, Alan Shafter and Eric Sandquist. They introduced me to scientific research and helped propel me on this journey. Eric took me on as an inexperienced student and blue straggler stars will always be interesting to me because of it. Alan fostered my love for observing by insisting on me spending a large portion of my senior year up on the mountain.

My day-to-day activities could not have occurred without financial assistance. I am forever indebted to Roger Penrose for establishing a fellowship which supported me for my first two years. The NRAO, NSF, and the Astronomy Department also provided financial assistance over the years. I am also grateful to the Graduate School for awarding me a Degree Dissertation Fellowship.

Last and certainly not least, I want to thank my parents, Barbara and David, and my sister, Valerie. You have always believed in me. I love you all very much.

To anybody else that I may have missed (I'm sure there are many), thank you all for the words of encouragement, support, and friendship.

Dedication

For my wife and parents.

The Starry Night - Vincent van Gogh

For my part I know nothing with any certainty, but the sight of the stars makes me dream.

- Vincent van Gogh

Astronomy, as nothing else can do, teaches men humility.

- Arthur C. Clarke

Abstract

This thesis presents four different studies of the interstellar medium (ISM) and stellar content of ∼40 nearby (D $\lesssim$ 4 Mpc), low-mass galaxies. We aim to address two fundamental questions: "How do stellar processes effect the ISM in low-mass galaxies?" and "What are the local gas conditions which lead to molecular cloud formation?"

Much of the data presented here come from our survey the "**V**ery **L**arge **A**rray - **A**dvanced Camera for Surveys **N**earby **G**alaxy **S**urvey **T**reasury" (VLA-ANGST). VLA-ANGST is a targeted atomic hydrogen (H I) emission line survey directed towards 35 low-mass galaxies selected from the ANGST *Hubble Space Telescope* (HST) galaxy sample of the nearby universe. The VLA-ANGST project is the largest survey of its kind, demanding nearly 600 hours of VLA observing time. This unprecedented amount of observing time gives us data which has long lasting legacy value for its wealth of high resolution and high sensitivity information on the H I gas content and dynamics in a large sample of nearby, low-mass galaxies. H I data from the VLA-ANGST project will be used to explore the interactions between the gas and stellar content as well as trace the underlying dark matter distribution. Combining the H I and HST data with other tracers of recent star formation (e.g., emission processes from far ultraviolet star light, dust in the infrared, and carbon monoxide in the submillimeter) provides a comprehensive census of each galaxy, useful for understanding their evolution.

We investigate the role of multiple generations of star formation in the formation of large, kiloparsec scale cavities observed in the global H I distributions of five nearby, low mass galaxies. The small gravitational potential wells of some low-mass galaxies allow the outflow of energy from stellar processes (e.g., winds, supernovae, etc.) to help shape their gas distributions. We find that stellar processes produce ample energy (at least an order of magnitude or more) to have been the dominant creation source for the observed cavities.

The molecular gas responsible for the formation of stars remains elusive in many of the low-mass galaxies. We present a novel new technique to trace the immediate precursor of the molecular gas: cold H I. We apply our technique to a large sample of 31 nearby, low-mass galaxies and detect cold H I in ∼85% of the final sample (23/27)

after quality control cuts are applied. The cold H I discoveries presented here represent a significant step forward in our ability to study the precursory gas to star formation where standard techniques fail. We find that the cold H I occupies only a small fraction of the total H I content in each galaxy, consistent with both theory and other observational techniques in the literature. The cold H I is typically found in higher density gas, but is markedly absent from the highest density peaks where current star formation is presumably heating the gas. Observations targeting the areas rich in cold H I gas may be the only way to study the conditions of star formation in some low-mass galaxies.

Finally, we present direct observations of the molecular hydrogen content in one of the only low-mass galaxies with a molecular gas detection, NGC 4214. We use the Infrared Spectrograph onboard the *Spitzer Space Telescope* to measure pure rotational lines of the ground state of molecular hydrogen (H_2). These observations are some of the only direct H_2 detections in a low-mass galaxy to date. They confirm the association on the carbon monoxide (CO) molecule with the H_2 molecule assumed in the literature. We provide limits to the gas phase temperatures and column densities of the warm H_2 along the lines-of-sight of three distinct CO clouds, two of which are actively forming stars.

The results presented here add to the growing understanding of how these low-mass systems form stars. This knowledge may be applicable to galaxy evolution in the early universe, which may have had similar star forming conditions.

Contents

List of Tables

List of Figures

Chapter 1

Introduction

Stellar feedback influences the evolution of the largest scales of galaxy cluster formation down to the smallest scales of atomic interactions. Thus, understanding how stars form and evolve will, in turn, allow astronomers to probe these interactions in greater detail. Interpreting the evolution of the universe from observations is made difficult by the complexities in both the limitations of the observations (e.g., resolution, wavelength coverage, etc.) and in the understanding of the underlying physics.

In the local environment of the Milky Way galaxy, where the basic fuel of star formation is abundant, astronomers have a fairly good understanding of how stars form and how their evolution influences the surrounding interstellar medium (ISM; see McKee & Ostriker 2007 for a current theoretical understanding of star formation). To first order, stars are formed in regions rich with very cold ($\sim$10 K), molecular material (gas and dust). However, the vast majority of the gas and dust in the Milky Way is too warm to form stars ($\sim$1000 - 1,000,000 K). Through processes that are not fully understood, the gas and dust cool enough to eventually form stars.

One idea of how this process works in the Milky Way goes as follows: 1) the gas and dust pile up in the spiral arms due to compression (akin to a traffic jam on a busy highway), 2) large complexes can then become gravitationally bound and start to collapse, 3) the available dust shields the gas from high energy photons, allowing the gas to cool and collapse further, 4) molecules begin to form and the gas becomes very dense, 5) the molecules help further shield from the photons and the gas collapses even more, 6) the first self-gravitating proto-stellar cores form, signifying the onset of star

formation. The above story relies very heavily on two major ingredients: collecting the gas to become gravitationally bound and having dust and molecules to help shield the gas from the high energy photons which allows the gas to efficiently cool and collapse.

Current observational techniques used to locate and study the dust and molecular content of the ISM in galaxies range from infrared observations of re-radiated starlight from dust grains to emission lines in the submillimeter from CO molecules (see Kennicutt 1998b). Direct observations of cold molecular hydrogen are difficult since it does not easily radiate on its own (stars are thought to ultimately form from the cold molecular hydrogen gas). In order to find the cold molecular hydrogen, astronomers resort to indirect tracers. The CO molecule is of particular importance in the study of the molecular content of galaxies since the distribution of the CO is correlated with the extent of the cold molecular hydrogen content in Milky Way type galaxies (see Fukui & Kawamura 2010). Molecular hydrogen, however, is thought to form on the surfaces of dust grains, thus, locations that harbor both cold dust and cold molecular gas are typically also filled cold molecular hydrogen. The galaxies of the early universe lacked the large reservoirs of dust and molecules, yet they still formed stars. In order to understand the evolution of the universe, we need to understand how these early galaxies produced stars without large concentrations of these important ingredients.

Observing the galaxies in the early universe in enough detail to discern the local conditions of star formation is currently impossible due to their great distances and the limited resolving power of our current telescopes. Luckily, there exists galaxies in the nearby universe that are thought to host similar conditions to the galaxies of the early universe: dwarf irregular galaxies.

Dwarf irregular (dIrr) galaxies have very low abundances of elements heavier than hydrogen and helium (see Mateo 1998 for a review of dIrr galaxies). The elements heavier than hydrogen and helium are responsible for the formation of dust grains (e.g., carbonaceous dust and silicate dust) and the bulk of the molecular gas responsible for cooling the ISM (e.g., CO). CO, which is the brightest molecular line in Milky Way type galaxies, is markedly absent in most dIrr galaxies, making the identification of molecular gas difficult. The lack of large amounts of dust and molecules makes the environments of star formation appreciably different than that of the conditions in the Milky Way. It remains a mystery how these galaxies form stars without the dust and molecules, but

one of extreme importance in understanding the early universe.

These nearby dIrr galaxies have the added benefit of being numerous and therefore close enough to resolve the important components of the star formation process. One of the most important pieces of information is the stellar distributions, which the Hubble Space Telescope can resolve into individual stars. Being able to see each star in a galaxy allows astronomers to derive basic characteristics of regions within the galaxies such as distances, ages, metallicites, and energy injected into the ISM by the stars (see Tolstoy et al. 2009 for more details). These basic characteristics can then be compared to the gas and dust distributions. The gas and dust (when observable) can be resolved on scales of a hundred parsecs, small enough to reliably disentangle the influences of the stars on the surrounding local ISM.

Without the ability to directly detect the molecular gas critical for the formation of stars, one must turn to observing the main ingredient of molecular hydrogen: neutral, atomic hydrogen (H I; see Dickey & Lockman 1990 for a review of the importance of H I). The hydrogen atom in its various states is the most abundant atomic species in the universe, consisting of $\sim$75% by mass of all of the baryonic matter. We can learn a lot about the evolution of stars and galaxies by understanding the content and dynamics of their H I distributions, especially in the interactions with the underlying stellar populations.

The large abundance of H I and its direct relationship with star formation make observations of H I fundamentally important to our basic understanding of galaxy and star formation. Analyzing H I data provides astronomers with some of the most basic properties of the galaxy. For example, on large scales we can compute a global H I mass and on smaller scales we can probe local turbulent energies. Bulk velocity fields derived from H I observations remain one of the most useful tools for probing the unseen "dark matter" that dominates the gravitational potentials of most galaxies. At some level, understanding the behavior and characteristics of H I is critically important to many areas of astronomy.

This thesis uses observations from two of the largest, targeted H I surveys of nearby galaxies along with ancillary data from a multitude of other large programs in order to understand the local conditions of star formation and how the stars influence the gas distributions of low-mass galaxies. The overarching goals we established were:

- To determine the role of the stellar populations in the formation and sustainability of the kiloparsec scale H I holes in five nearby dIrr galaxies.
- Trace the cold H I distributions of 31 dIrr galaxies .
- Detect and characterize the molecular hydrogen content in one of the few nearby dIrr galaxies detected in CO observations, NGC 4214.

The organization of this thesis follows the chronology in which the projects were undertaken. In Chapter 2, I introduce the Very Large Array - Advanced Camera for Surveys Nearby Galaxy Survey Treasury project (VLA-ANGST). The VLA-ANGST project occupied most of my graduate student career. I was directly responsible for much of the data acquisition, reduction, and subsequent analysis. The resulting VLA-ANGST data paper was a collaborative effort. I include it here for both context and because of my large contribution to the project. My contributions to the writing of the paper include authoring some of the sections and providing roughly half of the tables and figures. In Chapter 3, I describe how large, central cavities observed in the H I distributions of some dIrr galaxies are formed. Chapter 4 details the search for and discovery of cold H I gas in 31 dIrr galaxies. The cold H I gas may be the precursor to the elusive molecular gas critical in the star formation process. In Chapter 5, I describe the direct detection of one of the lowest energy emission states of molecular hydrogen in the low-mass galaxy NGC 4214. I summarize the main results of my work in Chapter 6.

Chapter 2

VLA-ANGST: A high-resolution H I Survey of Nearby Dwarf Galaxies

A slightly modified version of this chapter has been submitted to The Astronomical Journal with the following bibliographic reference: Ott, J, Stilp, A. M., Warren, S. R. et al. 2012, AJ, submitted

We present the "Very Large Array survey of Advanced Camera for Surveys Nearby Galaxy Survey Treasury galaxies (VLA-ANGST)." VLA-ANGST is a National Radio Astronomy Observatory Large Program consisting of high spectral ($0.6 - 2.6\,\mathrm{km\ s^{-1}}$) and spatial ($\sim 6''$) resolution observations of neutral, atomic hydrogen (H I) emission toward 35 nearby dwarf galaxies from the ANGST survey. ANGST is a systematic Hubble Space Telescope survey to establish a legacy of uniform multi-color photometry of resolved stars for a volume-limited sample of nearby galaxies ($D \lesssim 4$ Mpc). VLA-ANGST provides VLA H I observations of the sub-sample of ANGST galaxies with recent star formation that are observable from the northern hemisphere and that were not observed in the "The H I Nearby Galaxy Survey" (THINGS). The overarching scientific goal of VLA-ANGST is to investigate fundamental characteristics of the interstellar medium (ISM) of dwarf galaxies. Here

we describe the VLA observations, the data reduction, and the final VLA-ANGST data products. We present an atlas of the integrated H I maps, the intensity-weighted velocity fields, the second moment maps as a measure for the velocity dispersion of the H I, individual channel maps, and integrated H I spectra for each VLA-ANGST galaxy. We closely follow the observational setup and data reduction of THINGS to achieve comparable sensitivity and angular resolution. A major difference between VLA-ANGST and THINGS, however, is the high velocity resolution of the VLA-ANGST observations (0.65 and 1.3 km s^{-1} for the majority of the galaxies). The VLA-ANGST data products are made publicly available through a dedicated webpage[1] .

2.1 Introduction

Star formation is driven by complicated interactions between gas and stars. Untangling the interplay between these processes is difficult, because in most cases, the events that trigger star formation are not obvious, nor are those that shape the structure and dynamics of the ISM. For a full understanding it is therefore indispensable to obtain a comprehensive view of all processes that come together to form stars, stellar associations, and stellar clusters. Observationally, one requires knowledge of the gas distribution and kinematics as well as the stellar energy input into the ISM over time.

In recent years, large systematic surveys have made superb progress on the first of these requirements. The number of nearby galaxies for which high-quality H I data is available has dramatically increased in the last few years, including campaigns such as THINGS ("The H I Nearby Galaxy Survey"; Walter et al., 2008), FIGGS ("Faint Irregular Galaxies GMRT Survey"; Begum et al., 2008), LITTLE-THINGS ("LITTLE: Local Irregulars That Trace Luminosity Extremes"; Hunter et al., 2007), SHIELD ("Survey of H I in Extremely Low-mass Dwarfs"; Cannon et al., 2011), and LVHIS ("The Local Volume H I Survey"; Koribalski, 2008). The difficult work of mapping the molecular medium in the brighter galaxies has begun as well, e.g. in BIMA SONG ("The BIMA Survey of Nearby Galaxies" Helfer et al., 2003), HERACLES, ("The HERA CO

[1] `https://science.nrao.edu/science/surveys/vla-angst`

Line Extragalactic Survey"; Leroy et al., 2009), and STING ("CARMA Survey Toward Infrared-bright Nearby Galaxies"; Rahman et al., 2012).

Unfortunately, the needed measurements of time-resolved stellar energy input are more difficult to acquire. Large systematic surveys in the far-ultraviolet (GALEX) and the far-infrared (e.g., the Local Volume Legacy survey (LVL; Dale et al., 2009), SINGS ("Spitzer Infrared Nearby Galaxies Survey"; Kennicutt et al., 2003), Kingfish ("Key Insights on Nearby Galaxies: a Far-Infrared Survey with Herschel"; Kennicutt et al., 2011), etc) have made excellent progress in measuring the recent star formation rate (SFR), while surveys like 11HUGS ("The 11 Mpc Hα UV Galaxy Survey"; Lee et al., 2004) have provided the Hα mapping needed to trace star formation (SF) on much shorter timescales. However, these approaches to measuring star formation lack all but the broadest time resolution, with each tracer being sensitive to SF over a different timescale (with Hα emitted on the timescale of O-star lifetimes ($\lesssim 5$ Myr), the far-ultraviolet on the timescale of A-star lifetimes ($\lesssim 100$ Myr), and the far-infrared on the timescale of far-ultraviolet heating). These timescales are not necessarily well-matched to the relevant energy input timescales for the gas.

For the survey presented here, we take a different approach, and focus H I observations on galaxies which are sufficiently close that their stellar populations can be resolved with the *Hubble Space Telescope* (HST). The resulting color–magnitude diagrams (CMDs) allow one to construct spatially-resolved star formation histories (SFHs) via analyses of galaxies' stellar populations, and thus reveal the time-resolved SFR of these nearby galaxies over timescales of several hundred Myr at $\sim 5 - 10''$ spatial resolution (e.g., Dohm-Palmer et al., 2002; Cannon et al., 2003; Weisz et al., 2008). With nearly 300 orbits of *HST* time, one of the most ambitious programs to obtain spatially-resolved SFHs is the ACS Nearby Galaxy Survey Treasury program (ANGST; Dalcanton et al., 2009). The ANGST observations enable to map spatially-resolved SFHs for a volume-limited sample of 69 nearby (< 4 Mpc) galaxies, probing both group and field environments. These data provide an entirely new, statistically significant view on the SFH of the local universe.

The survey presented here, VLA-ANGST ("Very Large Array survey of ACS Nearby Galaxy Survey Treasury galaxies"), complements ANGST with high spatial and spectral resolution data cubes of the atomic gas traced by the 21 cm line of neutral atomic

hydrogen (H I). VLA-ANGST was designed to aim for the best available resolution and sensitivity, using the NRAO Very Large Array (VLA[2]) in multiple configurations in a Large Program worth ~ 500 hours of observing time to achieve that goal. VLA-ANGST is designed to match the H I spatial resolution ($\sim 6''$) to the cell sizes over which the SFHs can be determined. Furthermore, the majority of the VLA-ANGST galaxies were observed at very high spectral resolution of $0.6 - 1.3$ km s^{-1} which is important for detailed ISM dynamic modeling studies of the rather low-mass objects which dominate the galaxy population within 4 Mpc.

The VLA-ANGST survey has a number of features that make it a valuable addition to the many other H I surveys, beyond the existence of resolved stellar population data. First, the galaxies in VLA-ANGST are all quite close, which ensures high linear resolution for studying small-scale features in the H I distribution. Second, because care was taken to match the observational setups of THINGS, the VLA-ANGST survey can be readily combined with the THINGS survey, giving much broader coverage towards low galaxy masses. When further combined with surveys like LITTLE-THINGS and SHIELD, which have used a similar observational strategy, we will have a relatively uniform database of H I toward > 100 objects spanning a large variety of galaxy types that is comparable in terms of sensitivity, angular, and spectral resolution.

The variety of galaxy types in the sample allows the study of (1) the response of gas and star formation to the propagation of spiral arms and to interactions, as seen in massive spirals and starburst galaxies (2) star formation propagation in the absence of strong perturbations of the gas density; gas rich dwarfs are ideal for such a study due to their lack of internal shear and spiral density waves (3) star formation triggered in unusual kinematic environments such as in tidal dwarfs, and (4) dIrr/dSph transition-type galaxies, whose lack of current SF but ample gas reservoirs allow studies of galaxies that possess the raw material for star formation, but somehow remain dormant.

In the following we present the data of the VLA-ANGST survey, and in-depth scientific analyses will follow in subsequent publications. Section 2.2 describes the selection of the targets, followed by the observational setup and data reduction (Section 2.3). Our data products are presented in Section 2.4 and a summary of the VLA-ANGST given

[2] The National Radio Astronomy Observatory is a facility of the National Science Foundation operated under cooperative agreement by Associated Universities, Inc.

in Section 2.5.

2.2 Target Selection

The ANGST survey targeted a complete volume-limited sample of 69 galaxies. The volume consists of those galaxies above a Galactic latitude of $\mid b \mid > 20°$, outside the Local Group but within 3.5 Mpc, with additional cones out to 4 Mpc in the directions of the M 81 and Sculptor groups. This volume provides a wide variety of gas-rich galaxies of all morphological types (Sb, dIrr, dSph/dE types, and tidal dwarfs), spanning a range of 10 magnitudes in luminosity, 10^4 in current star formation rate (SFR), and 1.3 dex in metallicity.

To complement the ANGST HST data with interferometric H I observations, for VLA-ANGST we selected a sub-sample of ANGST targets that comprises galaxies with known H I content and galaxies with indications of recent star formation, even if H I was not previously detected by single dish observations. We excluded galaxies that are too far south for the VLA ($\delta < -30^{\circ}$) and galaxies that were previously covered by THINGS.

Due to the volume limited nature of ANGST, most of the objects that fit our selection criteria are rather low-mass, low-luminosity dwarf galaxies. An exception is the ANGST galaxy NGC 253, a massive barred starburst galaxy. The H I properties of NGC 253, in particular its large linewidth, are very different to the rest of our sample and can only be adequately observed with the new correlator capabilities of the upgraded Karl G. Jansky Very Large Array (JVLA; the "Expanded Very Large Array", EVLA, was recently renamed to JVLA to mark the end of the construction phase). Thus, we excluded the massive starburst galaxy NGC 253 from our sample. In total, the VLA-ANGST sample amounts to 35 galaxies, approximately half the objects that comprise the entire ANGST *HST* survey.

We list all VLA-ANGST galaxies and their basic properties in Table 2.1. Column (1) contains the galaxy names, and column (2) a range of alternative names as found on the "NASA/IPAC Extragalactic Database" (NED)[3] . Columns (3) and (4) are the central equatorial J2000 coordinates, followed by the distance D of the galaxies in

[3] `http://ned.ipac.caltech.edu/`

column (derived using the tip of the red giant branch [TRGB] method) (5). The optical diameters at 25 mag $''^2$ (D_{25}) surface brightness and the absolute B magnitudes M_B are listed in columns (6) and (7), respectively. Columns (8) contains the galaxies' 3.6μm far-infrared luminosities, followed by the morphological types in numerical code according to de Vaucouleurs et al. (1991) taken from Karachentsev et al. (2004) in column (9). Finally, we list the UV-based star formation rate in column (10).

In the VLA-ANGST sample, 29 galaxies are classified as T-type = 10, 2 as T-type = 9, 1 as T-type = 7, 1 as T-type = -3, and 2 as T-type = -3, where negative T-types are early type galaxies and positive T-types are late-type galaxies. Gas-rich irregulars are at the upper end of the -10 to 10 scale. Six galaxies were not detected in our H I observations. The two galaxies classified as T-type = -3 were non-detections, and the other 4 non-detections were T-type = 10. DDO 82 was a single dish H I non-detection but we detected the atomic hydrogen gas in VLA-ANGST.

Fig. 2.1 shows the distributions of VLA-ANGST galaxies as a function of distance, T-type, logarithmic stellar mass (based on the 3.6μm emission), and logarithmic H I mass, as compared to the THINGS sample. VLA-ANGST galaxies are on average more nearby, late type, and low mass galaxies, both in terms of stellar and H I mass. The VLA-ANGST sample is thus much more dominated by low-mass dwarf irregulars and thus provides a complementary sample to THINGS.

2.3 Observations and Data Reduction

The vast majority of the observations in VLA-ANGST are new. In a few cases, archival data were used in place of obtaining new observations to improve efficiency. Here we describe both the new and archival observations.

2.3.1 Description of Observations

The parameters for our new observations and the subsequent data reduction strategy closely followed the design of the THINGS survey (Walter et al., 2008), with the goal of obtaining comparable sensitivity and spatial resolution. A significant difference between the two surveys, however, is the ~ 5 times better velocity resolution of VLA-ANGST. Each of the VLA-ANGST galaxies was observed with the NRAO's VLA in the B- (9 h

total observing time per galaxy), C- (3 h), and D- (3 h) array configurations (under project code AO215). The compact D-configuration is necessary to image spatial scales up to $\sim 16'$, which is the maximum for the VLA, as the largest scale is limited by the minimum antenna separation. The addition of B-configuration observations yield spatial resolutions $\sim 6''$ or ~ 100 pc for the nearby ($D \sim 3$ Mpc) objects. This scale is necessary to compare star forming regions with their H I counterparts and matches well the resolution of surveys at other wavelengths such as LVL (SPITZER) and 11HUGS (GALEX). The southern sources NGC 3109, NGC 247, Antlia, and DDO 6 were observed mostly in the hybrid BnA-, CnB-, and DnC-array configurations that feature elongated placements of the antennas along the northern arm. The projected baselines of these antenna configurations produce a more circular beam toward southern targets.

At the time of the observations, 2007 October to 2008 August, the VLA was in the process of being upgraded EVLA. This transition implied that the observations were taken with a mix of already converted EVLA and original VLA antennas. The conversion period mostly affected the signal distribution from the front-ends to the correlator. At the time, the old VLA correlator was still in use, and we configured it in the 2AC or 2AD modes to capture both RR and LL polarization products. Doppler tracking in the transition phase would have introduced phase jumps on baselines involving EVLA antennas. Consequently, we calculated and fixed the appropriate observing frequency for each observing run such that the H I emission line was well placed within a VLA bandpass at the start of an observation (Doppler setting; see below for caveats). Line shifts during a single observation are minimal (< 0.5 km s^{-1}) and are corrected in post-processing (§. 2.3.2).

The observational parameters for each galaxy were based on its H I linewidth as taken from single dish H I spectra, plus $\sim 20\%$ additional line free channels to enable a good continuum subtraction. To reach our goal of the best possible velocity resolution, we used a correlator mode with 0.78 MHz bandwidth and 256 channels for 15 galaxies in our sample. This corresponds to a channel width of ~ 0.65 km s^{-1} over a total velocity range of ~ 120 km s^{-1} after cropping about 20% edge channels, 10% on each side. Eight galaxies had wider H I linewidths and were therefore observed with a bandwidth of 1.56 MHz and 256 channels (~ 300 km s^{-1} velocity range and ~ 1.3 km s^{-1} channel width; see Table 2.3). The systemic velocity of KK 77 is unknown. To maximize on the

range of velocities for this source, we used the 4IF mode for this galaxy, a correlator mode that enables observing with two simultaneous frequencies. NGC 247 was also observed in the 4IF mode because of its extreme H I linewidth of $\sim 200\,\mathrm{km\ s^{-1}}$, by far the widest line of our sample. In the presence of extremely strong, narrow line features, the response of the VLA can include signs of the Gibbs phenomenon, a *sinc* function that oscillates between channels. This oscillation can be suppressed by "Hanning" smoothing the data with a triangular smoothing kernel. We decided not to use online Hanning smoothing as the lines are too weak to show any signs of the Gibbs phenomenon. Some of the archival observations that we added in, however, were observed with online Hanning smoothing turned on. We also applied a 25 MHz frontend filter to reduce the impact on radio frequency interference (RFI) in our data.

For flux and bandpass calibration purposes, we observed the VLA standard flux calibrators 3C286 and/or 3C48 (with fluxes of $\sim 15.0\,\mathrm{Jy}$ and $\sim 16.5\,\mathrm{Jy}$, respectively) depending on their visibility at the time of the observations. Typical integration times were 12 minutes on the flux calibrator, split between the beginning and end of a track. We observed our target galaxies in 40 minute intervals alternating with 3 minutes on a nearby phase/complex gain calibrator. The complex gain calibrators were chosen to be nearby point sources with a minimum flux of $\sim 1\,\mathrm{Jy}$. B-configuration observations were obtained in single 9 hour programs, or, in the case of southern galaxies, two 4.5 hour observations. In C- and D-configurations we combined sources into a few observations to reduce overhead and to obtain an improved *uv*-coverage.

During the VLA to EVLA transition time, the EVLA-EVLA baselines showed considerable aliasing and were largely unusable. Since the D-configuration observations had the largest number of EVLA antennas and therefore EVLA-EVLA baselines, we obtained an additional hour of observing time per object to reach our original sensitivity goals. Overall we obtained a total of 3 h in D-configuration per galaxy. The aliasing is a monotonic function that affects the first $\sim 0.5\,\mathrm{MHz}$ (or $\sim 100\,\mathrm{km\ s^{-1}}$ at the H I frequency), decreasing from the bandpass edge toward the center[4] . In addition to the make-up time and using mostly baselines with old VLA antennas, we placed the H I lines away from the affected frequency ranges but could not fully eliminate the effects. As a result, the noise levels in our data products are not entirely uniform across all channels

[4] see `http://www.vla.nrao.edu/astro/guides/evlareturn/aliasing.shtml`

and increase toward lower frequencies where aliasing is strongest. Across the full width of our most narrow 0.78 MHz bandwidths the noise can vary up to 35%. For the smaller width of the spectral line feature, the effect is smaller. In addition, for part of the observations, we tried to place the H I signal away from the most affected frequency ranges and for most galaxies the noise level changes could be constrained to an rms variation of $\lesssim 15$ % over the width of the H I line. For the two galaxies that were observed in the 4IF mode, KK 77 and NGC 247, the full bandwidths were required to cover the requested velocity ranges. The aliased signal appears in each IF and, consequently, the full noise variations of up to 35% are visible across the combined spectrum. Overall, however, this will not have a huge impact on most of the data analysis; KK 77 is a non-detection, and NGC 247 is one of our brightest objects such that the signal-to-noise ratio is only moderately affected.

A few galaxies (marked "a" in Table 2.2) had H I emission whose velocity range overlapped with Galactic H I line features. We addressed this problem by observing the bandpass calibrator at two different frequencies, offset by ± 4 MHz from the source frequency, in order to interpolate the calibration to the source frequency.

In addition to the new observations, in preparing for the program, we identified a few archival VLA observations which would be of use to the program. Most archival data, however, were observed at the relatively lower spectral resolution of 2.6 km s^{-1} with online Hanning smoothing applied. To avoid interpolation, we kept the lower velocity resolution of the archival data and rebinned our new VLA-ANGST observations after calibration for the final cube.

Table 2.2 lists all of our observational setups. Column (1) lists the galaxy names followed by the array configurations of the observations and the project codes in columns (2) and (3). AO215 is the genuine VLA-ANGST project, while other project codes refer to archival data. The observing dates are listed in column (4). Asterisks denote observations that span across midnight, for which we refer to the start dates. The equatorial pointing positions are provided in columns (5) and (6) and the appropriate equinox is tabulated in column (7). Column (8) gives the phase calibrators that were used for the observations. The correlator setups are displayed in columns (9) through (14) with (9) the correlator modes, (10) the bandwidths, (11) the number of channels, and (12) the channel widths in km s^{-1} (for the rest frequency of H I at 1.420405752 GHz).

VLA-ANGST data were taken at the fixed sky frequencies listed in column (13) whereas many archival observations were Doppler tracked at the velocities listed in column (14). Finally, column (15) provides the number of converted EVLA antennas in the dataset with the remaining antennas being old, not yet converted, VLA antennas at the time.

2.3.2 Data Calibration

Data calibration was performed using the AIPS[5] package and deviated from the "standard" VLA data reduction procedure due to the effects from the VLA to EVLA transition period. As mentioned above, EVLA-EVLA baselines showed considerable aliasing that affected primarily the narrow bandwidth observations. Our reduction scheme followed the following steps.

To avoid low signal-to-noise solutions during calibration, we started by eliminating edge channels. About 20% of the entire bandwidths were cropped, $\sim 10\%$ at the upper and $\sim 10\%$ at the lower frequency ends (task UVCOP). After correcting the absolute antenna positions (VLANT), the absolute flux scale of the primary flux calibrators 3C286 and 3C48 (see §. 2.3.1) were calculated by the task SETJY using NRAO-provided models and "Perley-Taylor 99" flux scales. We manually inspected all calibrator data in each array configuration for bad visibilities due to RFI or cross-talk between antennas (AIPS tasks TVFLAG, SPFLG, UVFLG, WIPER). If calibrators showed higher than expected signal on short baselines due to solar interference, we excluded baselines with a *uv* range between 0 and 1 kλ in the calibration. Solar RFI was usually well removed by continuum subtraction in the source visibilities, so we performed no additional source flagging due to solar interference.

The data were then bandpass-corrected by deriving a channel-based, normalized gain solution from the flux calibrator data via BPASS. We produced a new broad band "channel zero" (CH0) map from these bandpass corrected data (AVSPC), and utilized the new CH0 map in all subsequent calibration steps. Next, we calculated the complex antenna gain as a function of time for all calibrators (CALIB). The complex gain is a solution for both gain and phase, and for all solutions we assumed that the complex gain calibrators are point-like. With CLCAL we linearly interpolated all phase/gain solutions for across all time intervals. GETJY transferred the flux calibration to the

[5] The Astronomical Image Processing System (AIPS) has been developed by the NRAO.

complex gain calibrator. At this stage, we manually inspected the quality of the calibration and repeated the above procedure if RFI corrupted the solution and further flagging was required. Finally, we applied all calibration solutions to the target galaxies. We estimate the calibration flux uncertainties to be $\sim 5\%$.

For galaxies whose H I emission is within the velocity range of the foreground Galactic emission (marked "a" in Table 2.2), the flux and bandpass calibrators were observed at offsets of ± 4 MHz relative to the frequency of the targets. The calibration of these data followed the same steps as above with each observed frequency calibrated separately. We then obtained an interpolated flux and bandpass solution calibration from a linear interpolation across these offset frequencies. The EVLA uses different internal local oscillator settings than the VLA. For our observations during the VLA to EVLA transition phase, this difference had the unfortunate effect that, for some observations, the 25 MHz frontend filter overlapped in frequency with the upper frequency offset bandpass observations. This resulted in an extreme phase gradient across that particular offset frequency and the affected observations were unusable. In these cases, we calibrated the source data by extrapolating the calibration from the single offset frequency that most closely matched the bandpass derived from the phase calibrator. This method provided bandpasses that are accurate to few percent. For observations where the *complex gain* calibrator was contaminated by Galactic H I, we simply flagged the affected channels before calculating a new CH0 to be used for the gain and phase solutions.

After applying all calibration tables to the source, the galaxy data were separated (SPLIT) from the flux and phase calibrator data for further processing. Both NGC 247 and KK 77 were observed in the 4IF mode. We calibrated each of the 2IF windows separately as described above, and "stitched" the data together, averaging overlapping velocity ranges in the process (UJOIN) prior to continuum subtraction.

To determine the continuum level, we fit a linear function to the line-free channels, typically 20 channels on each side of the spectrum. The fit was then subtracted from the complex *uv*-data (task UVLSF). Since the frequencies for each observing set up were fixed (see §.2.3.1), we regridded the H I data to a common heliocentric, optical velocity system (CVEL). Finally, data from all observations and array configurations were combined (DBCON) into a single data set for imaging. We produced dirty images

with IMAGR and inspected the cubes for artifacts. If further flagging was required, we went back to the original source data, flagged, and reapplied the calibration.

2.3.3 Mapping and Deconvolution

After satisfactory calibration and source editing, we used the AIPS task IMAGR to generate data cubes and final data products. We followed the THINGS protocol when possible so that the two data sets could be easily compared. For each VLA-ANGST galaxy, we imaged the visibilities with two different weighting schemes: one using natural weighting and one using the "robust" weighting (originally described by Briggs, 1995, with small modifications as described in the AIPS help files). Natural weighting yields high sensitivity at moderate resolution (typically $\sim 6 - 12''$ for our galaxies, or about $\sim 90 - 170$ pc for a distance of 3 Mpc), while robust weighting decreases the size of the synthesized beam at the cost of reduced surface brightness sensitivity. We applied a robust parameter of 0.5, which was found to be a good compromise between resolution and sensitivity and matches the maps generated by THINGS. When compared to the naturally-weighted cubes, the noise in the robust-weighted cubes is typically $\sim$ 20% higher and the beam size $\sim$ 40% smaller. Depending on the angular extent of each galaxy's H I emission, the cubes were imaged with either 1024^2 pixels at $1.5''$ per pixel or 2048^2 pixels at $1.0''$ per pixel. The cubes were deconvolved using the Clark CLEAN deconvolution algorithm (Clark, 1980), stopping at a residual flux threshold of 2.5 times the noise level as measured in the cubes. Finally, we produced primary beam corrected data cubes that were later used in the moment map analysis (§ 2.4).

The properties of all data cubes are listed in Table 2.3 where column (1) lists the galaxy names followed by columns (2), (3), (4), and (5) that contain the weighting algorithms and the resulting beam major and minor axes sizes as well as the position angles of the deconvolved data. The average root mean squared noise per channel is shown in column (6) and the channel width in (7), the number of pixels in each plane in column (8) followed by the pixel size in column (9).

To ensure that our datacubes would be as directly comparable to the THINGS datacubes as possible, we reduced THINGS observations using our calibration, mapping, and deconvolution protocols. Comparisons of our reductions of THINGS observations with the publicly available THINGS datacubes showed no significant differences. The

most important difference between the VLA-ANGST datacubes and the THINGS datacubes is the higher velocity resolution in the majority of the VLA-ANGST datacubes which was possible because of the overall smaller range in velocity of detectable H I in the VLA-ANGST sample of galaxies.

2.3.4 Mask Generation

To suppress noise for the production of moment maps, we generated image cube masks that defined regions containing detectable H I emission from the galaxies. To do so, we convolved the natural-weighted images to twice the original beam major axis and applied spectral Hanning smoothing with a three channel wide kernel. New "mask" cubes containing predominantly H I signal were constructed by keeping all regions corresponding to H I emission above the 1σ noise level and blanking all other regions. To remove the effects of sidelobes, noise spikes, or other spurious signals from the masks, any individual regions with an area smaller than the beam size were automatically removed. We then eliminated any remaining non-emission regions by eye inspection.

The result is a single mask cube per galaxy that we applied prior to the generation of the integrated spectra and moment maps. The same mask is used for both the natural and robust data cubes. New cubes containing predominantly H I signal were constructed by keeping all H I emission corresponding to unblanked regions in the mask cube. For our data, this method discriminated well between significant, low level emission and pure noise. Note that this process produces a lower limit to the total H I emission. Some very low surface brightness H I may be have been eliminated from these data cubes.

Note that mask generation is not entirely automatic, and, therefore, our mask generation cannot be said to be strictly following THINGS protocols. This is exacerbated by the differences in typical channel widths, which leads to differences between VLA-ANGST and THINGS in average noise levels in the individual channels. Nonetheless, we have followed the intentions of the THINGS project to use masking to suppress the noise and to provide optimal moment maps. However, one should be aware that small differences in masks are possible and that the resulting moment maps have a small inherent systematic uncertainty.

2.3.5 Flux Densities

Recovery of the total H I flux from each channel and the resulting H I spectra is more complicated than simply summing up the total emission. Jörsäter & van Moorsel (1995) have shown that standard CLEAN maps do not in actuality yield correct flux measurements. Maps in AIPS are created by summing the CLEAN components, convolved with the CLEAN beam, to the signal that is still present in the residuals. While both maps are purportedly measured in Jansky (beam area)$^{-1}$, the relevant beam is different in each map: the convolved CLEAN component map is measured in Jy (CLEAN beam area)$^{-1}$ while the residual map has units of Jy (dirty beam area)$^{-1}$. Because the areas of the CLEAN beam and the dirty beam are different, the flux in the CLEAN components and in the residuals must be corrected to obtain the proper H I flux. A full discussion of the following correction technique is given in Jörsäter & van Moorsel (1995). The corrected flux of a channel is given by:

$$G = C + \epsilon \times R \tag{2.1}$$

where G is the corrected flux, C is the flux in the convolved CLEAN components [with units of Jy (CLEAN beam)$^{-1}$], R is the flux in the residual map [with units of Jy (dirty beam)$^{-1}$], and ϵ is the correction factor that takes into account the ratio of the dirty beam area to the CLEAN beam area. IMAGR provides a method to automatically apply this correction and, following the THINGS protocol, we determined ϵ within the inner 50×50 pixels of the dirty and CLEAN beams. This produces a set of two new natural and robust weighted cubes with the above correction applied in addition to our standard cubes. When the residuals are scaled by ϵ, the noise in the corrected cubes is artificially suppressed. We thus produced two sets of data cubes for different analyses:

1. "Standard" cube: the standard output from our pipeline, with uncorrected H I fluxes but uniform noise properties. No primary beam correction is applied to these data. This cube should be used for any analysis that requires uniform noise properties or uses selection based on noise (e.g., fitting of individual profiles in order to construct velocity fields or measure profile shapes).

2. "Rescaled" cube: the cube with the flux correction applied, to be used only in regions with genuine H I emission. The flux values in this cube are correct,

and therefore any analysis that requires selection based on H I fluxes should use this cube (e.g., mass and column density measurements). The "rescaled" cube is corrected for the attenuation from the primary beam.

The data products that we make available follow this recipe; all global H I spectra (§ 2.3.6) and moment maps (§ 2.4) were derived using the masked, "rescaled cubes". The online data cubes themselves are the "standard" cubes, without primary beam attenuation or flux corrections.

2.3.6 Global H I Spectra and Masses

Global H I spectra are derived from the masked, rescaled data cubes. The spectra are used to derive velocity widths at 20% (w_{20}) and 50% (w_{50}) of the peak. The central H I velocity of each galaxy is calculated by taking the mid-point of the w_{20} boundaries.

We also use the integrated H I spectra to calculate the total H I masses of our galaxies using the following equation:

$$M_{\rm HI}\,[M_\odot] = 2.36 \times 10^5\ D^2 \times \sum_i S_i \Delta v \tag{2.2}$$

where D is the distance to the galaxy in Mpc (as given in Table 2.1) and $S_i\Delta v$ is the total flux of a single channel in Jy km s^{-1} (e.g. Rohlfs & Wilson, 2004). This formula assumes that the H I emission is optically thin, an assumption that is valid over a large flux range and may begin to fail at very extreme column densities of $\gtrsim 10^{22}$ cm^{-2} (e.g. Allen et al., 2012). At our spatial resolution, we do not observe column densities of this magnitude.

In Table 2.4, we present all of the derived H I parameters starting with the galaxy names in column (1), followed by the integrated H I flux densities $S_{\rm HI}$ and the derived H I masses in columns (2) and (3). For comparison, we compiled single dish fluxes $S_{\rm HI}^{\rm SD}$ from the literature and list them in column (4). The w_{20} and w_{50} values as well as the central velocities are shown in columns (5), (6), and (7), respectively, followed by the peak H I column density (§ 2.4.3) taken from the natural-weighted map in the final column (8). To derive upper limits for the non-detections, we assume an H I disk the same size as the optical diameter D_{25} and a hypothetical linewidth of 20 km s^{-1}.

Galaxies typically exhibit H I dispersions of 5-10 km s^{-1} and a linewidth of 20 km s^{-1} thus implies little rotation or face-on orientation.

In $\sim 70\%$ of all cases the single dish fluxes are somewhat larger than the interferometric VLA flux measurements. This difference is expected to some level given that the VLA can only image structures with an extent of up to $\sim 16'$ in D-configuration at 1.4 GHz (limited by the minimum distance between two antennas). Missing flux may therefore only be a significant issue for the most extended objects in our sample. Some single dish flux measurements deviate substantially from the trend of being slightly larger than the VLA fluxes. The deviations can be either way: galaxies like DDO 6, UGC 4483, DDO 113, and KK 230 have much larger single dish measurements whereas others like BK 3N, AO 0952+69, Sextans B, DDO 82, and DDO 190, have smaller single dish fluxes. Such discrepancies may be explained by difficulties in single dish baseline subtraction or by the larger single dish beam that tends to pick up larger fractions of Galactic H I emission as well as flux from nearby objects.

2.4 Data Products

2.4.1 H I Spectra

We used the naturally-weighted data cubes to derive H I spectra (§ 2.3.6) for our galaxies given their higher surface brightness sensitivity compared to the robust-weighted data. This approach captures as much low-level, extended emission as is possible with interferometric VLA data. All fluxes are calculated from the rescaled cubes described in §2.3.5 and are presented in Fig. 2.2. In the case of NGC 247, velocities around 108 km s^{-1} were strongly contaminated with RFI; to estimate the H I flux in this channel, we interpolated the emission from the adjacent channels.

Since our sample is composed primarily of dwarf galaxies, the galaxy spectra typically show narrow, singly-peaked profiles. Extreme cases like KDG 73 and KKH 86 exhibit linewidths of < 10 km s^{-1}, which implies very little velocity dispersion, maybe due to low signal to noise in the line wings. On the other end of the mass spectrum, a few galaxies (NGC 404 NGC 3741, DDO 190, Sextans A, DDO 181, NGC 3109, NGC 247) exhibit hints of the more familiar double-horned profile expected from larger spiral disks. The maximum linewidth is observed in NGC 247 with $w_{20} \sim 200$ km s^{-1}.

2.4.2 Channel Maps

Channel maps of the galaxies are presented in Figs. 2.3 through 2.31 (natural weighting). Given the high spectral resolution of our data, there is typically only little flux in each velocity bin. Some galaxies, mainly the more massive ones such as NGC 247 or NGC 3109 show the classic "butterfly" pattern of a spiral galaxy, a tell-tale sign for a flat rotation curve. The bulk of galaxies exhibit rotation despite the fact that the dispersion adds a stochastic component to the velocity structure. NGC 247 also features a H I absorption feature along the line of sight to the background quasar NVSS J004713-205114 at RA (J2000)= $00^h : 47^m : 13.6^s$ and DEC (J2000)= $-20^\circ : 51' : 15''$ (e.g., Dickey et al., 1992). Some data cubes are contaminated by Galactic foreground emission, but only for NGC 404 is the Galactic H I close to the systemic velocity of the source. Other data cubes, such as that for AO 0952+69, contain emission from a nearby object. AO 0952+69, in fact, is likely not a real galaxy but might be a feature within a spatially coincident spiral arm that belongs to the massive M 81 galaxy.

2.4.3 Moment Maps

We used the AIPS task XMOM to generate moment maps from the masked, flux-corrected cubes. For all calculations we require that each pixel in a moment map is calculated from at least four unmasked channels; pixels with fewer channels are masked in all moment maps.

Integrated H I Maps

Integrated H I column density maps are created from the masked, rescaled data cube by integrating along the velocity axis to generate the moment 0 map:

$$I_{\rm HI} = \sum_i S_i \times \Delta v \tag{2.3}$$

where i is the channel, S_i is the flux density in the ith channel in Jy beam^{-1}, and Δv is the channel spacing in km s^{-1}. We then convert the moment maps to column density with

$$N_{\rm HI} = 1.104 \times 10^{24} \frac{1}{b_{\rm maj}\ b_{\rm min}} \sum_i S_i \Delta v \tag{2.4}$$

where $b_{\rm maj}$ and $b_{\rm min}$ are the beam major and minor axes in arcseconds and $\sum_i S_i \Delta v$ is the value of moment 0 map at each pixel in units of Jy beam^{-1} km s^{-1}. In Figs. 2.3 to 2.31 we show column density maps for all galaxies with detected H I (upper left panels on the second page of each figure) We also show column density contours overlaid on optical images for each galaxy. On these maps (upper right), we placed the footprints of the HST observations that are available through ANGST.

The maps exhibit resolved H I structures comparable to their beam sizes. Some galaxies, like KK 230, or NGC 404 have low columns with peak values of a few times 10^{20} cm^{-2}. Other galaxies like DDO 190, or UGCA 292 reach columns of a few times 10^{21} cm^{-2} (or ~ 10 M$_\odot$ pc^{-2}), which is a canonical threshold for star formation (e.g., Skillman et al., 1987; Bigiel et al., 2008; Leroy et al., 2008).

Intensity-weighted Velocity Field Maps

The H I intensity-weighted velocity fields (moment 1) maps are calculated using

$$\langle v \rangle = \frac{\sum_i S_i \times v_i}{\sum_i S_i}. \tag{2.5}$$

For well-behaved disks this equation gives a good indication of the average velocity of gas in a given pixel. However, bulk motions, outflows, and other non-circular motions can shift the derived velocity to unexpected values. Therefore, profile fitting in order to determine the velocity of the peak of the emission is a more reliable method for finding the average rotational velocity of the gas at a given location in the galaxy. While the velocity fields of lower mass dwarfs are less ordered than those of their larger disky counterparts, most still show velocity gradients across their disks that are indicative of rotation, which is typical for H I in dwarf galaxies (Begum et al., 2008; Walter et al., 2008). The H I intensity-weighted velocity maps are shown in the lower right panels of the second page of for each galaxy in Figs. 2.3 to 2.31.

Second Moment Maps

The linewidth of H I emission can be characterized by the intensity-weighted second velocity moment as given by:

$$\sigma = \sqrt{\frac{\sum_i S_i \times (v_i - \langle v \rangle)^2}{\sum_i S_i}} \tag{2.6}$$

where $\langle v \rangle$ indicates the intensity-weighted velocity derived in the first moment map. While the second moment can be indicative of the turbulence of the ISM, it also reflects the influence of large scale gas flows such as expanding shells or tidal material. At lower resolution, the velocity dispersion can be artificially inflated by beam smearing over the gradient in the velocity field, especially towards the centers of the galaxies, where this gradient is steepest. Overall, the velocity dispersion values fall in a relatively narrow range of 5-15 km s^{-1}, as seen in the lower right panel on the second page of Figs. 2.3 to 2.31).

Pixels which yield first velocity moments outside the velocity range of the data cube are blanked in all moment maps. The first and second moment maps generated from the robust data cubes are noisier than those from natural-weighted cubes and occasionally have pixels with unrealistic values in low column density regions. To counter this problem, we blanked all pixels with column densities $N_{\rm HI} < 3 \times 10^{19}$ cm^{-2} in the robust moment maps.

2.5 Summary

Here we present the sample selection criteria, observational parameters, data reduction procedures, and data product description of the VLA-ANGST survey, a Large VLA project that targets nearby, mostly dwarf irregular galaxies. Of the 35 galaxies in the survey, we detect H I in 29. The calibrated VLA data for these objects are publicly available at `https://science.nrao.edu/science/surveys/vla-angst`. This leads to the following data products:

- Global H I spectra for all galaxies, derived from the masked, flux-corrected, primary beam corrected, natural-weighted data cubes.

- H I data cubes of both natural and robust weighting. The cubes are not primary beam or flux corrected and they are unmasked.

- Integrated intensity maps (moment 0 maps) in units of Jy beam^{-1} km s^{-1} as well as converted to H I column densities. These maps were derived from the masked, flux-corrected, primary beam corrected data cubes. We offer both, natural and robust-weighted maps for download.

- The intensity-weighted velocity field maps (moment 1 maps), derived from the same data products as the integrated intensity maps.

- Second moment maps which give a measure for the velocity dispersion of the gas; derived from the same data products as the integrated intensity maps.

This paper presents the observations; scientific analyses will follow in subsequent publications. A study that compares the H I kinematics of large H I shells to the supernovae and stellar wind output of the underlying stellar populations is presented in Warren et al. (2011). Detection and characterization of narrow H I components that presumably trace cold H I are provided in Warren et al. (2012). Stilp et al. (2012) correlate averaged H I dispersion values to the physical properties of the host galaxies. The true value of our H I survey is further unlocked by the extensive, multi-wavelength ancillary data that is available for many of our objects. The VLA-ANGST, THINGS, LITTLE THINGS, and SHIELD data products are furthermore similar in sensitivity, spatial and spectral resolution and provide H I data cubes for > 100 galaxies.

We thank the National Radio Astronomy Observatory for their generous time allocation, observing, and data reduction support for this Large Project. The National Radio Astronomy Observatory is a facility of the National Science Foundation operated under cooperative agreement by Associated Universities, Inc. Support for this work was provided by the National Science Foundation collaborative research grant 'Star Formation, Feedback, and the ISM: Time Resolved Constraints from a Large VLA Survey of Nearby Galaxies,' grant number AST-0807710. This material is based on work supported by the National Science Foundation under Grant No. DGE-0718124. SRW is grateful for support from a Penrose Fellowship, a University of Minnesota Degree Dissertation Fellowship, and a NRAO Research Fellowship number 807515. We would like to thank the LITTLE THINGS and THINGS teams for collaboration on the calibration and imaging pipeline. We have made use of the NASA/IPAC Extragalactic Database (NED), which is operated by the Jet Propulsion Laboratory, California Institute of Technology, under contract with NASA. This research has also made use of NASA's Astrophysics Data System (ADS).

2.6 Figures

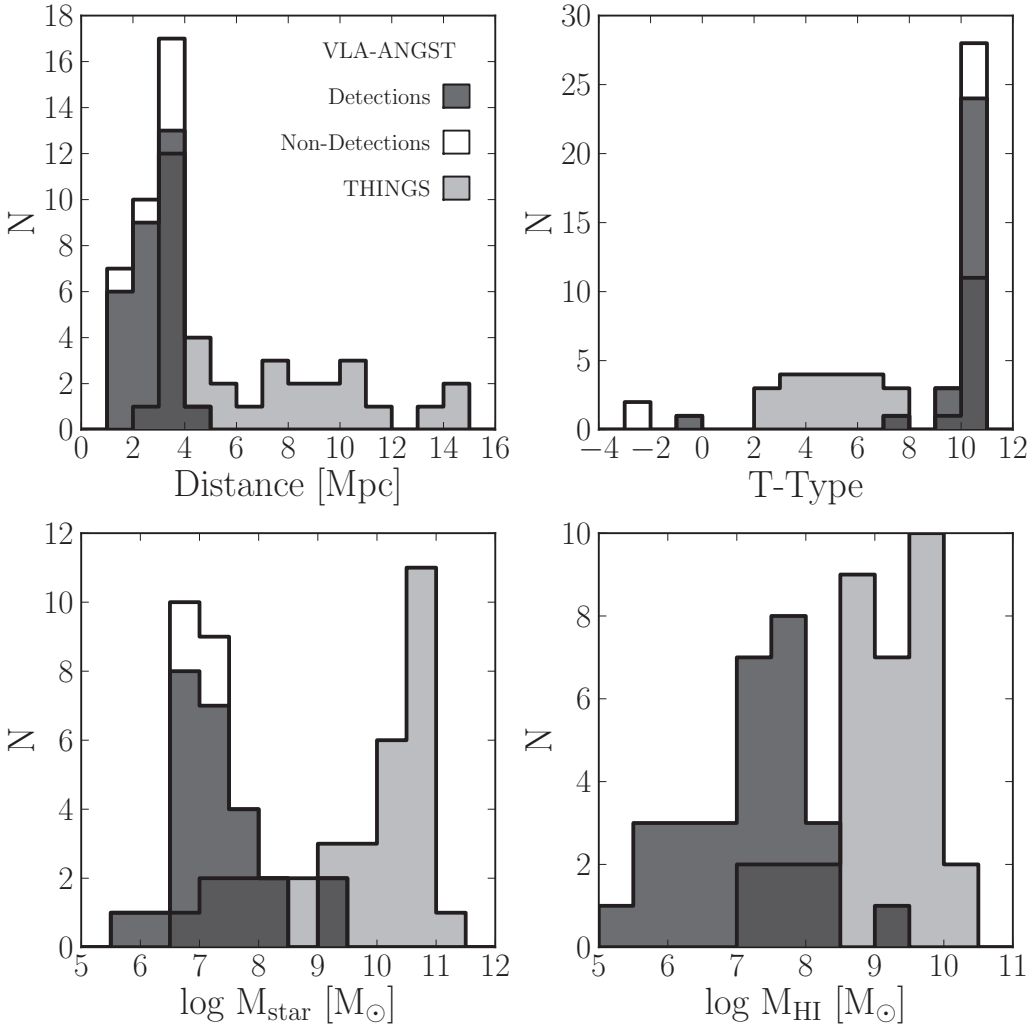

Figure 2.1 VLA-ANGST galaxy distribution across distance (upper left), T-Type (upper right), logarithmic stellar mass (lower left), and logarithmic H I mass (lower right). Galaxies that are detected in VLA-ANGST are shown in medium grey bins and non-detections, colored white, add to the distribution. THINGS galaxies are shown in light gray and the VLA-ANGST and THINGS overlap areas in dark gray color.

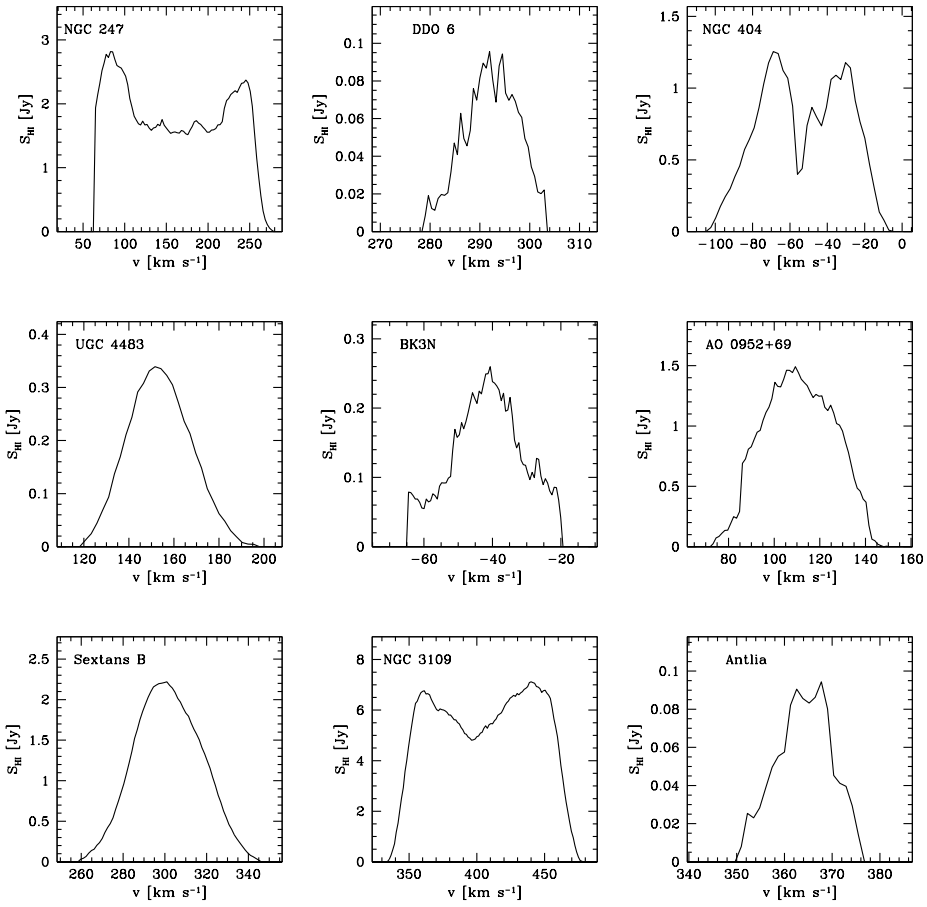

Figure 2.2 Spatially integrated H I spectra of the VLA-ANGST galaxies.

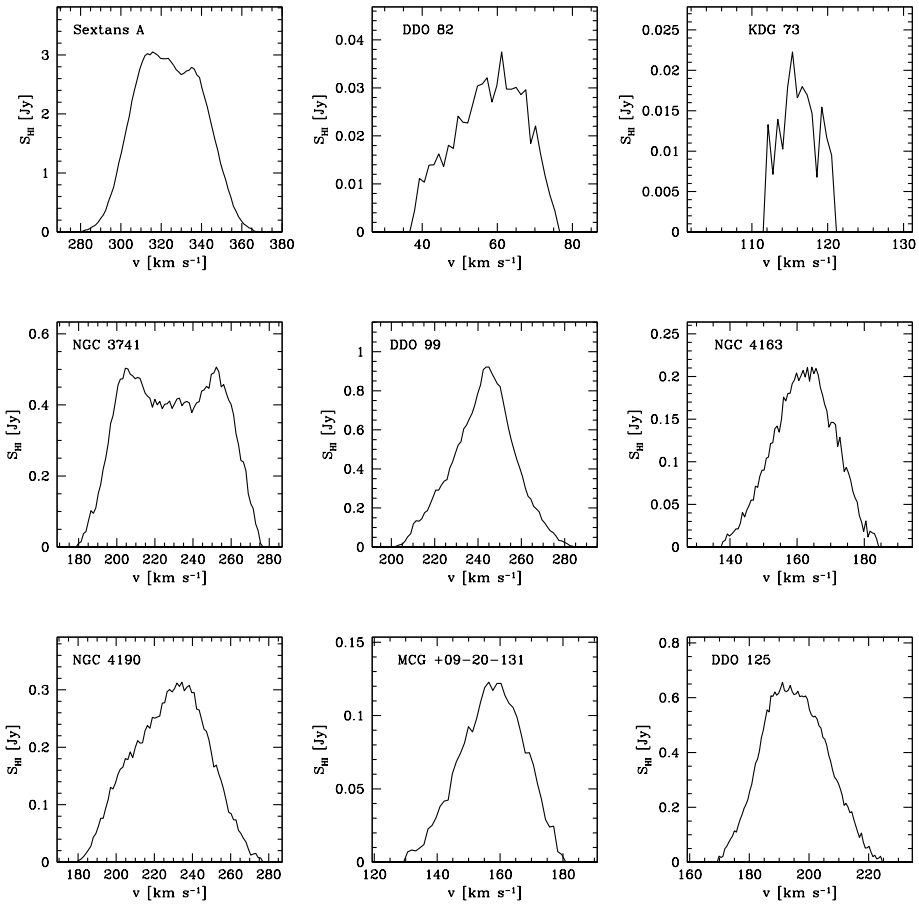

Figure 2.2 continued...

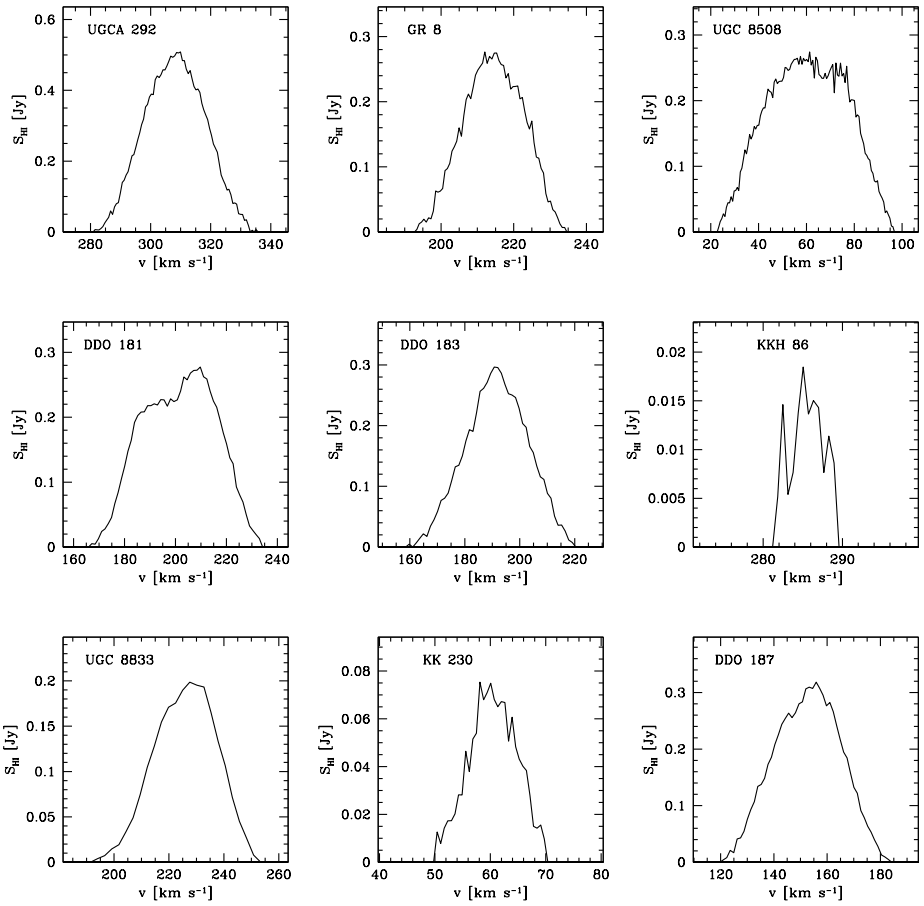

Figure 2.2 continued...

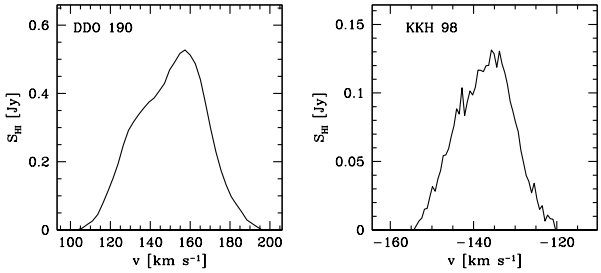

Figure 2.2 continued...

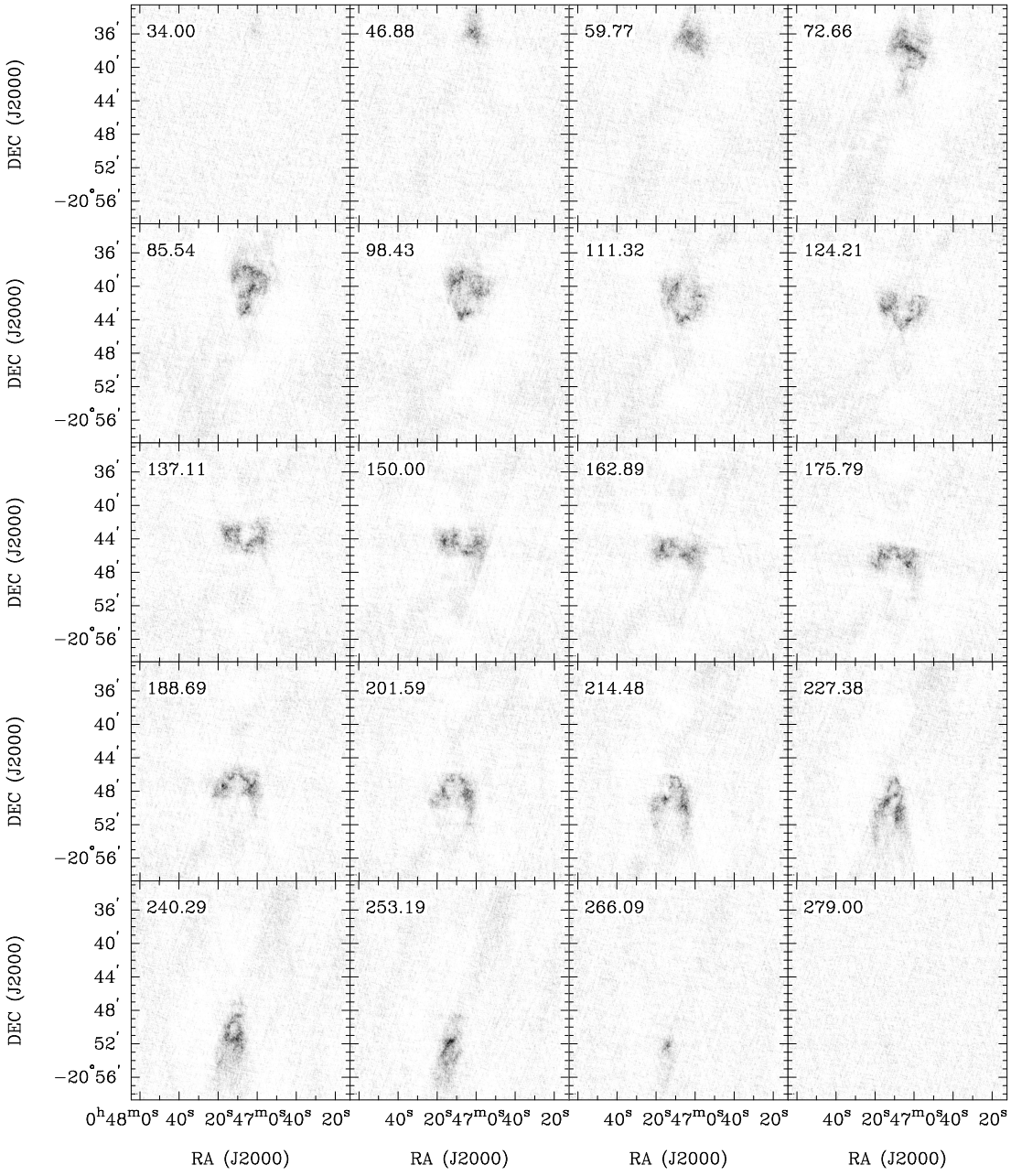

Figure 2.3 **NGC 247:** Channel maps based on the natural-weighted cube (grayscale range: -0.02 to $12.2\,\mathrm{mJy\,beam^{-1}}$). Every fourth channel is shown (channel width $2.6\,\mathrm{km\ s^{-1}}$) and each map has the same size as the moment maps in the following panels.

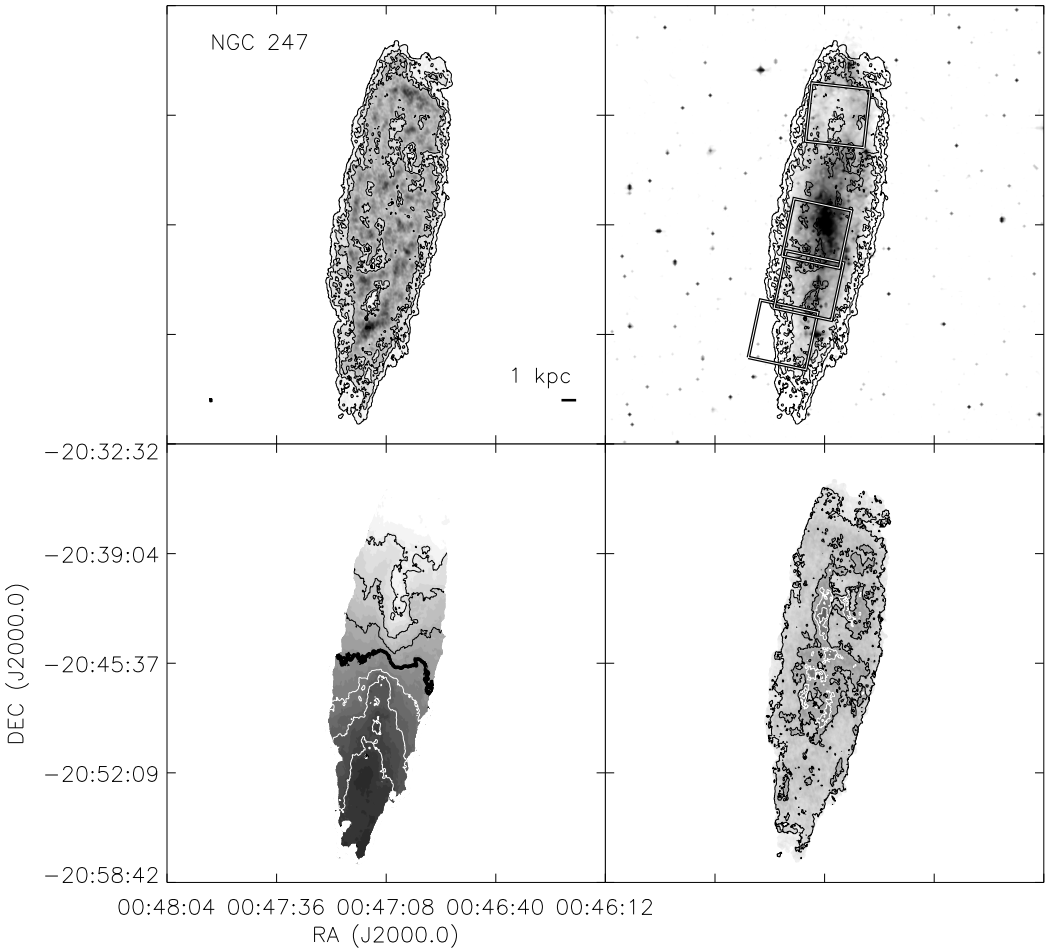

Figure 2.3 continued. *Top left:* The integrated H I intensity map for NGC 247. The grayscale covers a range from 1×10^{19} to 5.4×10^{21} cm^{-2}with contours of 1×10^{20}, 5×10^{20}, 1×10^{21}, and 5×10^{21} cm^{-2}. *Top Right:* An optical image from the DSS with the same column density contours overlaid. The HST ACS footprints are the fields covered by the ANGST survey. *Bottom Left:* The H I velocity field. Black contours (lighter grayscale) indicate approaching emission, white contours (darker grayscale) receding emission. The thick black contour is the central velocity ($v_{cen} = 163.7\,\mathrm{km\,s^{-1}}$) and the isovelocity contours are spaced by $\Delta v = 25\,\mathrm{km\,s^{-1}}$. *Bottom Right:* The H I velocity dispersion. Contours are plotted at 5, 10, 15, and 20 $\mathrm{km\,s^{-1}}$.

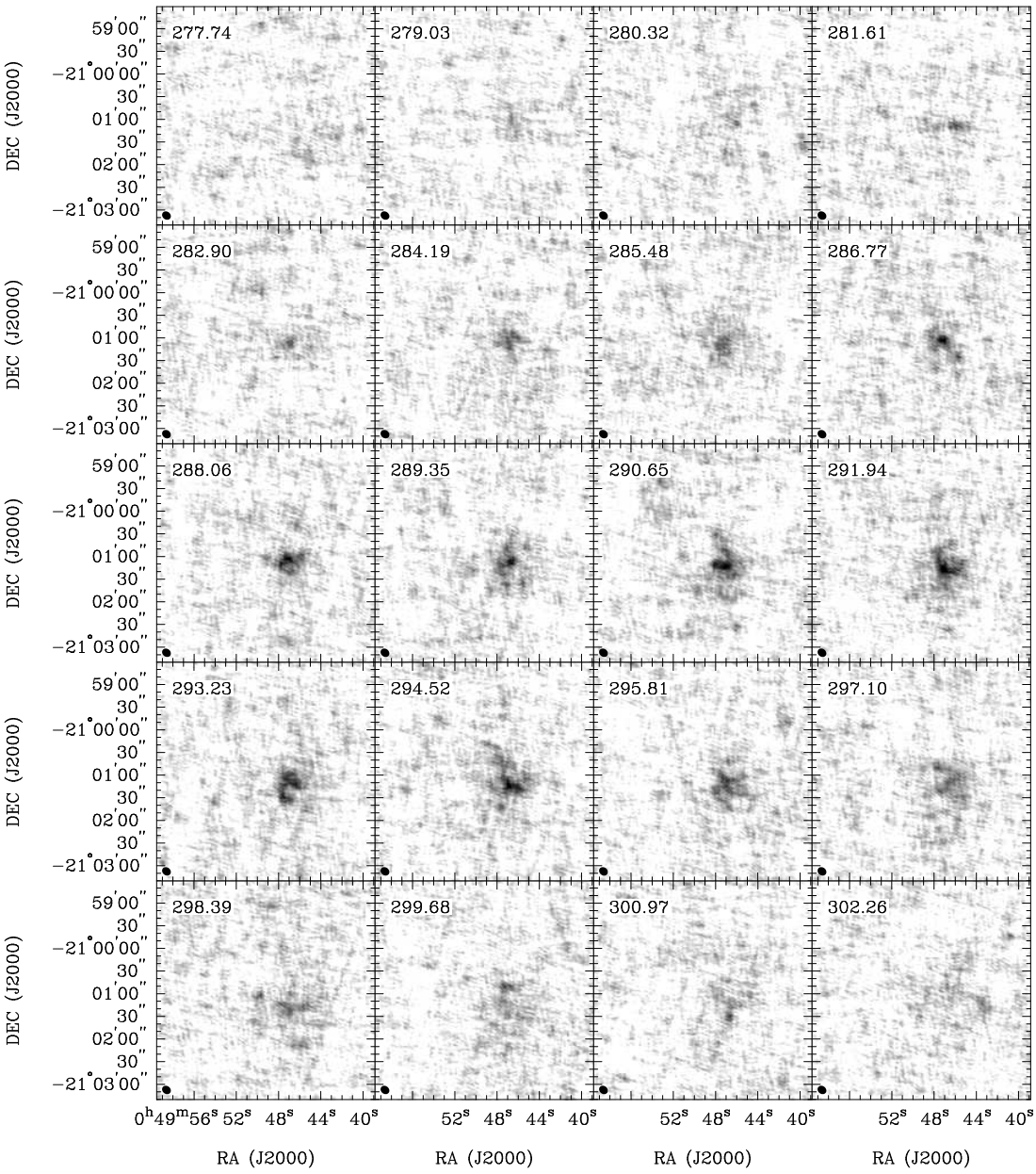

Figure 2.4 **DDO 6:** Channel maps based on the natural-weighted cube (grayscale range: -0.02 to $13.3\,\mathrm{mJy\,beam^{-1}}$). Every channel is shown (channel width $0.6\,\mathrm{km\ s^{-1}}$) and each map has the same size as the moment maps in the following panels.

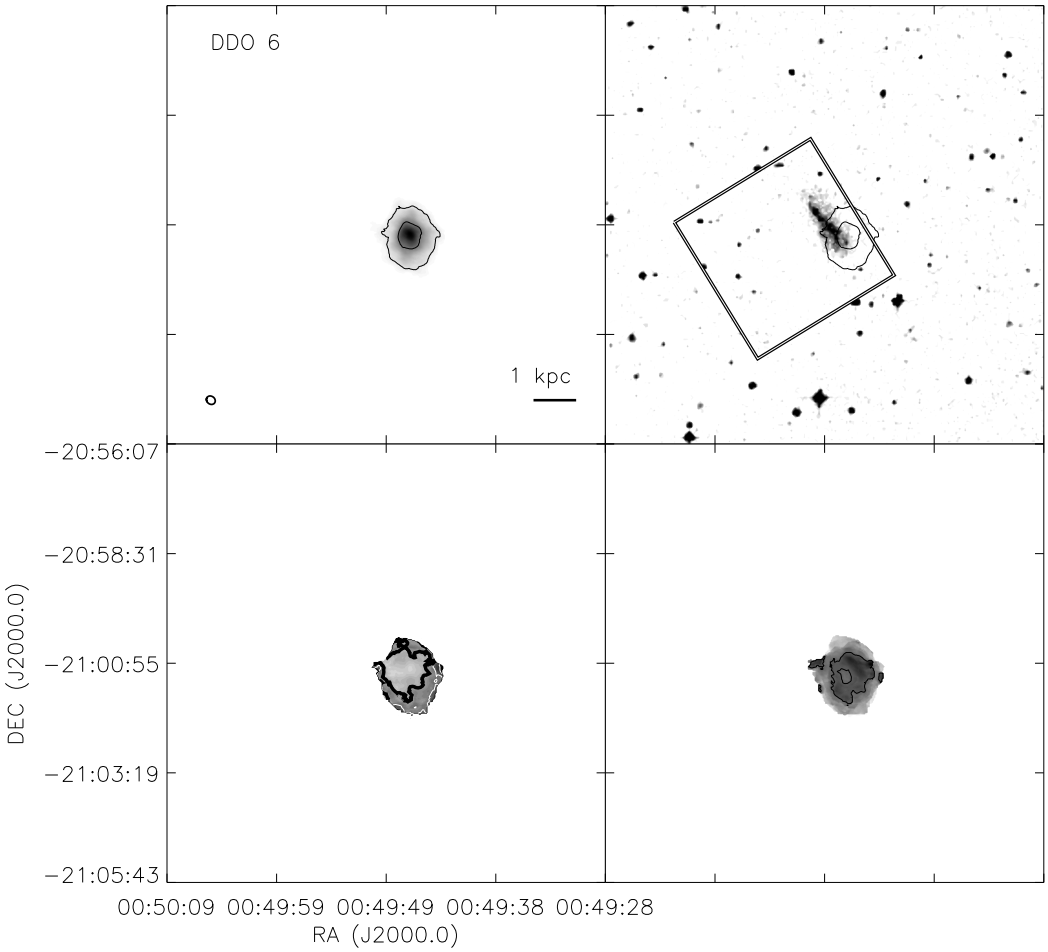

Figure 2.4 continued. *Top left:* The integrated H I intensity map for DDO 6. The greyscale covers a range from $1{\times}10^{19}$ to $9.4 \times 10^{20}\,\mathrm{cm}^{-2}$ with contours of $1{\times}10^{20}$ and $5{\times}10^{20}\,\mathrm{cm}^{-2}$. *Top Right:* An optical image from the DSS with the same column density contours overlaid. The HST ACS footprint is the field covered by the ANGST survey. *Bottom Left:* The H I velocity field. Black contours (lighter gray scale) indicate approaching emission, white contours (darker gray scale) receding emission. The thick black contour is the central velocity ($\mathrm{v}_{cen} = 292.5\,\mathrm{km\,s}^{-1}$) and the isovelocity contours are spaced by $\Delta\mathrm{v} = 3\,\mathrm{km\,s}^{-1}$. *Bottom Right:* The H I velocity dispersion. A contour is plotted at $5\,\mathrm{km\,s}^{-1}$.

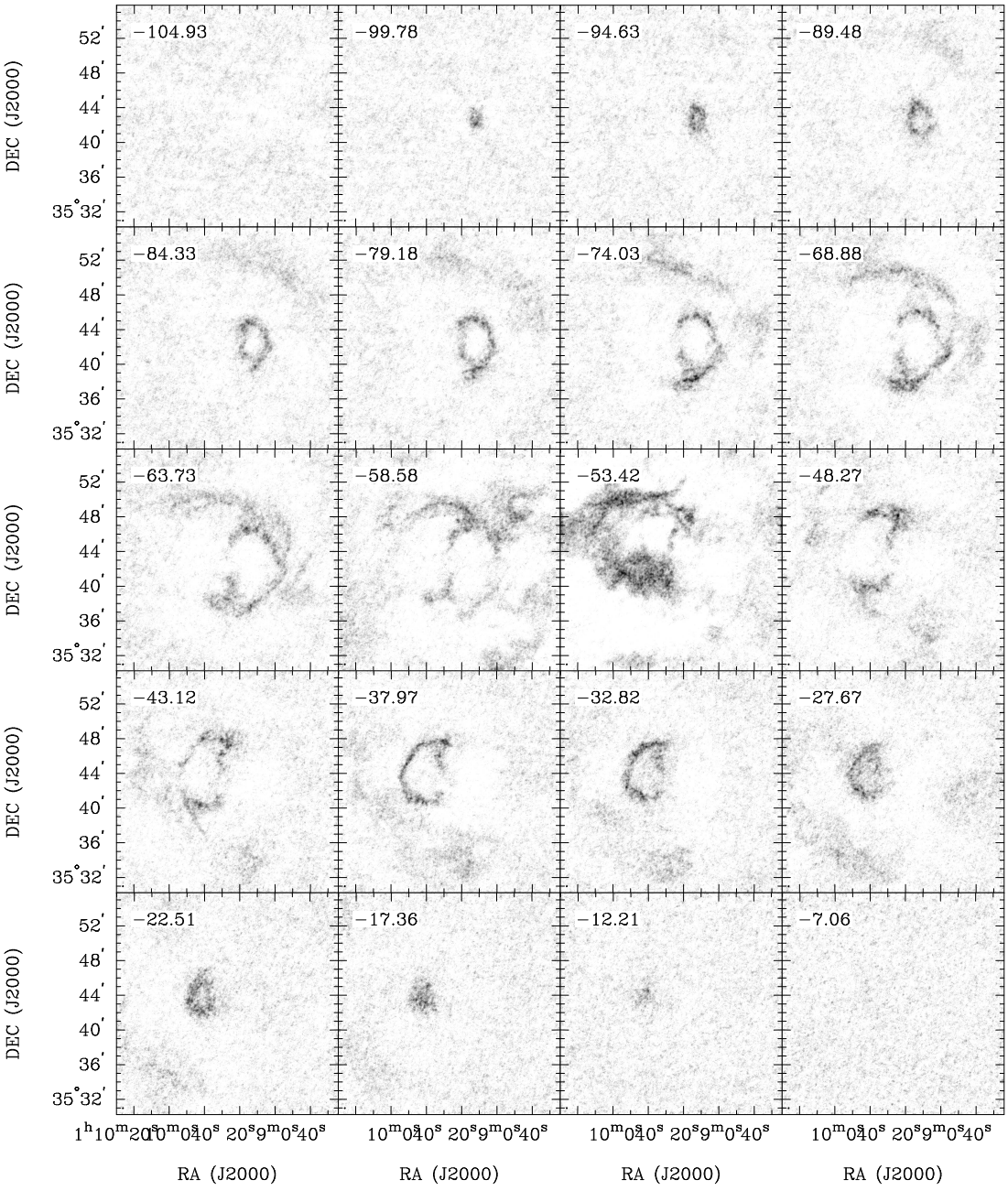

Figure 2.5 **NGC 404:** Channel maps based on the natural-weighted cube (grayscale range: −0.02 to 8.5 mJy beam^{-1}). Every channel is shown (channel width 2.6 km s^{-1}) and each map has the same size as the moment maps in the following panels. Confusion with H I emission from the Milky Way is present in this galaxy between velocities −58 to −50 km s^{-1} and can be seen in two of the above channels.

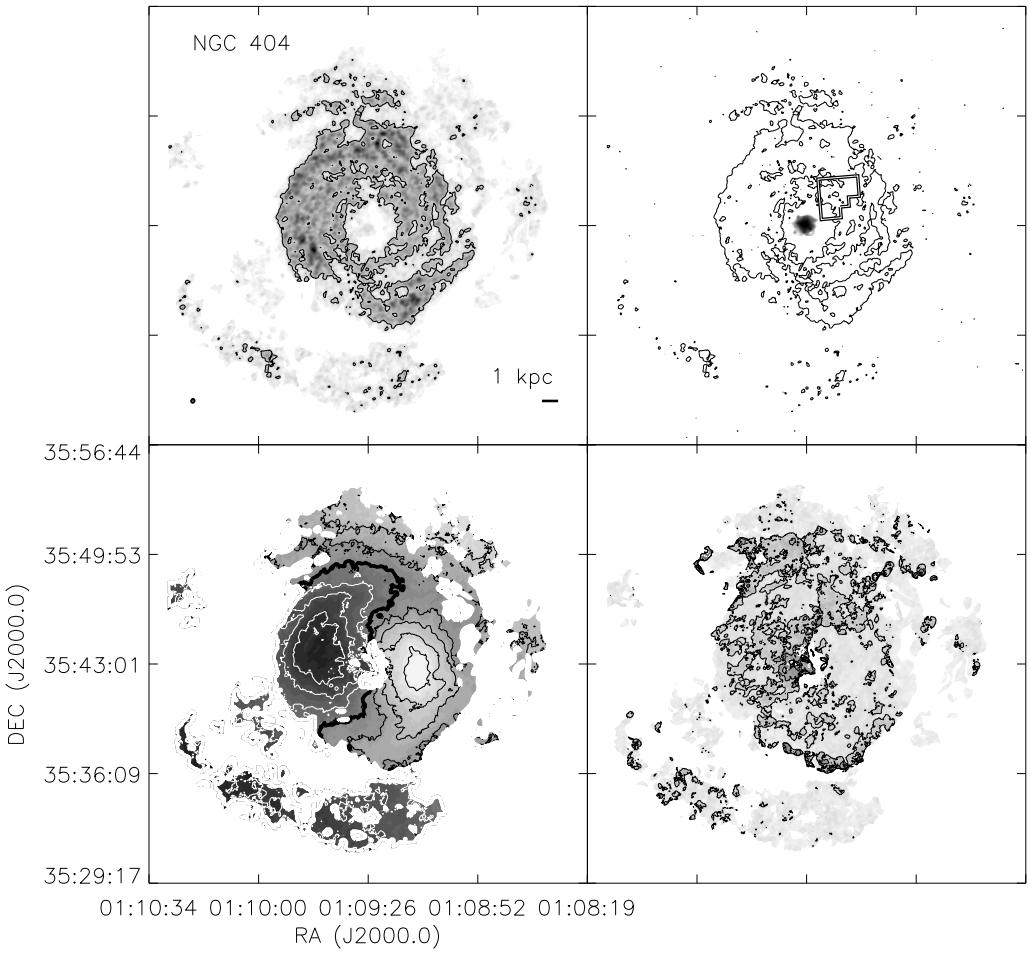

Figure 2.5 continued. *Top left:* The integrated H I intensity map for NGC 404. The greyscale covers a range from $1{\times}10^{19}$ to $5.0 \times 10^{20}\,\mathrm{cm}^{-2}$ with contours of $1{\times}10^{20}\,\mathrm{cm}^{-2}$ and $5{\times}10^{20}$ cm^{-2}. *Top Right:* An optical image from the DSS with the same column density contours overlaid. The HST WFPC2 footprint is the field covered by the ANGST survey. The bright, large disk in the lower right is a foreground star. *Bottom Left:* The H I velocity field. Black contours (lighter gray scale) indicate approaching emission, white contours (darker gray scale) receding emission. The thick black contour is the central velocity ($\mathrm{v}_{cen} = -54.0\,\mathrm{km\,s}^{-1}$) and the isovelocity contours are spaced by $\Delta\mathrm{v} = 10\,\mathrm{km\,s}^{-1}$. *Bottom Right:* The H I velocity dispersion. Contours are plotted at 5, 10, 15, and $20\,\mathrm{km\,s}^{-1}$.

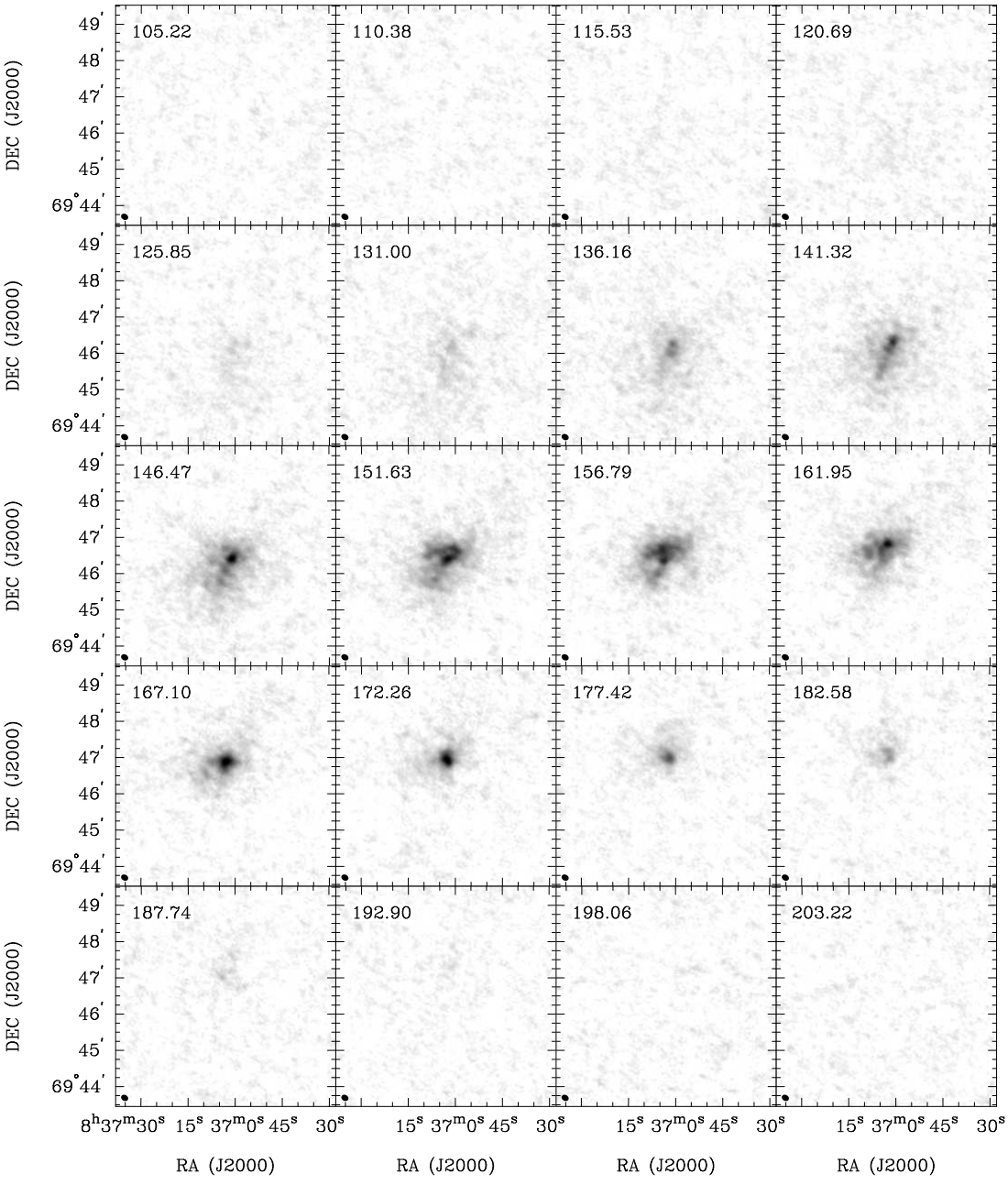

Figure 2.6 **UGC 4483:** Channel maps based on the natural-weighted cube (grayscale range: -0.02 to $14.8\,\mathrm{mJy\,beam^{-1}}$). Every channel is shown (channel width $2.6\,\mathrm{km\ s^{-1}}$) and each map has the same size as the moment maps in the following panels.

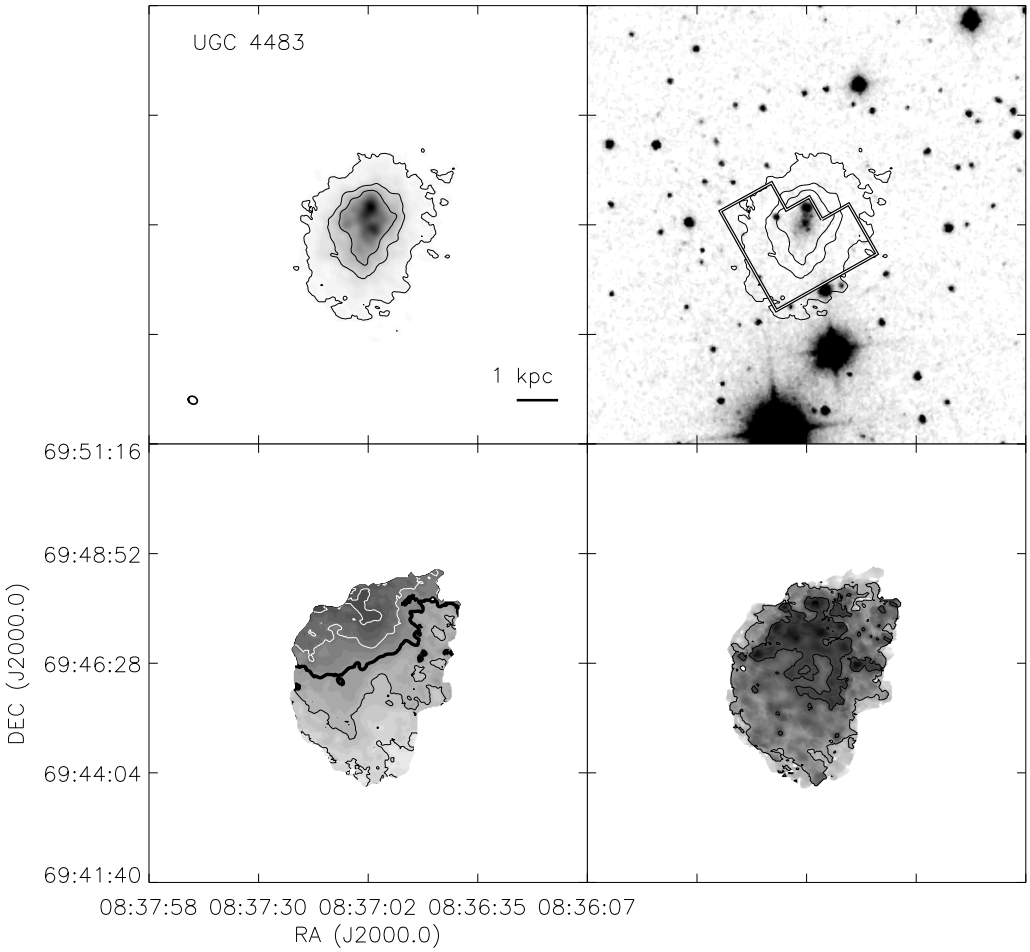

Figure 2.6 continued. *Top left:* The integrated H I intensity map for UGC 4483. The greyscale covers a range from 1×10^{19} to 3.2×10^{21} cm^{-2} with contours of 1×10^{20}, 5×10^{20}, and 1×10^{21} cm^{-2}. *Top Right:* An optical image from the DSS with the same column density contours overlaid. The HST WFPC2 footprint is the field covered by the ANGST survey. *Bottom Left:* The H I velocity field. Black contours (lighter gray scale) indicate approaching emission, white contours (darker gray scale) receding emission. The thick black contour is the central velocity (v_{cen} = 153.9 km s^{-1}) and the isovelocity contours are spaced by Δv = 10 km s^{-1}. *Bottom Right:* The H I velocity dispersion. Contours are plotted at 5 and 10 km s^{-1}.

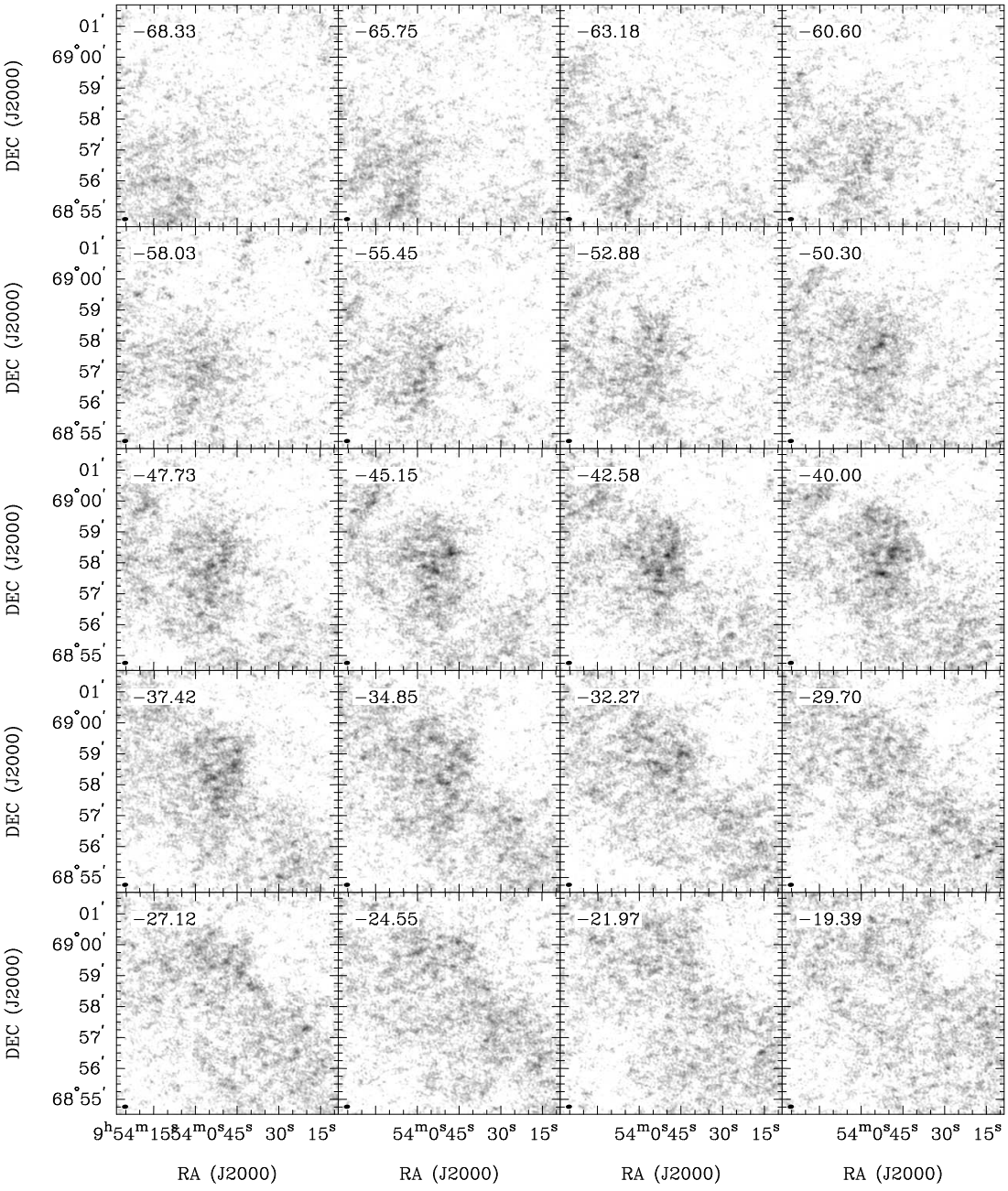

Figure 2.7 **BK3N:** Channel maps based on the natural-weighted cube (grayscale range: -0.02 to 12.9 mJy beam^{-1}). Every third channel is shown (channel width 0.6 km s^{-1}) and each map has the same size as the moment maps in the following panels. H I emission from M81 is present in every channel of the data cube.

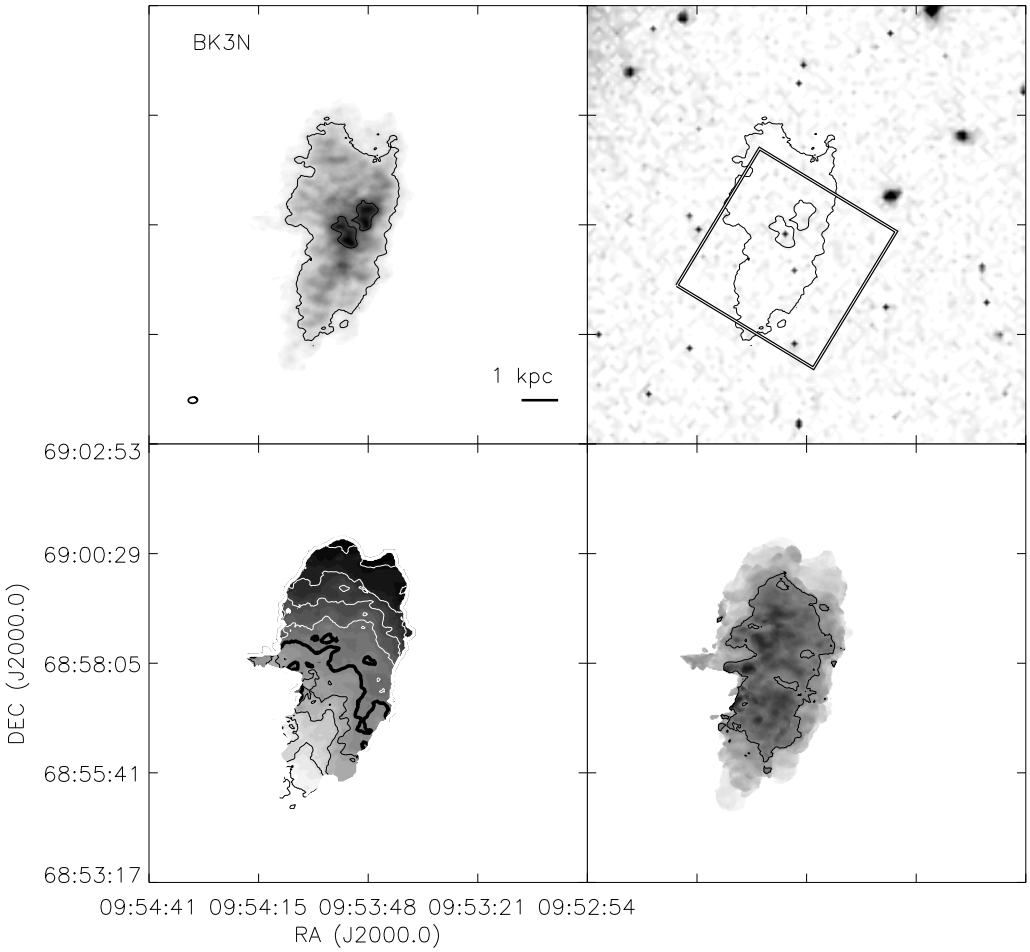

Figure 2.7 continued. *Top left:* The integrated H I intensity map for BK3N. The greyscale covers a range from $1{\times}10^{19}$ to $7.1 \times 10^{20}\,\mathrm{cm}^{-2}$ withcontours of $1{\times}10^{20}$ and $5{\times}10^{20}$ cm^{-2}. *Top Right:* An optical image from the SDSS with the same column density contours overlaid. The HST ACS footprint is the field covered by the ANGST survey. *Bottom Left:* The H I velocity field. Black contours (lighter gray scale) indicate approaching emission, white contours (darker gray scale) receding emission. The thick black contour is the central velocity ($\mathrm{v}_{cen} = -42.5\,\mathrm{km\,s}^{-1}$) and the isovelocity contours are spaced by $\Delta\mathrm{v} = -5\,\mathrm{km\,s}^{-1}$. *Bottom Right:* The H I velocity dispersion. Contours are plotted at 5 and $10\,\mathrm{km\,s}^{-1}$.

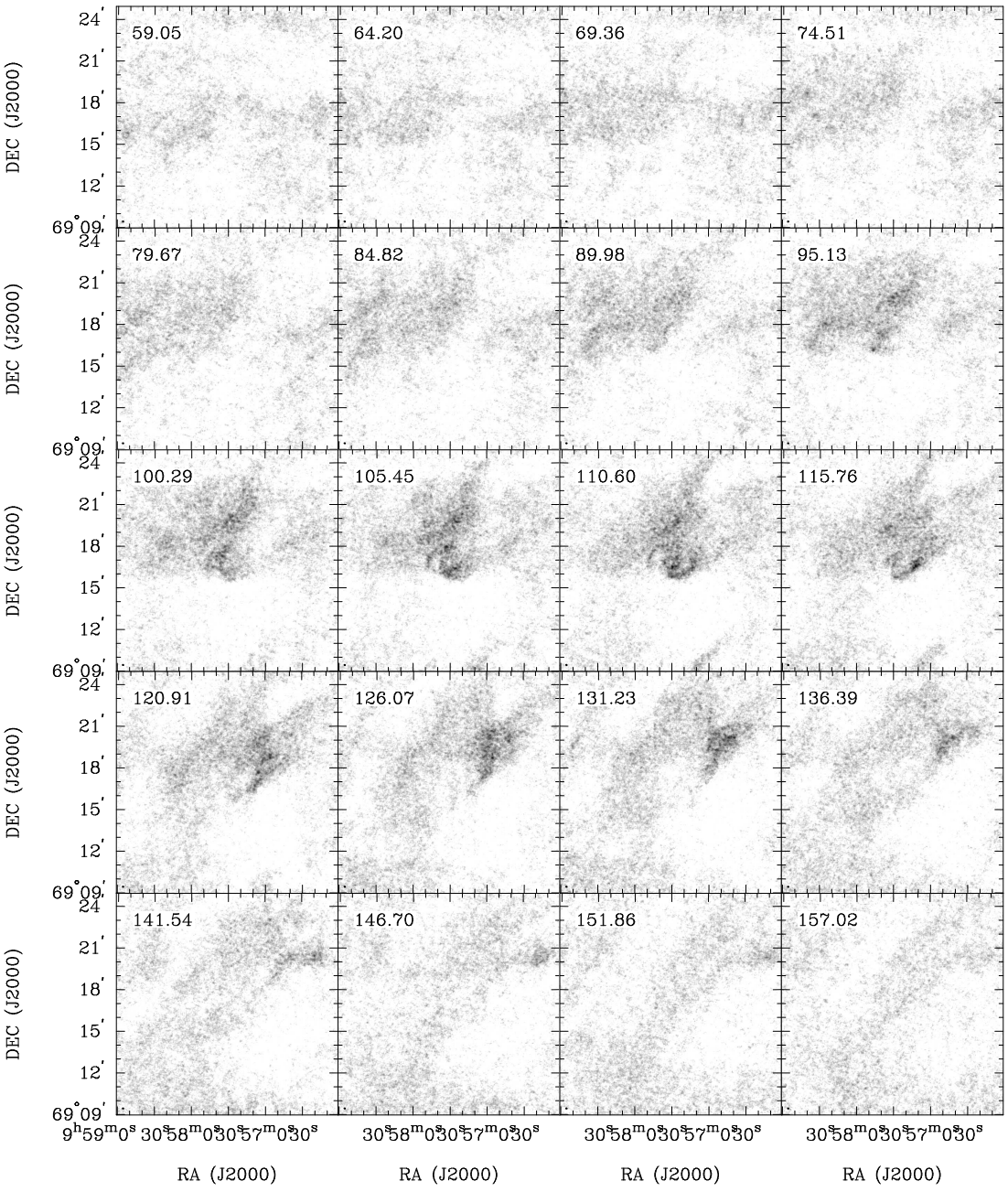

Figure 2.8 **AO 0952+69:** Channel maps based on the natural-weighted cube (grayscale range: -0.02 to $10.5\,\mathrm{mJy\,beam^{-1}}$). Every third channel is shown (channel width $1.3\,\mathrm{km\ s^{-1}}$) and each map has the same size as the moment maps in the following panels. This field is in the M81 group and therefore tidal H I from member interactions is also visible.

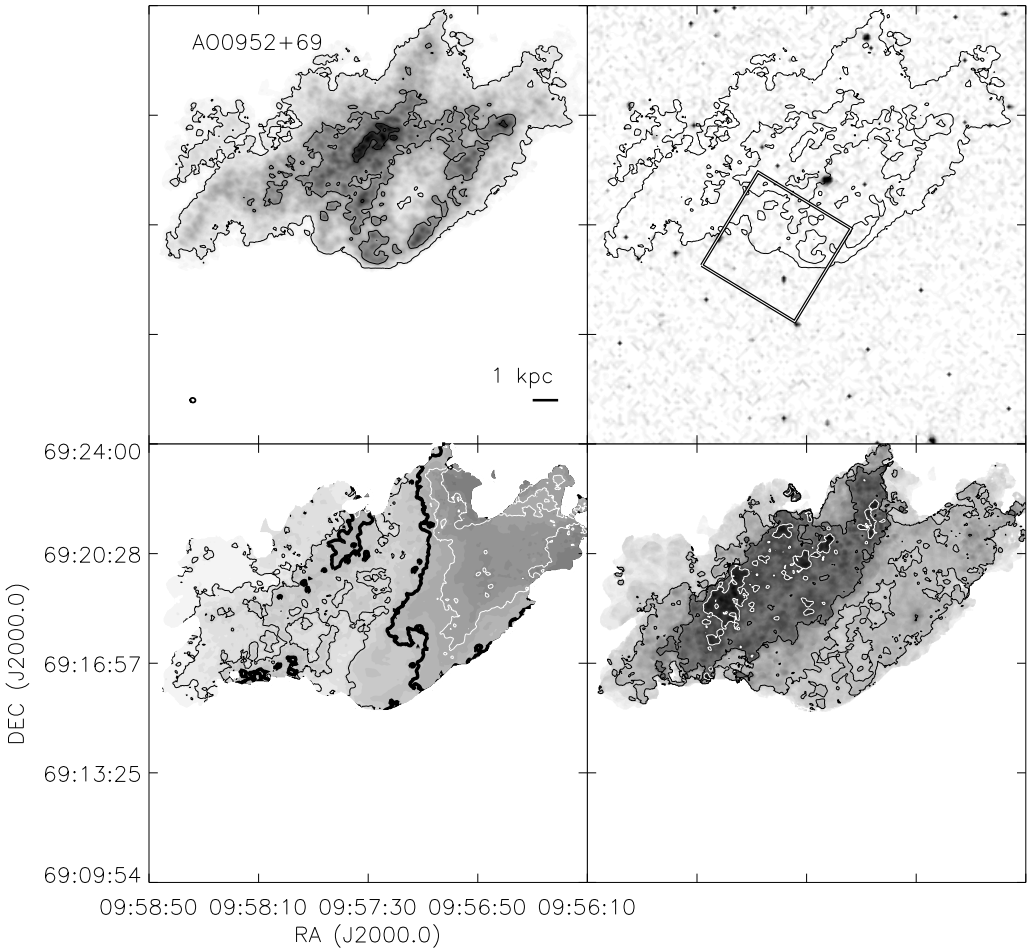

Figure 2.8 continued. *Top left:* The integrated H I intensity map for AO 0952+69. The greyscale covers a range from $1{\times}10^{19}$ to $1.13 \times 10^{21}\,\mathrm{cm}^{-2}$ with contours of $1{\times}10^{20}$, $5{\times}10^{20}$, and $1{\times}10^{21}\,\mathrm{cm}^{-2}$. *Top Right:* An optical image from the SDSS with the same column density contours overlaid. The HST ACS footprint is the field covered by the ANGST survey. *Bottom Left:* The H I velocity field. Black contours (lighter gray scale) indicate approaching emission, white contours (darker gray scale) receding emission. The thick black contour is the central velocity ($\mathrm{v}_{cen} = 112.8\,\mathrm{km\,s}^{-1}$) and the isovelocity contours are spaced by $\Delta\mathrm{v} = 10\,\mathrm{km\,s}^{-1}$. *Bottom Right:* The H I velocity dispersion. Contours are plotted at 5, 10, and $15\,\mathrm{km\,s}^{-1}$.

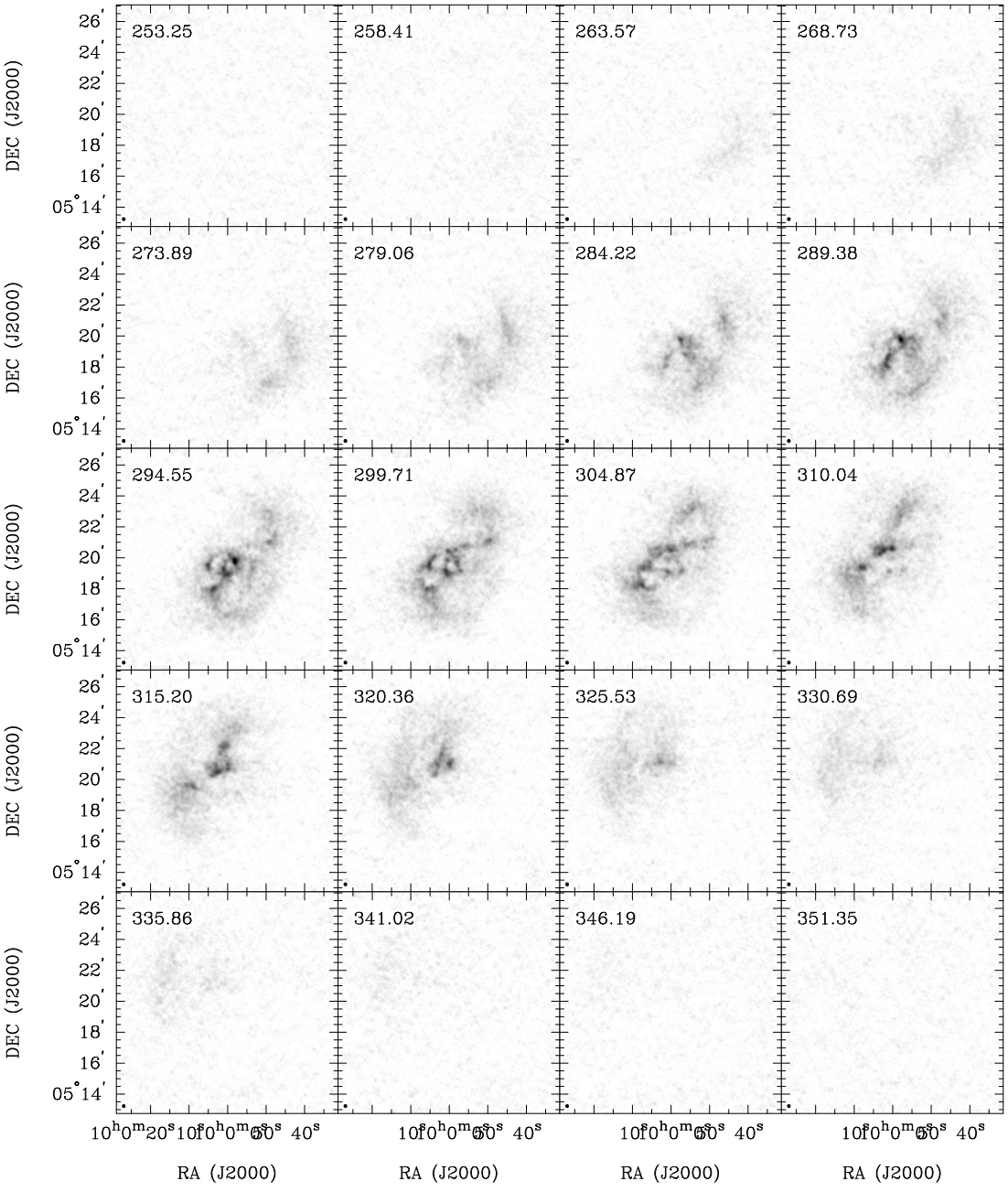

Figure 2.9 **Sextans B:** Channel maps based on the natural-weighted cube (grayscale range: -0.02 to $25.3\,\mathrm{mJy\,beam^{-1}}$). Every third channel is shown (channel width $1.3\,\mathrm{km\ s^{-1}}$) and each map has the same size as the moment maps in the following panels.

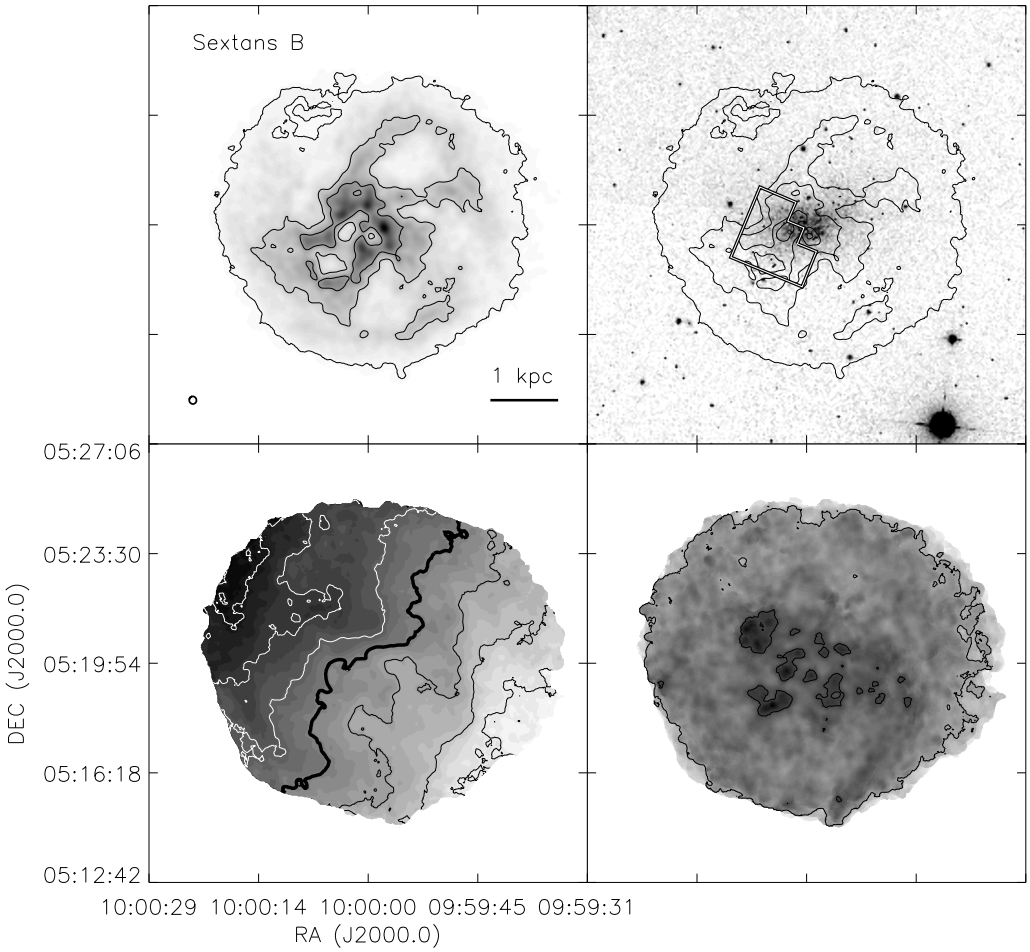

Figure 2.9 continued. *Top left:* The integrated H I intensity map for Sextans B. The greyscale covers a range from 1×10^{19} to 2.6×10^{21} cm^{-2} with contours of 1×10^{20}, 5×10^{20}, and 1×10^{21} cm^{-2}. *Top Right:* An optical image from the SDSS with the same column density contours overlaid. The HST WFPC2 footprint is the field covered by the ANGST survey. *Bottom Left:* The H I velocity field. Black contours (lighter gray scale) indicate approaching emission, white contours (darker gray scale) receding emission. The thick black contour is the central velocity ($v_{cen} = 302.2\,\mathrm{km\,s^{-1}}$) and the isovelocity contours are spaced by $\Delta v = 10\,\mathrm{km\,s^{-1}}$. *Bottom Right:* The H I velocity dispersion. Contours are plotted at 5 and $10\,\mathrm{km\,s^{-1}}$.

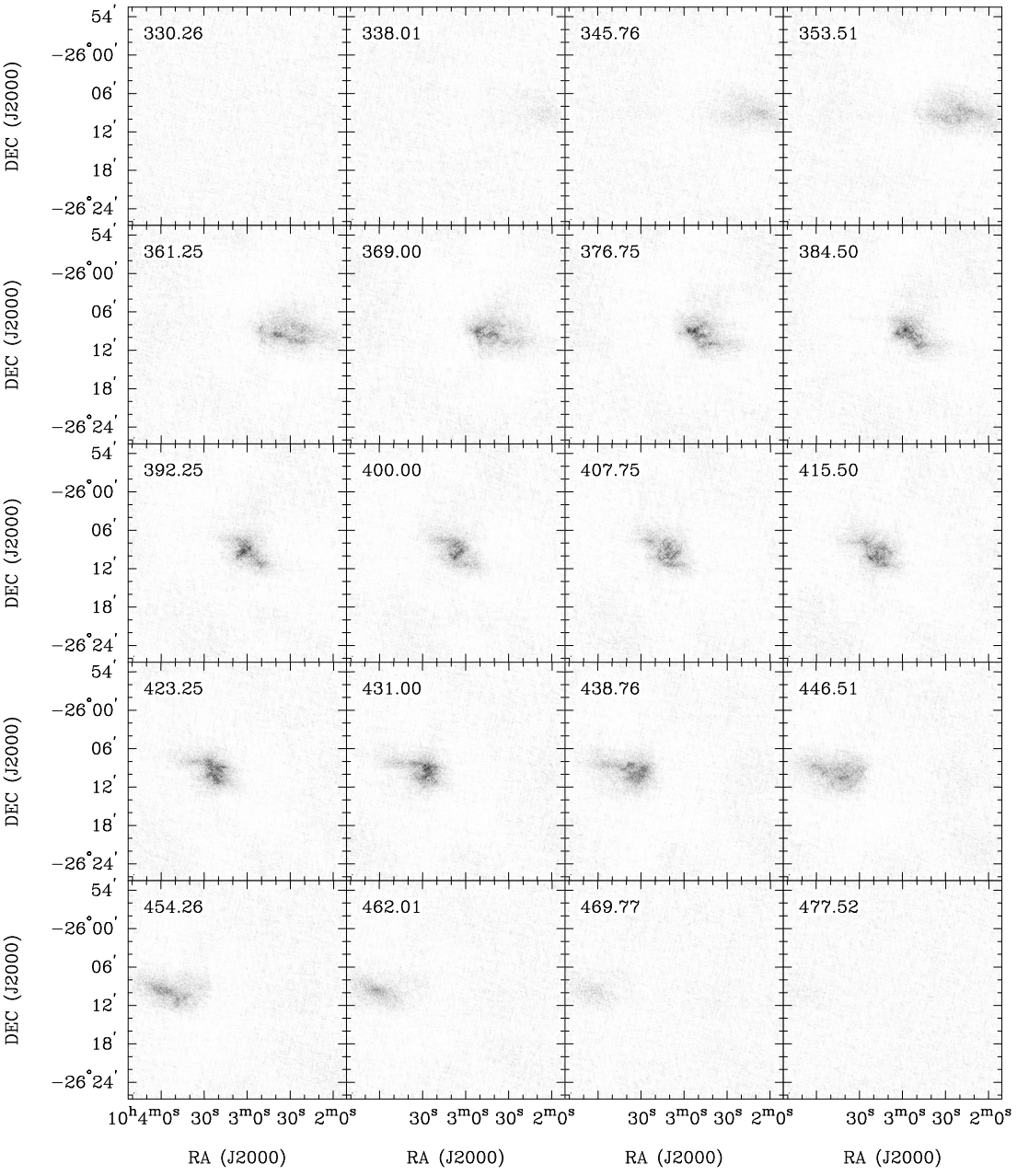

Figure 2.10 **NGC 3109:** Channel maps based on the natural-weighted cube (grayscale range: -0.02 to $31.7\,\mathrm{mJy\,beam^{-1}}$). Every fifth channel is shown (channel width $1.3\,\mathrm{km\ s^{-1}}$) and each map has the same size as the moment maps in the following panels.

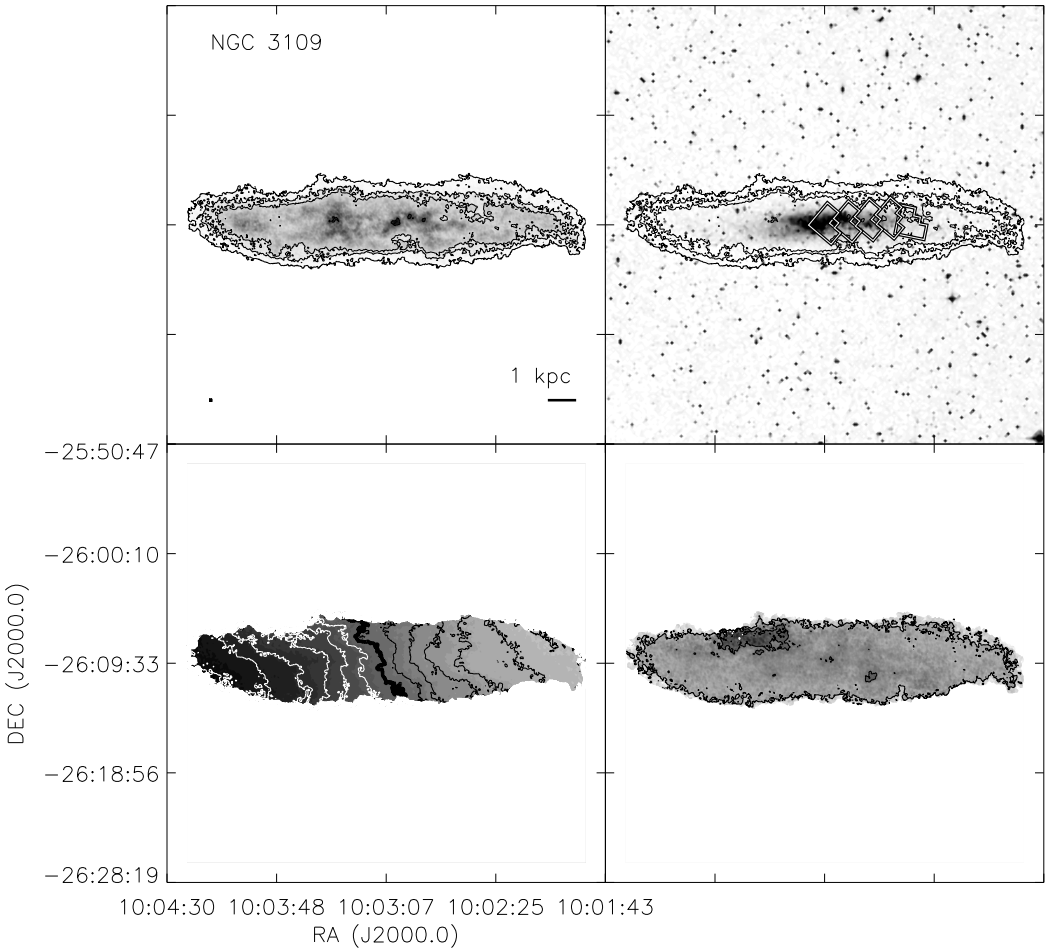

Figure 2.10 continued. *Top left:* The integrated H I intensity map for NGC 3109. The grayscale covers a range from 1×10^{19} to 6.6×10^{21} cm^{-2} with contours of 1×10^{20}, 5×10^{20}, 1×10^{21}, and 5×10^{21} cm^{-2}. *Top Right:* An optical image from the DSS with the same column density contours overlaid. The HST WFPC2 footprints are the fields covered by the ANGST survey. *Bottom Left:* The H I velocity field. Black contours (lighter grayscale) indicate approaching emission, white contours (darker grayscale) receding emission. The thick black contour is the central velocity ($v_{cen} = 405.1\,\mathrm{km\,s^{-1}}$) and the isovelocity contours are spaced by $\Delta v = 10\,\mathrm{km\,s^{-1}}$. *Bottom Right:* The H I velocity dispersion. Contours are plotted at 5, 10, and 15 $\mathrm{km\,s^{-1}}$.

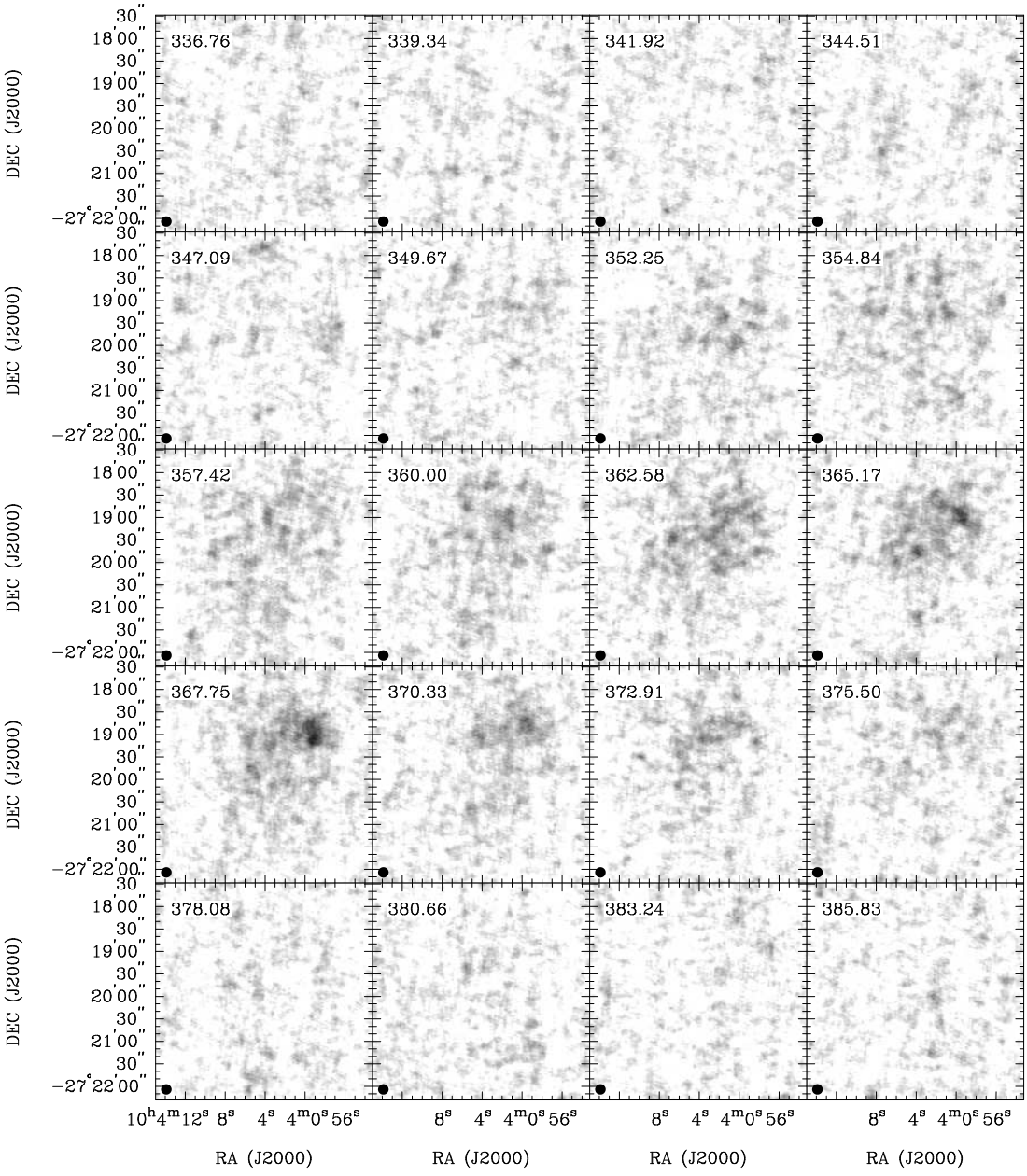

Figure 2.11 **Antlia:** Channel maps based on the natural-weighted cube (grayscale range: -0.02 to $8.8\,\mathrm{mJy\,beam^{-1}}$) and each map has the same size as the moment maps in the following panels.

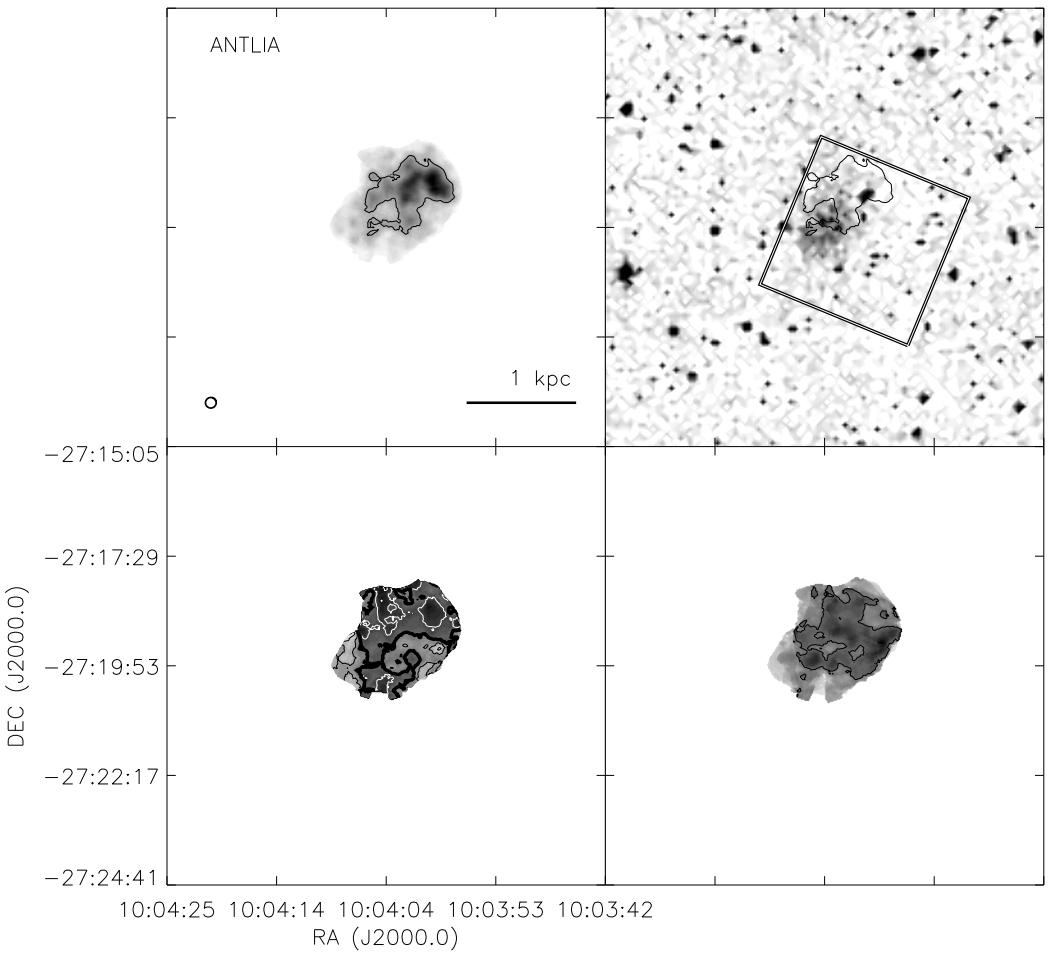

Figure 2.11 continued. *Top left:* The integrated H I intensity map for Antlia. The grayscale covers a range from 1×10^{19} to $2.9\times10^{20}\,\mathrm{cm}^{-2}$ with a contour of $1\times10^{20}\,\mathrm{cm}^{-2}$. *Top Right:* An optical image from the DSS with the same column density contours overlaid. The HST ACS footprint is the field covered by the ANGST survey. *Bottom Left:* The H I velocity field. Black contours (lighter grayscale) indicate approaching emission, white contours (darker grayscale) receding emission. The thick black contour is the central velocity ($\mathrm{v}_{cen} = 363.0\,\mathrm{km\,s}^{-1}$) and the isovelocity contours are spaced by $\Delta\mathrm{v} = 3\,\mathrm{km\,s}^{-1}$. *Bottom Right:* The H I velocity dispersion. A contour is plotted at $5\,\mathrm{km\,s}^{-1}$.

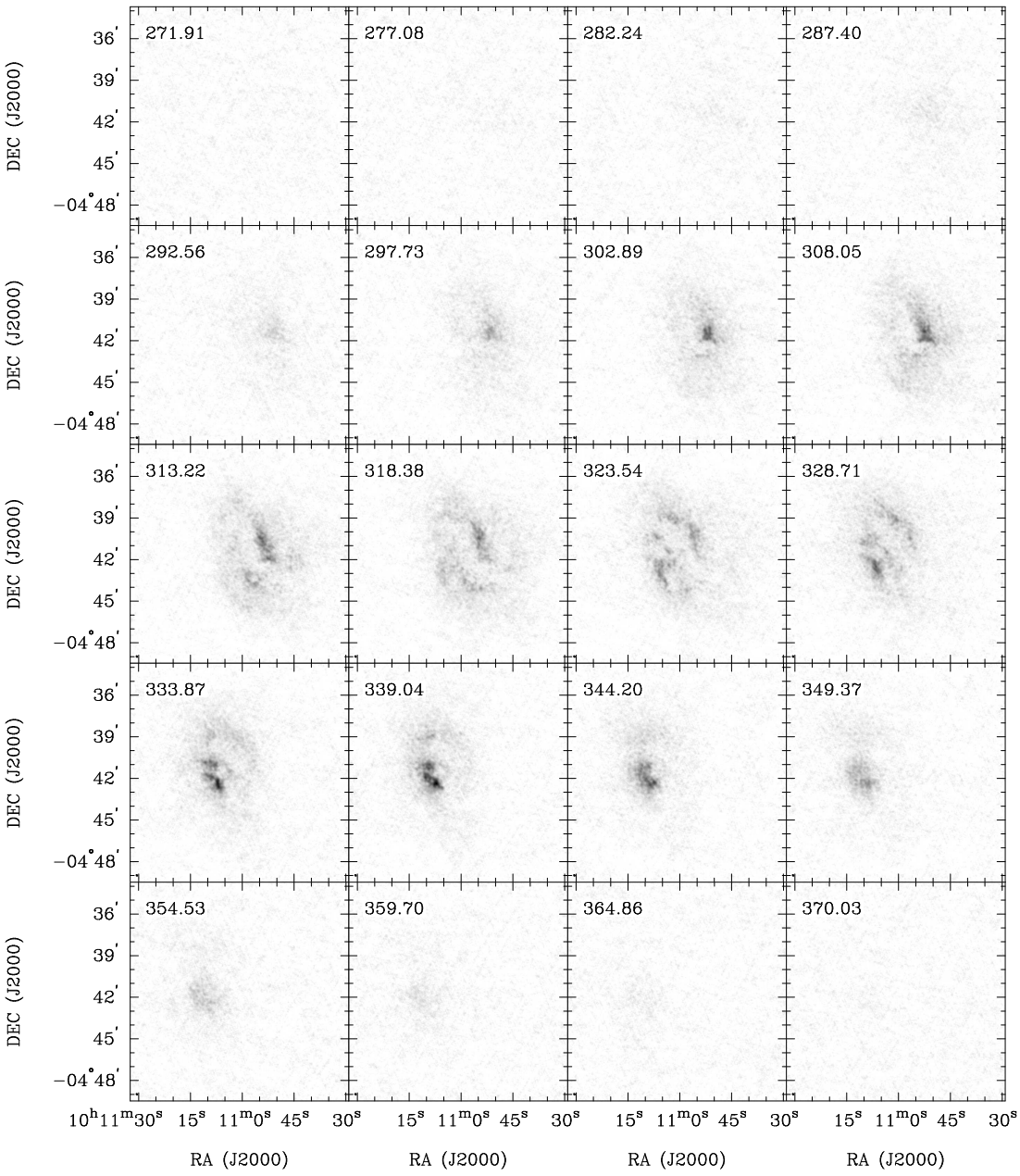

Figure 2.12 **Sextans A:** Channel maps based on the natural-weighted cube (grayscale range: -0.02 to $35.4\,\mathrm{mJy\,beam^{-1}}$). Every third channel is shown (channel width $1.3\,\mathrm{km\ s^{-1}}$) and each map has the same size as the moment maps in the following panels.

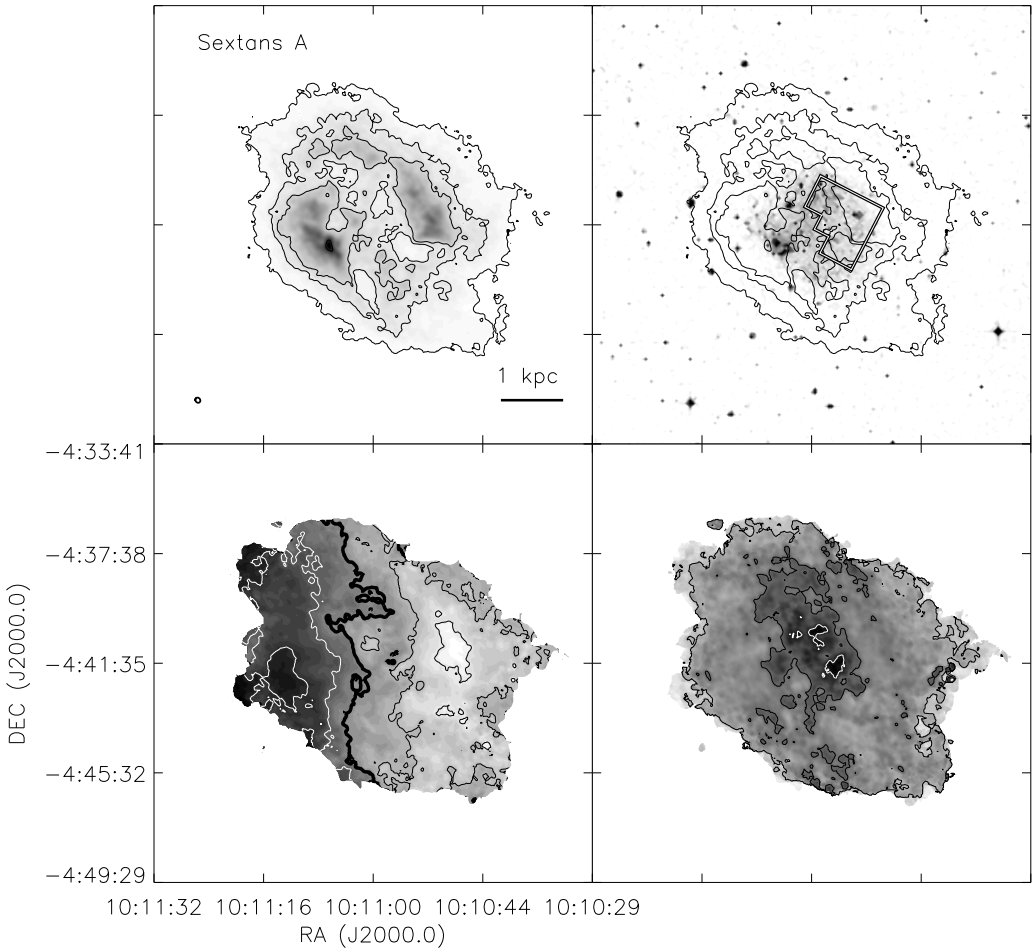

Figure 2.12 continued. *Top left:* The integrated H I intensity map for Sextans A. The greyscale covers a range from 1×10^{19} to 6.1×10^{21} cm^{-2} with contours of 1×10^{20}, 5×10^{20}, 1×10^{21}, and 5×10^{21} cm^{-2}. *Top Right:* An optical image from the DSS with the same column density contours overlaid. The HST WFPC2 footprint is the field covered by the ANGST survey. *Bottom Left:* The H I velocity field. Black contours (lighter gray scale) indicate approaching emission, white contours (darker gray scale) receding emission. The thick black contour is the central velocity ($v_{cen} = 324.8\,\mathrm{km\,s^{-1}}$) and the isovelocity contours are spaced by $\Delta v = 10\,\mathrm{km\,s^{-1}}$. *Bottom Right:* The H I velocity dispersion. Contours are plotted at 5, 10, and $15\,\mathrm{km\,s^{-1}}$.

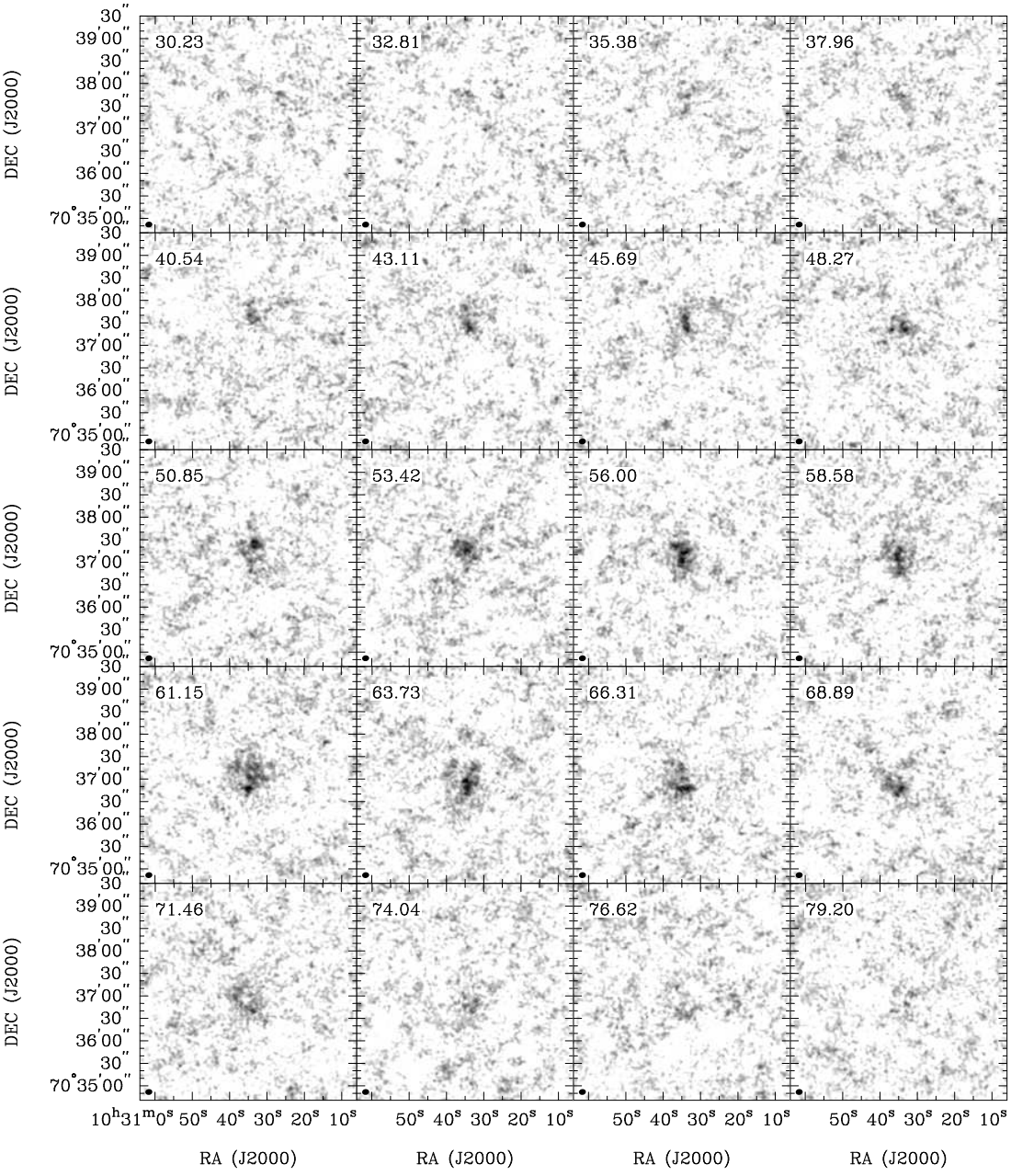

Figure 2.13 **DDO 82:** Channel maps based on the natural-weighted cube (grayscale range: -0.02 to 6.7 mJy beam^{-1}). Every channel is shown (channel width 1.3 km s^{-1}) and each map has the same size as the moment maps in the following panels.

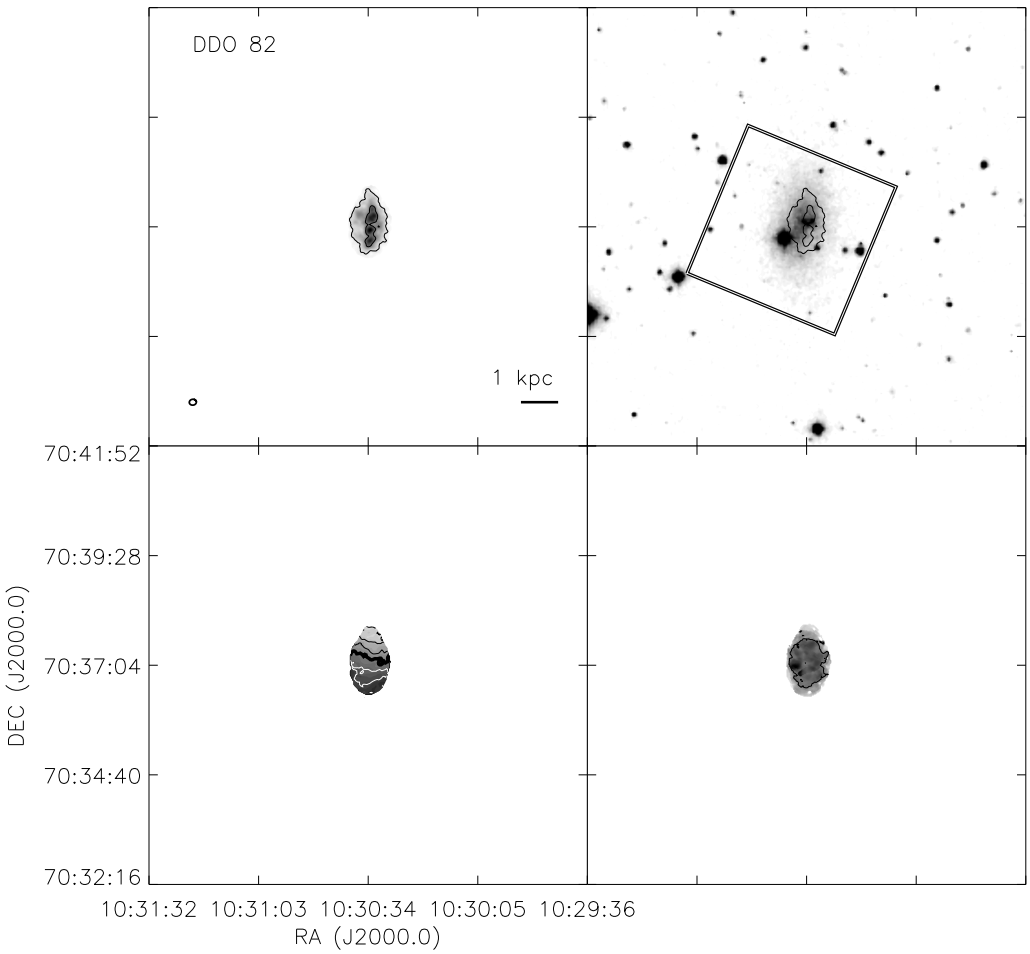

Figure 2.13 continued. *Top left:* The integrated H I intensity map for DDO 82. The greyscale covers a range from $1{\times}10^{19}$ to $9.3 \times 10^{20}\,\mathrm{cm}^{-2}$ with contours of $1{\times}10^{20}$ and $5{\times}10^{20}\,\mathrm{cm}^{-2}$. *Top Right:* An optical image from the DSS with the same column density contours overlaid. The HST ACS footprint is the field covered by the ANGST survey. *Bottom Left:* The H I velocity field. Black contours (lighter gray scale) indicate approaching emission, white contours (darker gray scale) receding emission. The thick black contour is the central velocity ($\mathrm{v}_{cen} = 56.2\,\mathrm{km\,s}^{-1}$) and the isovelocity contours are spaced by $\Delta\mathrm{v} = 5\,\mathrm{km\,s}^{-1}$. *Bottom Right:* The H I velocity dispersion. A contour is plotted at $5\,\mathrm{km\,s}^{-1}$.

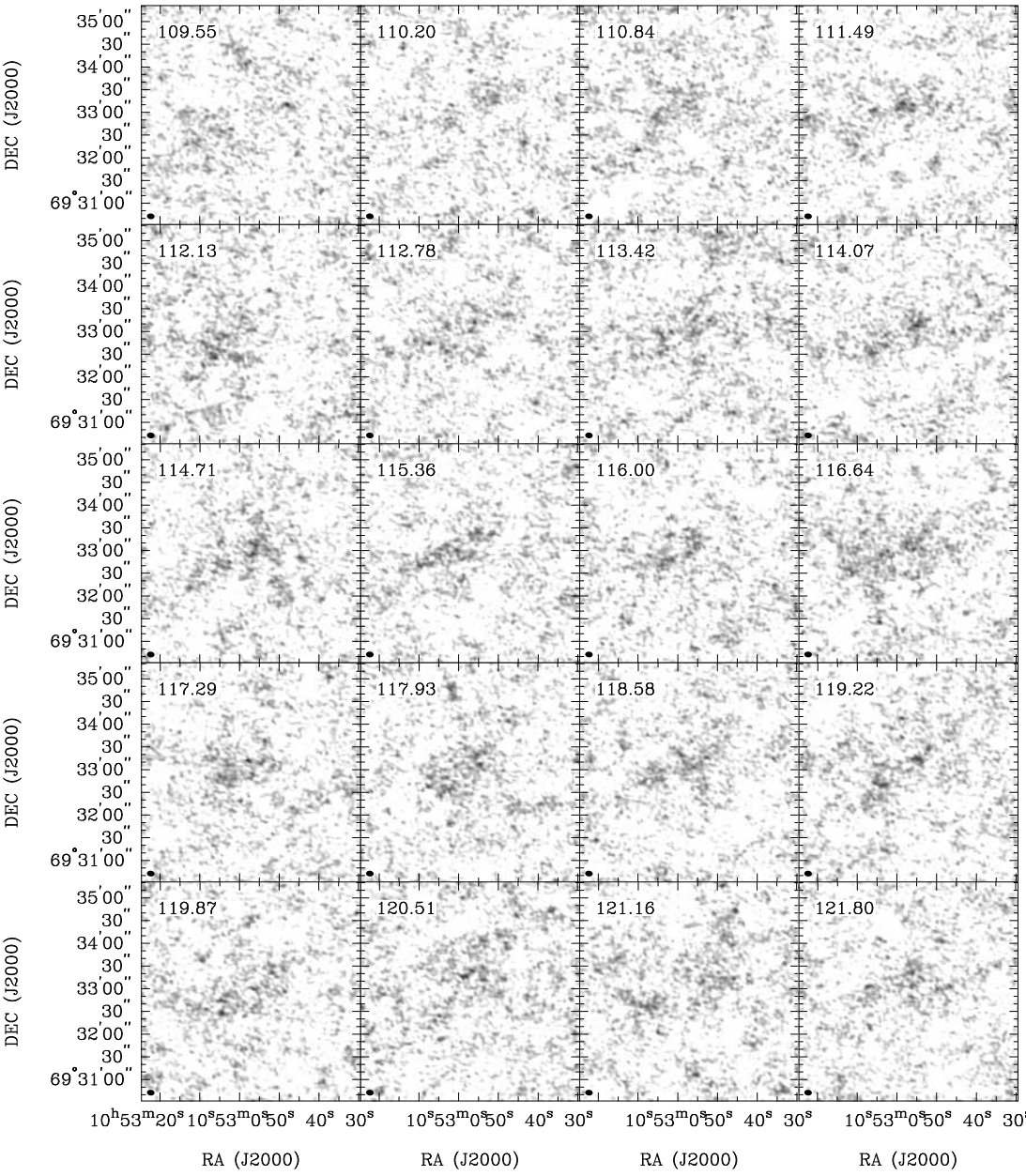

Figure 2.14 **KDG 73:** Channel maps based on the natural-weighted cube (grayscale range: -0.02 to $8.6\,\mathrm{mJy\,beam^{-1}}$). Every third channel is shown (channel width $0.6\,\mathrm{km\ s^{-1}}$) and each map has the same size as the moment maps in the following panels.

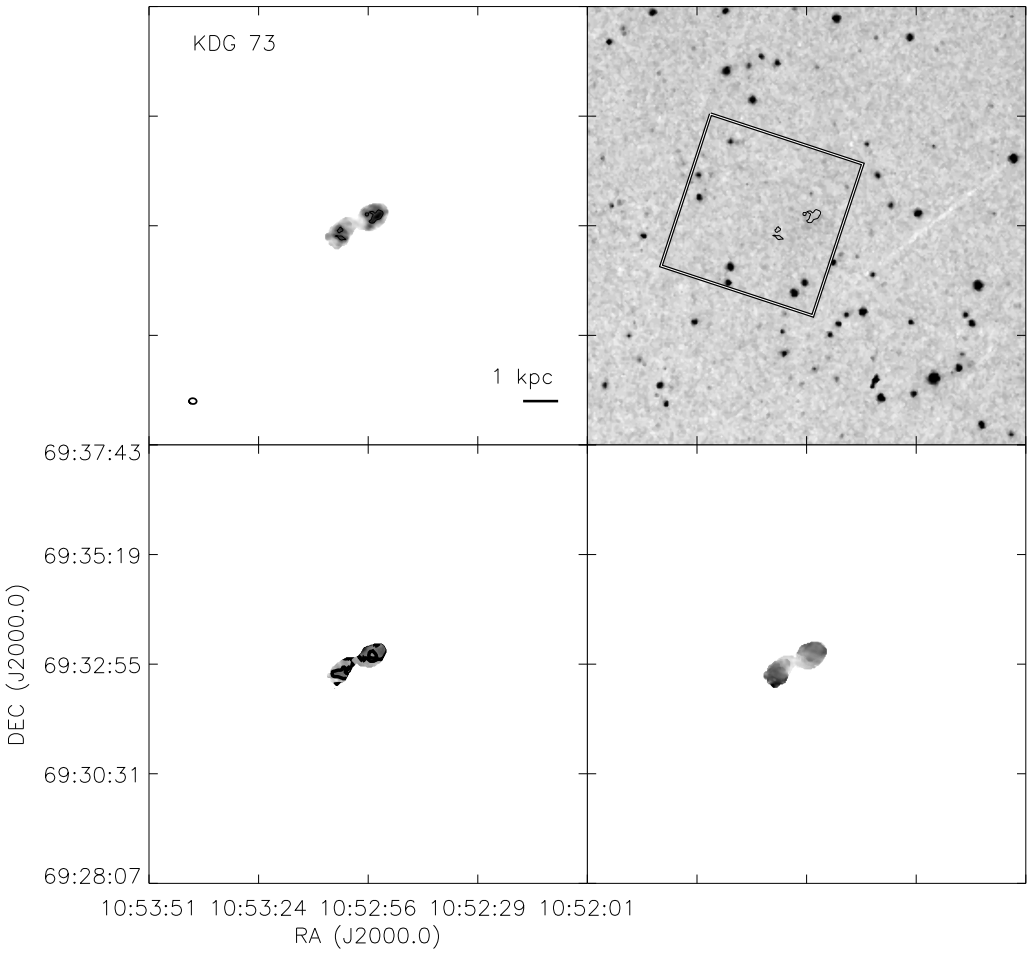

Figure 2.14 continued. *Top left:* The integrated H I intensity map for KDG 73. The greyscale covers a range from 1×10^{19} to $1.4\times10^{20}\,\mathrm{cm}^{-2}$ with a contour of $1\times10^{20}\,\mathrm{cm}^{-2}$. *Top Right:* An optical image from the DSS with the same column density contours overlaid. The HST ACS footprint is the field covered by the ANGST survey. *Bottom Left:* The H I velocity field. Black contours (lighter gray scale) indicate approaching emission, white contours (darker gray scale) receding emission. The thick black contour is the central velocity ($\mathrm{v}_{cen} = 116.3\,\mathrm{km\,s}^{-1}$) and the isovelocity contours are spaced by $\Delta\mathrm{v} = 10\,\mathrm{km\,s}^{-1}$. *Bottom Right:* The H I velocity dispersion.

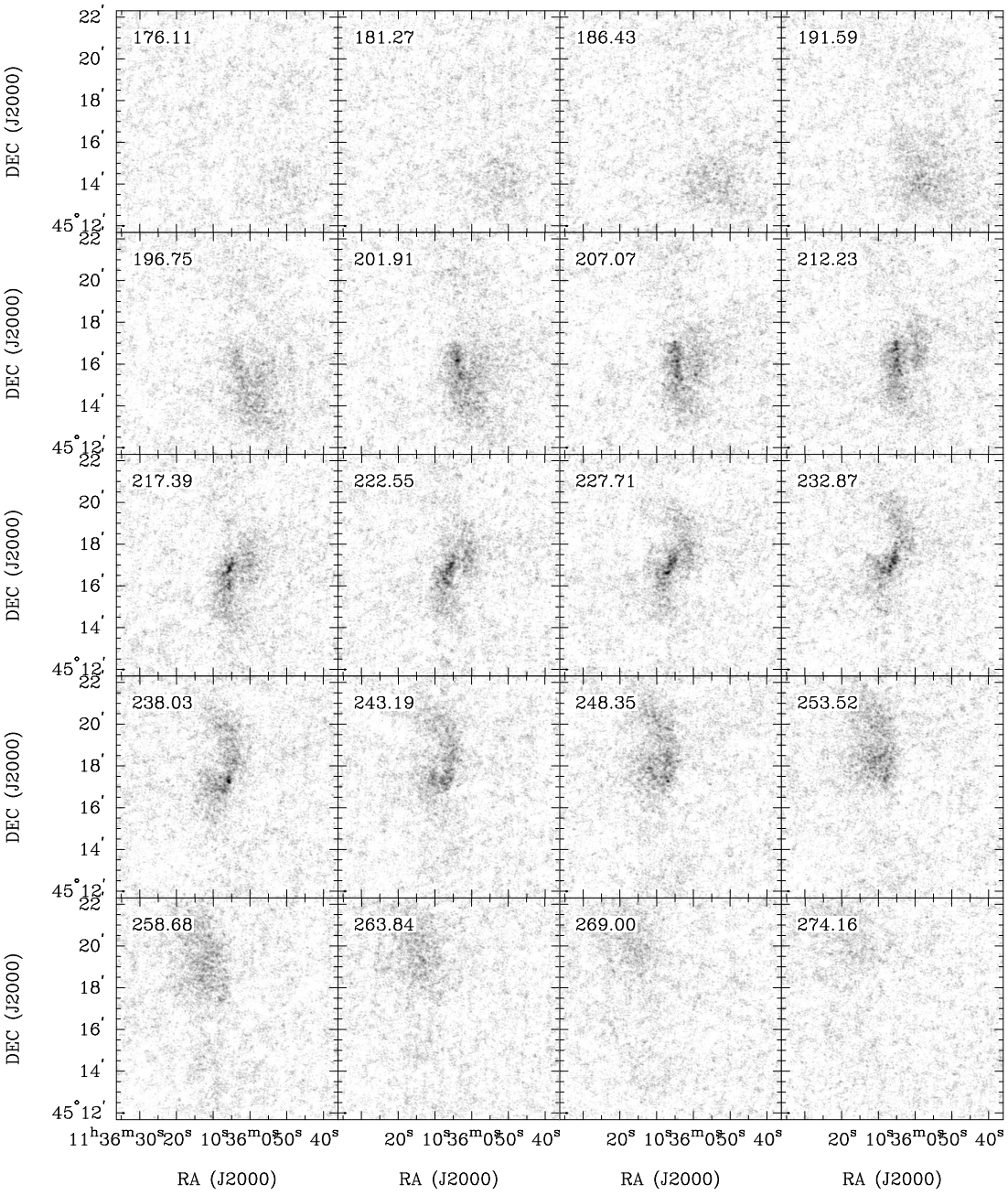

Figure 2.15 **NGC 3741:** Channel maps based on the natural-weighted cube (grayscale range: -0.02 to $9.6\,\mathrm{mJy\,beam^{-1}}$). Every third channel is shown (channel width $1.3\,\mathrm{km\ s^{-1}}$) and each map has the same size as the moment maps in the following panels.

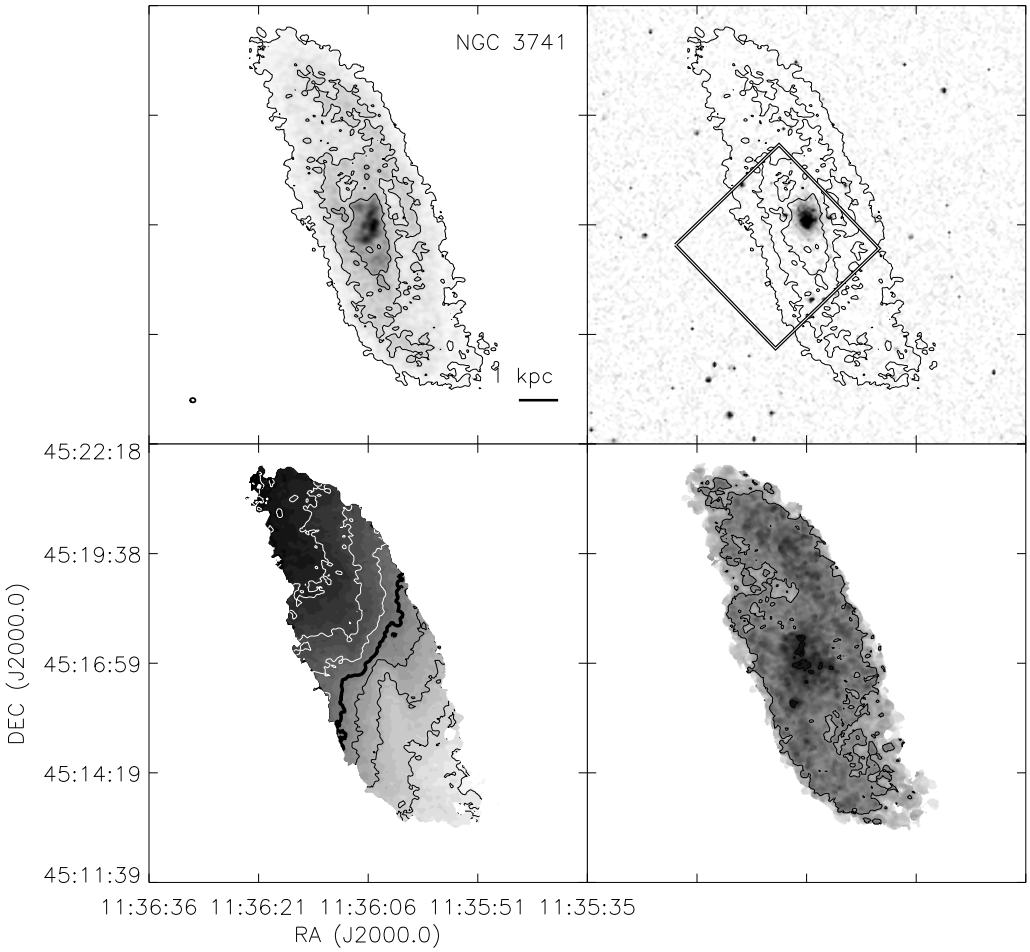

Figure 2.15 continued. *Top left:* The integrated H I intensity map for NGC 3741. The greyscale covers a range from 1×10^{19} to 3.4×10^{21} cm^{-2} with contours of 1×10^{20}, 5×10^{20}, and 1×10^{21} cm^{-2}. *Top Right:* An optical image from the SDSS with the same column density contours overlaid. The HST ACS footprint is the field covered by the ANGST survey. *Bottom Left:* The H I velocity field. Black contours (lighter gray scale) indicate approaching emission, white contours (darker gray scale) receding emission. The thick black contour is the central velocity (v_{cen} = 229.1 km s^{-1}) and the isovelocity contours are spaced by Δv = 10 km s^{-1}. *Bottom Right:* The H I velocity dispersion. Contours are plotted at 5 and 10 km s^{-1}.

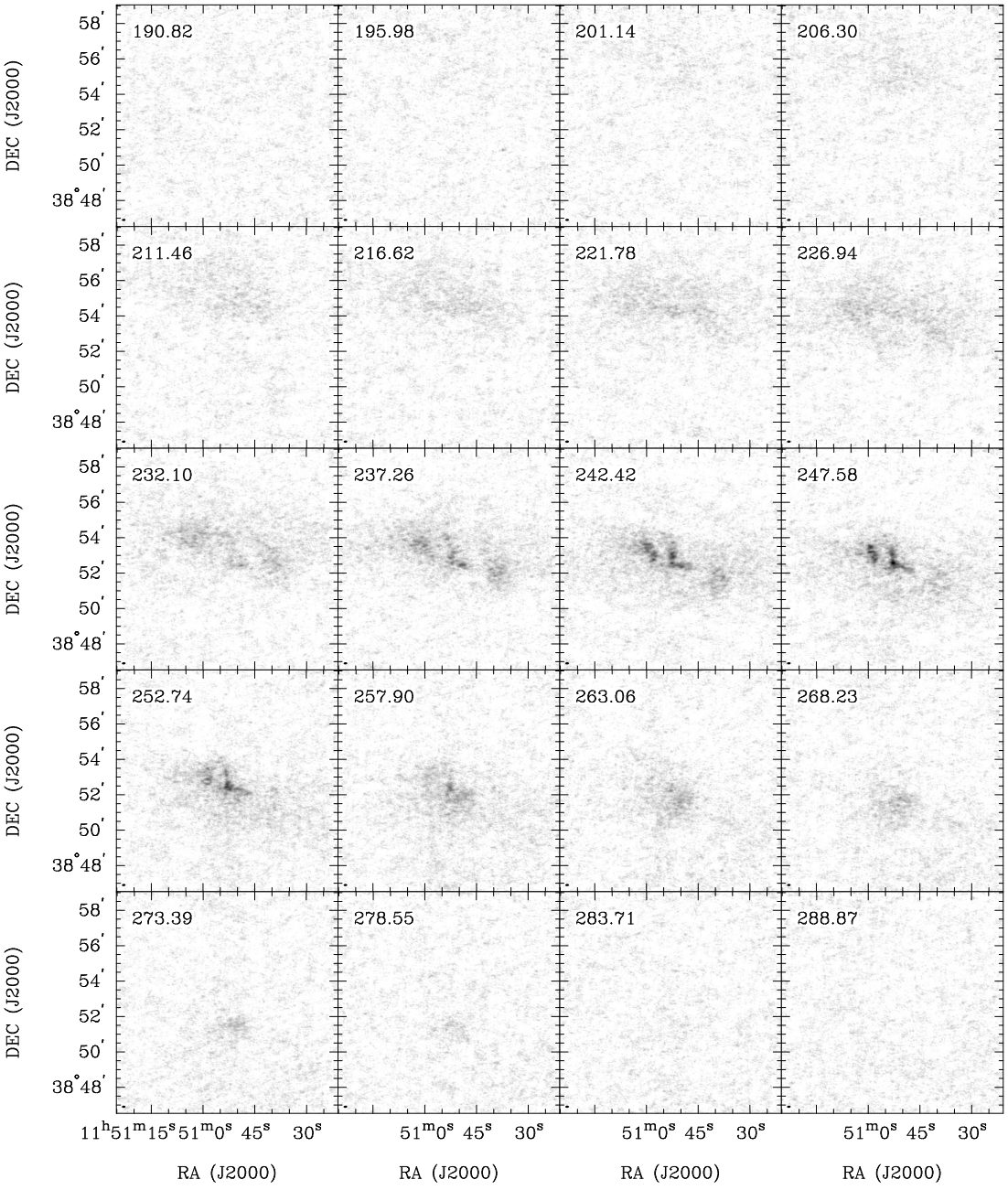

Figure 2.16 **DDO 99:** Channel maps based on the natural-weighted cube (grayscale range: -0.02 to $14.7\,\mathrm{mJy\,beam^{-1}}$). Every third channel is shown (channel width $1.3\,\mathrm{km\ s^{-1}}$) and each map has the same size as the moment maps in the following panels.

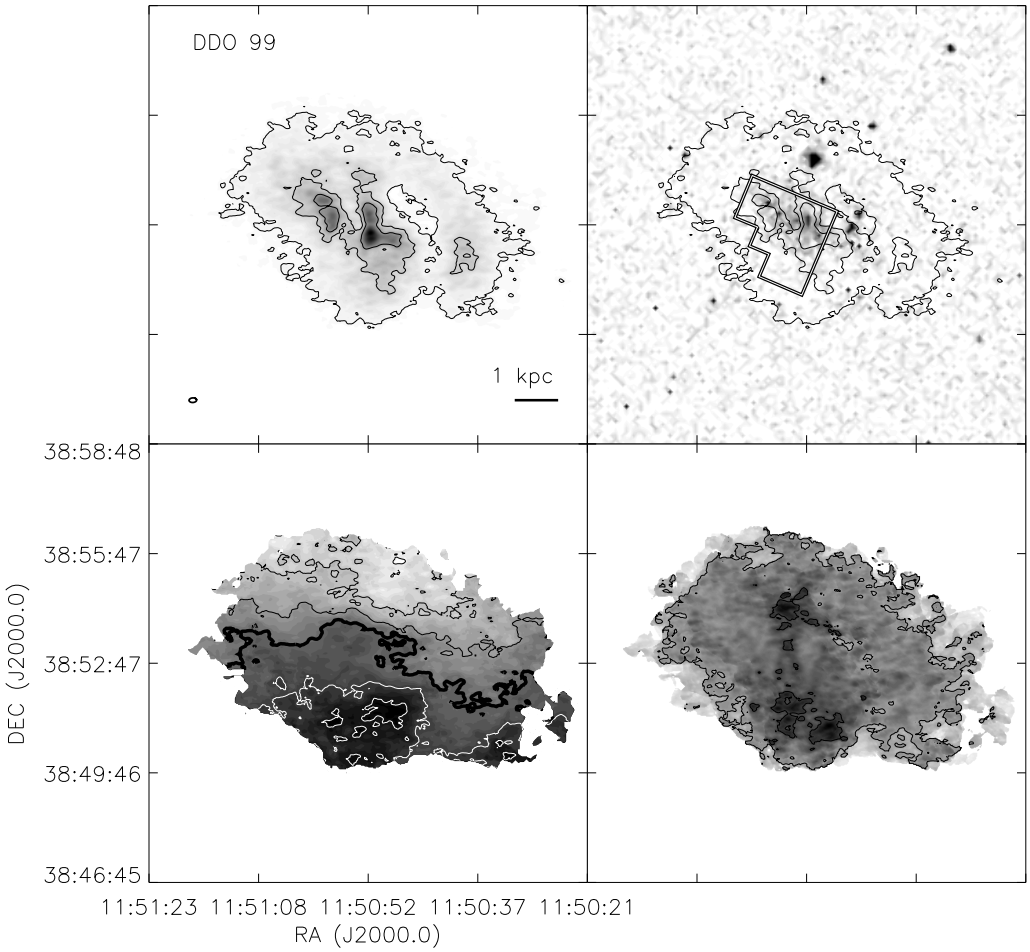

Figure 2.16 continued. *Top left:* The integrated H I intensity map for DDO 99. The greyscale covers a range from 1×10^{19} to 2.6×10^{21} cm^{-2} with contours of 1×10^{20}, 5×10^{20}, and 1×10^{21} cm^{-2}. *Top Right:* An optical image from the SDSS with the same column density contours overlaid. The HST WFPC2 footprint is the field covered by the ANGST survey. *Bottom Left:* The H I velocity field. Black contours (lighter gray scale) indicate approaching emission, white contours (darker gray scale) receding emission. The thick black contour is the central velocity (v_{cen} = 242.1 km s^{-1}) and the isovelocity contours are spaced by Δv = 10 km s^{-1}. *Bottom Right:* The H I velocity dispersion. Contours are plotted at 5 and 10 km s^{-1}.

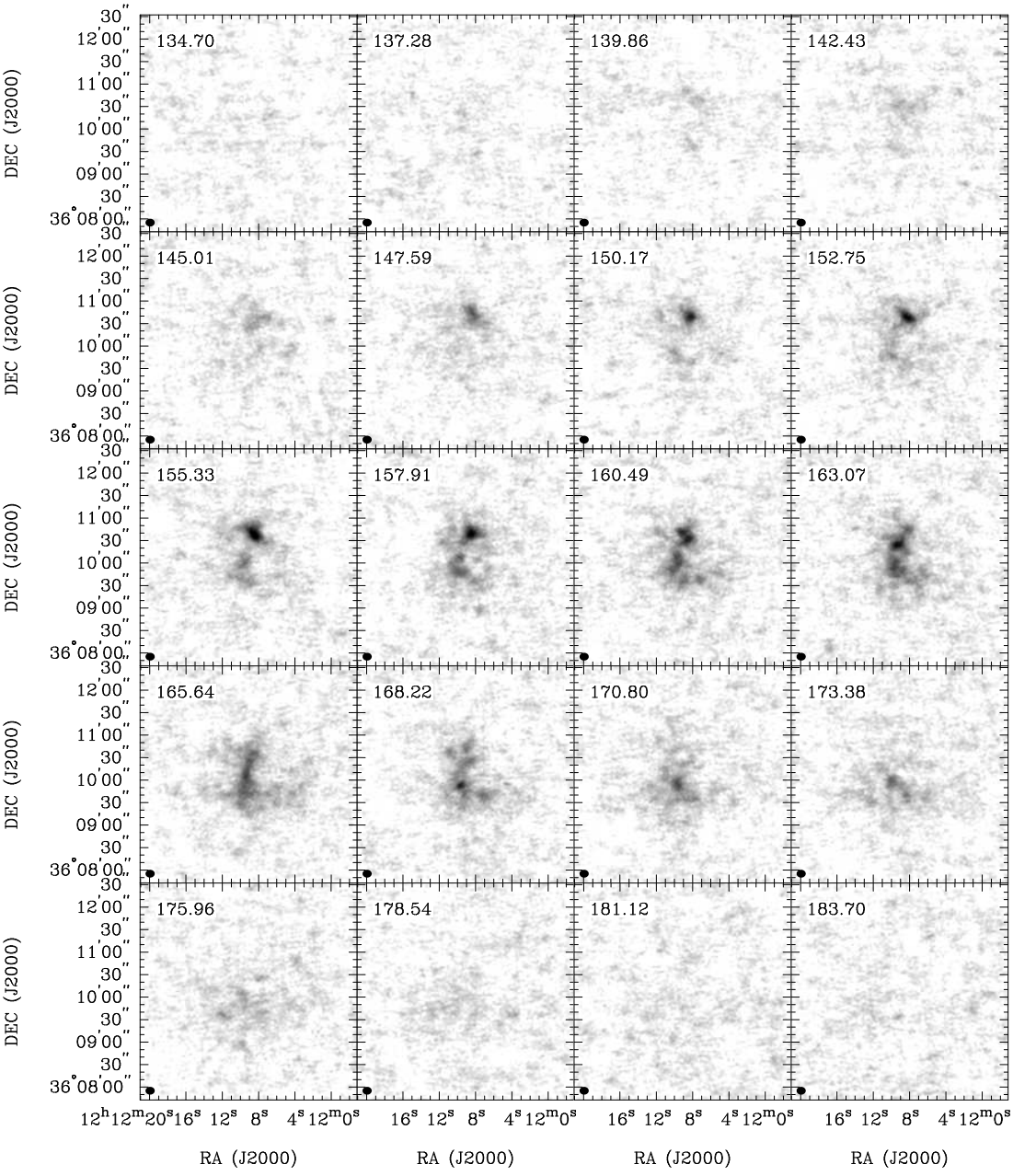

Figure 2.17 **NGC 4163:** Channel maps based on the natural-weighted cube (grayscale range: -0.02 to $16.1\,\mathrm{mJy\,beam^{-1}}$). Every third channel is shown (channel width $0.6\,\mathrm{km\ s^{-1}}$) and each map has the same size as the moment maps in the following panels.

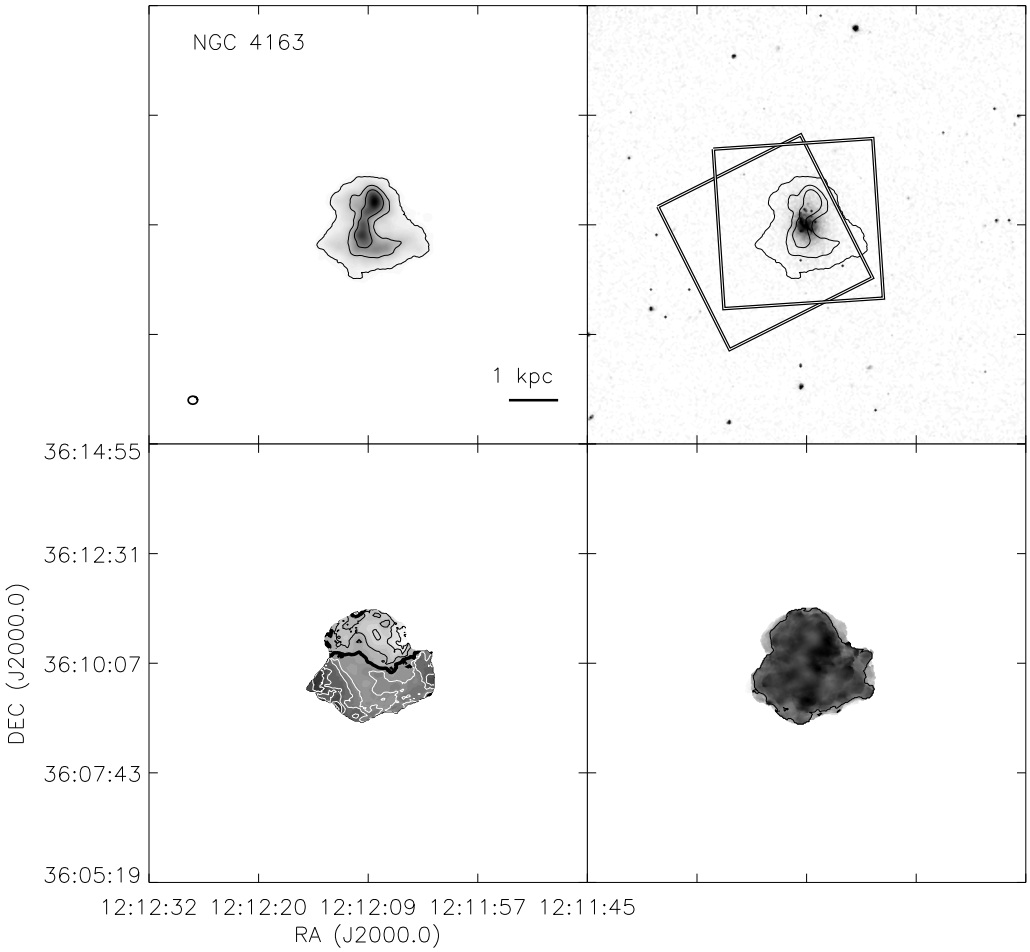

Figure 2.17 continued. *Top left:* The integrated H I intensity map for NGC 4163. The greyscale covers a range from 1×10^{19} to 2.1×10^{21} cm^{-2} with contours of 1×10^{20}, 5×10^{20}, and 1×10^{21} cm^{-2}. *Top Right:* An optical image from the SDSS with the same column density contours overlaid. The HST ACS footprints are the fields covered by the ANGST survey. *Bottom Left:* The H I velocity field. Black contours (lighter gray scale) indicate approaching emission, white contours (darker gray scale) receding emission. The thick black contour is the central velocity ($v_{cen} = 161.6\,\mathrm{km\,s^{-1}}$) and the isovelocity contours are spaced by $\Delta v = 3\,\mathrm{km\,s^{-1}}$. *Bottom Right:* The H I velocity dispersion. Contours are plotted at 5 and $10\,\mathrm{km\,s^{-1}}$.

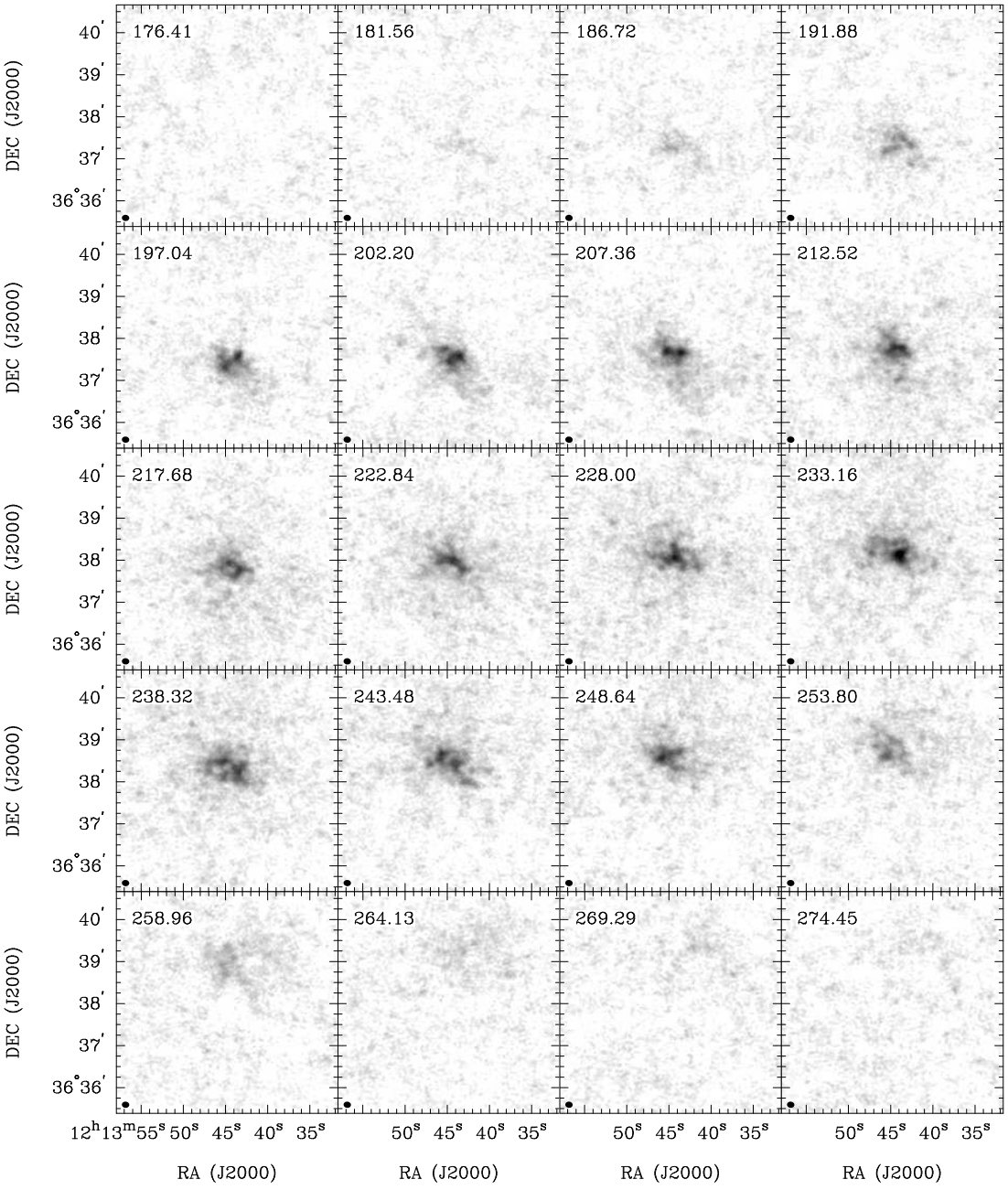

Figure 2.18 **NGC 4190:** Channel maps based on the natural-weighted cube (grayscale range: -0.02 to $14.7\,\mathrm{mJy\,beam^{-1}}$). Every third channel is shown (channel width $1.3\,\mathrm{km\ s^{-1}}$) and each map has the same size as the moment maps in the following panels.

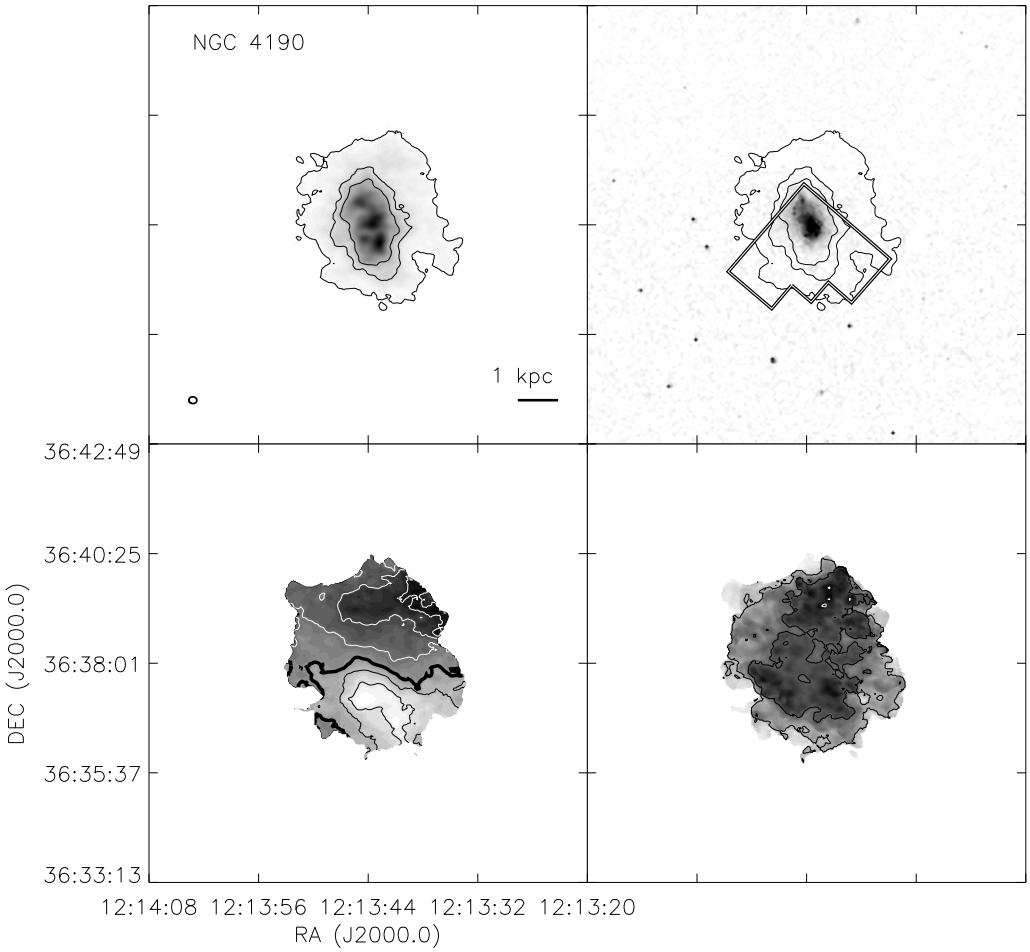

Figure 2.18 continued. *Top left:* The integrated H I intensity map for NGC 4190. The greyscale covers a range from $1{\times}10^{19}$ to $3.5 \times 10^{21}\,\mathrm{cm}^{-2}$ with contours of $1{\times}10^{20}$, $5{\times}10^{20}$, and $1{\times}10^{21}\,\mathrm{cm}^{-2}$. *Top Right:* An optical image from the SDSS with the same column density contours overlaid. The HST WFPC2 footprint is the field covered by the ANGST survey. *Bottom Left:* The H I velocity field. Black contours (lighter gray scale) indicate approaching emission, white contours (darker gray scale) receding emission. The thick black contour is the central velocity ($\mathrm{v}_{cen} = 227.0\,\mathrm{km\,s}^{-1}$) and the isovelocity contours are spaced by $\Delta\mathrm{v} = 10\,\mathrm{km\,s}^{-1}$. *Bottom Right:* The H I velocity dispersion. Contours are plotted at 5, 10, and $15\,\mathrm{km\,s}^{-1}$.

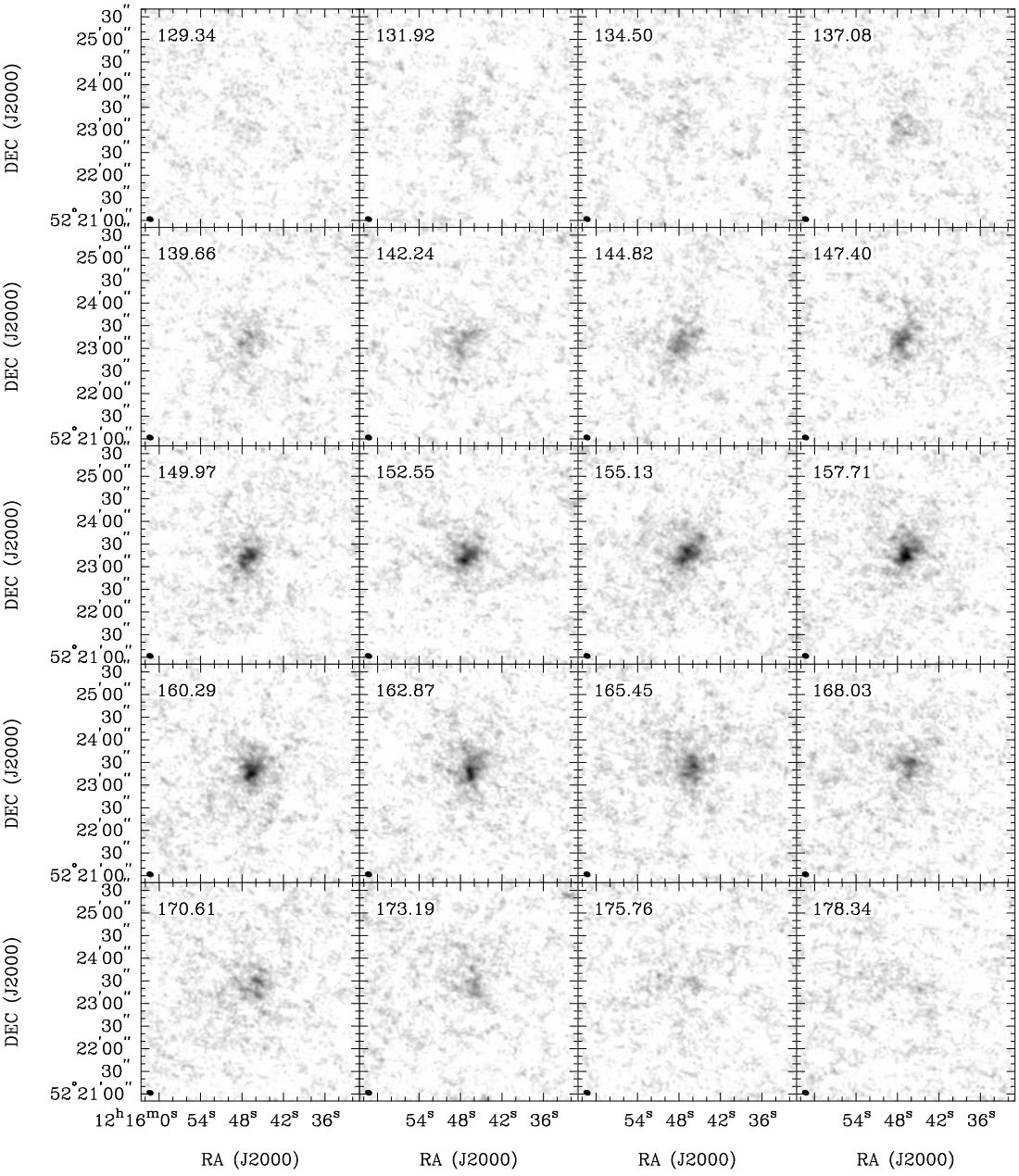

Figure 2.19 **MCG +09-20-131:** Channel maps based on the natural-weighted cube (grayscale range: -0.02 to 12.3 mJy beam^{-1}). Every channel is shown (channel width 1.3 km s^{-1}) and each map has the same size as the moment maps in the following panels.

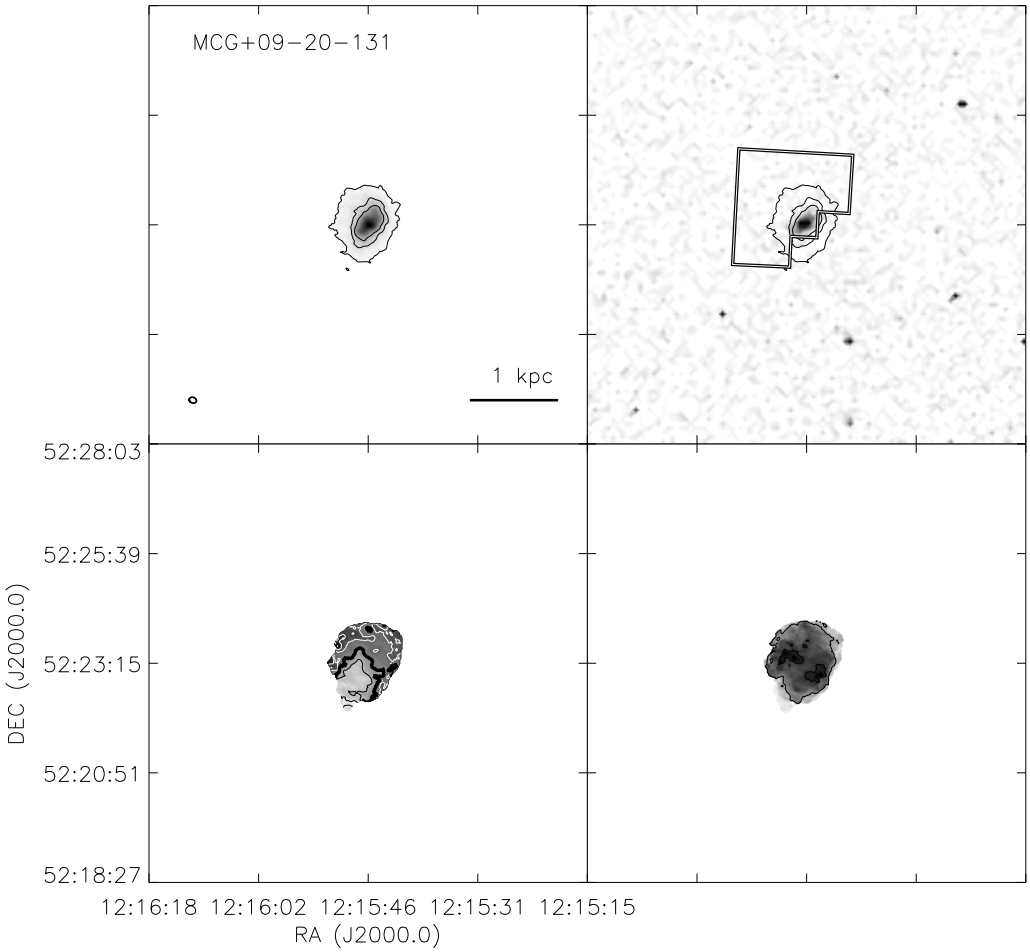

Figure 2.19 continued. *Top left:* The integrated H I intensity map for MCG +09-20-131. The greyscale covers a range from $1{\times}10^{19}$ to $3.3 \times 10^{21}\,\mathrm{cm}^{-2}$ with contours of $1{\times}10^{20}$, $5{\times}10^{20}$, and $1{\times}10^{21}\,\mathrm{cm}^{-2}$. *Top Right:* An optical image from the SDSS with the same column density contours overlaid. The HST WFPC2 footprint is the field covered by the ANGST survey. *Bottom Left:* The H I velocity field. Black contours (lighter gray scale) indicate approaching emission, white contours (darker gray scale) receding emission. The thick black contour is the central velocity ($\mathrm{v}_{cen} = 157.6\,\mathrm{km\,s}^{-1}$) and the isovelocity contours are spaced by $\Delta\mathrm{v} = 5\,\mathrm{km\,s}^{-1}$. *Bottom Right:* The H I velocity dispersion. Contours are plotted at 5 and $10\,\mathrm{km\,s}^{-1}$.

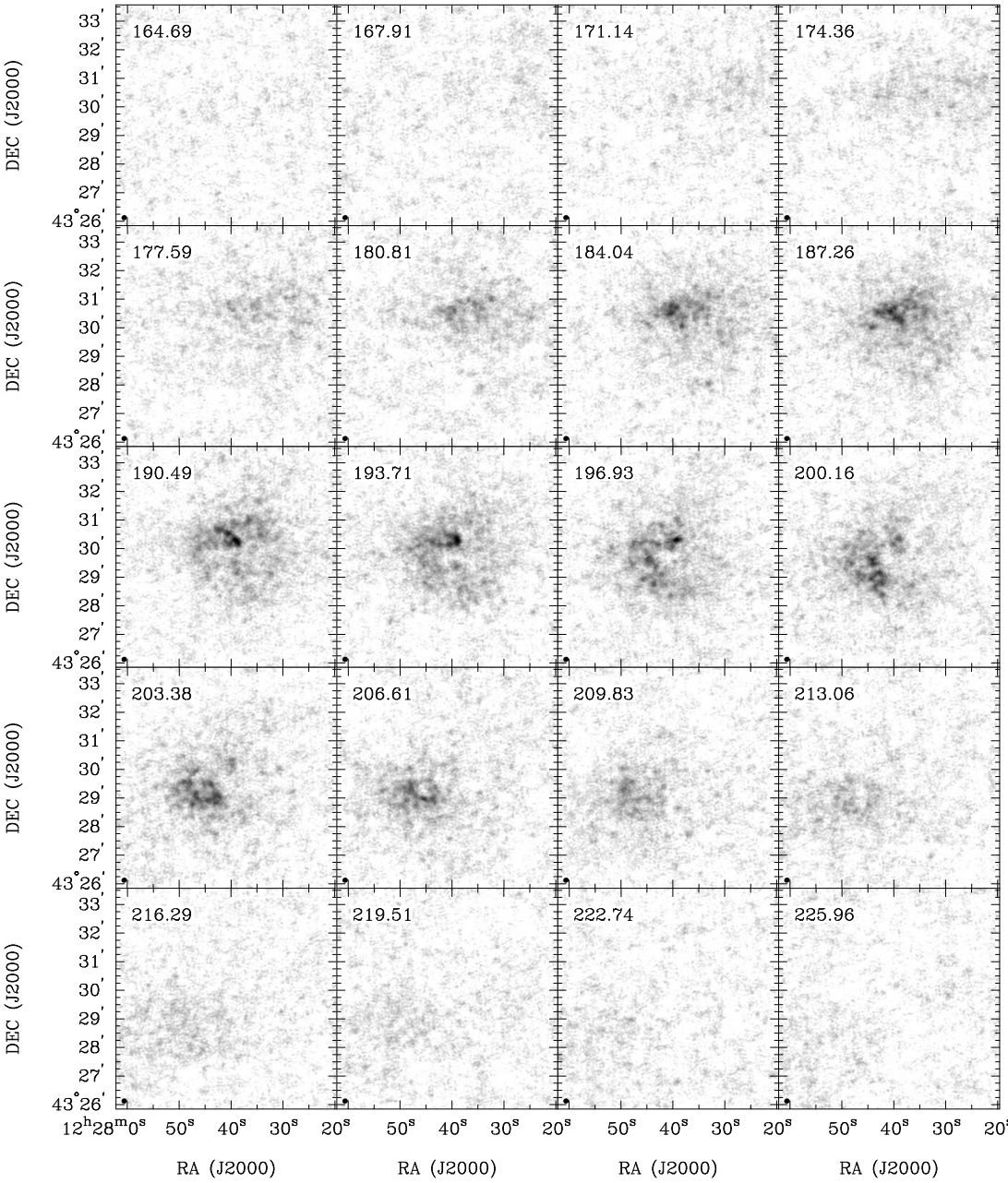

Figure 2.20 **DDO 125:** Channel maps based on the natural-weighted cube (grayscale range: -0.02 to $16.0\,\mathrm{mJy\,beam^{-1}}$). Every fourth channel is shown (channel width $0.6\,\mathrm{km\ s^{-1}}$) and each map has the same size as the moment maps in the following panels.

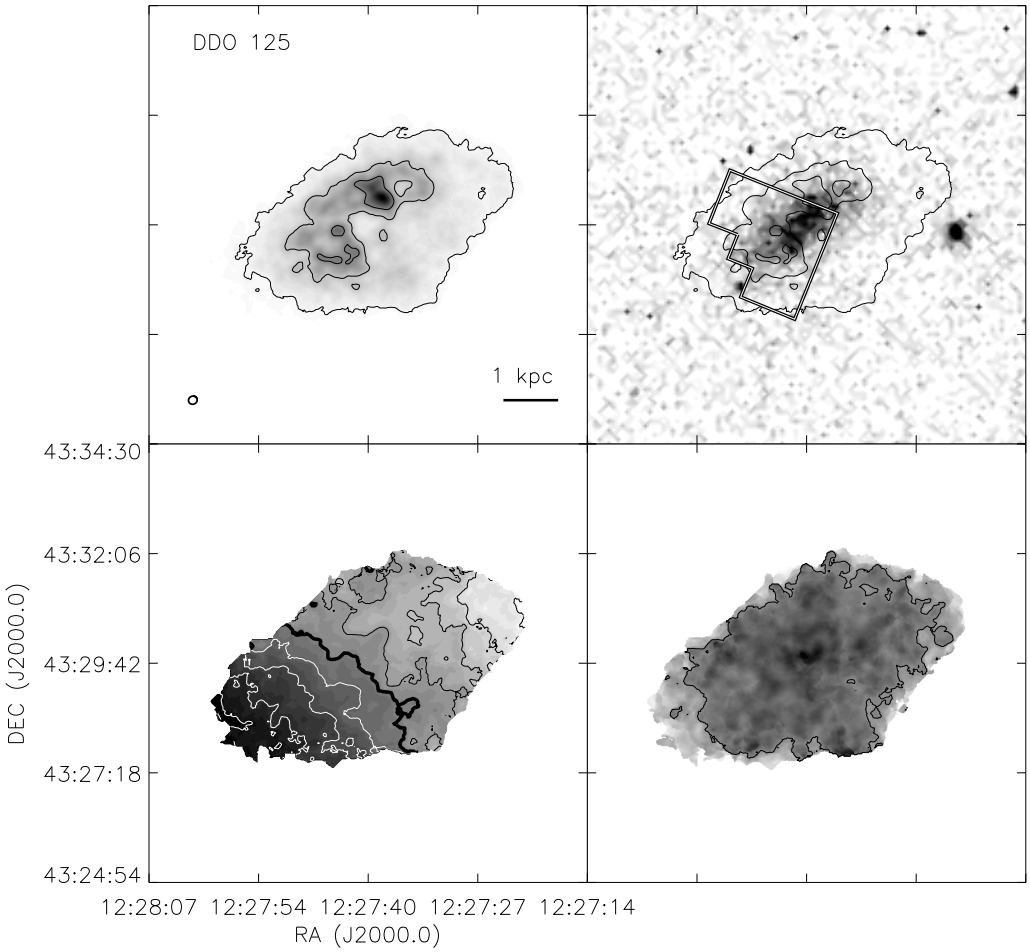

Figure 2.20 continued. *Top left:* The integrated H I intensity map for DDO 125. The greyscale covers a range from 1×10^{19} to 2.1×10^{21} cm^{-2} with contours of 1×10^{20}, 5×10^{20}, and 1×10^{21} cm^{-2}. *Top Right:* An optical image from the SDSS with the same column density contours overlaid. The HST WFPC2 footprint is the field covered by the ANGST survey. *Bottom Left:* The H I velocity field. Black contours (lighter gray scale) indicate approaching emission, white contours (darker gray scale) receding emission. The thick black contour is the central velocity ($v_{cen} = 196.1\,\mathrm{km\,s^{-1}}$) and the isovelocity contours are spaced by $\Delta v = 5\,\mathrm{km\,s^{-1}}$. *Bottom Right:* The H I velocity dispersion. Contours are plotted at 5 and $10\,\mathrm{km\,s^{-1}}$.

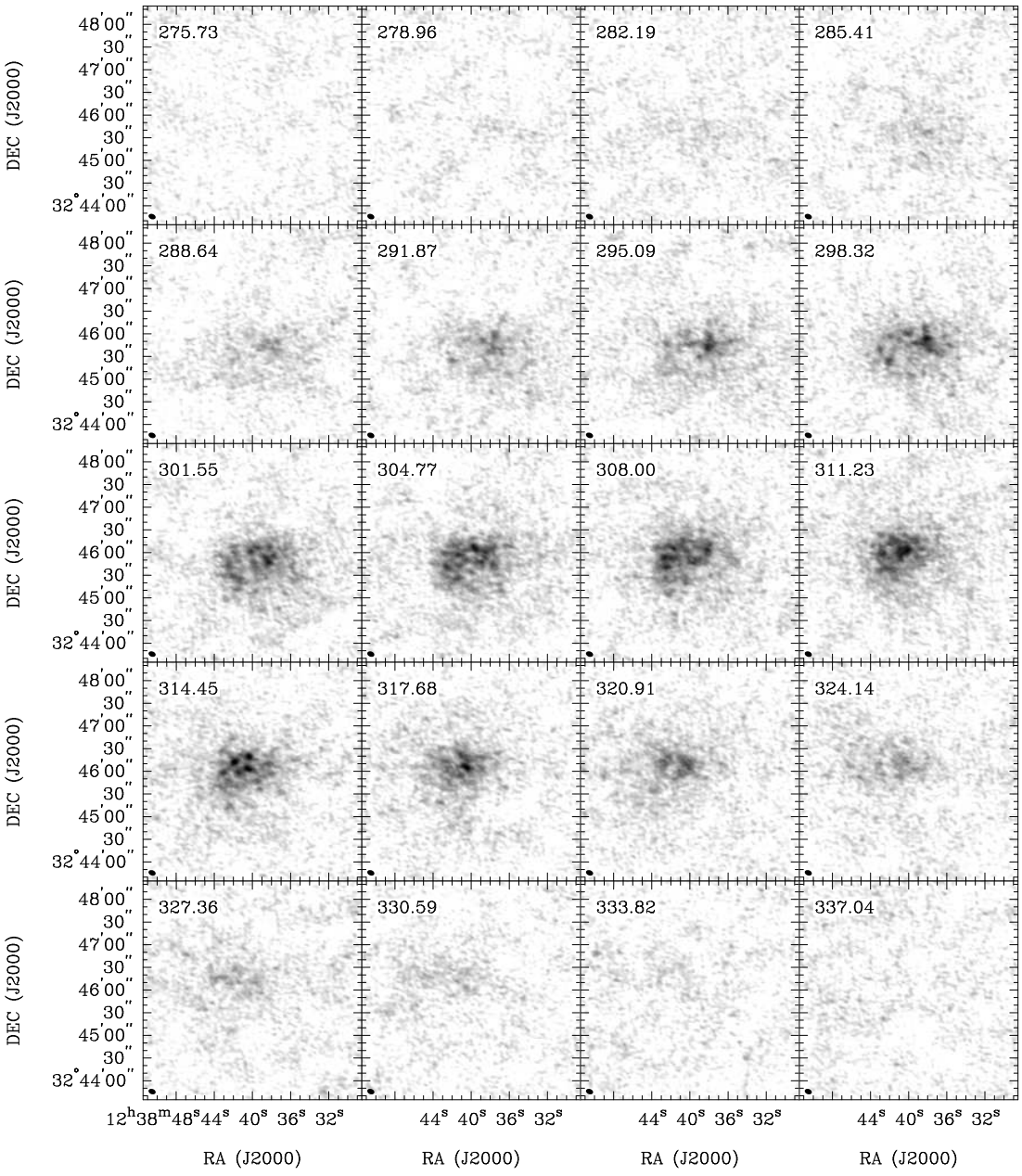

Figure 2.21 **UGCA 292:** Channel maps based on the natural-weighted cube (grayscale range: -0.02 to $15.8\,\mathrm{mJy\,beam^{-1}}$). Every fourth channel is shown (channel width $0.6\,\mathrm{km\ s^{-1}}$) and each map has the same size as the moment maps in the following panels.

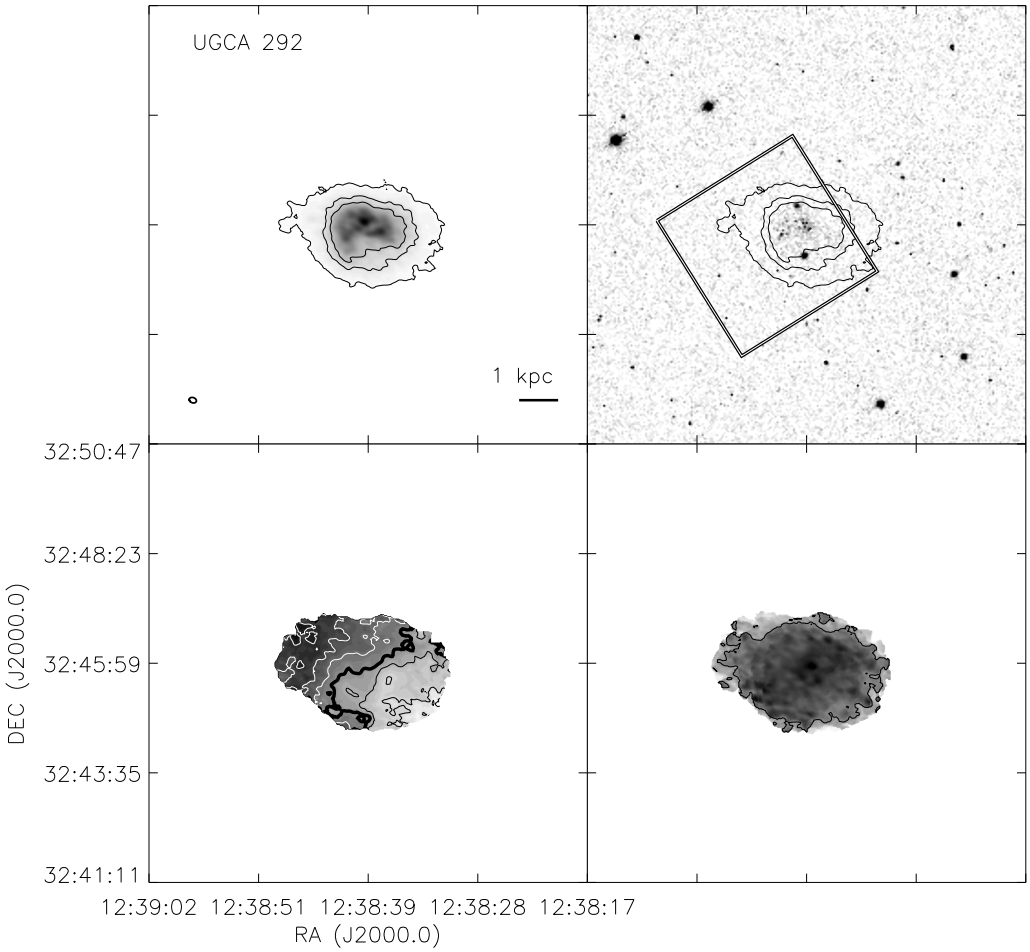

Figure 2.21 continued. *Top left:* The integrated H I intensity map for UGCA 292. The greyscale covers a range from 1×10^{19} to 4.2×10^{21} cm^{-2} with contours of 1×10^{20}, 5×10^{20}, and 1×10^{21} cm^{-2}. *Top Right:* An optical image from the SDSS with the same column density contours overlaid. The HST ACS footprint is the field covered by the ANGST survey. *Bottom Left:* The H I velocity field. Black contours (lighter gray scale) indicate approaching emission, white contours (darker gray scale) receding emission. The thick black contour is the central velocity ($v_{cen} = 308.3\,\mathrm{km\,s^{-1}}$) and the isovelocity contours are spaced by $\Delta v = 5\,\mathrm{km\,s^{-1}}$. *Bottom Right:* The H I velocity dispersion. Contours are plotted at 5 and $10\,\mathrm{km\,s^{-1}}$.

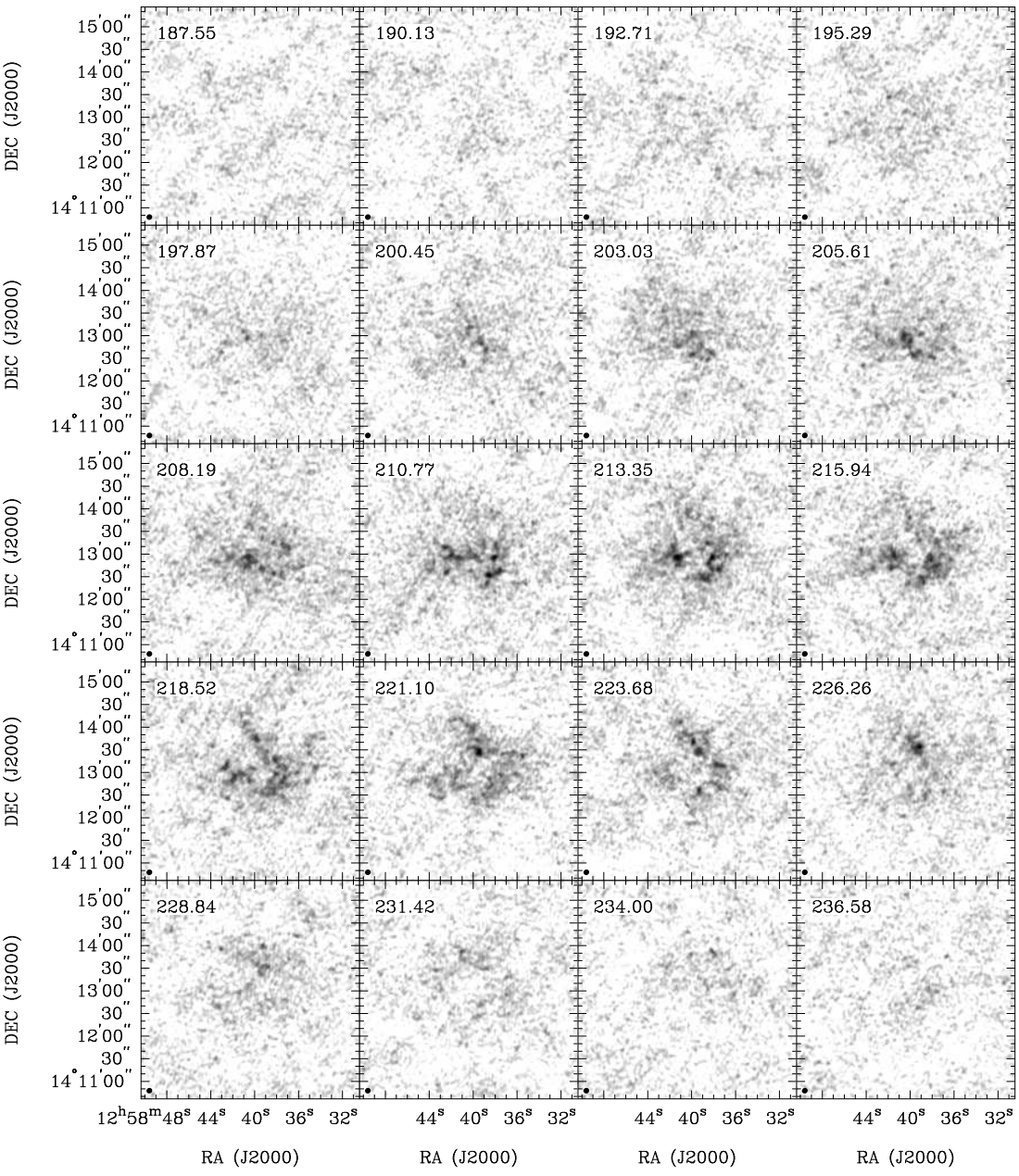

Figure 2.22 **GR 8:** Channel maps based on the natural-weighted cube (grayscale range: -0.02 to 10.6 mJy beam^{-1}). Every third channel is shown (channel width 0.6 km s^{-1}) and each map has the same size as the moment maps in the following panels.

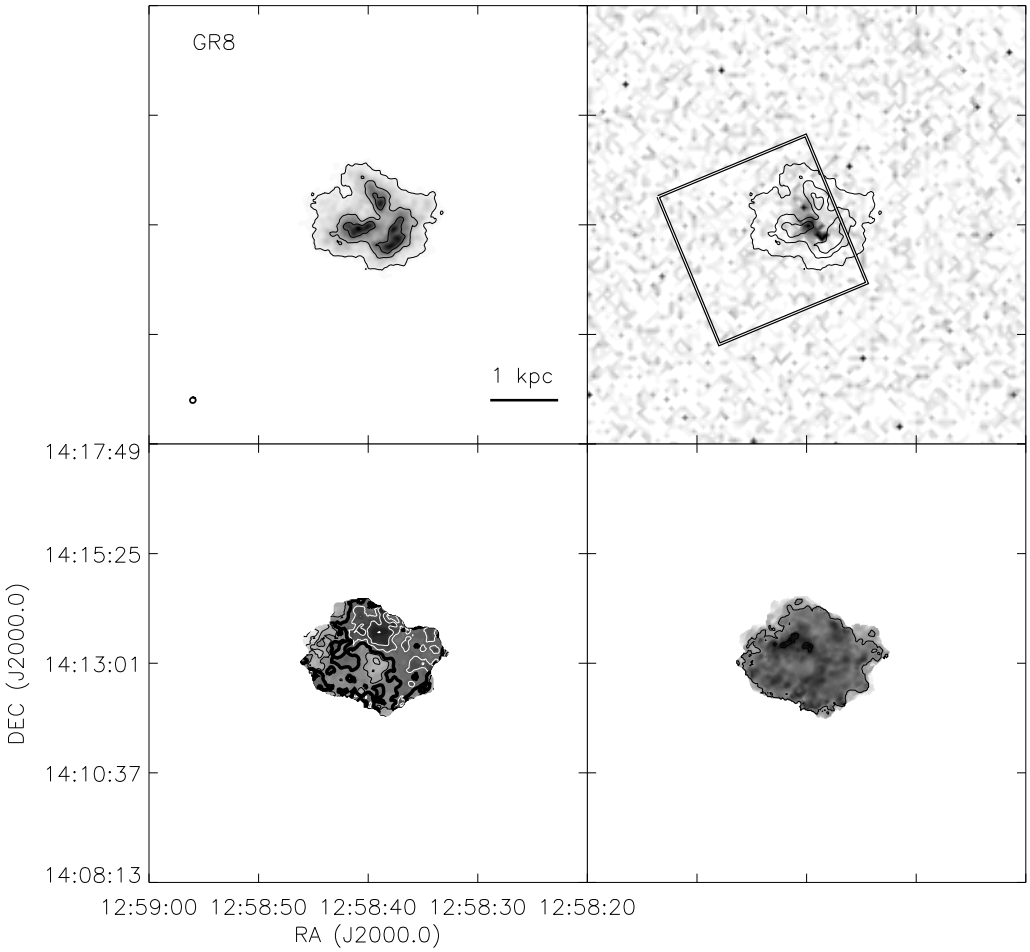

Figure 2.22 continued. *Top left:* The integrated H I intensity map for GR 8. The greyscale covers a range from 1×10^{19} to 1.7×10^{21} cm^{-2} with contours of 1×10^{20}, 5×10^{20}, and 1×10^{21} cm^{-2}. *Top Right:* An optical image from the SDSS with the same column density contours overlaid. The HST ACS footprint is the field covered by the ANGST survey. *Bottom Left:* The H I velocity field. Black contours (lighter gray scale) indicate approaching emission, white contours (darker gray scale) receding emission. The thick black contour is the central velocity (v_{cen} = 213.7 km s^{-1}) and the isovelocity contours are spaced by Δv = 3 km s^{-1}. *Bottom Right:* The H I velocity dispersion. Contours are plotted at 5 and 10 km s^{-1}.

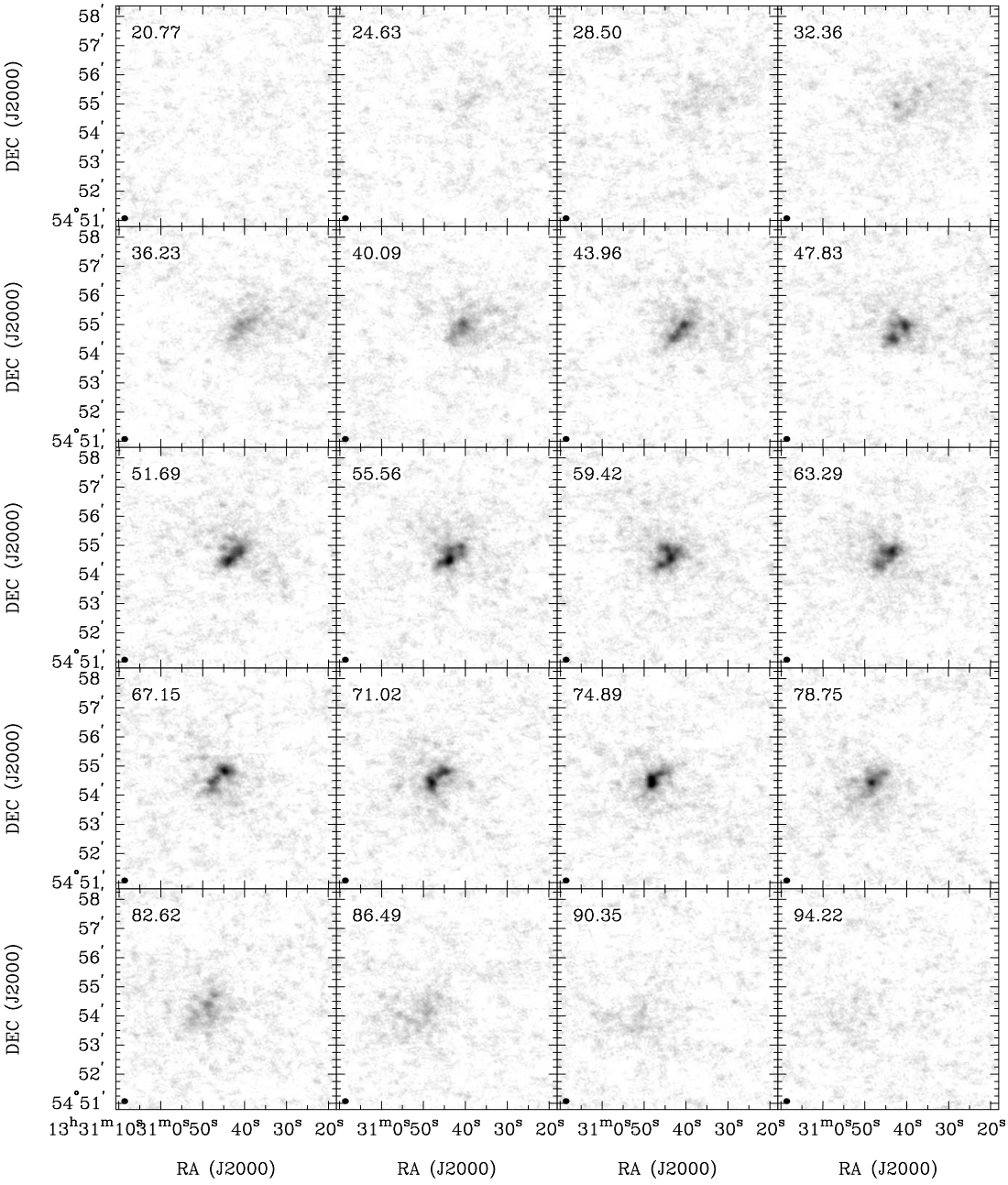

Figure 2.23 **UGC 8508:** Channel maps based on the natural-weighted cube (grayscale range: -0.02 to $23.0\,\mathrm{mJy\,beam^{-1}}$). Every fifth channel is shown (channel width $0.6\,\mathrm{km\ s^{-1}}$) and each map has the same size as the moment maps in the following panels.

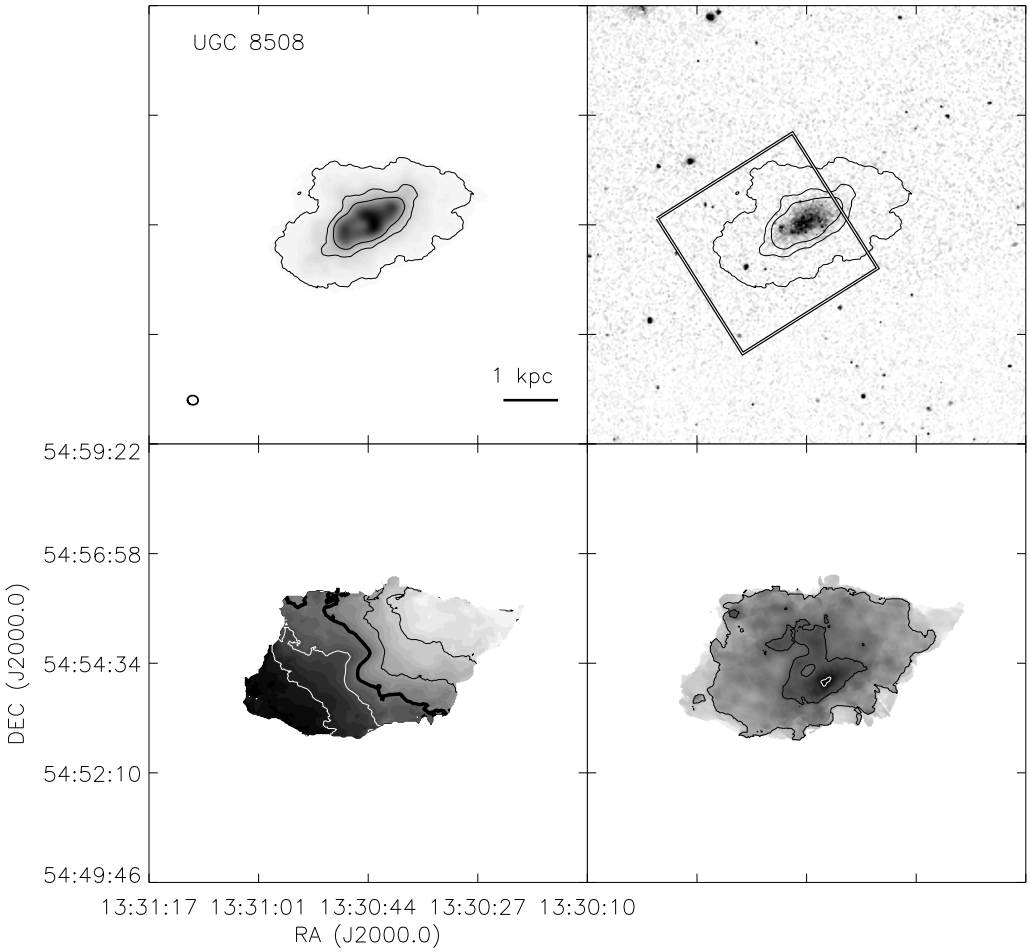

Figure 2.23 continued. *Top left:* The integrated H I intensity map for UGC 8508. The greyscale covers a range from 1×10^{19} to 2.9×10^{21} cm^{-2} with contours of 1×10^{20}, 5×10^{20}, and 1×10^{21} cm^{-2}. *Top Right:* An optical image from the SDSS with the same column density contours overlaid. The HST ACS footprint is the field covered by the ANGST survey. *Bottom Left:* The H I velocity field. Black contours (lighter gray scale) indicate approaching emission, white contours (darker gray scale) receding emission. The thick black contour is the central velocity (v_{cen} = 62.0 km s^{-1}) and the isovelocity contours are spaced by Δv = 10 km s^{-1}. *Bottom Right:* The H I velocity dispersion. Contours are plotted at 5, 10, and 15 km s^{-1}.

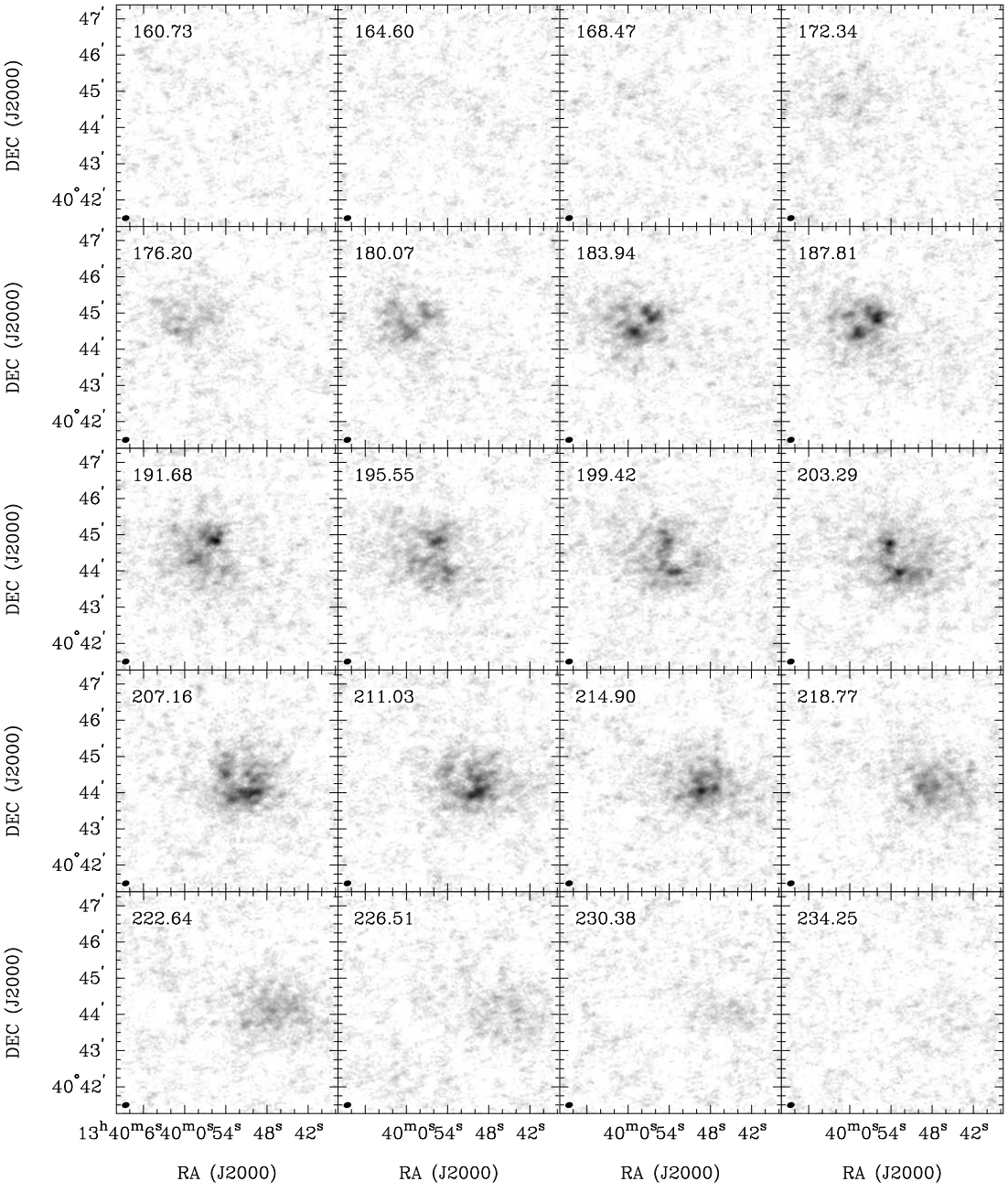

Figure 2.24 **DDO 181:** Channel maps based on the natural-weighted cube (grayscale range: -0.02 to 13.9 mJy beam^{-1}). Every second channel is shown (channel width 1.3 km s^{-1}) and each map has the same size as the moment maps in the following panels.

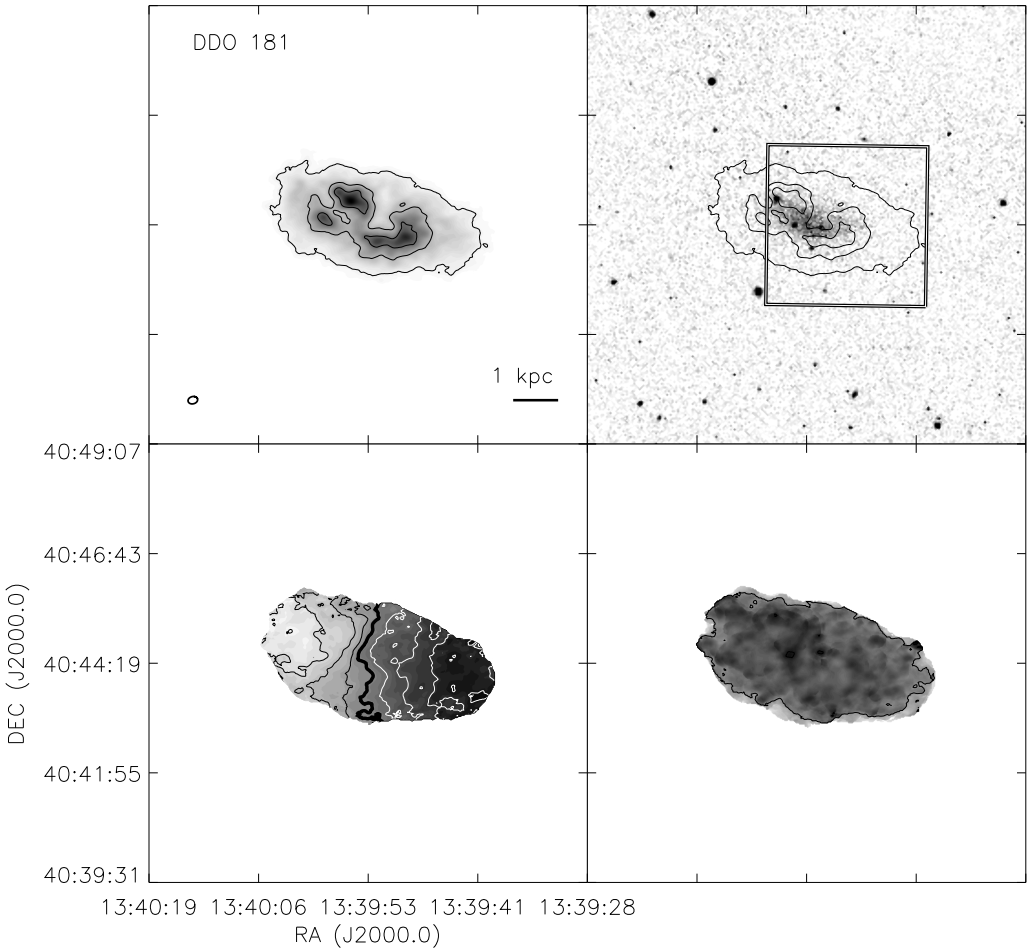

Figure 2.24 continued. *Top left:* The integrated H I intensity map for DDO 181. The greyscale covers a range from 1×10^{19} to 1.7×10^{21} cm^{-2} with contours of 1×10^{20}, 5×10^{20}, and 1×10^{21} cm^{-2}. *Top Right:* An optical image from the SDSS with the same column density contours overlaid. The HST ACS footprint is the field covered by the ANGST survey. *Bottom Left:* The H I velocity field. Black contours (lighter gray scale) indicate approaching emission, white contours (darker gray scale) receding emission. The thick black contour is the central velocity ($v_{cen} = 201.4\,\mathrm{km\,s^{-1}}$) and the isovelocity contours are spaced by $\Delta v = 5\,\mathrm{km\,s^{-1}}$. *Bottom Right:* The H I velocity dispersion. Contours are plotted at 5 and $10\,\mathrm{km\,s^{-1}}$.

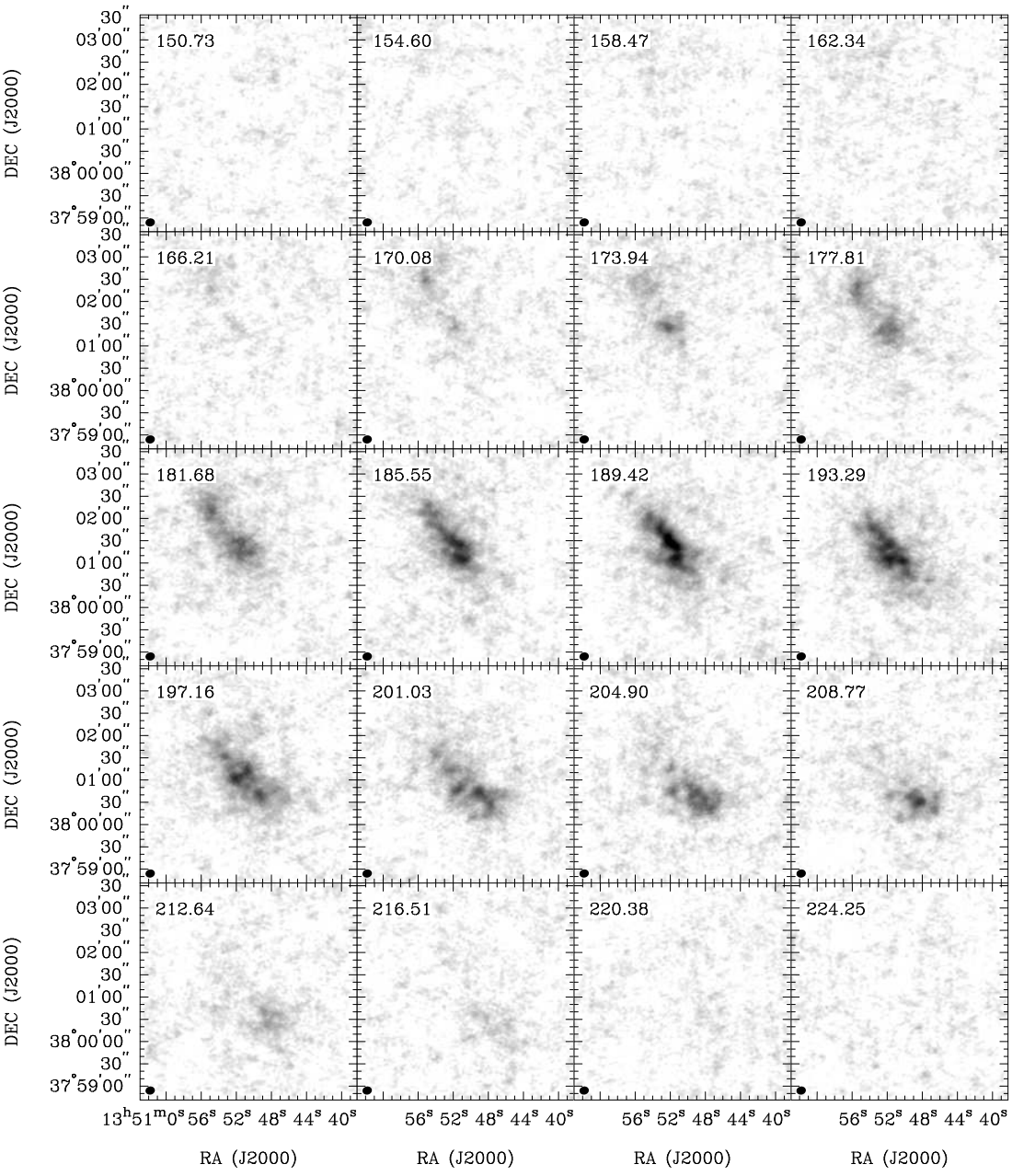

Figure 2.25 **DDO 183:** Channel maps based on the natural-weighted cube (grayscale range: -0.02 to $15.7\,\mathrm{mJy\,beam^{-1}}$). Every second channel is shown (channel width $1.3\,\mathrm{km\ s^{-1}}$) and each map has the same size as the moment maps in the following panels.

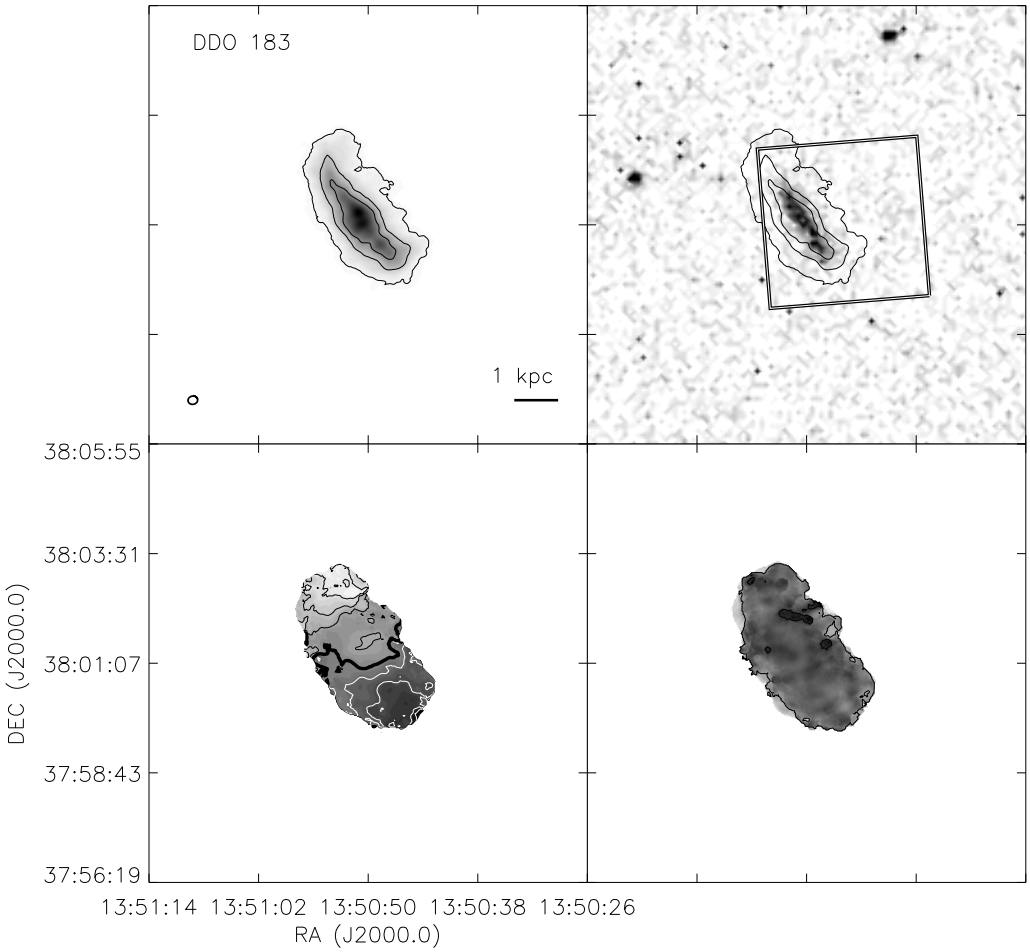

Figure 2.25 continued. *Top left:* The integrated H I intensity map for DDO 183. The greyscale covers a range from 1×10^{19} to 2.2×10^{21} cm^{-2} with contours of 1×10^{20}, 5×10^{20}, and 1×10^{21} cm^{-2}. *Top Right:* An optical image from the SDSS with the same column density contours overlaid. The HST ACS footprint is the field covered by the ANGST survey. *Bottom Left:* The H I velocity field. Black contours (lighter gray scale) indicate approaching emission, white contours (darker gray scale) receding emission. The thick black contour is the central velocity ($v_{cen} = 191.2\,km\,s^{-1}$) and the isovelocity contours are spaced by $\Delta v = 5\,km\,s^{-1}$. *Bottom Right:* The H I velocity dispersion. Contours are plotted at 5 and $10\,km\,s^{-1}$.

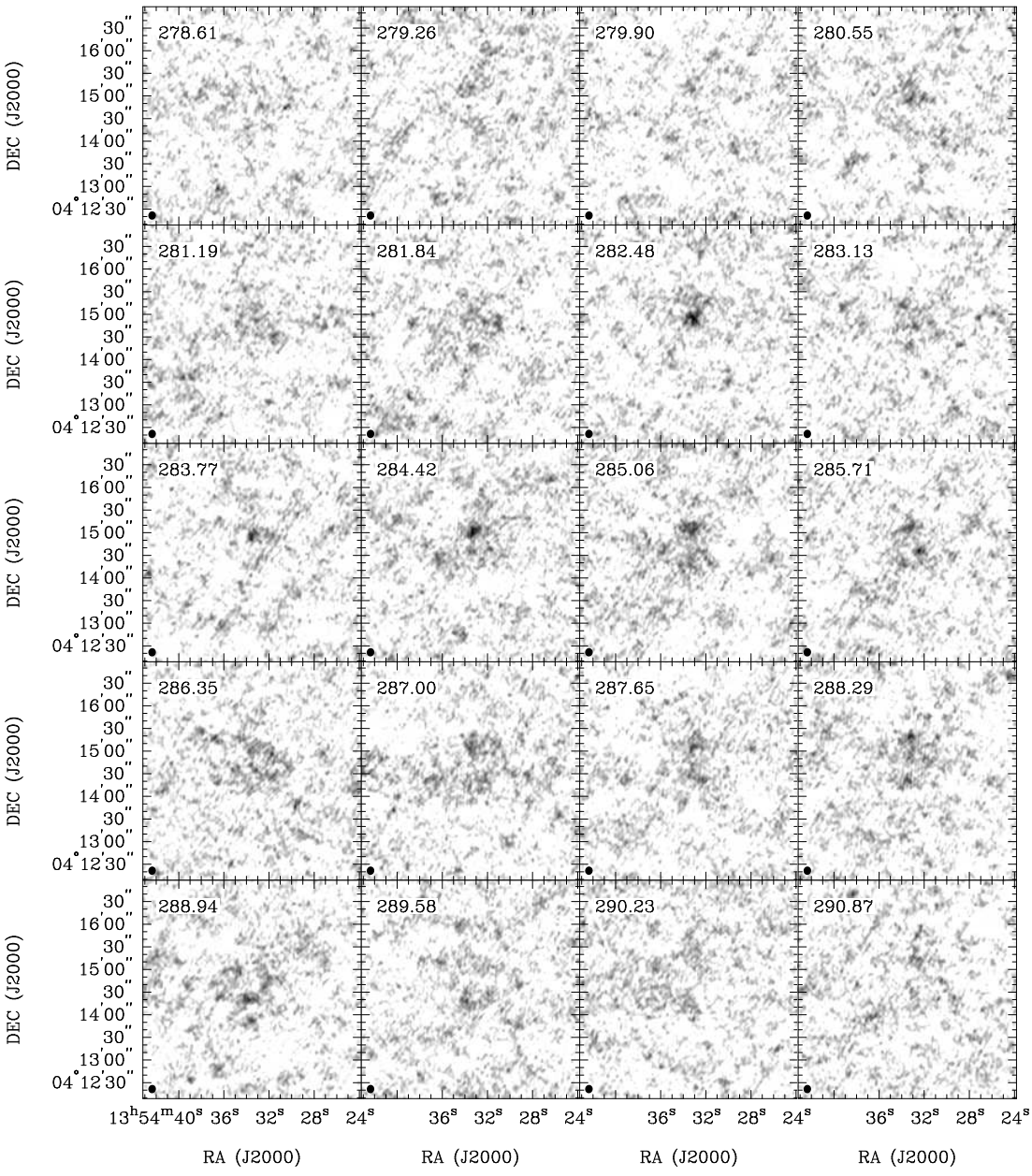

Figure 2.26 **KKH 86:** Channel maps based on the natural-weightedcube (grayscale range: -0.02 to $7.7\,\mathrm{mJy\,beam^{-1}}$). Every channel is shown (channel width $0.6\,\mathrm{km\ s^{-1}}$) and each map has the same size as the moment maps in the following panels.

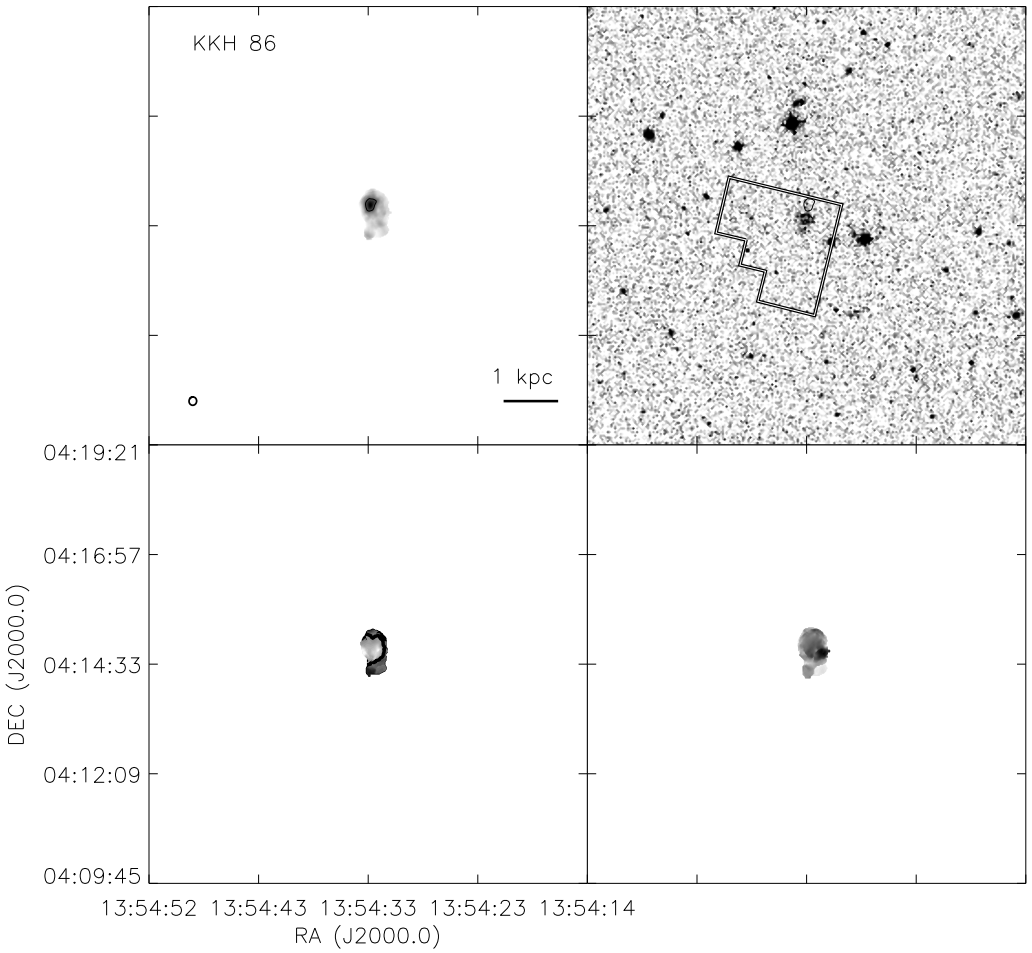

Figure 2.26 continued. *Top left:* The integrated H I intensity map for KKH 86. The greyscale covers a range from 1×10^{19} to $1.5\times10^{20}\,\mathrm{cm}^{-2}$ with a contour of $1\times10^{20}\,\mathrm{cm}^{-2}$. *Top Right:* An optical image from the SDSS with the same column density contours overlaid. The HST WFPC2 footprint is the field covered by the ANGST survey. *Bottom Left:* The H I velocity field. Black contours (lighter gray scale) indicate approaching emission, white contours (darker gray scale) receding emission. The thick black contour is the central velocity ($\mathrm{v}_{cen} = 285.5\,\mathrm{km\,s}^{-1}$) and the isovelocity contours are spaced by $\Delta\mathrm{v} = 10\,\mathrm{km\,s}^{-1}$. *Bottom Right:* The H I velocity dispersion.

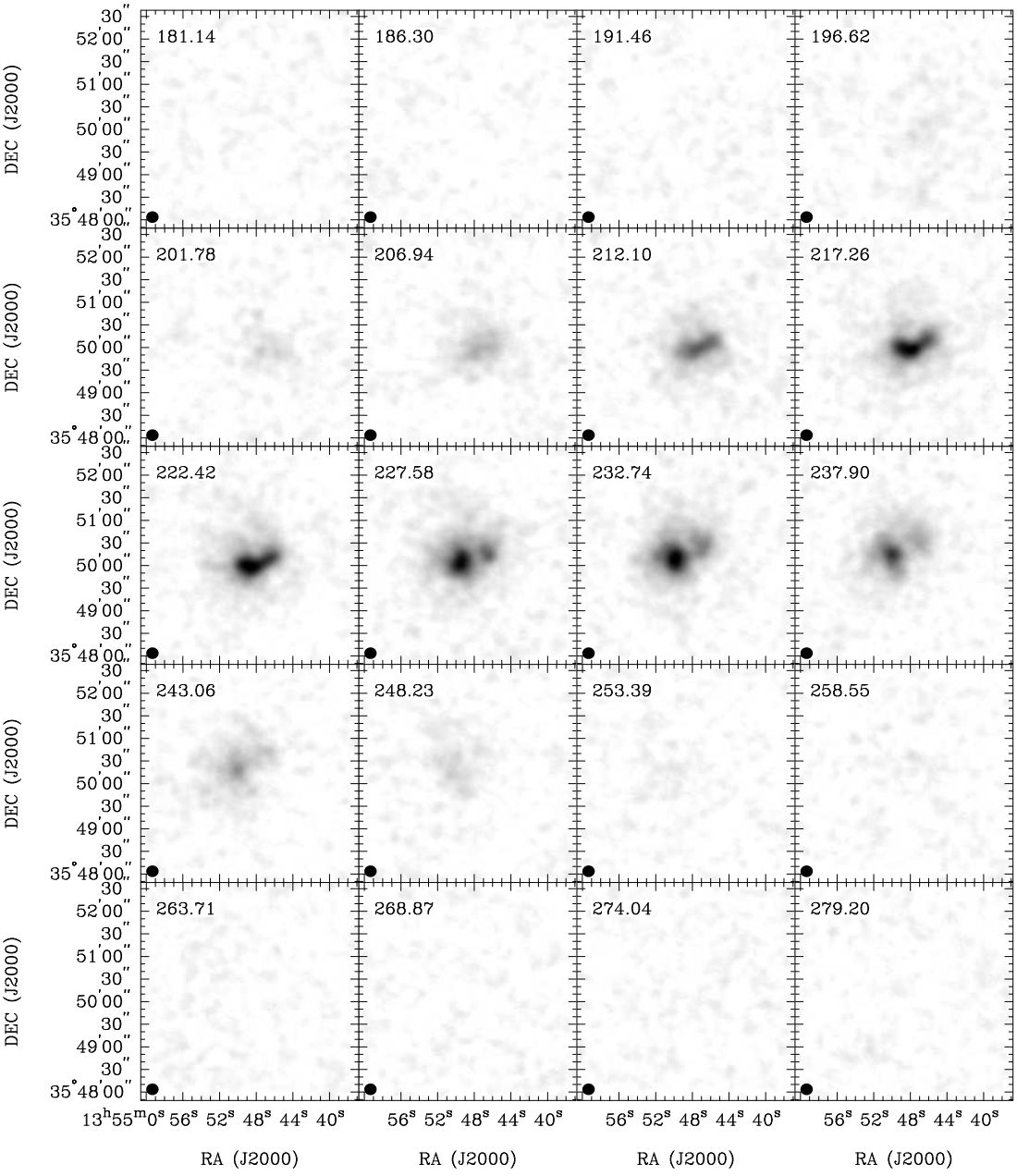

Figure 2.27 **UGC 8833:** Channel maps based on the natural-weighted cube (grayscale range: -0.02 to 20.8 mJy beam^{-1}). Every channel is shown (channel width 2.6 km s^{-1}) and each map has the same size as the moment maps in the following panels.

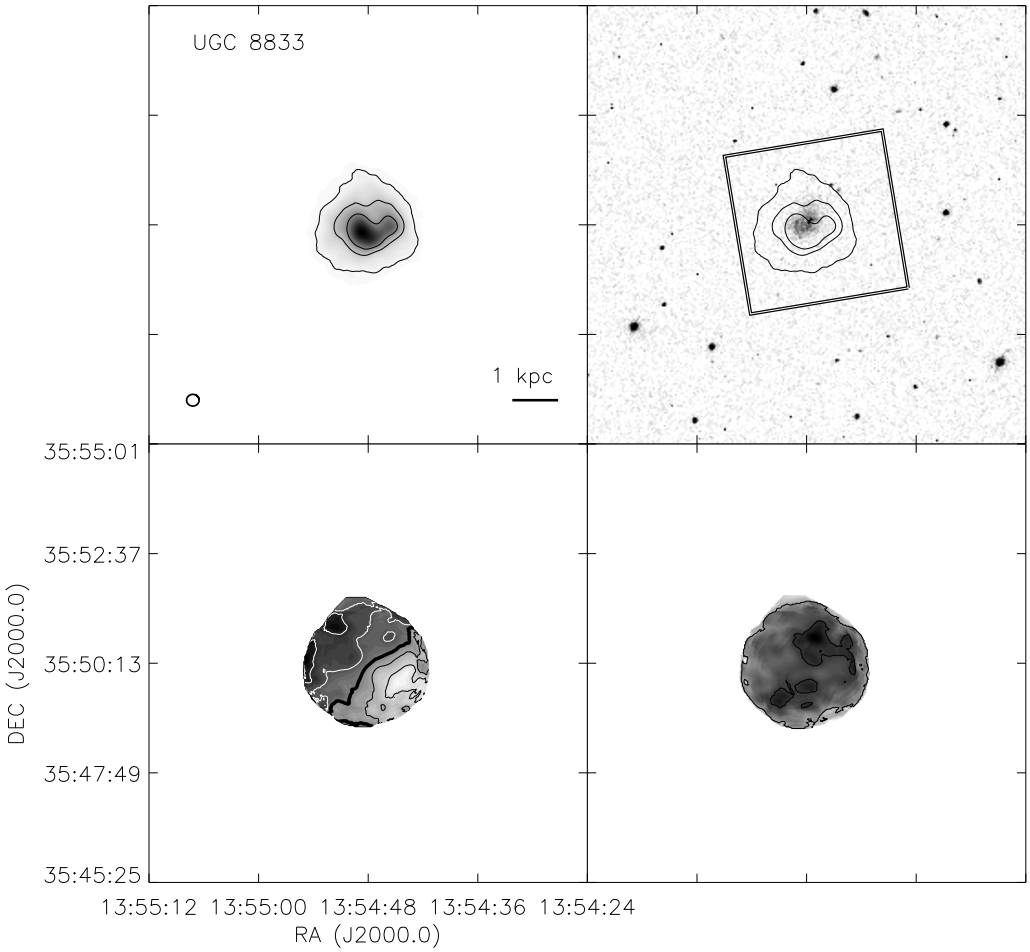

Figure 2.27 continued. *Top left:* The integrated H I intensity map for UGC 8833. The greyscale covers a range from 1×10^{19} to 2.2×10^{21} cm^{-2} with contours of 1×10^{20}, 5×10^{20}, and 1×10^{21} cm^{-2}. *Top Right:* An optical image from the SDSS with the same column density contours overlaid. The HST ACS footprint is the field covered by the ANGST survey. *Bottom Left:* The H I velocity field. Black contours (lighter gray scale) indicate approaching emission, white contours (darker gray scale) receding emission. The thick black contour is the central velocity (v_{cen} = 225.9 km s^{-1}) and the isovelocity contours are spaced by Δv = 5 km s^{-1}. *Bottom Right:* The H I velocity dispersion. Contours are plotted at 5 and 10 km s^{-1}.

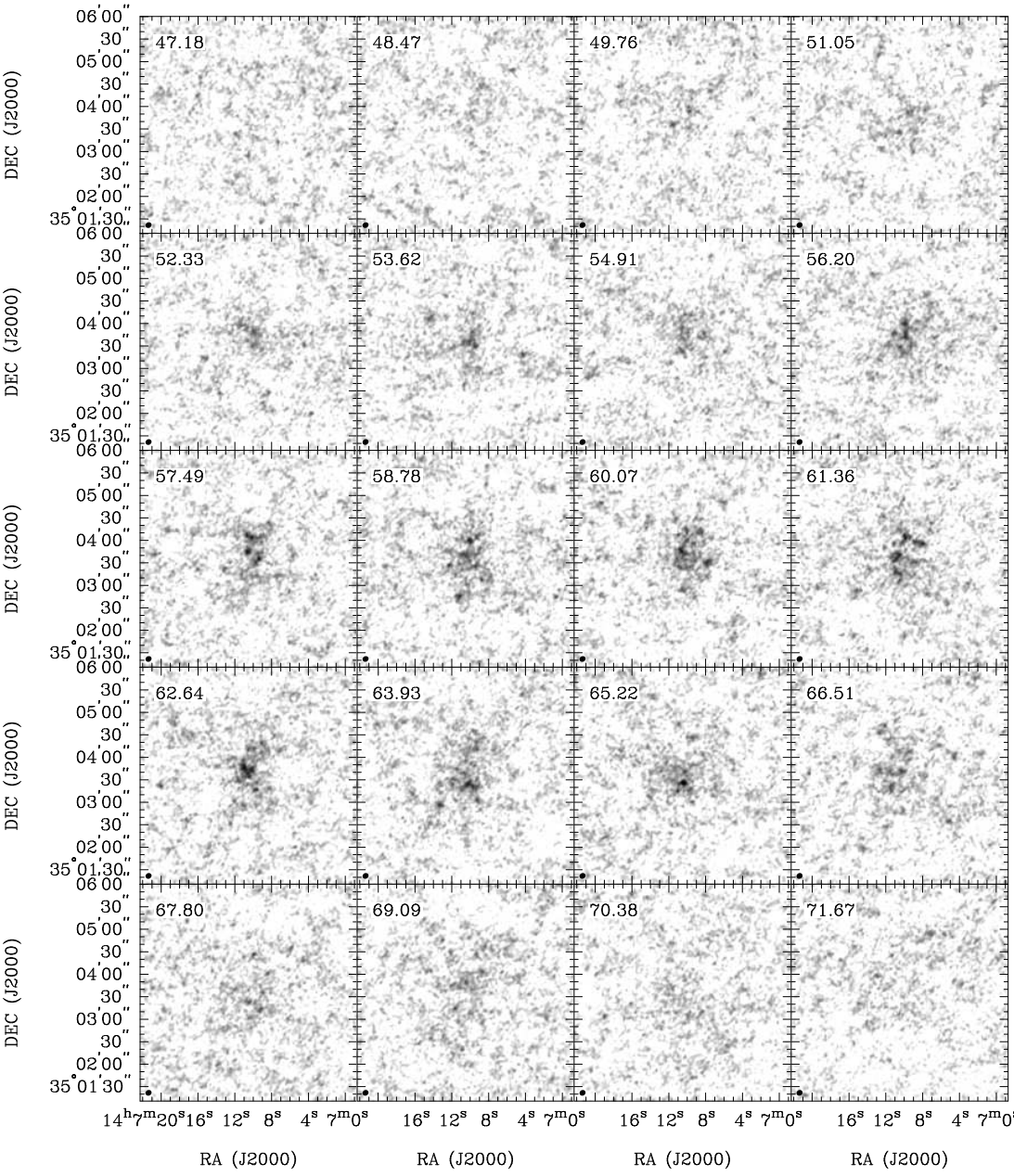

Figure 2.28 **KK 230:** Channel maps based on the natural-weighted cube (grayscale range: -0.02 to $8.2\,\mathrm{mJy\,beam^{-1}}$). Every channel is shown (channel width $0.6\,\mathrm{km\ s^{-1}}$) and each map has the same size as the moment maps in the following panels.

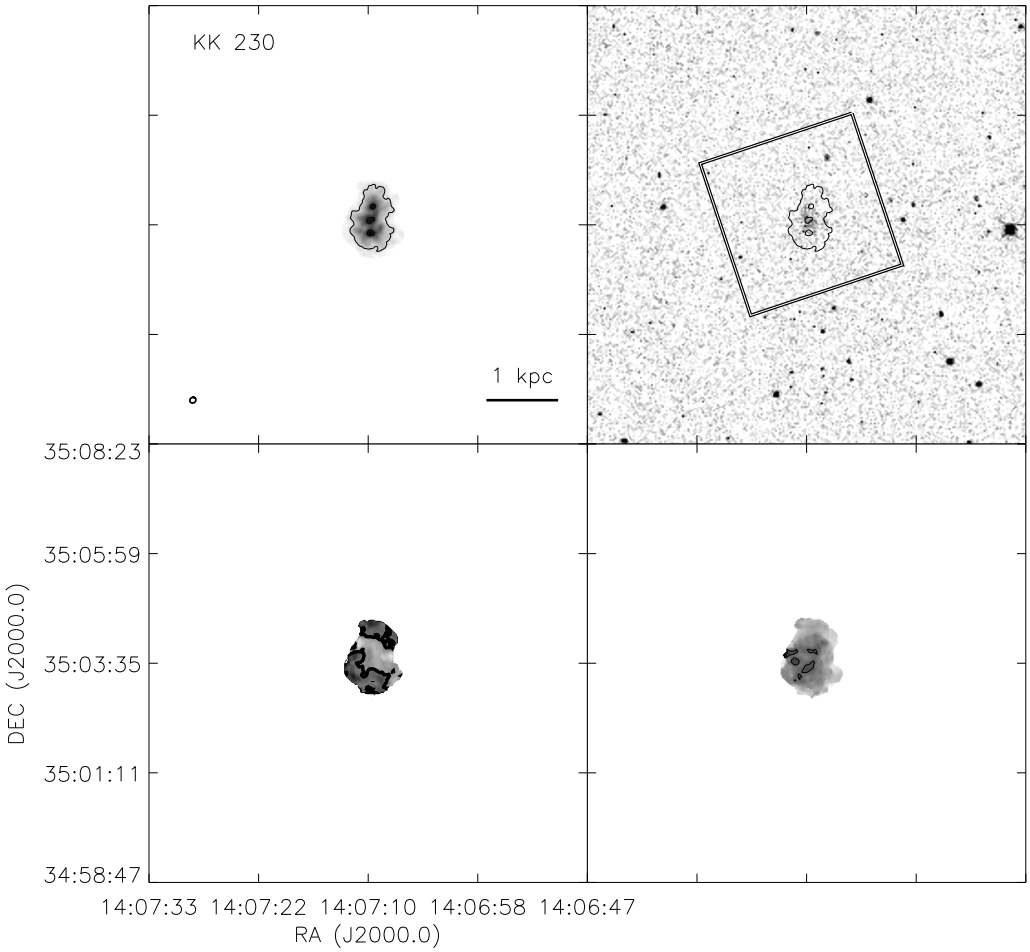

Figure 2.28 continued. *Top left:* The integrated H I intensity map for KK 230. The greyscale covers a range from $1{\times}10^{19}$ to $6.1 \times 10^{20}\,\mathrm{cm}^{-2}$ with contours of $1{\times}10^{20}$ and $5{\times}10^{20}\,\mathrm{cm}^{-2}$. *Top Right:* An optical image from the SDSS with the same column density contours overlaid. The HST ACS footprint is the field covered by the ANGST survey. *Bottom Left:* The H I velocity field. Black contours (lighter gray scale) indicate approaching emission, white contours (darker gray scale) receding emission. The thick black contour is the central velocity ($\mathrm{v}_{cen} = 60.6\,\mathrm{km\,s}^{-1}$) and the isovelocity contours are spaced by $\Delta\mathrm{v} = 5\,\mathrm{km\,s}^{-1}$. *Bottom Right:* The H I velocity dispersion. A contour is plotted at $5\,\mathrm{km\,s}^{-1}$.

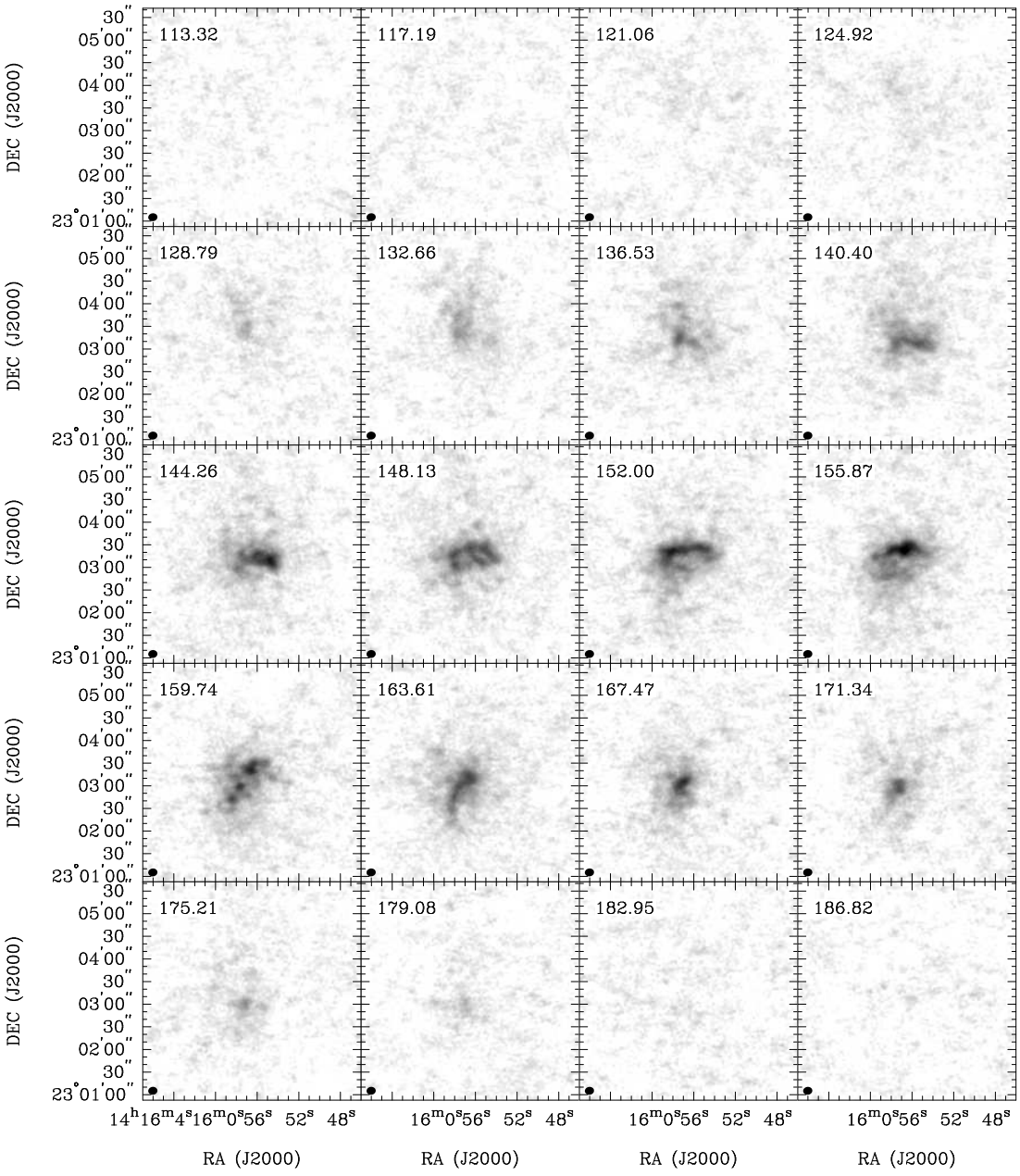

Figure 2.29 **DDO 187:** Channel maps based on the natural-weighted cube (grayscale range: -0.02 to 17.1 mJy beam^{-1}). Every second channel is shown (channel width 1.3 km s^{-1}) and each map has the same size as the moment maps in the following panels.

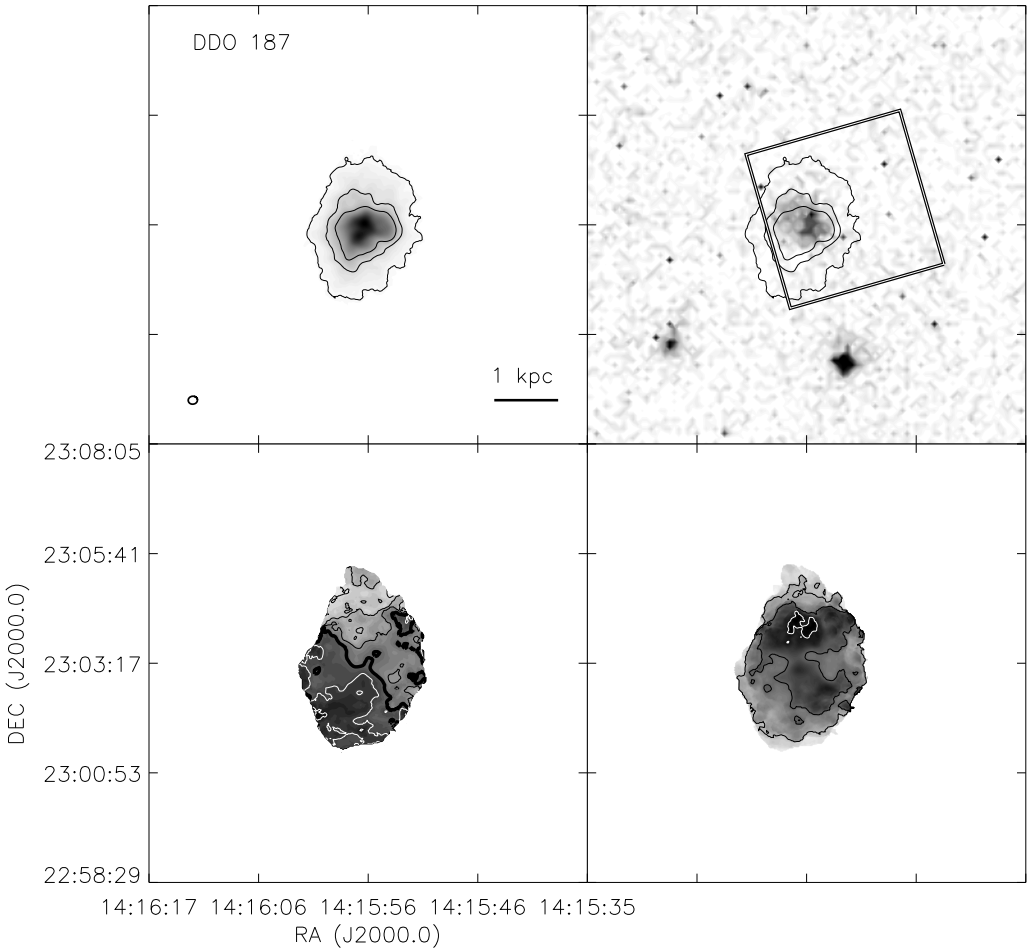

Figure 2.29 continued. *Top left:* The integrated H I intensity map for DDO 187. The greyscale covers a range from 1×10^{19} to 3.2×10^{21} cm^{-2} with contours of 1×10^{20}, 5×10^{20}, and 1×10^{21} cm^{-2}. *Top Right:* An optical image from the SDSS with the same column density contours overlaid. The HST ACS footprint is the field covered by the ANGST survey. *Bottom Left:* The H I velocity field. Black contours (lighter gray scale) indicate approaching emission, white contours (darker gray scale) receding emission. The thick black contour is the central velocity ($v_{cen} = 152.2$ km s^{-1}) and the isovelocity contours are spaced by $\Delta v = 5$ km s^{-1}. *Bottom Right:* The H I velocity dispersion. Contours are plotted at 5, 10, and 15 km s^{-1}.

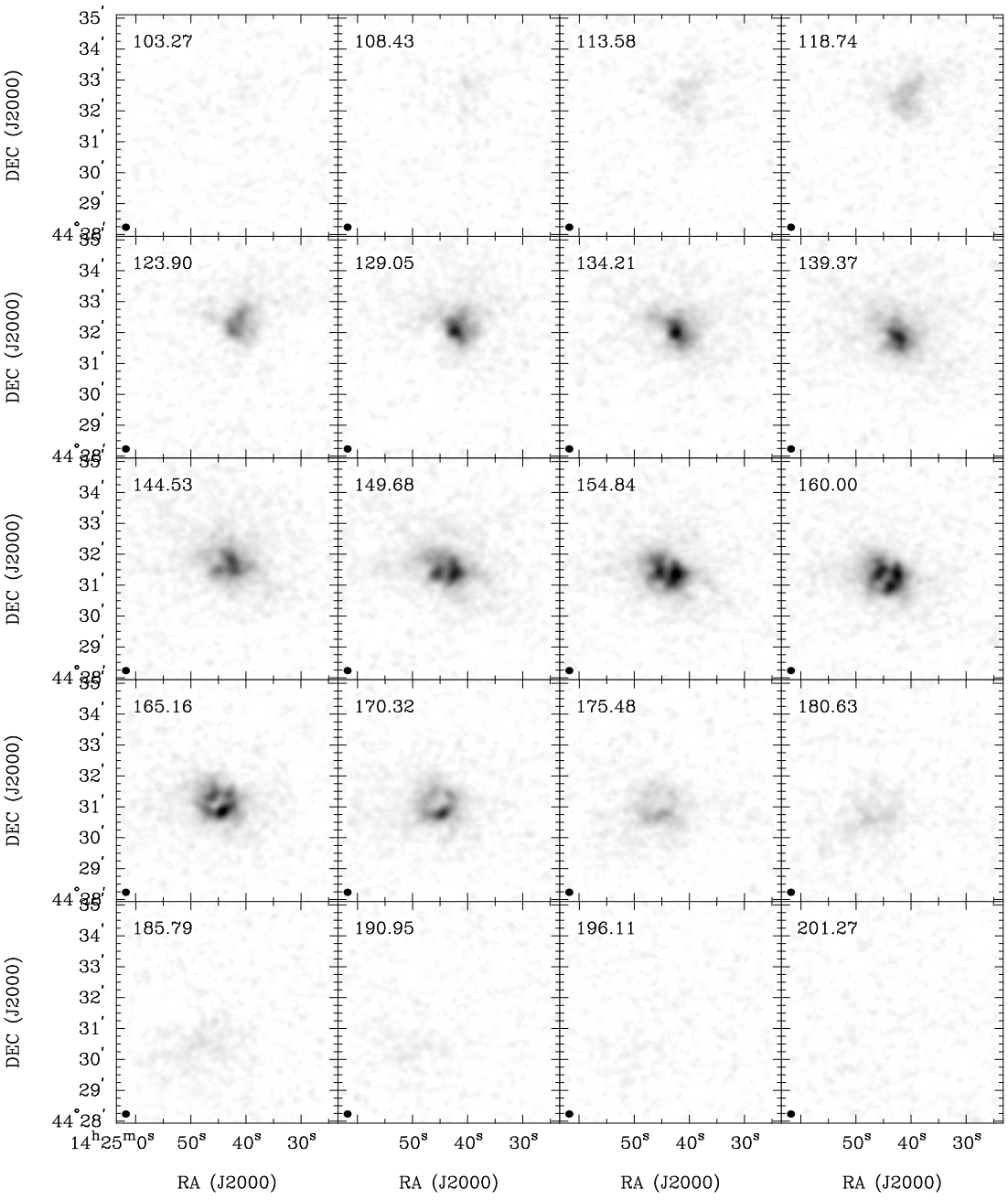

Figure 2.30 **DDO 190:** Channel maps based on the natural-weighted cube (grayscale range: -0.02 to 27.5 mJy beam^{-1}). Every channel is shown (channel width 2.6 km s^{-1}) and each map has the same size as the moment maps in the following panels.

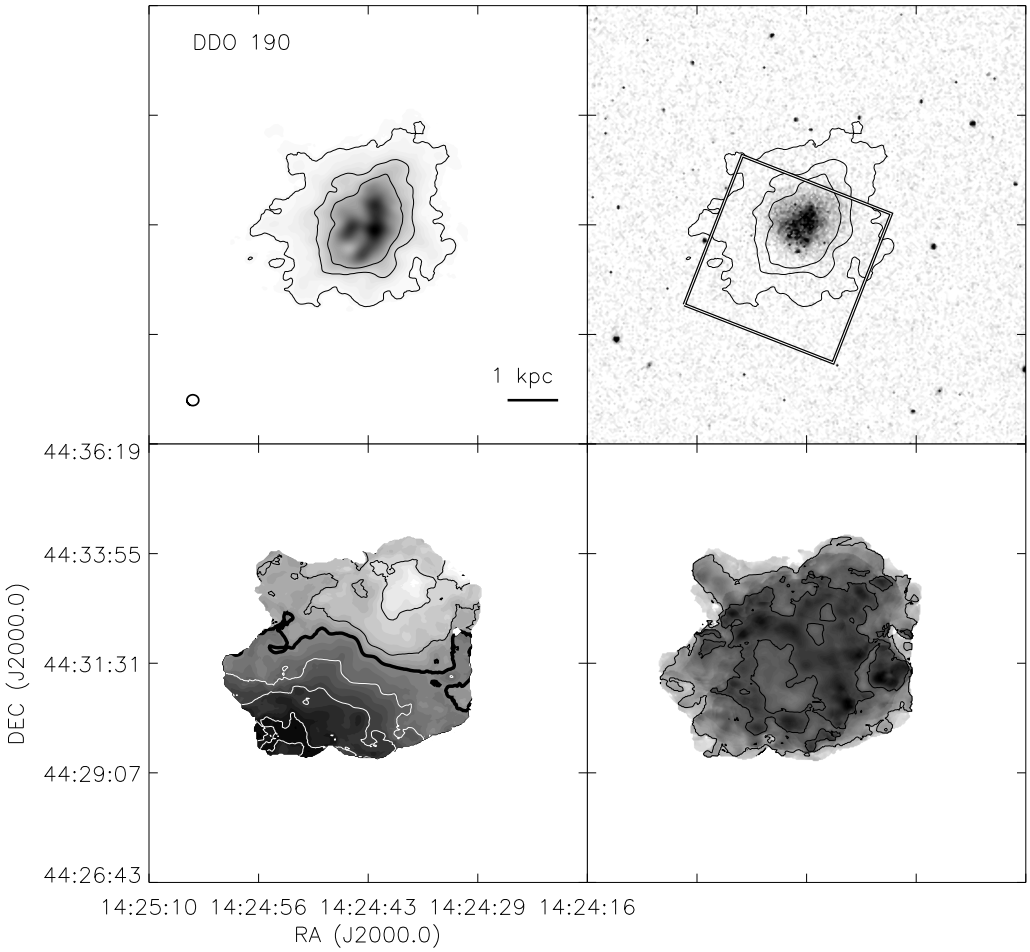

Figure 2.30 continued. *Top left:* The integrated H I intensity map for DDO 190. The greyscale covers a range from 1×10^{19} to 3.6×10^{21} cm^{-2} with contours of 1×10^{20}, 5×10^{20}, and 1×10^{21} cm^{-2}. *Top Right:* An optical image from the SDSS with the same column density contours overlaid. The HST ACS footprint is the field covered by the ANGST survey. *Bottom Left:* The H I velocity field. Black contours (lighter gray scale) indicate approaching emission, white contours (darker gray scale) receding emission. The thick black contour is the central velocity (v_{cen} = 148.8 km s^{-1}) and the isovelocity contours are spaced by Δv = 10 km s^{-1}. *Bottom Right:* The H I velocity dispersion. Contours are plotted at 5 and 10 km s^{-1}.

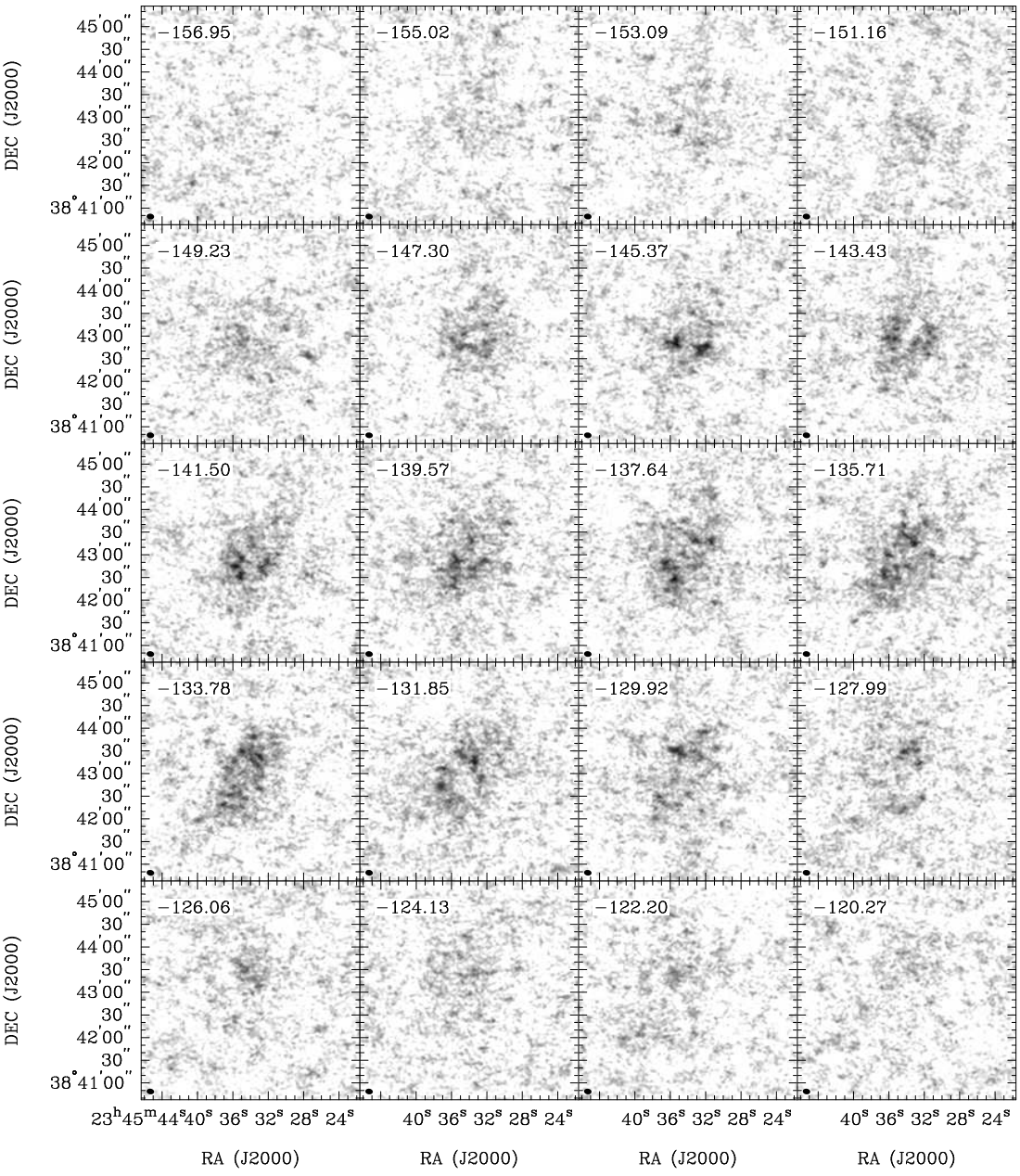

Figure 2.31 **KKH 98:** Channel maps based on the natural-weighted cube (grayscale range: −0.02 to 8.4 mJy beam^{-1}). Every second channel is shown (channel width 0.6 km s^{-1}) and each map has the same size as the moment maps in the following panels.

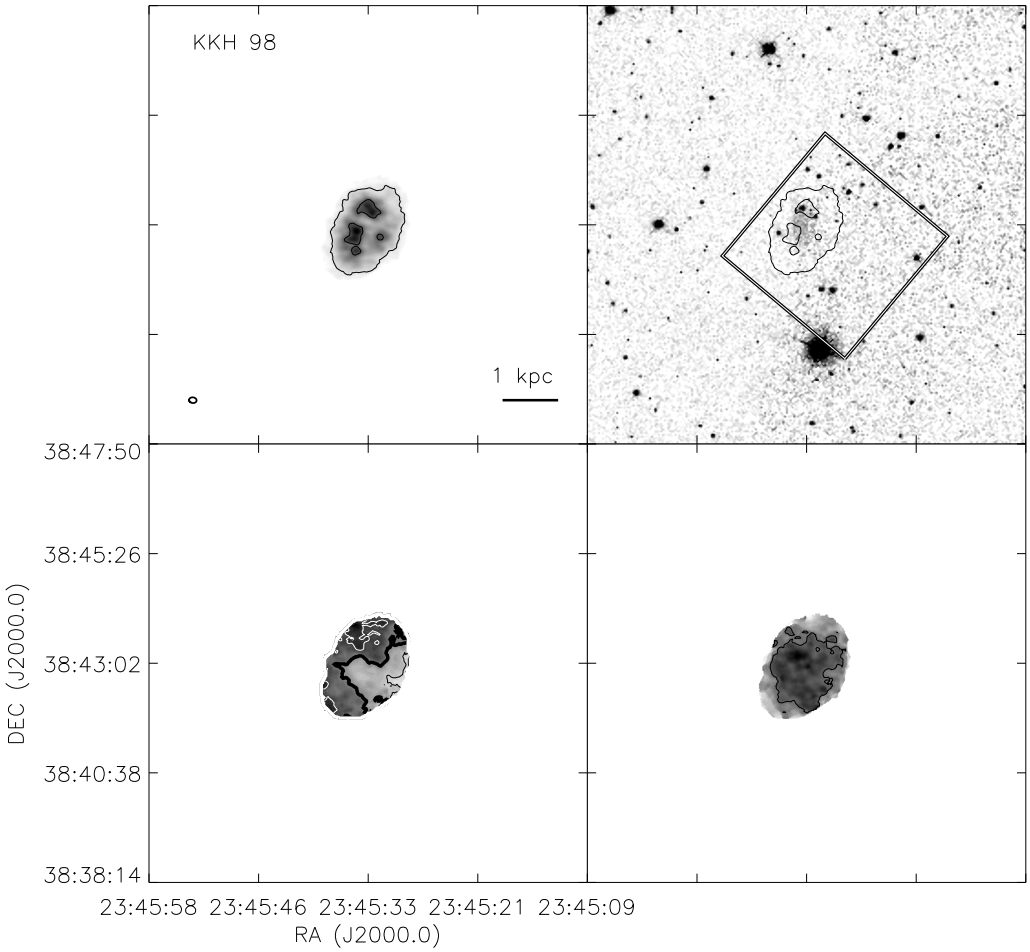

Figure 2.31 continued. *Top left:* The integrated H I intensity map for KKH 98. The greyscale covers a range from $1{\times}10^{19}$ to $7.7 \times 10^{20}\,\mathrm{cm}^{-2}$ with contours of $1{\times}10^{20}$ and $5{\times}10^{20}\,\mathrm{cm}^{-2}$. *Top Right:* An optical image from the SDSS with the same column density contours overlaid. The HST ACS footprint is the field covered by the ANGST survey. *Bottom Left:* The H I velocity field. Black contours (lighter gray scale) indicate approaching emission, white contours (darker gray scale) receding emission. The thick black contour is the central velocity ($\mathrm{v}_{cen} = -137.8\,\mathrm{km\ s}^{-1}$) and the isovelocity contours are spaced by $\Delta\mathrm{v} = 5\,\mathrm{km\,s}^{-1}$. *Bottom Right:* The H I velocity dispersion. A contour is plotted at $5\,\mathrm{km\,s}^{-1}$.

Table 2.1. General properties of the VLA-ANGST galaxy sample.

(1) Name	(2) Alt. Name	(3) RA (J2000) [^{h}:^{m}:^{s}]	(4) DEC (J2000) [$^\circ$:$'$:$''$]	(5) D [Mpc]	(6) D_{25} [kpc]	(7) M_B [mag]	(8) νL_ν (3.6μm) [10^6 L$_\odot$]	(9) Type	(10) SFR (UV) [10^{-3} $M_\odot$ yr^{-1}]
NGC 247	ESO 540-G022, UGCA 11	00:47:08.3	-20:45:36	3.50	15.7	-13.82	270.52	7	151.74
DDO 6	ESO 540-G031, UGCA 15	00:49:49.3	-21:00:58	3.31	1.6	-12.41	···	10	0.95
NGC 404	UGC 718	01:09:26.9	35:43:03	3.05	2.2	-16.21	···	-1	4.34
KKH 37	LEDA 95597	06:47:45.8	80:07:26	3.26	1.1	-11.17	0.69	10	0.21
UGC 4483	CGCG 331-051	08:37:03.0	69:46:31	3.41	1.2	-12.71	0.57	10	2.67
KK 77	LEDA 166101	09:50:10.0	67:30:24	3.55	2.5	-11.45	0.00	-3	···
BK3N	PGC 28529	09:53:48.5	68:58:09	3.86	0.6	-9.15	<0.03	10	0.20
AO 0952+69[a]	Arp's Loop	09:57:29.0	69:16:20	3.78	2.0	-11.09	···	10	0.75
Sextans B	UGC 5373, DDO 70	10:00:00.1	05:19:56	1.39	2.1	-13.87	2.48	10	2.96
NGC 3109	ESO 499-G036, DDO 236	10:03:07.2	-26:09:36	1.26	6.2	-15.11	12.40	10	18.95
Antlia	PGC 29194	10:04:04.0	-27:19:55	1.29	0.8	-9.36	···	10	1.15
KDG 63	UGC 5428 DDO71	10:05:07.3	66:33:18	3.53	1.7	-11.73	1.36	-3	···
Sextans A	UGCA 205, DDO 075	10:11:00.8	-04:41:34	1.38	2.2	-13.84	1.82	10	8.10
HS 117	···	10:21:25.2	71:06:58	3.82	1.7	-11.41	1.08	10	···
DDO 82	UGC 5692	10:30:35.0	70:37:10	3.80	3.8	-14.33	···	9	1.72
KDG 73	PGC 32667	10:52:55.3	69:32:45	4.03	0.7	-10.94	0.81	10	0.21
NGC 3741	UGC 6572	11:36:06.4	45:17:07	3.24	1.9	-13.17	1.29	10	4.07
DDO 99	UGC 6817	11:50:53.0	38:52:50	2.59	3.1	-13.37	1.43	10	3.63
NGC 4163	NGC 4167, UGC 7199	12:12:08.9	36:10:10	2.86	1.6	-13.65	3.66	10	2.64
NGC 4190	UGC 07232	12:13:44.6	36:38:00	3.50[b]	1.7	-14.20	5.80	10	6.69
DDO 113	UGCA 276	12:14:57.9	36:13:08	2.95	1.3	-11.65	0.61	10	···
MCG +09-20-131	CGCG 269-049	12:15:46.7	52:23:15	1.60[c]	0.6	-10.72	···	10	0.26
DDO 125	UGC 7577	12:27:41.8	43:29:38	2.58	3.2	-14.11	4.15	10	3.47
UGCA 292	PGC 42275	12:38:40.0	32:46:00	3.62	1.1	-11.69	0.48	10	1.90
GR 8	UGC 8091, DDO 155	12:58:40.4	14:13:03	2.08	0.7	-11.98	0.34	10	1.59
UGC 8508	I Zw 60	13:30:44.4	54:54:36	2.58	1.3	-12.94	1.40	10	···
DDO 181	UGC 8651	13:39:53.8	40:44:21	3.14	2.1	-13.03	1.51	10	2.53
DDO 183	UGC 8760	13:50:51.1	38:01:16	3.22	2.1	-13.09	1.63	9	2.11
KKH 86	LEDA 2807150	13:54:33.6	04:14:35	2.59	0.5	-10.19	0.22	10	0.05
UGC 8833	PGC 49452	13:54:48.7	35:50:15	3.08	0.8	-12.29	0.60	10	0.93
KK 230	KKR 3	14:07:10.7	35:03:37	1.97	0.3	-8.57	0.05	10	0.10
DDO 187	UGC 9128	14:15:56.5	23:03:19	2.21	1.1	-12.34	0.39	10	0.71
DDO 190	UGC 9240	14:24:43.5	44:31:33	2.79	1.5	-14.13	3.12	10	4.06
KKR 25	LEDA 2801026	16:13:47.6	54:22:16	1.93	0.6	-9.98	<0.02	10	···
KKH 98	LEDA 2807157	23:45:34.0	38:43:04	2.54	0.8	-10.32	0.40	10	0.38

Table 2.1 (cont'd)

(1) Name	(2) Alt. Name	(3) RA (J2000) [^{h}:^{m}:^{s}]	(4) DEC (J2000) [$^\circ$:$'$:$''$]	(5) D [Mpc]	(6) D_{25} [kpc]	(7) M_B [mag]	(8) νL_ν (3.6μm) [10^6 L$_\odot$]	(9) Type	(10) SFR (UV) [10^{-3} $M_\odot$ yr^{-1}]

References. — (5) tip of the red giant branch distances from Dalcanton et al. (2009); (6) taken from Dalcanton et al. (2009) and converted to physical diameters; (7) apparent blue magnitudes from Karachentsev et al. (2004) and converted to absolute blue magnitudes; (8) converted from infrared fluxes given by Dale et al. (2009); (9) T-type form Dalcanton et al. (2009); (10) converted from GALEX FUV asymptotic magnitudes given by Lee et al. (2011) and using $SFR = 1.4 \times 10^{-28}\ L_\nu(\mathrm{erg\,s^{-1}\,Hz^{-1}})$ (Kennicutt, 1998a)

[a]object might be a feature in the spiral arm of M 81 rather than a galaxy

[b]TRGB distance from Karachentsev et al. (2004)

[c]the TRGB branch was not unambiguously identified in Dalcanton et al. (2009)

Table 2.2. List of Observations

(1) Galaxy	(2) Conf.	(3) Project	(4) Date [yyyy-mm-dd]	(5) RA [^{h}:^{m}:^{s}]	(6) Dec [$^\circ$:$'$:$''$]	(7) Equ.	(8) Cal	(9) Mode	(10) BW [MHz]	(11) Chan #	(12) Δ v [km s^{-1}]	(13) $\nu_{\rm obs1}$ [MHz]	(14) $v_{\rm obs1}$ [km s^{-1}]	(15) N_{EVLA}
NGC 247	BnA	AO215	2007-10-10	00:47:08.5	-20:45:37	2000	0110-076	4	1.56	128	2.6	1419.098[a]	···	12
												1420.222[a]	···	
NGC 247	BnA	AO215	2007-10-11	00:47:08.5	-20:45:37	2000	0110-076	4	1.56	128	2.6	1419.098[a]	···	12
												1420.222[a]	···	
NGC 247	B	AO215	2008-01-11	00:47:08.5	-20:45:37	2000	0110-076	4	1.56	128	2.6	1419.008[a]	···	13
												1420.132[a]	···	
NGC 247	B	AO215	2008-01-12	00:47:08.5	-20:45:37	2000	0110-076	4	1.56	128	2.6	1419.008[a]	···	13
												1420.132[a]	···	
NGC 247	CnB	AO215	2008-02-17	00:47:08.5	-20:45:37	2000	0110-076	4	1.56	128	2.6	1419.059[a]	···	13
												1420.182[a]	···	
NGC 247	DnC	AO215	2008-06-12	00:47:08.5	-20:45:37	2000	0116-208	4	1.56	128	2.6	1419.233[a]	···	15
DDO 6	BnA	AO215	2007-10-05	00:49:49.2	-21:00:54	2000	0145-275	2AD	0.78	256	0.6	1419.010	···	12
DDO 6	BnA	AO215	2007-10-07	00:49:49.2	-21:00:54	2000	0145-275	2AD	0.78	256	0.6	1419.010	···	12
DDO 6	CnB	AO215	2008-02-16	00:49:49.2	-21:00:54	2000	0145-275	2AC	0.78	256	0.6	1418.953	···	13
DDO 6	DnC	AO215	2008-06-12	00:49:49.2	-21:00:54	2000	0116-208	2AC	0.78	256	0.6	1419.158	···	15
DDO 6	DnC	AO215	2008-07-11	00:49:49.2	-21:00:54	2000	0116-208	2AC	0.78	256	0.6	1419.140	···	16
NGC 404	B	AO215	2007-11-13	01:09:27.0	+35:43:04	2000	0119+321	2AD	0.78	256	0.6	1420.598[a]	···	12
NGC 404	C	AC459	1996-01-01	01:06:39.0	+35:28:00	1950	0116+319	2AD	1.56	128	2.6	···	-56.0	0
NGC 404	D	AO215	2008-08-21	01:09:27.0	+35:43:04	2000	0119+321	2AC	0.78	256	0.6	1420.753[a]	···	17
NGC 404	D	AC459	1996-07-16	01:06:39.0	+35:28:00	1950	0116+319	2AD	1.56	128	2.6	···	-56.0	0
KKH 37	B	AO215	2007-12-15	06:47:45.8	+80:07:26	2000	0410+769	2AD	0.78	256	0.6	1421.121[a]	···	12
KKH 37	C	AO215	2008-04-11	06:47:45.8	+80:07:26	2000	0410+769	2AC	0.78	256	0.6	1421.033[a]	···	15

Table 2.2 (cont'd)

(1) Galaxy	(2) Conf.	(3) Project	(4) Date [yyyy-mm-dd]	(5) RA [^{h}:^{m}:^{s}]	(6) Dec [$^\circ$:$'$:$''$]	(7) Equ.	(8) Cal	(9) Mode	(10) BW [MHz]	(11) Chan #	(12) Δ v [km s^{-1}]	(13) $\nu_{\rm obs1}$ [MHz]	(14) $v_{\rm obs1}$ [km s^{-1}]	(15) N_{EVLA}
KKH 37	D	AO215	2008-07-12	06:47:45.8	+80:07:26	2000	0410+769	2AC	0.78	256	0.6	1421.150[a]	···	16
KKH 37	D	AO215	2008-08-11	06:47:45.8	+80:07:26	2000	0410+769	2AC	0.78	256	0.6	1421.161[a]	···	16
UGC 4483	B	AO215	2007-12-22	08:37:03.0	+69:46:31	2000	0834+555	2AD	1.56	256	1.3	1419.698[a]	···	12
UGC 4483	B	AZ090	1997-04-01	08:32:06.0	+69:58:00	1950	0831+557	2AD	1.56	128	2.6	···	180.0	0
UGC 4483	B	AZ090	1997-04-11	08:32:06.0	+69:58:00	1950	0831+557	2AD	1.56	128	2.6	···	180.0	0
UGC 4483	B	AZ090	1997-04-12	08:32:06.0	+69:58:00	1950	0831+557	2AD	1.56	128	2.6	···	180.0	0
UGC 4483	C	AZ090	1997-06-28	08:32:06.0	+69:58:00	1950	0831+557	2AD	1.56	128	2.6	···	180.0	0
UGC 4483	C	AZ090	1997-08-14	08:32:06.0	+69:58:00	1950	0831+557	2AD	1.56	128	2.6	···	180.0	0
UGC 4483	D	AO215	2008-07-10	08:37:03.0	+69:46:31	2000	0834+555	2AC	1.56	256	1.3	1419.700[a]	···	16
UGC 4483	D	AO215	2008-08-16	08:37:03.0	+69:46:31	2000	0834+555	2AC	1.56	256	1.3	1419.200[a]	···	17
KK 77	B	AO215	2007-12-07	09:50:10.5	+67:30:24	2000	1035+564	4	1.56	128	2.2	1419.174[a]	···	12
												1420.298[a]	···	
KK 77	C	AO215	2008-03-31	09:50:10.5	+67:30:24	2000	1035+564	4	1.56	128	2.6	1419.025[a]	···	14
												1420.148[a]	···	
KK 77	D	AO215	2008-08-10	09:50:10.5	+67:30:24	2000	1035+564	4	1.56	128	2.6	1419.139[a]	···	16
												1420.262[a]	···	
KK 77	D	AO215	2008-08-19	09:50:10.5	+67:30:24	2000	1035+564	4	1.56	128	2.6	1419.118[a]	···	17
												1420.242[a]	···	
BK3N	B	AO215	2007-12-18	09:53:48.5	+68:58:08	2000	1035+564	2AD	0.78	256	0.6	1420.644[a]	···	12
BK3N	C	AO215	2008-03-16	09:53:48.5	+68:58:08	2000	1035+564	2AC	0.78	256	0.6	1420.522[a]	···	14
BK3N	D	AO215	2008-07-18	09:53:48.5	+68:58:08	2000	1035+564	2AC	0.78	256	0.6	1420.590[a]	···	16
BK3N	D	AO215	2008-08-15	09:53:48.5	+68:58:08	2000	1035+564	2AC	0.78	256	0.6	1420.631[a]	···	17

Table 2.2 (cont'd)

(1) Galaxy	(2) Conf.	(3) Project	(4) Date [yyyy-mm-dd]	(5) RA [^{h}:^{m}:^{s}]	(6) Dec [$^\circ$:$'$:$''$]	(7) Equ.	(8) Cal	(9) Mode	(10) BW [MHz]	(11) Chan #	(12) Δ v [km s^{-1}]	(13) $\nu_{\rm obs1}$ [MHz]	(14) $v_{\rm obs1}$ [km s^{-1}]	(15) N_{EVLA}
AO 0952+69	B	AO215	2007-12-09	09:57:31.0	+69:16:60	2000	1035+564	2AD	1.56	256	1.3	1419.996[a]	···	12
AO 0952+69	C	AO215	2008-03-31	09:57:31.0	+69:16:60	2000	1035+564	2AC	1.56	256	1.3	1419.855[a]	···	14
AO 0952+69	D	AO215	2008-08-11	09:57:31.0	+69:16:60	2000	1035+564	2AC	1.56	256	1.3	1419.967[a]	···	16
Sextans B	B	AO215	2007-11-16	10:00:00.1	+05:19:56	2000	1024-008	2AD	1.56	256	1.3	1419.103	···	12
Sextans B	C	AM561	1997-08-02	09:59:59.9	+05:19:43	2000	1008+075	2AD	0.78	128	1.3	···	301.0	0
Sextans B	D	AO215	2008-08-03	10:00:00.1	+05:19:56	2000	0943-083	2AC	1.56	256	1.3	1418.890	···	16
NGC 3109	BnA	AO215	2007-10-07	10:03:06.9	-26:09:34	2000	0921-263	2AD	1.56	256	1.3	1418.570	···	12
NGC 3109	BnA	AO215	2007-10-08	10:03:06.9	-26:09:34	2000	0921-263	2AD	1.56	256	1.3	1418.570	···	12
NGC 3109	CnB	AO215	2008-02-26	10:03:06.9	-26:09:34	2000	0921-263	2AC	1.56	256	1.3	1418.526	···	14
NGC 3109	DnC	AO215	2008-06-15	10:03:06.9	-26:09:34	2000	0921-263	2AC	1.56	256	1.3	1418.402	···	15
NGC 3109	DnC	AO215	2008-07-12	10:03:06.9	-26:09:34	2000	0921-263	2AC	1.56	256	1.3	1418.470	···	16
Antlia	BnA	AO215	2007-10-06	10:04:04.1	-27:19:52	2000	0921-263	2AD	0.78	256	0.6	1418.740	···	12
Antlia	BnA	AO215	2007-10-13	10:04:04.1	-27:19:52	2000	0921-263	2AD	0.78	256	0.6	1418.755	···	12
Antlia	CnB	AA232	1998-11-02	10:01:47.5	-27:05:15	1950	1015-314	2AD	0.78	128	1.3	···	360.0	0
Antlia	CnB	AA232	1998-11-13	10:01:47.5	-27:05:15	1950	1015-314	2AD	0.78	128	1.3	···	360.0	0
Antlia	DnC	AO215	2008-06-15	10:04:04.1	-27:19:52	2000	0921-263	2AC	0.78	256	0.6	1418.578	···	15
Antlia	DnC	AO215	2008-07-26	10:04:04.1	-27:19:52	2000	0921-263	2AC	0.78	256	0.6	1418.614	···	16
KDG 63	B	AO215	2007-11-29	10:05:06.4	+66:33:32	2000	1035+564	2AD	0.78	256	0.6	1421.093[a]	···	12
KDG 63	C	AO215	2008-04-05	10:05:06.4	+66:33:32	2000	1035+564	2AC	0.78	256	0.6	1420.930[a]	···	14
KDG 63	D	AO215	2008-08-08	10:05:06.4	+66:33:32	2000	1035+564	2AC	0.78	256	0.6	1421.010[a]	···	16

Table 2.2 (cont'd)

(1) Galaxy	(2) Conf.	(3) Project	(4) Date [yyyy-mm-dd]	(5) RA [^{h}:^{m}:^{s}]	(6) Dec [$^\circ$:$'$:$''$]	(7) Equ.	(8) Cal	(9) Mode	(10) BW [MHz]	(11) Chan #	(12) Δ v [km s^{-1}]	(13) $\nu_{\rm obs1}$ [MHz]	(14) $v_{\rm obs1}$ [km s^{-1}]	(15) N_{EVLA}
KDG 63	D	AO215	2008-08-17	10:05:06.4	+66:33:32	2000	1035+564	2AC	0.78	256	0.6	1421.052[a]	···	17
Sextans A	B	AO215	2007-11-21	10:11:00.8	-04:41:34	2000	1024-008	2AD	1.56	256	1.3	1418.981	···	12
Sextans A	C	AO215	2008-03-16	10:11:00.8	-04:41:34	2000	1024-008	2AC	1.56	256	1.3	1418.799	···	14
Sextans A	D	AO215	2008-04-12	10:11:00.8	-04:41:34	2000	1024-008	2AC	1.56	256	1.3	1418.770	···	16
Sextans A	D	AO215	2008-08-17	10:11:00.8	-04:41:34	2000	0943-083	2AC	1.56	256	1.3	1418.819	···	17
HS 117	B	AO215	2007-11-28	10:21:25.2	+71:06:51	2000	1035+564	2AD	0.78	256	0.6	1420.649[a]	···	12
HS 117	C	AO215	2008-04-11	10:21:25.2	+71:06:51	2000	1035+564	2AC	0.78	256	0.6	1420.500[a]	···	15
HS 117	D	AO215	2008-07-14	10:21:25.2	+71:06:51	2000	1035+564	2AC	0.78	256	0.6	1420.575[a]	···	16
HS 117	D	AO215	2008-08-11	10:21:25.2	+71:06:51	2000	1035+564	2AC	0.78	256	0.6	1420.608[a]	···	16
NG DDO 82	B	AO215	2007-12-13	10:30:35.0	+70:37:07	2000	1035+564	2AD	1.56	256	1.3	1420.194[a]	···	12
DDO 82	C	AO215	2008-04-08	10:30:35.0	+70:37:07	2000	1035+564	2AC	1.56	256	1.3	1420.061[a]	···	14
DDO 82	D	AO215	2008-08-11	10:30:35.0	+70:37:07	2000	1035+564	2AC	1.56	256	1.3	1420.165[a]	···	16
DDO 82	D	AO215	2008-08-16	10:30:35.0	+70:37:07	2000	1035+564	2AC	1.56	256	1.3	1420.150[a]	···	16
KDG 73	B	AO215	2007-11-27	10:52:57.1	+69:32:58	2000	1313+675	2AD	0.78	256	0.6	1419.928[a]	···	12
KDG 73	C	AO215	2008-04-11	10:52:57.1	+69:32:58	2000	1313+675	2AC	0.78	256	0.6	1419.778[a]	···	15
KDG 73	D	AO215	2008-07-14	10:52:57.1	+69:32:58	2000	1313+675	2AC	0.78	256	0.6	1419.845[a]	···	16
KDG 73	D	AO215	2008-08-16	10:52:57.1	+69:32:58	2000	1313+675	2AC	0.78	256	0.6	1419.883[a]	···	17
NGC 3741	B	AO215	2007-11-06	11:36:06.2	+45:17:01	2000	1146+399	2AD	1.56	256	1.3	1419.434[a]	···	12
NGC 3741	C	AO215	2008-05-05	11:36:06.2	+45:17:01	2000	1146+399	2AC	1.56	256	1.3	1419.218[a]	···	15
NGC 3741	D	AO215	2008-08-04	11:36:06.2	+45:17:01	2000	1146+399	2AC	1.56	256	1.3	1419.295[a]	···	17

Table 2.2 (cont'd)

(1) Galaxy	(2) Conf.	(3) Project	(4) Date [yyyy-mm-dd]	(5) RA [^{h}:^{m}:^{s}]	(6) Dec [$^\circ$:$'$:$''$]	(7) Equ.	(8) Cal	(9) Mode	(10) BW [MHz]	(11) Chan #	(12) Δ v [km s^{-1}]	(13) $\nu_{\rm obs1}$ [MHz]	(14) $v_{\rm obs1}$ [km s^{-1}]	(15) N_{EVLA}
DDO 99	B	AO215	2007-12-04	11:50:53.0	+38:52:49	2000	1146+399	2AD	1.56	256	1.3	1419.363	···	12
DDO 99	C	AO215	2008-04-05	11:50:53.0	+38:52:49	2000	1146+399	2AC	1.56	256	1.3	1419.180	···	14
DDO 99	D	AO215	2008-08-07	11:50:53.0	+38:52:49	2000	1146+399	2AC	1.56	256	1.3	1419.180	···	16
DDO 99	D	AO215	2008-08-10	11:50:53.0	+38:52:49	2000	1146+399	2AC	1.56	256	1.3	1419.204	···	16
NGC 4163	B	AO215	2007-11-23	12:12:09.1	+36:10:09	2000	1227+365	2AD	0.78	256	0.6	1419.740	···	12
NGC 4163	B	AH927[b]	2008-02-12	12:12:09.1	+36:10:09	2000	1227+365	2AC	0.78	256	0.6	1419.719[a]	···	13
NGC 4163	C	AO215	2008-04-08	12:12:09.1	+36:10:09	2000	1227+365	2AC	0.78	256	0.6	1419.563	···	14
NGC 4163	C	AH927[b]	2008-06-01	12:12:09.1	+36:10:09	2000	1227+365	2AC	0.78	256	0.6	1419.546[a]	···	15
NGC 4163	D	AO215	2008-08-06	12:12:09.1	+36:10:09	2000	1227+365	2AC	0.78	256	0.6	1419.540	···	16
NGC 4190	B	AO215	2007-24-24	12:13:44.8	+36:38:03	2000	1227+365	2AD	1.56	256	1.3	1419.441[a]	···	13
NGC 4190	C	AO215	2008-03-09	12:13:44.8	+36:38:03	2000	1227+365	2AC	1.56	256	1.3	1419.323[a]	···	14
NGC 4190	D	AO215	2008-08-11	12:13:44.8	+36:38:03	2000	1227+365	2AC	1.56	256	1.3	1419.275[a]	···	16
DDO 113	B	AO215	2007-12-01	12:14:57.9	+36:13:08	2000	1227+365	2AD	1.56	256	1.3	1419.179	···	12
DDO 113	C	AO215	2008-04-04	12:14:57.9	+36:13:08	2000	1227+365	2AC	1.56	256	1.3	1419.007	···	14
DDO 113	D	AO215	2008-08-15	12:14:57.9	+36:13:08	2000	1227+365	2AC	1.56	256	1.3	1419.040	···	16
DDO 113	D	AO215	2008-08-17	12:14:57.9	+36:13:08	2000	1227+365	2AC	1.56	256	1.3	1419.020	···	17
MCG +09-20-131	B	AO215	2007-11-30	12:15:46.8	+52:23:17	2000	1219+484	2AD	1.56	256	1.3	1419.749[a]	···	12
MCG +09-20-131	C	AO215	2008-05-05	12:15:46.8	+52:23:17	2000	1219+484	2AC	1.56	256	1.3	1419.566[a]	···	15
MCG +09-20-131	D	AO215	2008-08-10	12:15:46.8	+52:23:17	2000	1219+484	2AC	1.56	256	1.3	1419.626[a]	···	16

Table 2.2 (cont'd)

(1) Galaxy	(2) Conf.	(3) Project	(4) Date [yyyy-mm-dd]	(5) RA [^{h}:^{m}:^{s}]	(6) Dec [$^\circ$:$'$:$''$]	(7) Equ.	(8) Cal	(9) Mode	(10) BW [MHz]	(11) Chan #	(12) Δ v [km s^{-1}]	(13) $\nu_{\rm obs1}$ [MHz]	(14) $v_{\rm obs1}$ [km s^{-1}]	(15) N_{EVLA}
DDO 125	B	AO215	2007-11-25	12:27:40.9	+43:29:44	2000	1227+365	2AD	0.78	256	0.6	1419.588	···	12
DDO 125	C	AO215	2008-03-09	12:27:40.9	+43:29:44	2000	1227+365	2AC	0.78	256	0.6	1419.478	···	14
DDO 125	D	AO215	2008-08-06	12:27:40.9	+43:29:44	2000	1227+365	2AC	0.78	256	0.6	1419.410	···	16
DDO 125	D	AO215	2008-08-15	12:27:40.9	+43:29:44	2000	1227+365	2AC	0.78	256	0.6	1419.446	···	17
UGCA 292	B	AO215	2007-12-03	12:38:40.0	+32:46:01	2000	1227+365	2AD	0.78	256	0.6	1419.062	···	12
UGCA 292	C	AH927[b]	2008-02-06	12:38:40.0	+32:46:01	2000	1227+365	2AC	0.78	256	0.6	1419.053	···	13
UGCA 292	D	AO215	2008-07-11	12:38:40.0	+32:46:01	2000	1227+365	2AC	0.78	256	0.6	1418.865	···	16
UGCA 292	D	AO215	2008-08-16	12:38:40.0	+32:46:01	2000	1227+365	2AC	0.78	256	0.6	1418.892	···	17
UGCA 292	D	AH927[b]	2008-07-21	12:38:40.0	+32:46:01	2000	1227+365	2AC	0.78	256	0.6	1418.874	···	16
GR 8	B	AO215	2007-11-12	12:58:40.4	+14:13:03	2000	1254+116	2AD	0.78	256	0.6	1419.485	···	11
GR 8	C	AH927[b]	2008-02-10	12:58:40.4	+14:13:03	2000	1347+122	2AC	0.78	256	0.6	1419.524	···	13
GR 8	D	AO215	2008-08-02	12:58:40.4	+14:13:03	2000	1254+116	2AC	0.78	256	0.6	1419.285	···	16
GR 8	D	AO215	2008-08-17	12:58:40.4	+14:13:03	2000	1254+116	2AC	0.78	256	0.6	1419.304	···	17
GR 8	D	AH927[b]	2008-08-02	12:58:40.4	+14:13:03	2000	1347+122	2AC	0.78	256	0.6	1419.287	···	16
UGC 8508	B	AO215	2007-12-10	13:30:44.4	+54:54:36	2000	1400+621	2AD	0.78	256	0.6	1420.190[a]	···	12
UGC 8508	B	AH927[b]	2008-02-09	13:30:44.4	+54:54:36	2000	1400+621	2AC	0.78	256	0.6	1420.175[a]	···	13
UGC 8508	C	AO215	2008-03-15	13:30:44.4	+54:54:36	2000	1400+621	2AC	0.78	256	0.6	1420.102[a]	···	14
UGC 8508	C	AH927[b]	2008-05-31	13:30:44.4	+54:54:36	2000	1400+621	2AC	0.78	256	0.6	1420.062[a]	···	15
UGC 8508	D	AO215	2008-07-31	13:30:44.4	+54:54:36	2000	1400+621	2AC	0.78	256	0.6	1420.060[a]	···	16
UGC 8508	D	AH927[b]	2008-08-03	13:30:44.4	+54:54:36	2000	1400+621	2AC	0.78	256	0.6	1420.071[a]	···	16
UGC 8508	D	AO215	2008-08-17	13:30:44.4	+54:54:36	2000	1400+621	2AC	0.78	256	0.6	1420.084[a]	···	17

Table 2.2 (cont'd)

(1) Galaxy	(2) Conf.	(3) Project	(4) Date [yyyy-mm-dd]	(5) RA [^{h}:^{m}:^{s}]	(6) Dec [$^\circ$:$'$:$''$]	(7) Equ.	(8) Cal	(9) Mode	(10) BW [MHz]	(11) Chan #	(12) Δ v [km s^{-1}]	(13) $\nu_{\rm obs1}$ [MHz]	(14) $v_{\rm obs1}$ [km s^{-1}]	(15) N_{EVLA}
DDO 181	B	AO215	2007-12-06	13:39:53.8	+40:44:21	2000	1331+305	2AD	1.56	256	1.3	1419.543[a]	···	12
DDO 181	C	AO215	2008-03-09	13:39:53.8	+40:44:21	2000	1331+305	2AC	1.56	256	1.3	1419.474[a]	···	14
DDO 181	D	AO215	2008-08-16	13:39:53.8	+40:44:21	2000	1331+305	2AC	1.56	256	1.3	1419.388[a]	···	17
DDO 181	D	AO215	2008-08-18	13:39:53.8	+40:44:21	2000	1331+305	2AC	1.56	256	1.3	1419.390[a]	···	17
DDO 183	B	AO215	2007-12-08	13:50:50.6	+38:01:09	2000	1331+305	2AD	1.56	256	1.3	1419.591[a]	···	12
DDO 183	C	AO215	2008-03-15	13:50:50.6	+38:01:09	2000	1331+305	2AC	1.56	256	1.3	1419.518[a]	···	14
DDO 183	D	AO215	2008-08-11	13:50:50.6	+38:01:09	2000	1331+305	2AC	1.56	256	1.3	1419.433[a]	···	16
DDO 183	D	AO215	2008-08-11	13:50:50.6	+38:01:09	2000	1331+305	2AC	1.56	256	1.3	1419.424[a]	···	16
KKH 86	B	AO215	2007-11-11	13:54:33.5	+04:14:35	2000	1347+122	2AD	0.78	256	0.6	1419.105	···	11
KKH 86	C	AO215	2008-03-28	13:54:33.5	+04:14:35	2000	1347+122	2AC	0.78	256	0.6	1419.074	···	14
KKH 86	D	AO215	2008-08-08	13:54:33.5	+04:14:35	2000	1347+122	2AC	0.78	256	0.6	1418.944	···	16
UGC 8833	B	AO215	2007-11-18	13:54:48.7	+35:50:15	2000	1331+305	2AD	0.78	256	0.6	1419.406	···	12
UGC 8833	C	AZ121	2000-04-15	13:52:38.2	+36:04:60	1950	1413+349	2AD	1.56	128	2.6	···	225.0	0
UGC 8833	D	AO215	2008-08-05	13:54:48.7	+35:50:15	2000	1331+305	2AC	0.78	256	0.6	1419.265	···	16
UGC 8833	D	AO215	2008-08-15	13:54:48.7	+35:50:15	2000	1331+305	2AC	0.78	256	0.6	1419.259	···	17
KK 230	B[c]	AO215	2007-11-10	14:07:10.5	+35:03:37	2000	1331+305	2AD	0.78	256	0.6	1420.171[a]	···	12
KK 230	C	AO215	2008-04-03	14:07:10.5	+35:03:37	2000	1331+305	2AC	0.78	256	0.6	1420.114[a]	···	13
KK 230	D	AO215	2008-08-15	14:07:10.5	+35:03:37	2000	1331+305	2AC	0.78	256	0.65	1420.036[a]	···	17
DDO 187	B	AO215	2007-11-17	14:15:56.5	+23:03:19	2000	1330+251	2AD	1.56	256	1.3	1419.751[a]	···	13
DDO 187	B	AH927[b]	2008-02-10	14:15:56.5	+23:03:19	2000	1330+251	2AC	1.56	256	1.3	1419.805[a]	···	13

Table 2.2 (cont'd)

(1) Galaxy	(2) Conf.	(3) Project	(4) Date [yyyy-mm-dd]	(5) RA [^{h}:^{m}:^{s}]	(6) Dec [$^\circ$:$'$:$''$]	(7) Equ.	(8) Cal	(9) Mode	(10) BW [MHz]	(11) Chan #	(12) Δ v [km s^{-1}]	(13) $\nu_{\rm obs1}$ [MHz]	(14) $v_{\rm obs1}$ [km s^{-1}]	(15) N_{EVLA}
DDO 187	B	AH927[b]	2008-02-12	14:15:56.5	+23:03:19	2000	1330+251	2AC	1.56	256	1.3	1419.805[a]	···	13
DDO 187	C	AO215	2008-03-28	14:15:56.5	+23:03:19	2000	1330+251	2AC	1.56	256	1.3	1419.704[a]	···	14
DDO 187	C	AH927[b]	2008-05-30	14:15:56.5	+23:03:19	2000	1330+251	2AC	1.56	256	1.3	1419.674[a]	···	14
DDO 187	D	AH927[b]	2008-08-05	14:15:56.5	+23:03:19	2000	1330+251	2AC	1.56	256	1.3	1419.580[a]	···	16
DDO 187	D	AO215	2008-08-06	14:15:56.5	+23:03:19	2000	1330+251	2AC	1.56	256	1.3	1419.598[a]	···	16
DDO 187	D	AO215	2008-08-16	14:15:56.5	+23:03:19	2000	1330+251	2AC	1.56	256	1.3	1419.588[a]	···	17
DDO 190	B	AO215	2007-12-14	14:24:43.4	+44:31:33	2000	1506+375	2AD	0.78	256	0.6	1419.776	···	12
DDO 190	C	AZ121	2000-04-20	14:22:48.8	+44:44:60	1950	1413+349	2AD	1.56	128	2.6	···	160.0	0
DDO 190	D	AO215	2008-08-16	14:24:43.4	+44:31:33	2000	1506+375	2AC	0.78	256	0.6	1419.637	···	17
KKR 25	B	AO215	2008-01-31	16:13:47.9	+54:22:16	2000	1634+627	2AD	0.78	256	0.6	1421.112[a]	···	13
KKR 25	C	AO215	2008-04-03	16:13:47.9	+54:22:16	2000	1634+627	2AC	0.78	256	0.6	1421.083[a]	···	13
KKR 25	D	AO215	2008-08-07	16:13:47.9	+54:22:16	2000	1634+627	2AC	0.78	256	0.6	1421.035[a]	···	16
KKR 25	D	AO215	2008-08-16	16:13:47.9	+54:22:16	2000	1634+627	2AC	0.78	256	0.6	1421.030[a]	···	17
KKH 98	B	AO215	2007-12-07	23:45:34.0	+38:43:04	2000	0029+349	2AD	0.78	256	0.6	1420.954[a]	···	12
KKH 98	C	AO215	2008-03-15	23:45:34.0	+38:43:04	2000	0029+349	2AC	0.78	256	0.6	1421.016[a]	···	14
KKH 98	D	AO215	2008-07-10	23:45:34.0	+38:43:04	2000	0029+349	2AC	0.78	256	0.6	1421.150[a]	···	16
KKH 98	D	AO215	2008-08-21	23:45:34.0	+38:43:04	2000	0029+349	2AC	0.78	256	0.6	1421.135[a]	···	17

[a]Potential MW Interference; offset flux calibrators

[b]additional data from the LITTLE THINGS survey

[c]Source is named KKR 25 but is actually KK 230

Table 2.3. Properties of the VLA-ANGST Data Cubes.

(1) Galaxy	(2) Weighting	(3) B_{major} [″]	(4) B_{minor} [″]	(5) BPA [°]	(6) Noise [mJy beam^{-1}]	(7) Channel Width [km s^{-1}]	(8) N_{pixels}	(9) Pixel scale [″]
NGC 247	Natural	9.0	6.2	10.5	0.9	2.6	2048^2	1.0
	Robust	6.5	4.8	12.7	0.9			
DDO 6	Natural	12.3	10.3	52.0	1.9	0.65	1024^2	1.5
	Robust	7.2	6.3	49.0	2.1			
NGC 404	Natural	13.7	12.4	-34.7	0.9	2.6	1024^2	1.5
	Robust	7.1	6.1	-32.6	0.9			
KKH 37[a]	Natural	9.7	8.1	-86.2	1.6	0.65	1024^2	1.5
	Robust	6.5	5.8	-66.9	1.8			
UGC 4483	Natural	12.2	9.8	61.3	0.5	2.6	1024^2	1.5
	Robust	7.6	5.7	57.1	0.6			
KK 77[a]	Natural	12.2	8.1	-79.0	0.9	2.6	1024^2	1.5
	Robust	6.1	5.8	-66.6	0.7			
BK3N	Natural	12.0	8.1	-85.1	1.8	0.65	1024^2	1.5
	Robust	6.3	5.8	61.5	1.8			
AO 0952+69	Natural	10.1	8.8	73.5	1.3	1.3	1024^2	1.5
	Robust	6.4	5.9	-71.0	1.2			
Sextans B	Natural	15.0	14.1	10.5	0.8	1.3	1024^2	1.5
	Robust	9.5	7.5	41.6	1.0			
NGC 3109	Natural	10.3	8.8	22.0	1.6	1.3	2048^2	1.0
	Robust	7.6	5.0	8.8	1.7			
Antlia	Natural	14.1	13.9	-81.3	1.0	1.3	1024^2	1.5
	Robust	10.5	9.6	71.1	1.2			
KDG 63[a]	Natural	10.8	9.2	85.5	1.4	0.65	1024^2	1.5
	Robust	6.2	6.0	77.0	1.6			
Sextans A	Natural	11.8	10.1	38.5	1.2	1.3	1024^2	1.5

Table 2.3 (cont'd)

(1) Galaxy	(2) Weighting	(3) B_{major} [″]	(4) B_{minor} [″]	(5) BPA [°]	(6) Noise [mJy beam^{-1}]	(7) Channel Width [km s^{-1}]	(8) N_{pixels}	(9) Pixel scale [″]
	Robust	7.3	6.0	35.1	1.3			
HS 117[a]	Natural	13.2	8.5	-59.6	1.6	0.65	1024^2	1.5
	Robust	8.6	6.1	-77.8	1.7			
DDO 82	Natural	9.3	7.7	-81.0	1.3	1.3	1024^2	1.5
	Robust	5.8	5.7	65.0	1.4			
KDG 73	Natural	10.0	7.6	84.3	1.6	0.65	1024^2	1.5
	Robust	6.9	5.6	65.2	1.7			
NGC 3741	Natural	7.6	6.2	81.1	1.0	1.3	1024^2	1.5
	Robust	5.5	4.8	75.4	1.1			
DDO 99	Natural	12.4	7.6	-86.7	1.0	1.3	1024^2	1.5
	Robust	7.7	5.2	72.5	1.1			
NGC 4163	Natural	12.3	10.4	-89.6	1.3	0.65	1024^2	1.5
	Robust	7.6	5.4	-85.2	1.4			
NGC 4190	Natural	10.5	8.9	83.8	0.9	1.3	1024^2	1.5
	Robust	6.1	5.3	81.4	1.0			
DDO 113[a]	Natural	15.0	14.0	-55.2	1.4	1.3	1024^2	1.5
	Robust	9.9	7.7	82.8	1.5			
MCG +09−20−131	Natural	9.7	7.4	69.7	1.0	1.3	1024^2	1.5
	Robust	6.1	5.3	69.1	1.1			
DDO 125	Natural	11.5	10.6	-68.2	1.5	0.65	1024^2	1.5
	Robust	6.3	5.4	-80.1	1.5			
UGCA 292	Natural	9.7	6.9	69.4	1.5	0.65	1024^2	1.5
	Robust	7.0	5.0	65.2	1.6			
GR 8	Natural	7.6	7.3	-55.9	1.5	0.65	1024^2	1.5
	Robust	5.8	5.4	-28.8	1.6			

Table 2.3 (cont'd)

(1) Galaxy	(2) Weighting	(3) B_{major} [″]	(4) B_{minor} [″]	(5) BPA [°]	(6) Noise [mJy beam^{-1}]	(7) Channel Width [km s^{-1}]	(8) N_{pixels}	(9) Pixel scale [″]
UGC 8508	Natural	13.9	12.1	83.6	1.3	0.65	1024^2	1.5
	Robust	8.2	6.4	86.1	1.5			
DDO 181	Natural	12.8	9.5	-75.7	1.0	1.3	1024^2	1.5
	Robust	7.6	5.5	-80.4	1.1			
DDO 183	Natural	12.7	10.9	-76.7	1.1	1.3	1024^2	1.5
	Robust	7.6	6.2	88.2	1.2			
KKH 86	Natural	11.0	9.9	-8.2	1.5	0.65	1024^2	1.5
	Robust	7.5	5.8	-21.2	1.7			
UGC 8833	Natural	16.4	15.4	-87.4	0.6	2.6	1024^2	1.5
	Robust	12.4	11.2	81.4	0.6			
KK 230	Natural	8.2	7.3	-56.5	1.4	0.65	1024^2	1.5
	Robust	5.9	5.2	-41.6	1.5			
DDO 187	Natural	12.2	10.4	-82.4	0.9	1.3	1024^2	1.5
	Robust	7.1	5.7	88.5	1.0			
DDO 190	Natural	15.6	14.2	88.1	0.6	2.6	1024^2	1.5
	Robust	10.8	9.9	84.1	0.6			
KKR 25[a]	Natural	8.5	5.0	63.8	0.4	0.65	1024^2	1.5
	Robust	5.5	4.4	65.0	0.4			
KKH 98	Natural	9.9	7.4	82.2	1.3	0.65	1024^2	1.5
	Robust	6.2	5.2	80.4	1.4			

[a]Non-detection

Table 2.4. Galaxy H I Properties.

(1) Galaxy	(2) $S_{\rm HI}$ [Jy km s^{-1}]	(3) $M_{\rm HI}$ [$10^6 M_\odot$]	(4) $S_{\rm HI}^{\rm SD}$ [Jy km s^{-1}]	(5) w_{20} [km s^{-1}]	(6) w_{50} [km s^{-1}]	(7) $v_{\rm cen}$ [km s^{-1}]	(8) Peak $N_{\rm HI}$ [10^{21} cm^{-2}]
NGC 247	382.6	1106.2	608[a]	201.3	193.9	163.7	5.4
DDO 6	1.2	3.2	3.7[b]	20.9	13.7	292.5	0.9
NGC 404 [c]	66.7	146.4	76[d]	80.5	63.2	-54.0	0.5
KKH 37[e]	< 3.4	< 0.8	1.8[f,g]	...	...	...	< 0.08
UGC 4483	12.0	32.8	13.6[h]	51.2	34.3	153.9	3.2
KK 77[e]	< 4.4	< 2.3	< 5.5[i]	...	...	...	< 0.06
BK3N	6.3	22.0	< 0.75[j]	44.4	20.0	-42.5	0.7
AO 0952+69 [k]	61.3	206.6	< 0.59[j]	56.0	45.6	112.8	1.3
Sextans B	91.0	41.5	72.9[h]	58.1	40.6	302.2	2.6
NGC 3109	720.9	270.1	1148[a]	127.7	116.0	405.1	6.6
Antlia	1.4	0.5	1.7[l]	23.4	13.4	363.4	0.3
KDG 63[e]	< 4.2	< 1.1	< 0.2[m]	...	...	...	< 0.06
Sextans A	138.1	62.1	169[a]	59.8	46.2	324.8	6.1
HS 117[e]	< 1.7	< 0.6	...	...	...	...	< 0.03
DDO 82	0.8	2.8	< 0.62[j]	35.8	26.7	56.2	0.9
KDG 73	0.1	0.5	1.0[h]	9.2	8.5	116.3	0.1
NGC 3741	32.8	81.1	44.6[o]	85.4	70.6	229.1	3.4
DDO 99	29.7	46.9	47.1[o]	51.6	28.6	242.1	2.6
NGC 4163	4.8	9.3	9.6[p]	33.5	22.7	161.6	2.1
NGC 4190	15.5	44.8	23.2[p]	73.2	52.8	227.0	3.5
DDO 113[e]	< 1.6	< 0.4	23.6[p]	...	...	...	< 0.04
MCG +09-20-131	3.1	11.9	5.2[q]	39.0	26.1	157.6	3.3
DDO 125	18.3	28.7	21.8[h]	39.7	27.0	196.1	2.1
UGCA 292	12.9	40.0	14.3[h]	37.1	25.2	308.3	4.2
GR 8	5.8	5.9	7.8[h]	30.7	21.4	213.7	1.7

Table 2.4 (cont'd)

(1) Galaxy	(2) $S_{\rm HI}$ [Jy km s^{-1}]	(3) $M_{\rm HI}$ [$10^6 M_\odot$]	(4) $S_{\rm HI}^{\rm SD}$ [Jy km s^{-1}]	(5) w_{20} [km s^{-1}]	(6) w_{50} [km s^{-1}]	(7) $v_{\rm cen}$ [km s^{-1}]	(8) Peak $N_{\rm HI}$ [10^{21} cm^{-2}]
UGC 8508	12.3	19.3	14.8[p]	62.7	48.1	59.8	2.9
DDO 181	10.5	24.4	12.5[o]	52.1	40.8	201.4	1.7
DDO 183	8.2	20.1	9.6[p]	42.2	26.4	191.2	2.2
KKH 86	0.1	0.1	0.5[h]	7.7	6.9	285.5	0.2
UGC 8833	5.9	13.1	6.0[h]	41.0	29.4	225.9	2.2
KK 230	0.8	0.7	2.6[h]	17.4	11.5	60.6	0.6
DDO 187	10.1	11.6	12.0[h]	46.0	31.8	152.2	3.2
DDO 190	22.5	41.3	8.5[o]	62.3	45.2	148.8	3.6
KKR 25[e]	< 1.0	< 0.1	2.2[g]	...	...	...	< 0.03
KKH 98	2.2	3.3	4.1[h]	25.5	17.0	-137.8	0.8

[a]Huchtmeier & Richter (1989);[b]Meyer et al. (2004);[c]NGC 404 is contaminated by foreground Milky Way H I emission.; [d]Baars & Wendker (1976);[e]VLA-ANGST non-detection. Limits based on a width of 20 km s^{-1} and the optical diameter D_{25}.;[f]Karachentsev et al. (2001);[g]might be Galactic H I;[h]Huchtmeier et al. (2003);[i]Huchtmeier et al. (2000); [j]van Driel et al. (1998);[k]AO 0952+62 is contaminated by M81 tidal H I emission.;[l]Barnes & de Blok (2001); [m]Schneider et al. (1990);[n]Barnes & de Blok (2004);[o]Springob et al. (2005);[p]Koribalski et al. (2004);[q]Pustilnik & Martin (2007); [r]Huchtmeier et al. (2000)

Chapter 3

The Formation of Kiloparsec-Scale H I Holes in Dwarf Galaxies

A slightly modified version of this chapter has been published in The Astrophysical Journal with the following bibliographic reference: Warren, S. R., Weisz, D. R., Skillman, E. D., et al. 2011, ApJ, 738, 10

The origin of kpc-scale holes in the atomic hydrogen (H I) distributions of some nearby dwarf irregular galaxies presents an intriguing problem. Star formation histories (SFHs) derived from resolved stars give us the unique opportunity to study past star forming events that may have helped shape the currently visible H I distribution. Our sample of five nearby dwarf irregular galaxies spans over an order of magnitude in both total H I mass and absolute B-band magnitude and is at the low mass end of previously studied systems. We use Very Large Array H I line data to estimate the energy required to create the centrally dominant hole in each galaxy. We compare this energy estimate to the past energy released by the underlying stellar populations computed from SFHs derived from data taken with the Hubble

The VLA telescope of the National Radio Astronomy Observatory is operated by Associated Universities, Inc. under a cooperative agreement with the National Science Foundation.

Space Telescope . The inferred integrated stellar energy released within the characteristic ages exceeds our energy estimates for creating the holes in all cases, assuming expected efficiencies. Therefore, it appears that stellar feedback provides sufficient energy to produce the observed holes. However, we find no obvious signature of single star forming events responsible for the observed structures when comparing the global SFHs of each galaxy in our sample to each other or to those of dwarf irregular galaxies reported in the literature. We also fail to find evidence of a central star cluster in FUV or Hα imaging. We conclude that large H I holes are likely formed from multiple generations of star formation and only under suitable interstellar medium conditions.

3.1 Introduction

Atomic hydrogen (H I) observations of nearby galaxies reveal complex gas distributions. In many systems, the neutral interstellar medium (ISM) contains holes, shells, and/or cavities (e.g., Heiles 1979; Brinks & Bajaja 1986; Puche et al. 1992; Oey & Massey 1995; Kim et al. 1999; Walter & Brinks 1999; Walter et al. 2001; Muller et al. 2003; Relaño et al. 2007; Chu 2008). Some holes in dwarf irregular (dIrr) galaxies are large enough that they become the dominant feature of the ISM, encompassing most, if not all of the optical disk (e.g., M81 Dwarf A - Sargent et al. 1983, Sagittarius DIG - Young & Lo 1997, Holmberg I - Ott et al. 2001, DDO 88 - Simpson et al. 2005, DDO 165 - Cannon et al. 2011).

It has been suggested that these structures are created by feedback from stellar processes (e.g., stellar winds and supernovae (SNe) in OB associations; Weaver et al. 1977; Cash et al. 1980; McCray & Kafatos 1987; Tenorio-Tagle & Bodenheimer 1988). Indeed, Ott et al. (2001), Simpson et al. (2005), Weisz et al. (2009), and Cannon et al. (2011) examined the stellar content within the H I holes of Holmberg I, DDO 88, Holmberg II, and DDO 165 respectively, and determined that the underlying stellar populations provide sufficient mechanical energy needed to create the observed holes

Based on observations made with the NASA/ESA Hubble Space Telescope which is operated by the Association of Universities for Research in Astronomy, Inc., under NASA contract NAS 5-26555.

within their estimated ages.

However, the premise that stellar winds and SNe are responsible for forming H I holes has been called into question. Heiles (1984) pointed out that the largest (∼1 kpc) Galactic "supershells" seemed to require more energy than is available in a typical OB association. Looking at holes in the Large Magellanic Cloud, Kim et al. (1999) concluded that there is only a weak correlation between the locations of Hα emission and H I holes. Perna & Gaensler (2004) compared the locations of radio pulsars with Galactic holes and concluded that the largest holes are not consistent with the multiple SNe from a single-aged cluster formation scenario. Similarly, Hatzidimitriou et al. (2005) compared the locations of known H I holes in the Small Magellanic Cloud to OB associations, supergiants, Cepheids, Wolf-Rayet stars, SN remnants, and star clusters, and found that there are ∼1.5 times as many holes without evidence for recent star formation as there are with recent star formation tracers. Further, the largest H I shell in the Local Group dIrr IC 1613 contains ∼27 OB associations in projection (Borissova et al. 2004; Silich et al. 2006), but the inferred stellar input energy does not account for the estimated hole creation energy (Silich et al., 2006). Taken together, these findings argue against a single-aged cluster being responsible for forming large H I holes; however, stellar processes from multiple generations of star formation remains viable.

Other authors have proposed alternative formation hypotheses to the SNe origin. Efremov et al. (1998) and Loeb & Perna (1998) postulate that a high-energy gamma ray burst (GRB) from the death of a single massive star could create kpc sized holes in the ISM, thus offering an explanation for holes without a detectable underlying cluster. These authors assume the energy from GRBs is emitted isotropically. However, GRBs release most of their energy in bi-directional beams (Rhoads, 1997), making this scenario less likely to produce large H I holes. Other models of H I hole formation without SNe are gravitational and thermal instabilities (Wada et al. 2000; Dib & Burkert 2005), a fractal ISM (Elmegreen, 1997), H I dissolution by UV radiation (Vorobyov & Shchekinov, 2004), and ram pressure stripping (Bureau & Carignan, 2002).

Yet another alternative formation model was suggested by Tenorio-Tagle (1981), who investigated the effect of high velocity cloud (HVC) collisions with the gas disks of galaxies, concluding that the amount of energy deposited into the ISM can be of the same order as a SN ($\sim 10^{51}$ erg) or more. One observational prediction of this model

is a half-circle arc seen in an H I position-velocity diagram. The half-circle arc arises from the gas being pushed to one direction, corresponding to the direction of travel of the HVC. Some observational support for this idea is reported by Heiles (1979, 1984) who point out the most energetic Galactic shells in their study all have half-circle arc signatures in position-velocity space.

It is likely that to a certain degree most of the above physical processes must play a role in the formation of at least some H I holes. To determine which process is the most crucial, Vorobyov & Basu (2005) carried out numerical simulations. They investigated three of the above H I hole formation scenarios (multiple SNe, a single GRB, and a HVC collision) by simulating the ISM structure of the dIrr galaxy Holmberg I. They showed that multiple SNe explosions more accurately reproduce the H I morphology of Holmberg I than the GRB or HVC models.

The study of Rhode et al. (1999) raised doubt about the stellar feedback from a single-aged cluster idea. These authors investigated the numerous H I holes of Holmberg II with Very Large Array (VLA) H I, ground based BVR, and narrowband Hα images. They expected to find the remnants of the OB associations (A, F, and G type main sequence stars) left behind in the holes, but instead discovered that the integrated light was inconsistent with the required cluster masses needed for a multiple SNe formation scenario from a single-aged cluster. However, Stewart & Walter (2000) found that the most prominent hole in IC 2574 is coincident with a prominent stellar cluster. Recently, Weisz et al. (2009) used deep HST photometry to resolve some of the stellar population of Holmberg II and showed that all of the holes observed with HST contain evidence of multiple stellar generations and are consistent with the holes being formed from the energy input into the ISM by these past stars. Their study brought to light the need to reconstruct the star formation histories (and thus the available stellar input energy) from the resolved stars using the methodology developed by Dolphin (2002). These conclusions have been reinforced by the Cannon et al. (2011) investigation of a large ($\sim$775 pc) H I hole in DDO 165. These authors compared the energy budget of the underlying stellar population versus time to estimated hole creation energies. They conclude that the stars have produced more than enough energy to create the observed H I hole.

Evidence is mounting that large H I holes are not formed by a single-aged stellar

cluster but by multiple generations of star formation working in concert. In this study we investigate dwarf galaxies in which centrally dominant H I holes have been identified in order to address the multiple stellar generation hypothesis: DDO 181 (UGC 8651), Holmberg I (UGC 5139, DDO 63, KDG 57) (Ott et al., 2001), M81 Dwarf A (KDG 52) (Sargent et al., 1983), Sextans A (UGCA 205, DDO 75) (Skillman et al., 1988), and UGC 8508 . Studying the specific problem of large holes in dIrr galaxies has some advantages over studies of larger spiral galaxies. For example, dIrr galaxies rotate as solid bodies for the bulk of their H I disks (e.g., Skillman 1996), limiting the effects of destructive shearing forces due to differential rotation. These forces can shorten the lifetimes of the holes in spiral arms of larger galaxies. Also, solid body rotation allows the young stars to remain very near their birth places on timescales of $\sim 10^8$ years (for observational support of this see Dohm-Palmer et al. 2002 and for a statistical approach see Bastian et al. 2011). Given the above, we can use deep HST imaging of regions within the radii of the holes to create spatially resolved star formation histories (SFHs). From the SFHs we calculate a cumulative stellar energy budget (i.e., stellar input energy over time). We compare the input stellar energy to the energy required to create the holes derived from VLA H I images. This comparison gives us a handle on the ability of stellar feedback to create large holes in the neutral ISM of dIrr galaxies. We analyze the SFHs for these five galaxies and compare them to SFHs of dIrr galaxies without central H I holes to determine if any obvious hole creation signature is seen. Finally, we search for centralized clusters responsible for forming the hole in each galaxy with FUV and Hα imaging.

3.2 Data Products

3.2.1 H I Data

H I data were taken from two large atomic hydrogen surveys: The H I Nearby Galaxy Survey (THINGS; AW0605; Walter et al. 2008) and the Very Large Array - Advanced Camera for Surveys Nearby Galaxy Survey Treasury (VLA-ANGST; AO0215; Ott et al. 2008). Observations were made using the VLA in B, C, and D array configurations. Reduction of the THINGS data has been described in detail by Walter et al. (2008). Standard AIPS spectral line reduction procedures were followed. Flux, bandpass, and

phase calibration were performed using VLA calibrators. The final moment 0 maps were flux corrected (Jörsäter & van Moorsel, 1995) and produced images with a natural weighted resolution of $\sim 14'' = \sim 260$ pc for Holmberg I and $\sim 15'' = \sim 260$ pc for M81 Dwarf A.

Reduction of the VLA-ANGST data is described in an upcoming paper, but closely followed the procedures of the THINGS pipeline. Deviations from the THINGS reduction pipeline were only required where problems arose due to the addition of Extended VLA (EVLA) antennas into the array. Baselines between EVLA antennas were affected by power aliased into the first 0.5 MHz of the baseband in the conversion of the signal from digital to analog. These baselines were subsequently removed from the data. The baselines between VLA and EVLA antennas were unaffected and remain in the data. The final moment 0 maps were flux corrected (Jörsäter & van Moorsel, 1995) and produced images with a natural weighted resolution of $\sim 12'' = \sim 175$ pc for DDO 181, $\sim 11'' = \sim 75$ pc for Sextans A, and $\sim 13'' = \sim 165$ pc for UGC 8508. We show the H I integrated intensity maps for the sample galaxies in the top panels of Figures 3.1 - 3.5. Table 3.1 gives the relevant H I image properties for each galaxy and Table 3.9 gives the general observed properties of each galaxy in our sample.

3.2.2 HST Data

HST/ACS and WFPC2 imaging were obtained as part of three HST programs. Data for Sextans A were first described in Dohm-Palmer et al. (1997) and Dohm-Palmer et al. (2002) and were reprocessed by Holtzman et al. (2006). Imaging of Holmberg I and M81 Dwarf A were obtained as part of a larger HST program aimed at studying M81 Group dwarf galaxies (GO-10605; PI: Skillman)(Weisz et al., 2008) and were reprocessed along with DDO 181 and UGC 8508 within the ACS Nearby Galaxy Survey Treasury (ANGST) project (Dalcanton et al., 2009). Here, we briefly summarize the details of the photometry and measurements of the star formation histories. Full details of the photometry are listed in Holtzman et al. (2006) and Dalcanton et al. (2009), while details of the star formation histories are listed in Weisz et al. (2008) and Weisz et al. (2011). Following standard data reduction with the HST pipeline, photometry for WFPC2 data was performed using HSTphot (Dolphin, 2000) while the ACS data were processed with the ACS-specific module of DOLPHOT (Dolphin, 2000). The raw photometry was then

filtered to exclude non-stellar point spread functions, and the resultant photometric catalogs range from a low of 17,450 stars for M81 Dwarf A to 121,198 stars for Holmberg I. Approximately 500,000 artificial star tests were performed for each galaxy to compute the completeness functions and quantify uncertainties due to observational effects. The bottom panels of Figures 3.1 - 3.5 show the F814W images of each galaxy.

3.2.3 FUV and Hα Data

We utilize FUV and Hα imaging obtained through the 11 Mpc Hα UV Galaxy Survey (11HUGS; Kennicutt et al. 2008). Full details of the observations and calibrations can be found in Kennicutt et al. (2008) and Lee et al. (2011). Briefly, standard GALEX calibration and data processing were used following procedures outlined in Morrissey et al. (2007). The GALEX UV images were initially cleaned of foreground stars and background galaxies before photometry was performed. Background levels were estimated from pixels beyond the B-band 25 mag arcsec^{-1} isophote where UV galaxy flux is assumed to be zero. The background flux is required to estimate the asymptotic magnitude of the galaxy. Azimuthally averaged surface brightness profiles were made and a cumulative magnitude versus cumulative-magnitude gradient was fit by a line, where the y-intercept is determined to be the asymptotic magnitude of the galaxy.

Hα imaging was obtained from three different telescopes between 2001-2005: the Steward Observatory Bok 2.3m telescope on Kitt Peak, the Lennon 1.8m Vatican Advanced Technology Telescope (VATT) on Mt. Graham, AZ, and the 0.9m telescope at the Cerro Tololo Interamerican Observatory (CTIO). Common IRAF reduction procedures were followed. R-band imaging was scaled to the continuum level of narrowband imaging containing Hα and [N II]$\lambda\lambda$6548,84 emission lines. The Hα + [N II] images were then continuum subtracted to isolate the emission lines. Finally, images were flux calibrated using spectrophotometric standard stars.

3.3 Hole Definitions

Holes in the H I distribution of dIrr galaxies come in a variety of shapes and sizes. Brinks & Bajaja (1986) defined three different types of holes depending on their characteristics in a position-velocity (P-V) diagram. A Type 1 hole is a structure that has expanded

out of the disk (i.e., blow-out) and shows a discontinuous profile in a P-V diagram. Type 1 holes are among the most commonly observed as they are readily visible as depressions in H I integrated intensity maps. Type 2 holes are those offset from the plane of the host galaxy such that only one side has undergone blow-out. These holes have a half-circle arc signature in a P-V diagram similar to what might be observed from a HVC collision (e.g., Vorobyov & Basu 2005). Finally, a Type 3 hole is a "classic" hole where a coherent expanding structure can be seen in a P-V or radius-velocity diagram. This hole type allows for its current expansion velocity to be measured directly. Figure 3.6 shows a representative P-V diagram of each galaxy. All of the centrally dominant holes in this study are Type 1 holes, that is, their P-V diagrams are discontinuous and show no signs of expansion discernible from their average velocity dispersions. We are therefore unable to define expansion velocities for the holes and instead use the average velocity dispersion as a proxy for this value; we discuss this further in §3.4.1.

We define the locations and shapes of the holes visually from the H I integrated intensity maps. We assume circular shapes for Holmberg I, M81 Dwarf A, and Sextans A, but define elliptical shapes for the holes in DDO 181 and UGC 8508. Defining holes visually from the integrated intensity map is straightforward for the large structures in our sample of galaxies. Recent work by Bagetakos et al. (2011) also identified holes visually on a sample of 20 THINGS galaxies, although they also used P-V diagrams in order to identify smaller, less obvious holes. Automated search algorithms designed to detect H I holes do exist (e.g., Thilker et al. 1998; Mashchenko et al. 1999; Daigle et al. 2003; Ehlerová & Palouš 2005). These routines are used mainly to find holes not readily seen in the integrated intensity maps but within the spectral data cubes. Since our holes are all easily identifiable in the integrated intensity maps (Figures 3.1 - 3.5) these algorithms are unnecessary for this work.

The large hole identified in each galaxy is a single structure except for that of Sextans A. Sextans A has a complex H I distribution consisting of a general depression surrounded by two larger, higher column density clouds. The central depression seems to be filled with multiple holes of various sizes and shapes (Puche & Westpfahl, 1994). However, previous authors, based on lower angular resolution data (e.g., Skillman et al. 1988; van Dyk et al. 1998) have described this feature as a single hole. This gives us a unique opportunity to test the effect of resolution on our observed holes. The holes we

observe in the more distant galaxies of our sample may also be filled with numerous, smaller holes that we are not sensitive to. If we describe the H I morphology of Sextans A as a single, large hole the amount of energy we derive for its creation will be larger than required to form many smaller holes. So if it is shown that the underlying stars have ample energy to create one large hole, then certainly they could produce many smaller holes; thus we include it here and treat it as a single, central hole.

The radial extents of the holes were defined by plotting the average H I column density versus radius as was done previously by Ott et al. (2001) and Simpson et al. (2005). This procedure was done with the IRAF task ELLIPSE which computes the average value on the boundary of an input ellipse incrementally from the starting location outward in predefined step sizes. The hole radius is then defined as the peak in this radial profile. If a hole is created in a uniformly dense medium, the hole boundary will be defined as the location of the shock front and will be identified as a delta function in a similar radial profile. Once the hole stops expanding, the shock front will broaden and disperse over time. We do not find any evidence for a shock front, but if the gas were being piled up our assumption of treating the peak of this profile as the radius of the hole is reasonable. Figure 3.7 shows the radius versus average column density profiles. For the elliptical holes in DDO 181 and UGC 8508 the radius is defined as the semi-major axis length. Each profile rises to a maximum before declining again, except for the H I profile of Sextans A. The radial profile for Sextans A shows substructure before the global peak. This substructure is due to the non-uniform nature of the central depression mentioned above, including a region of higher column density gas clumped just offset from the defined hole center. The holes range in radius from ∼285 pc (UGC 8508) to ∼970 pc (Holmberg I). We plot the hole boundary with a blue circle or ellipse on the H I and optical images (Figures 3.1 - 3.5) as well as list their individual properties in Table 3.9.

3.4 Energetics

We use a blast wave model to estimate the total amount of energy needed to make a cavity in the ISM. We then compare this to an estimate of the stellar feedback energy derived from the resolved stellar population to test the idea that the energy from stellar

feedback is the dominant source in shaping the neutral ISM in these galaxies. To make this comparison we determine three things: 1) the amount of energy that was required to form the H I holes, 2) the amount of available energy from stellar feedback, and 3) the relevant timescale for energy injection. A timescale in which to compare these two calculations is not so straightforward and is described below.

3.4.1 Timescales

We must first determine the relevant timescale over which the input stellar energy shaped the hole. One such timescale is the kinematic age of the hole, defined as the ratio of the radius of the hole by the expansion velocity. Looking at different cuts in a position-velocity diagram we find no evidence for current expansion in any of these holes. This behavior is expected for holes that have blown out of the disk as the input energy will preferentially follow the path of least resistance (along the blow out direction). Further expansion will quickly stall out and become indistinguishable from the velocity dispersion of the background gas distribution (e.g., Vorobyov et al. 2004).

Since there is no evidence that the holes are currently expanding, we use the average velocity dispersion of the gas as a proxy for the expansion velocity. We define the average velocity dispersion as the mean value of the second moment map over the entire galaxy. For holes that have not blown out of the disk, using this value will provide an upper limit to the true age of the hole, because it assumes the expansion rate was constant throughout the evolution, which certainly was not true during the initial formation stages. However, since all of our holes are of Type 1, the kinematic age can be thought of as a characteristic age (τ_{char}), not as an upper or lower limit, since we can not know for sure how long the structure has maintained its current configuration. Our computed characteristic ages are all roughly 100 Myr (see Table 3.9) with the exception of UGC 8508 which has an age $\sim$30 Myr. These ages fall in the range of reported hole ages in other galaxies of $\sim 10^6$-10^8 yr (e.g., Oey & Massey 1995; Walter & Brinks 1999; Hatzidimitriou et al. 2005; Weisz et al. 2009; Bagetakos et al. 2011).

3.4.2 Energy required to form H I holes

In 1974, Chevalier derived an empirical relation between the total energy of an explosion, E_{Hole}, the radius, r, and the expansion velocity, v, of the cavity left behind, taking into account the initial volume density, n_o, of the medium:

$$E_{Hole} \; = \; 5.3 \times 10^{43} \; \left(\frac{n_o}{\mathrm{cm}^{-3}}\right)^{1.12} \; \left(\frac{r}{\mathrm{pc}}\right)^{3.12} \; \left(\frac{v}{\mathrm{km\ s}^{-1}}\right)^{1.40} \; \mathrm{erg}. \tag{3.1}$$

This equation has been used by many authors to estimate the energy required to make H I holes (e.g., Ott et al. 2001; Simpson et al. 2005; Weisz et al. 2009). However, one must keep in mind the many assumptions that go into using Equation 3.1. First, Equation 3.1 assumes a homogeneous medium throughout the entire evolution of the blast wave. For smaller holes that have not blown out of the disk, this assumption provides an *upper* limit to the required energy, since a realistic ISM density profile is stratified, allowing the shock wave to propagate with less resistance and grow to larger sizes. In the scenario of larger holes that have blown out of the disk, Equation 3.1 just gives us an estimate of the needed energy, but can not be interpreted as an upper or lower limit. Secondly, defining the initial volume density for the cavity is non-trivial. One needs to know the thickness (column density) and distribution (e.g., exponential, Gaussian, etc.) of the gas to accurately define the volume density at any given point of an H I map. Further complicating matters, n_o is the *initial* gas volume density and since there already exists an evacuated cavity, this number can only be estimated. The uncertainty in the calculated energy value may be as high as an order of magnitude and possibly more depending on the true initial conditions. For example, if one assumes a value for n_o of 0.01 whereas the 'true' value should be 0.1, the derived energy value will be off by ∼8%, assuming the radius and expansion velocity used are correct.

To address these issues, we have decided to follow the method of Ott et al. (2001) to estimate a lower limit to the volume density. For this we assume the gas follows a Gaussian distribution from the midplane, which leads to

$$N_{\mathrm{HI}} \; = \; \sqrt{2\pi} h n_o \tag{3.2}$$

where N_{HI} is the H I column density, h is the gas scale height, and n_o is the midplane

gas volume density. Thus in principle, a measurement of h leads to an estimate of n_o. Defining the gas scale height, however, is not straightforward.

There have been many ideas put forth as to how one would correctly estimate the gas scale height from the observables of face on galaxies (e.g., van der Kruit 1981; Padoan et al. 2001; Elmegreen et al. 2001; Weisz et al. 2009). Weisz et al. (2009) and Cannon et al. (2011) used a method described in Oh et al. (2008) to define the scale height as a function of radius. This process involves defining the stellar mass surface density of the galactic disk from Spitzer 3.6 μm imaging, and then assuming that the stars are the only significant source of surface density. For galaxies with baryonic masses greater than $\sim 10^9$ $M_\odot$, the stars in the disk should dominate the local gravitational potential (see Mac Low & Ferrara 1999 and references therein). However, for less massive galaxies, the dark matter plays an increasing role in the gravitational potential and the gas scale height will be smaller than that derived from the stellar distribution alone. Banerjee et al. (2011) recently modeled the effects of dark matter, gas self-gravity, and the stellar content of four dwarf galaxies, including Holmberg II, on the H I vertical scale height. Their derived scale height as a function of radius is generally smaller than the one derived by Weisz et al. (2009). The effect is more pronounced at larger radii. Unfortunately, we do not have the correct inputs to follow the method of Banerjee et al. (2011), thus for uniformity we follow the steps of Ott et al. (2001) who used the gas scale height equation derived by van der Kruit (1981) to relate the gas scale height to the average gas velocity dispersion, $\sigma_{\rm gas}$, and the disk total mass density, $\rho_{\rm t}$:

$$h(R) \;=\; \frac{\sigma_{\rm gas}}{\sqrt{4\pi G \rho_{\rm t}}}. \tag{3.3}$$

The gas velocity dispersion should be affected by the underlying dark matter potential as well as the stellar mass distribution.

Ott et al. (2001) combined Equations 3.2 and 3.3 yielding

$$\begin{aligned} h &= (\sqrt{8\pi} G m_p)^{-1} \frac{\sigma_{\rm gas}^2}{(\rho_{\rm t}/\rho_{\rm HI}) N_{\rm HI}} \\ &= 579 \left(\frac{\sigma_{\rm gas}}{10 \text{ km s}^{-1}}\right)^2 \left(\frac{N_{\rm HI}}{10^{21} \text{ cm}^{-2}}\right)^{-1} \left(\frac{\rho_{\rm HI}}{\rho_{\rm t}}\right) \text{ pc}, \end{aligned} \tag{3.4}$$

where G is the gravitational constant, m_p is the proton mass, and $\rho_{\rm HI}$ is the H I mass

density. Similarly to Ott et al. (2001), we assume that $(\rho_{\rm HI}/\rho_{\rm t}) = ({\rm M_{HI}/M_t})$ with $\rm M_t$ = $\rm M_{HI}$ + $\rm M_{He}$ + $\rm M_{stars}$, $\rm M_{He} = 0.3M_{HI}$, and a stellar mass-to-light ratio $(\rm M_{stars}/L_{\it B}) =$ 1. We then use the $\rm M_{HI}$, $\rm L_{\it B}$ and the average $\rm N_{\it HI}$ values given in Table 3.9 to derive $(\rho_{\rm HI}/\rho_{\rm t})$, h, and midplane n_o. Finally, we calculate *lower* limits to the input energies ($\rm E_{\it min}$) required to create the hole in the H I distribution by substituting Equations 3.2 and 3.4 into Equation 3.1.

Skillman et al. (1987) find that massive stars form around H I column density peaks of $\gtrsim 10^{21}$ cm^{-2}. Therefore, we can derive *upper* limits to the required input energy ($\rm E_{\it max}$) for hole formation by assuming this $N_{\rm HI}$ value for each galaxy. This new energy value represents an upper limit because using $N_{\rm HI} = 10^{21}$ cm^{-2} assumes the entire ISM within the radius of the hole was at this value prior to forming the hole. This was not the case for each of the galaxies in our sample, with the possible exception of UGC 8508. The column density of the gas within and around the hole in UGC 8508 is on the order of 10^{21} cm^{-2}; thus the resulting energy estimate may be closer to the expected value than it is for the holes in the other galaxies. The new $N_{\rm HI}$ value leads to new estimates of n_o using Equations 3.4 and 3.2. Equation 3.1 then leads us to upper limits to the amount of hole formation energy. Table 3.9 gives the estimated lower and upper limits required to form the holes for each galaxy.

An alternative method of calculating hole formation energies to the Chevalier (1974) model was proposed by McCray & Kafatos (1987) and implemented recently by Chakraborti & Ray (2011). The McCray & Kafatos (1987) model disregards the single stellar explosion model in favor of continuous energy injection. They propose the number of supernovae required to make the hole is given by

$$(N_* E_{51}/n_0) \; = \; (R_S/97 \text{ pc})^2 (V_S/5.7 \text{ km s}^{-1})^3, \tag{3.5}$$

where $\rm N_*$ is the number of supernovae, $\rm E_{51}$ is the energy per supernova in units of 10^{51} erg, n_0 is the initial volume density of the gas, $\rm R_{\it S}$ is the radius of the hole, and $\rm V_{\it S}$ is the current expansion velocity of the hole. This equation provides values slightly lower than those given by Equation 3.1. For example, using the radius and velocity dispersion defined above for DDO 181 in place of $\rm R_{\it S}$ and $\rm V_{\it S}$, respectively, Equation 3.5 gives us 105 supernovae = 1.05×10^{53} erg. This value is lower than the 5.3×10^{53} erg

that Equation 3.1 provides us with. The larger values provided by Equation 3.1 give us more confidence that we are truly deriving upper limits for the amount of energy required to make these large holes. The lower limits that we derive using Equation 3.1 are also slightly higher than what Equation 3.5 would provide for the same reasons as the above example. However, if the amount of available energy from the stars (see §3.4.4) far exceeds our upper limit derived using Equation 3.1, the value used for our lower limit is less important. Our estimates for the amount of energy needed to create the observed H I holes are in the ranges derived by other authors for similar holes in other galaxies (e.g., Ott et al. 2001; Simpson et al. 2005; Cannon et al. 2011).

3.4.3 Individual Calculations of H I Hole Energetics

DDO 181

DDO 181 was first listed in the dwarf galaxy catalog of van den Bergh (1959). Using the tip of the red giant branch, Dalcanton et al. (2009) estimate a distance to DDO 181 of 3.1 Mpc. At this distance, the linear size of the H I disk has a maximum of ∼4.4 kpc. DDO 181 has an integrated H I flux density of 11.5 Jy km s^{-1} corresponding to a total H I mass of 2.6×10^7 M$_\odot$.

The hole in DDO 181 is readily visible in the H I integrated intensity map (Figure 3.1) as a peanut shaped depression near the center of the H I disk. To determine the size of the H I hole we plot the average H I column density versus radius (Figure 3.7). We defined the center and ellipticity of the hole in DDO 181 visually from the H I integrated intensity maps, placing the center of the hole at $\alpha = 13^h39^m52\overset{s}{.}1, \delta = +40°44'39\overset{''}{.}0$. Following the procedure outlined in §3.3 we derive a radius of 740 pc. Using Equation 3.1 we derive a range of hole creation energies of 3.9×10^{52} - 5.3×10^{53} erg.

Holmberg I

Holmberg I is a dIrr galaxy discovered by Holmberg (1950) in a photometric study of nearby galaxies. Dalcanton et al. (2009) fit the tip of the red giant branch to determine a distance to Holmberg I of 3.9 Mpc. Its distance and apparent B-band magnitude of 13.4 give it an absolute B-band magnitude of −14.5, placing it among the least luminous observed dIrr galaxies (Begum et al., 2008). The H I integrated flux density of 40.1 Jy

km s^{-1} corresponds to a total H I mass for Holmberg I of 1.4×10^{8} M$_{\odot}$. Figure 3.2 is the H I integrated intensity map which shows the large hole in the ISM, roughly 45″ South of the dynamical center of the galaxy (Ott et al., 2001). The H I hole also dominates the optical disk of the galaxy (Figure 3.2). We present the observed characteristics of Holmberg I in Table 3.9.

We perform the same radial analysis as above to characterize the size of the hole. We plot the azimuthally averaged H I column density versus radius in Figure 3.7. The peak in this distribution is at ∼53″ or a radius of 1000 pc. Ott et al. (2001) derive a hole radius of ∼52″ but used a distance of 3.6 Mpc, giving the hole a radius of 850 pc. Also, the VLA data has been reprocessed by the THINGS (Walter et al., 2008) reduction pipeline, changing some of the observed parameters. For example, Ott et al. (2001) observed an average velocity dispersion of roughly 9.0 km s^{-1} whereas we measure 7.9 km s^{-1}. Despite these differences, their hole creation value (E_{hole} $\lesssim$1.2×10^{53} erg) falls within the range of values we derive for Holmberg I of 6.7×10^{52} - 1.2×10^{54} erg. On the other hand, Bagetakos et al. (2011) used the P-V diagram instead of the column density radial profile we use to derive the size of this same hole. They derive a very discrepant hole radius of only 67.5 pc and thus a hole creation value of 2.4 × 10^{50} erg.

A check of the plausibility of our hole creation values comes from the numerical study of Vorobyov et al. (2004). They simulated the H I morphology of Holmberg I with a 2-D hydrodynamics code (ZEUS-2D) and injected different energies over 30 Myr to approximate multiple SNe from a single age cluster of varying masses. The model that best matched the observed morphology of Holmberg I injected the energy of ∼ 300 SNe of 10^{51} erg each or a total input energy of 3 × 10^{53} erg. This value falls within our estimated hole creation energies from above.

M81 Dwarf A

M81 Dwarf A was first listed in a survey of Sculptor type dwarf galaxies by Karachentseva (1968). Eleven years later Lo & Sargent (1979) rediscovered M81 Dwarf A in an atomic hydrogen search around Holmberg II in the M81 group of galaxies. Recent estimates place M81 Dwarf A at a distance of 3.4 Mpc (Dalcanton et al., 2009). This sets the observed angular size of the H I disk of ∼ 220″ equal to a linear diameter of ∼3.6 kpc. The integrated H I flux density of 4.1 Jy km s^{-1} implies a total H I mass of

1.1×10^7 $M_\odot$. M81 Dwarf A was the least massive galaxy observed in the THINGS sample and is near the lower mass end of observed dIrr galaxies. Table 3.9 lists the relevant properties of M81 Dwarf A.

The detailed study of Sargent et al. (1983) investigated the overall H I morphology of M81 Dwarf A, pointing out the dominant ring feature seen in the ISM. Figure 3.3 shows the VLA H I integrated intensity map of M81 Dwarf A. This image reveals the large hole seen in the ISM which encompasses most of the optical disk (see Figure 3.3). The peak in the average H I column density versus radius (Figure 3.7) corresponds to a radius of $\sim$45″ or $\sim$745 pc. From this radius and properties listed in Table 3.9 we derive a range of hole creation energies of 3.5×10^{51} - 5.0×10^{53} erg.

Sextans A

Sextans A is a relatively close galaxy at a distance of 1.4 Mpc (Dalcanton et al., 2009). Given its distance, it has also been extensively studied. Skillman et al. (1988) studied the H I distribution of Sextans A noting the ring-like central depression. Puche & Westpfahl (1994) described this depression as "twisted and sheared". These authors also point out that the majority of the optical disk is contained within the central depression (see Figure 3.4). Dohm-Palmer et al. (1997) and Dohm-Palmer et al. (2002) used HST observations of the resolved stars to derive a SFH of Sextans A, noting that the most recent star formation is occurring near the peaks in the H I. van Dyk et al. (1998) used ground based observations to confirm these results and went on to show that the older stars (50 - 100 Myr old) are more centrally concentrated than the youngest stars. This seems to follow a propagating star formation hypothesis (Gerola & Seiden, 1978) suggested to occur in a supernova and stellar wind driven hole expansion (Puche & Westpfahl, 1994). This pattern, however, is not seen in the HST data of Dohm-Palmer et al. (2002).

Although the central depression is comprised of multiple holes in our observation as discussed in §3.3, for uniformity we treat it here as one large hole. We define the center of the hole to be located at $\alpha = 10^h11^m01\overset{s}{.}1, \delta = -04^\circ41'37\overset{''}{.}0$, just offset from a small, higher density cloud of gas to the east. The average column density versus radius plot (Figure 3.7) give us a hole radius of 850 pc. Figure 3.4 shows a blue circle denoting the boundary of the hole. This radius combined with the galaxy properties given in Tables

3.9 and 3.9 gives us a range of hole formation energies of 1.1×10^{53} - 6.4×10^{53} erg.

UGC 8508

First cataloged by Vorontsov-Velyaminov (1962), UGC 8508 has been studied in detail by Mould et al. (1986). These authors conclude UGC 8508 to be at a state between quiescence and bursting based upon its optical colors. UGC 8508 is relatively close by at a distance of 2.6 Mpc (Dalcanton et al., 2009). Its H I angular size of roughly $110''\times50''$ corresponds to a linear size of about 1400×630 pc. UGC 8508 has an H I integrated intensity of 13.8 Jy km s^{-1} giving a total H I mass of 2.2×10^7 $M_\odot$.

The H I hole is clearly observed in the Southeastern part of the disk as an elliptical depression (Figure 3.5). We define the center of the hole to be at $\alpha = 13^h30^m45\overset{s}{.}9, \delta = +54°54'33\overset{''}{.}0$. From the radial profile (Figure 3.7) we determine the radius of the hole to be 285 pc leading to a hole creation energy range of 9.2×10^{50} - 2.2×10^{52} erg. This is the smallest and least energetic hole in our sample, yet it still occupies a large fraction of the optical extent of the galaxy (Figure 3.5).

3.4.4 Energy input from stars

To quantify the available energy from stellar processes we derive SFHs, i.e., a star formation rate as a function of time and metallicity, from the resolved stars. Color-magnitude diagrams (CMDs) contain the 'fossil record' of star formation over the lifetime of a galaxy, from which we can determine a SFH. The upper left panel of Figures 3.8 - 3.12 show the CMDs of the stars contained within the holes. We derived SFHs by the analysis of HST-based optical CMDs using the technique described in Dolphin (2002). Briefly, this method involves the construction of single age synthetic CMDs based on a specified stellar evolution model. These individual synthetic CMDs are then linearly combined along with a model foreground CMD to produce a composite synthetic CMD. Linear weights on the individual CMDs are adjusted to obtain the best fit as measured by a Poisson maximum likelihood statistic; the weights corresponding to the best fit represent the most probable SFH.

As input, we specified a standard power law initial mass function with x = −2.3 from 0.1 to 100 $M_\odot$, a binary fraction = 0.35, the stellar evolution models of Marigo et al. (2008), distances measured from the tip of the red giant branch (Dalcanton et al.,

2009), and foreground extinction values as specified by Schlegel et al. (1998). Each SFH calculation included the results from 500,000 artificial star tests, in order to simulate observational errors and completeness. For each galaxy we compared the completeness functions from the hole-only regions to the entire galaxy and found little difference. This similarity is unsurprising as our sample of galaxies does not feature significant surface brightness gradients and the holes typically cover a large portion of the HST fields. Because the CMDs considered in this analysis do not reach the ancient main sequence turnoff, the measured chemical enrichment is uncertain (e.g., Gallart et al., 2005). We thus constrained the metallicity of each SFH to monotonically increase as a function of time, preventing potentially unphysical chemical evolution models.

To quantify the errors in the SFHs, we consider both statistical and random uncertainties. As a proxy for systematic effects, we computed the SFHs for a grid of small shifts ($\pm$0.05 mag) in distance and extinction. The RMS per time bin from the grid of SFHs roughly probes systematic uncertainties in the stellar models. However, Weisz et al. (2011) show that this method may underestimate the magnitude of the systematic uncertainties by factors of a few. For the purposes of the energetics analysis in this paper, the adopted technique of deriving errors is sufficiently precise, given the larger uncertainties on HI energetic determinations as discussed in §3.4.2. We further computed 50 Monte Carlo realizations of the model CMD to test for effects of Poisson fluctuations on the SFH, i.e., the random uncertainties. The final error bars are simply the quadrature sum of the systematic and random errors. The lower left panel of Figures 3.8 - 3.12 shows the derived SFHs over the past 500 Myr for the stars within the holes of each galaxy.

Using the above methods we produce two sets of SFHs. One set describes the global SFHs derived from all of the stars within a given galaxy. We can compare the global star formation histories from the galaxies in our sample that have created large H I holes to SFHs of dwarf galaxies presented in the literature that have not created large H I holes. We then look for distinguishing star forming features which may have created the observed structures. The second set of SFHs is derived using only the stars within the radius of the hole. We use these SFHs to calculate the available energy from the evolving underlying stellar population.

We next quantify the available energy from stellar evolution. The amount of stellar

feedback energy produced per time bin is calculated from the galaxy evolution modeling code STARBURST99 (Leitherer et al., 1999). STARBURST99 uses stellar evolution models to estimate feedback (e.g., chemical, spectrophotometric, and stellar energy evolution) for a given SFH. We follow the method outlined in Weisz et al. (2009) in which we simulate a single burst of star formation with an initial mass of 10^6 $M_\odot$ and assuming a metallicity of 2% Solar, which is consistent with the expected low metallicities of these low luminosity dwarf galaxies. We then normalize the output from the single star formation simulation by the inferred mass from the star formation history, sampled in 5 Myr intervals. We plot the cumulative stellar input energies on the right panel of Figures 3.8 - 3.12 and discuss their implications in §3.5.

3.5 Comparison with the Stellar Energy Budget

We now compare the energy available from stellar feedback processes from §3.4.4 to the range of estimated hole formation energies in Table 3.9. The right panels of Figures 3.8 - 3.12 show the cumulative energy from stellar processes over the past 500 Myr. This energy profile represents a *lower* limit to the available stellar energy as energy estimates from STARBURST99 ignore any contribution of Type Ia supernovae (contained within the hole, but created by previous generations of star formation). The vertical dashed line is the characteristic age (τ_{char}) of the hole and the shaded region is the likely range of required hole formation energies (see §3.4.2). In Table 3.9 we list the total amount of energy created by the stars within the characteristic age (E_{stars}). In each galaxy $E_{stars} \gg E_{min}$ implying the amount of energy available due to stellar processes within the characteristic age of the holes exceeds the minimum energies for hole formation. Using values of E_{min} implies minimum stellar feedback efficiencies ($\epsilon_{min} = E_{min}/E_{stars}$) of roughly 0.5% to 4%.

Alternatively, using the values for E_{max} we derive maximum formation efficiencies ($\epsilon_{max} = E_{max}/E_{stars}$) between 3% and 48% (see Table 3.9). Note that the largest of these feedback efficiencies are above the range of ∼1% - 20% inferred by models of star formation interactions with the ISM (Theis et al. 1992; Cole et al. 1994; Padoan et al. 1997; Thornton et al. 1998). However, our estimated characteristic ages are not particularly well defined. For example, Weisz et al. (2009) provide evidence that multiple

generations of star formation are required to form and maintain large H I holes. Recchi & Hensler (2006) produced a model that maintains H I holes for time scales as long as ∼600 Myr by injecting energy from multiple generations of SNe, prohibiting the gas from cooling and recollapsing.

With these limitations in mind we can try to determine the age of the holes in another manner. Since the models of interactions between stellar feedback processes and the ISM predict efficiencies of 1% - 20%, we can use this to determine an age for the holes assuming our upper limit for hole creation energy estimates to be correct. The dashed horizontal lines of Figures 3.8 - 3.12 show efficiencies of 10% and 20% using the upper limit hole creation energy estimates. For example, a 10% feedback efficiency would require the energy of 10 times E_{max} to create the hole. These lines should give us upper limits on the ages of the holes for each feedback efficiency. Clearly the inferred characteristic ages are underestimating the likely age of formation of the holes in each of the galaxies (except for UGC 8505) if energy input from multiple stellar populations have prohibited the holes from recollapsing. The inferred characteristic age of the hole in UGC 8508 is comparable to the ages determined for both 10% and 20% efficiencies, which is most likely due to the relatively small amount of required hole creation energy.

These results illustrate the significant level of uncertainty when dealing with large H I holes that have blown out of the disk. Without the ability to accurately pin down the expansion velocity and initial distribution of the holes, estimating creation energies and hole ages are highly uncertain and perhaps even arbitrary when one assumes the standard toy model of a single burst of star formation. More likely, multiple generations of star formation work in collaboration to grow these structures to the sizes we observe today. However, even with these uncertainties, it is clear that there is no evidence yet against forming these holes through stellar feedback. Although the absolute values may vary, we have shown that the amount of energy available in the underlying stellar population is more than enough to likely be the dominant creation source.

3.6 Comparison of Global SFHs

We now address the question "Is there an imprint on the global SFH of the event(s) that create the centrally dominant hole in the ISM?". To do so, we compare the recent

global SFHs derived from all of the resolved stars of the five galaxies in this study to the recent global SFHs presented in Dohm-Palmer et al. (1998) and Weisz et al. (2008). We present the recent global SFHs of the five galaxies in our sample in Figure 3.13. There is no single feature beyond 100 Myr ago in common when comparing the five galaxies from our large hole sample with each other. However, the most recent star formation activity (<100 Myr) for each galaxy in our sample shows a systematic rise that is likely due to star formation on the edges of our defined holes (see §3.7). Likewise, when we compare the SFHs in our sample with those presented in Dohm-Palmer et al. (1998) and Weisz et al. (2008) nothing obvious stands out as a major difference between the two populations. Many of the galaxies have a systematic rise in the most recent time bins whether they have created a large hole or not. Our sample contains galaxies with very low, near constant levels of star formation over the last Gyr and certainly provides no obvious recent burst that can be interpreted as a "hole creation" signature (e.g., GR8; Dohm-Palmer et al. 1998 and M81 Dwarf A). Our sample also includes galaxies that have significant star formation activity in their recent histories. However, some of these galaxies have created large, centrally dominant holes (i.e., Holmberg I), but others have not (i.e., NGC 2366; Weisz et al. 2008). This result, combined with the results from the previous section, suggests that sustained star formation is a necessary phenomenon to create large H I holes, but not a sufficient one.

This global comparison confirms the general results of Weisz et al. (2009). These authors looked at the many holes seen in the H I distribution of Holmberg II and compared the SFHs of the stars within the holes to those within control fields. The control fields consisted of regions of similar size but in locations where there were no H I holes. The expectation in this previous study was to find an increased level of star formation in the regions of the holes compared to the control fields. However, the control fields contained amounts of energy comparable to (and in some cases greater than) the areas with holes. This surprising result suggests that the local conditions of the ISM and where stars form in the galaxy play a critical factor in whether or not a hole is created. For example, perhaps the surrounding ISM must be dense enough over a large region to sustain a coherent structure prior to blow out. It is likely that the porosity of the ISM plays a very important role. A more porous medium may prohibit the formation of holes by allowing the ionized gases needed for pressure support to leak out before

structures can be formed. Also, the output energy produced by star formation occurring in multiple regions within a galaxy may destructively interfere, thus destroying newly formed holes. In contrast, if star formation occurs in a consecutive and concentrated manner, the output energy may result in holes that combine to create the observed large features.

An alternative to the suggestion that these large holes are created by sustained star formation over multiple generations is that the stars play no role whatsoever and that local conditions of the ISM (e.g., gravitational instabilities) alone determine where holes are created. We do not favor this explanation since it is known that stellar processes do indeed contribute to the heating and ionization of the ISM. Our results for the large amount of available stellar energy from §3.5 and the results of the SFH comparison above seem to confirm that the stars must play a role in creating the holes, however, not at the one-to-one level. The local conditions of the ISM must also play a critical role in this process. However, the overall importance of each process is difficult to measure.

Numerical studies may be helpful to test which conditions are needed for stellar processes to create large H I holes. This exercise is beyond the scope of this work, but we can suggest some areas of focus. Ideally, 3-D magnetohydrodynamical simulations of a realistic dwarf galaxy ISM should be modeled. A parameter search should then follow including, but not necessarily limited to, simulating different total H I masses, varying ISM porosity values, and a range of star formation histories and locations within the disk. These suggestions would expand upon the pioneering work of Recchi & Hensler (2006) and Stinson et al. (2007). Fragile et al. (2003) investigated chemical enrichment in dwarf galaxies through the simulation of supernovae in a model galaxy. Their Figures 2 and 7 show tantalizing similarities to our observed galaxies. Recchi & Hensler (2006) showed that multiple generations of star formation can support large H I structures for $\sim$500 Myr or more. Stinson et al. (2007) suggested that dwarf galaxies undergo rapid star formation in which the gas is pushed out of the galaxy core, cools, and infalls back to the core where the process is repeated in a pulsation-like "breathing mode" on 100 Myr timescales. At first glance, our findings seem to support the longer duration hole ages of Recchi & Hensler (2006), and not the short-lived holes with a "breathing mode" as suggested by Stinson et al. (2007). We can not rule out the model of Stinson et al. (2007) on longer breathing mode time scales, however. At a minimum, new models

would give insight into which, if any, of these parameters plays the biggest role in the creation and sustainability of large H I holes.

3.7 Searching for a Progenitor

If the large hole in each of our galaxies were formed by a single, centralized stellar association and not via multiple stellar generations as we suggest, then observational evidence for the remnant cluster should exist. To try and identify these clusters we use GALEX FUV and ground based Hα imaging. Each of these wavelengths probe stellar life cycles over different timescales. UV wavelengths probe timescales up to $\sim$100 Myr while Hα probes shorter $\sim$10 Myr timescales. Note that these timescales are shorter than the $\sim$200 Myr stellar dissolution timescales seen by Bastian et al. (2011). Figures 3.14 - 3.18 show the FUV and Hα images for each of our galaxies. We have overlaid the hole location onto each image for comparison. UGC 8508 could not be observed by GALEX due to bright foreground stars and/or too bright background levels (Lee et al., 2011) so we only show the Hα image.

The FUV and Hα images show diffuse emission within some of the holes in our sample but no bright, central feature expected for a cluster. However, each galaxy has bright features associated with recent star formation at or near the edges of our defined hole. DDO 181 has a bright FUV feature towards the southern edge of the the hole that has no associated Hα emission. In Holmberg I, FUV and associated Hα emission features are located around most of the edge of the hole. The southern half of M81 Dwarf A has FUV emission, with most of it on the southeastern edge of the hole; however, M81 Dwarf A was not detected in Hα. The large hole in Sextans A is filled with faint, diffuse and point-like FUV and Hα emission. The brightest features are near the southeastern and northwestern edges of the hole. Lastly, UGC 8508 has bright Hα knots all around the edge of the defined hole. Each of the above bright FUV and Hα features are associated with the densest H I columns, and are not located in the center of the hole. This alone does not mean that multiple generations of stellar processes are responsible for the formation of these holes, but it does seem to rule out a young, single-aged cluster as being responsible.

Tenorio-Tagle & Bodenheimer (1988) point out that large holes may have a stellar

age gradient where the oldest stars populate the inner regions and the youngest stars fall along the edges of the hole. In this scenario of self-propagating star formation we would expect to see knots of Hα and FUV emission at or near the edge of the observed hole where the conditions of star formation are suitable. However, we do not expect a one-to-one relationship between the hole boundaries and the Hα and FUV emission. This is due to the possibility that some of the current star formation is not associated with the large hole (i.e., stochastic star formation). None-the-less, we indeed see hints of possible propagating star formation in some of the Ha and FUV images. These observations are consistent with the hypothesis that multiple generations of stars may provide the mechanical energy to create the large hole in each galaxy.

Sextans A is perhaps the strongest case for multiple generations of star formation creating large holes in the ISM of these galaxies. Sextans A's relatively close distance of 1.4 Mpc allows us to resolve ISM structures on scales of $\sim$75 pc (compared to the $\sim$300 pc reported by Skillman et al. 1988). The central depression breaks up into multiple smaller holes when observed at our high angular resolution. Perhaps some, if not all, of the large holes in the other galaxies in our sample would also break up into multiple, smaller holes at higher angular resolution and signal to noise. Even with our incorrect assumption of a very large, single hole in Sextans A, the underlying stellar population has produced an ample amount of energy to have created a single, large hole, much less many smaller holes. The Hα and FUV emission only cement the idea that multiple generations of star formation, not single-aged clusters, produce large H I holes.

3.8 Conclusions

We have investigated the genesis of large H I holes in the ISM of five nearby dwarf irregular galaxies by comparing the energy required to create the holes to the inferred input energy from the underlying stellar populations. In each galaxy, we have shown that the input energy from the stars far exceeded the required energy derived from a single blast wave model. However, based on the observations here, there is no evidence of a single star formation event associated with hole creation. Considering there is ample energy in the underlying stellar population, we conclude that multiple generations of stars are likely responsible for the creation and support of these large structures.

However, since there seems to be no correlation between the SFHs and a resultant hole, stars can not be the only player in this game. It seems plausible that the local conditions of the ISM must also be suitable for H I holes to be created and sustained. Star formation has been shown to occur on the rims of holes (e.g., Weisz et al. 2009), and indeed some of the UV and Hα images of our sample galaxies also show evidence of star formation on the rim of the large H I holes. These new sites of star formation can either help inflate the holes to larger sizes or destroy the holes by pushing the gas back into the cavities. It is presumably this delicate interplay between these effects that will ultimately determine whether a galaxy will or will not form a large H I hole.

In summary, the idea that a single-aged cluster is required to form the holes does not work based on the evidence at hand. Past numerical studies of hole creation have relied upon this tenet (see, for example, Vorobyov et al. 2004), although some numerical studies intentionally use massive, single-aged clusters to produce Type 1 holes (e.g., Mac Low & Ferrara 1998). Future numerical studies aiming to accurately investigate hole creation should consider focusing on multiple generations of star formation occurring at different locations throughout the disk. This study reaffirms that the physics of the ISM of dwarf irregular galaxies is complicated and one can not use simplified approximations to predict observed distributions.

3.9 Figures

We thank the anonymous referee for a prompt and detailed report which significantly improved the clarity of the manuscript. Support for this work was provided by NRAO through the National Science Foundation collaborative research grant 807515. NRAO is operated by Associated Universities, Inc., under cooperative agreement with the National Science Foundation. SRW is grateful for support from a Penrose Fellowship. This research has made use of NASA's Astrophysics Data System Bibliographic Services and the NASA/IPAC Extragalactic Database (NED), which is operated by the Jet Propulsion Laboratory, California Institute of Technology, under contract with the National Aeronautics and Space Administration.

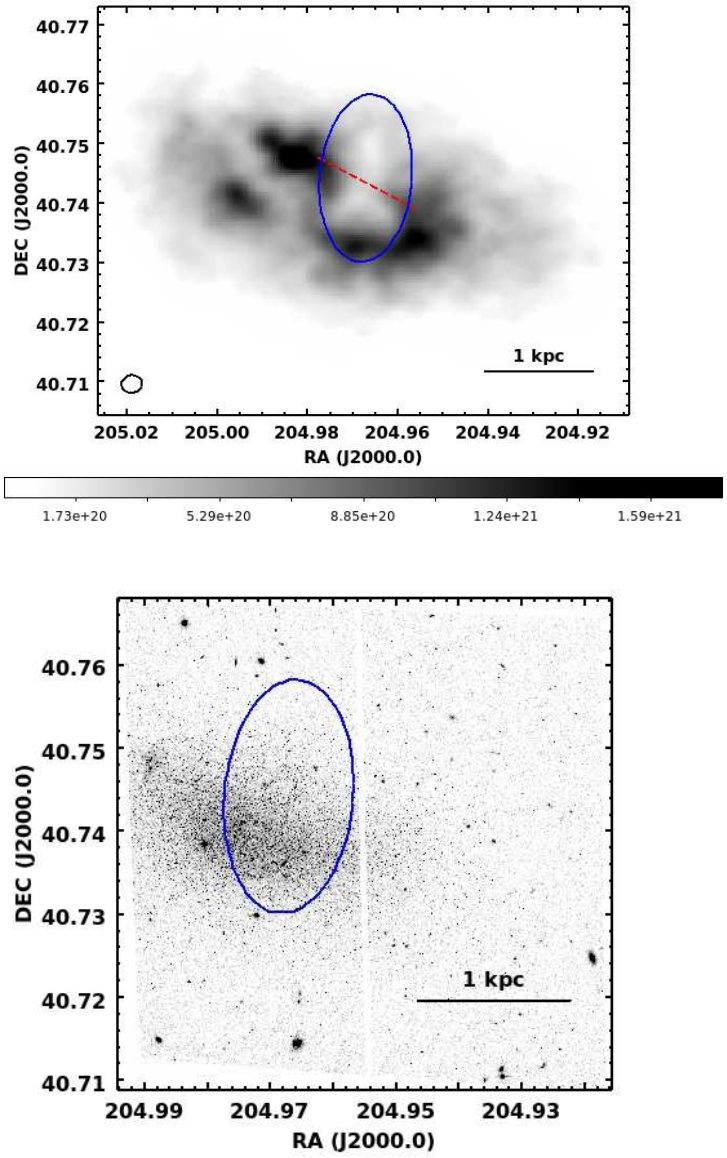

Figure 3.1 VLA H I integrated intensity map (top) and F814W HST image (bottom) of DDO 181. The blue ellipses denote the area of the hole. The red dashed line shows the cut used to make the P-V diagram for Figure 3.6. The units of the scale bar for the H I image are cm^{-2} and the black ellipse at the lower left denotes the size and shape of the synthesized beam.

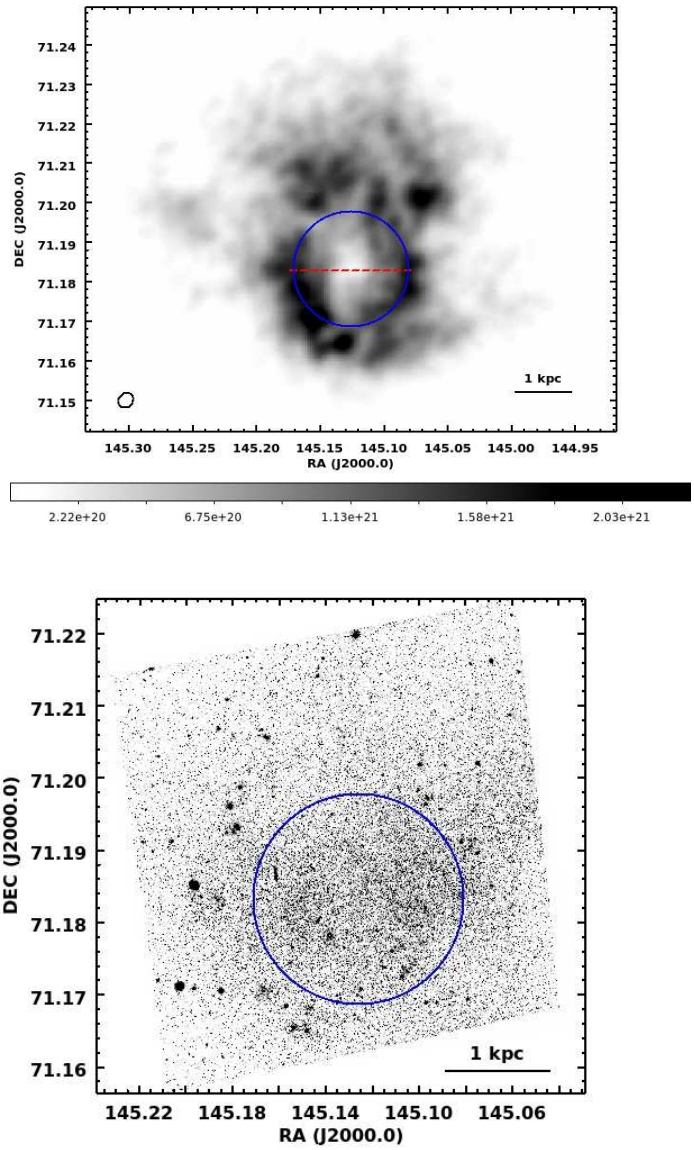

Figure 3.2 VLA H I integrated intensity map (top) and F814W HST image (bottom) of Holmberg I. The blue circles denote the area of the hole. The red dashed line shows the cut used to make the P-V diagram for Figure 3.6. The units of the scale bar for the H I image are cm^{-2} and the black ellipse at the lower left denotes the size and shape of the synthesized beam.

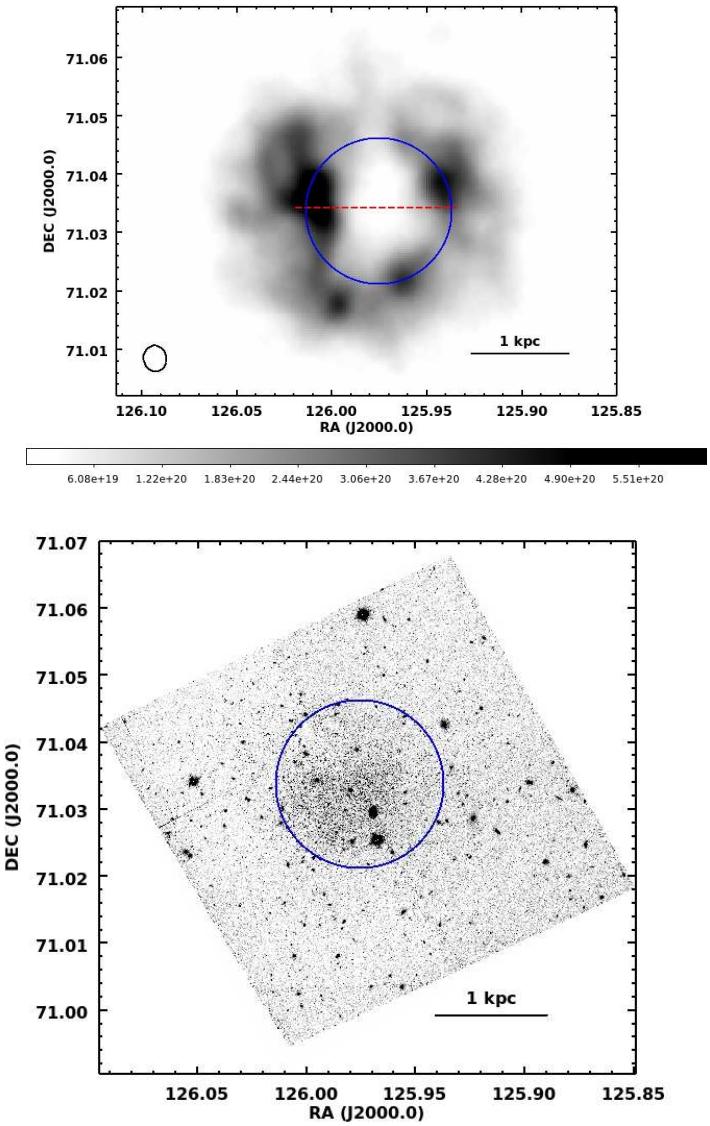

Figure 3.3 VLA H I integrated intensity map (top) and F814W HST image (bottom) of M81 Dwarf A. The blue circles denote the area of the hole. The red dashed line shows the cut used to make the P-V diagram for Figure 3.6. The units of the scale bar for the H I image are cm^{-2} and the black ellipse at the lower left denotes the size and shape of the synthesized beam.

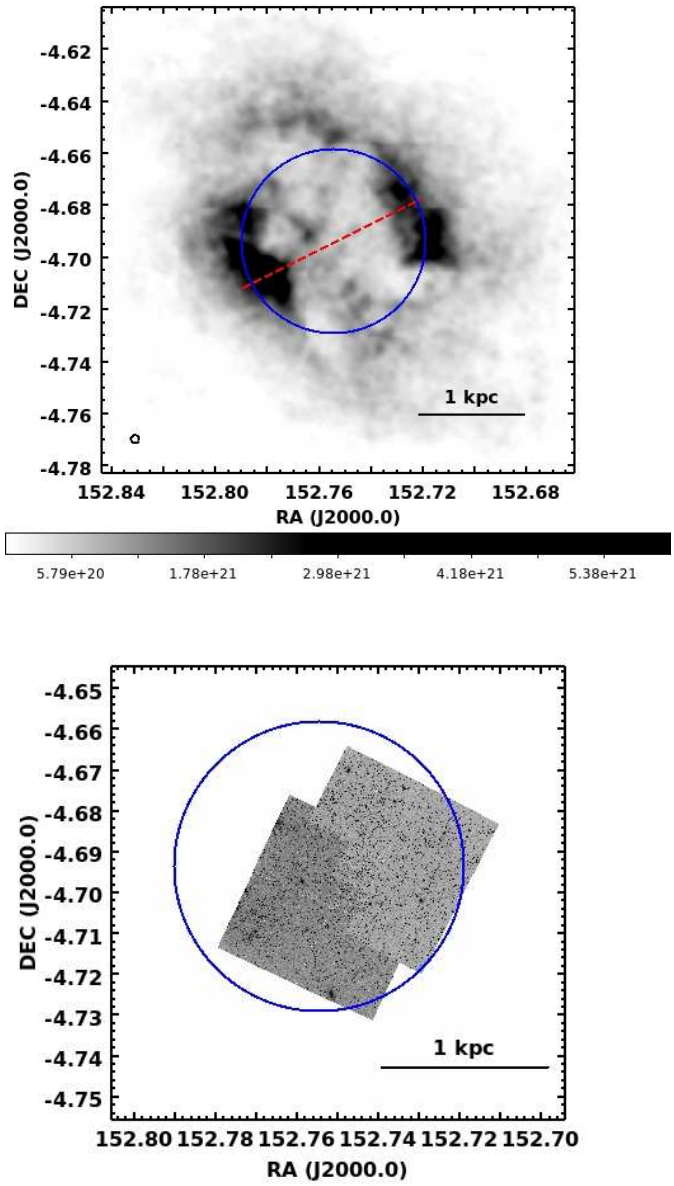

Figure 3.4 VLA H I integrated intensity map (top) and F814W HST image (bottom) of Sextans A. The blue circles denote the area of the hole. The red dashed line shows the cut used to make the P-V diagram for Figure 3.6. The units of the scale bar for the H I image are cm^{-2} and the black ellipse at the lower left denotes the size and shape of the synthesized beam.

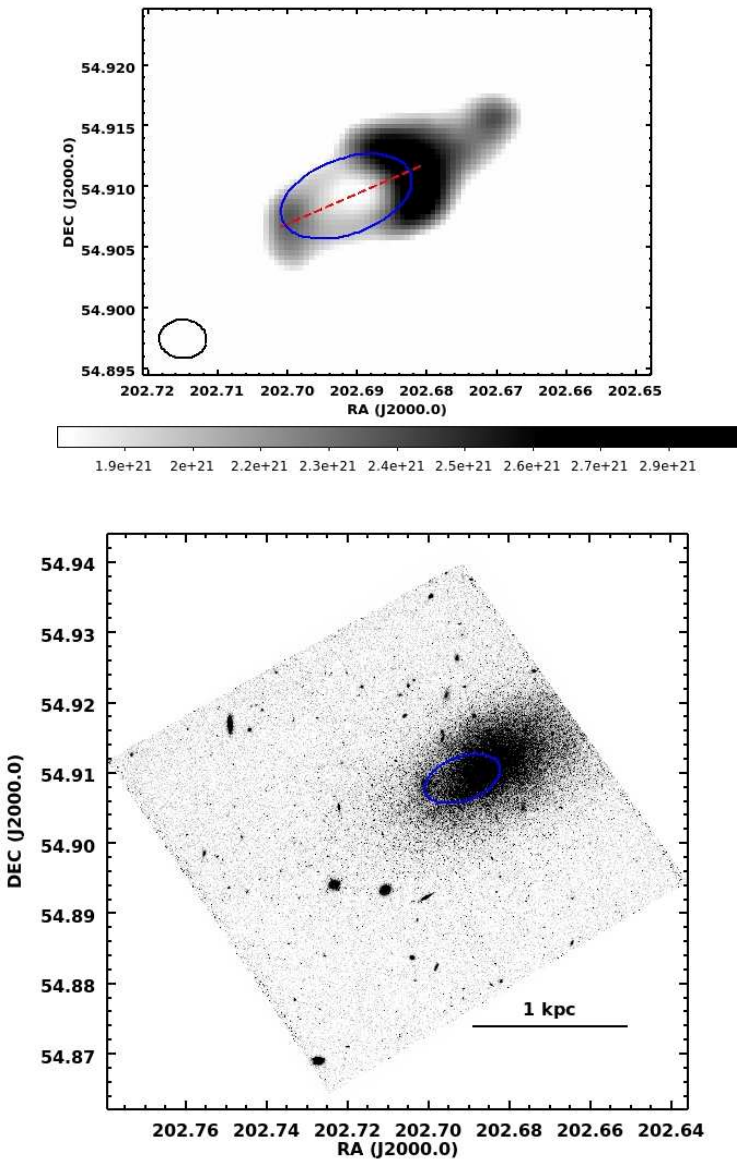

Figure 3.5 VLA H I integrated intensity map (top) and F814W HST image (bottom) of UGC 8508. The blue ellipses denote the area of the hole. The red dashed line shows the cut used to make the P-V diagram for Figure 3.6. The units of the scale bar for the H I image are cm^{-2} and the black ellipse at the lower left denotes the size and shape of the synthesized beam.

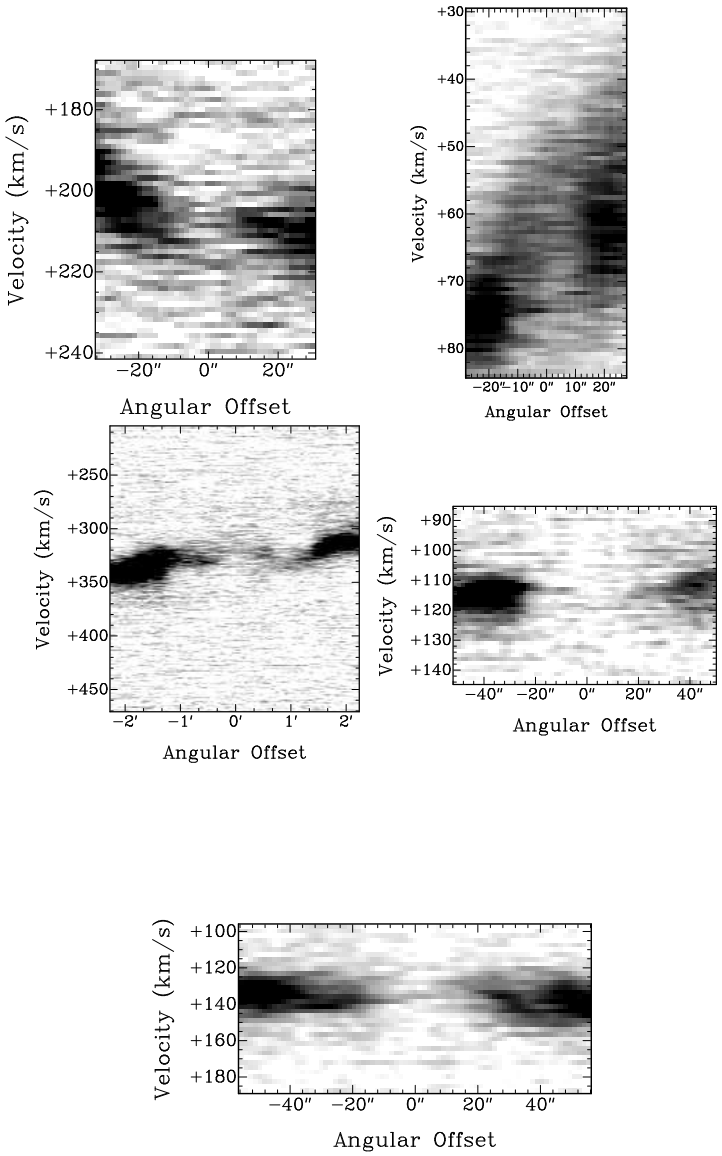

Figure 3.6 Position-velocity diagrams for the centrally dominant holes in (top to bottom, left to right) DDO 181, UGC 8508, Sextans A, M81 Dwarf A, and Holmberg I. Each diagram is discontinuous, representing a type 1 hole. Expansion velocities for these galaxies can not be measured from these diagrams since they are indistinguishable from the average velocity dispersion in the galaxy. The grey scale reflects the H I intensity.

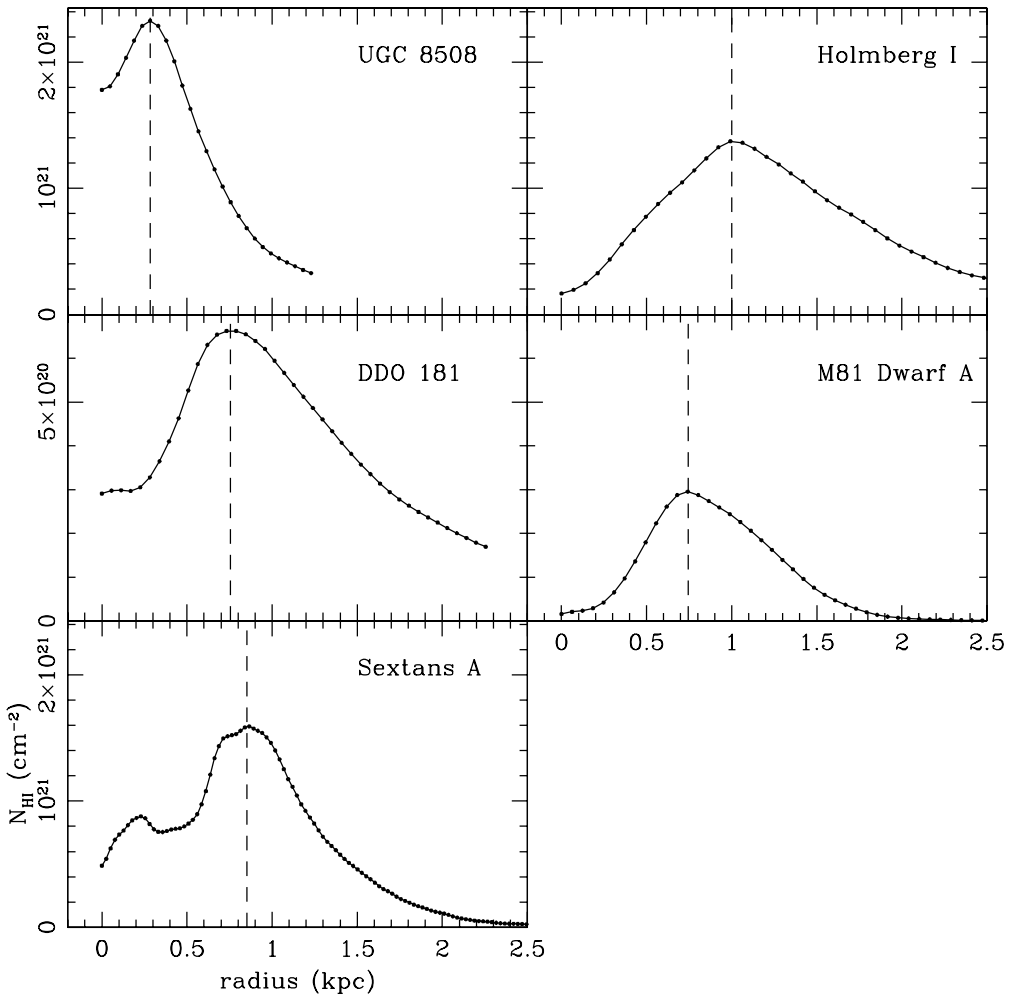

Figure 3.7 Azimuthally averaged column density versus radius for each galaxy. The vertical dashed lines denote the adopted radii of the holes.

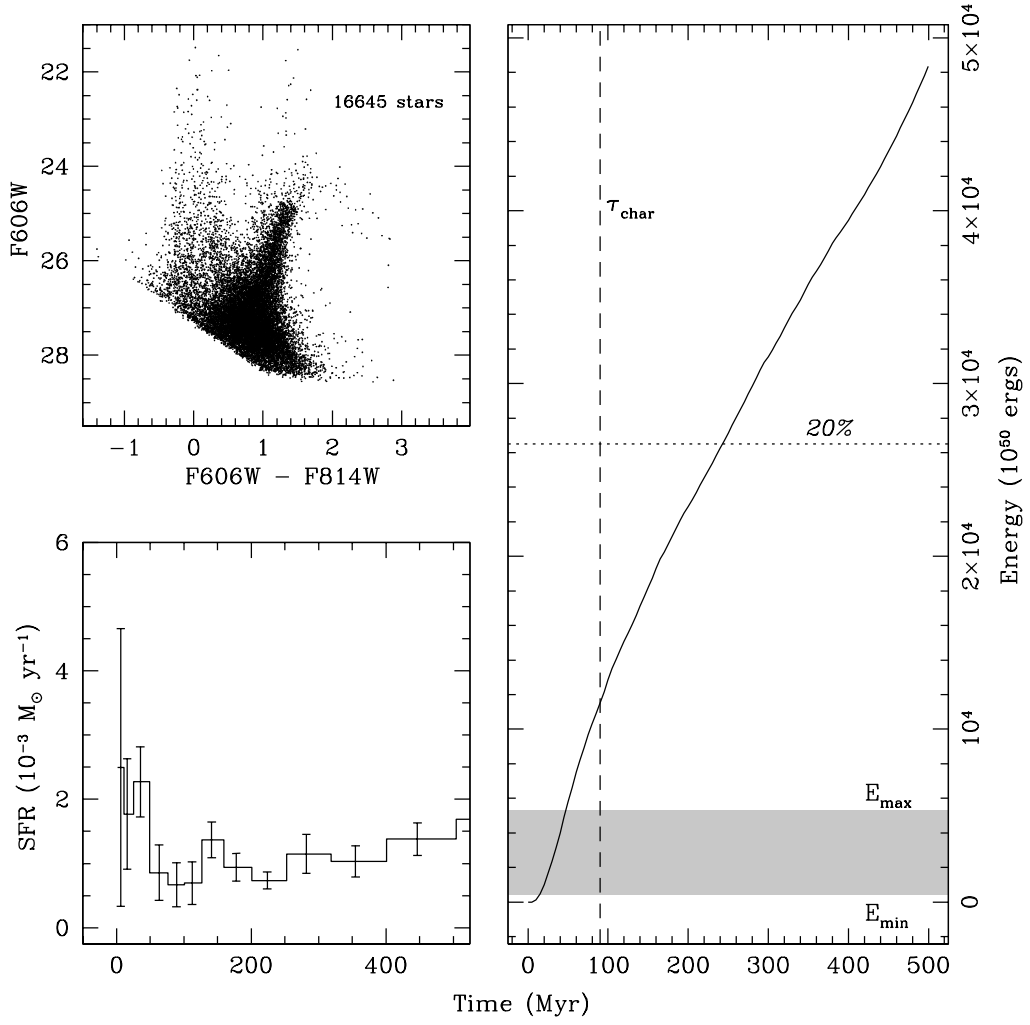

Figure 3.8 DDO 181: *Upper left* - The (F606W, F606W-F814W) CMD for the stars within the the radius of the central H I hole. *Lower left* - The SFH over the past 500 Myr for the stars within the central H I hole. *Right* - The cumulative energy due to stellar winds and SNe calculated by using the SFH as input into STARBURST99 (Leitherer et al., 1999). The shaded region denotes the range in energy needed to create the H I hole from section 3.4.2. The vertical, dashed line is the characteristic age of the hole. The horizontal dashed lines represents the 10% and/or 20% feedback efficiency levels using the upper limit of hole creation energy.

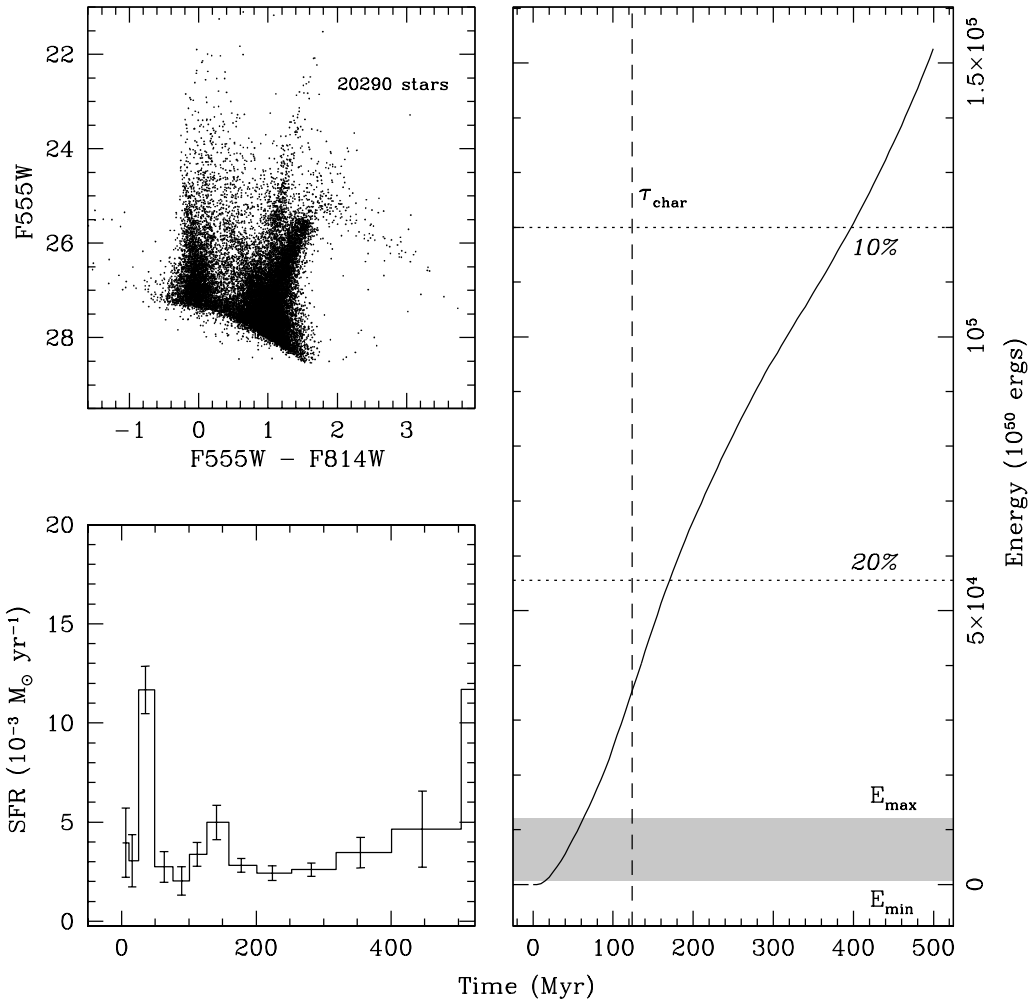

Figure 3.9 Same as Figure 3.8 except for Holmberg I.

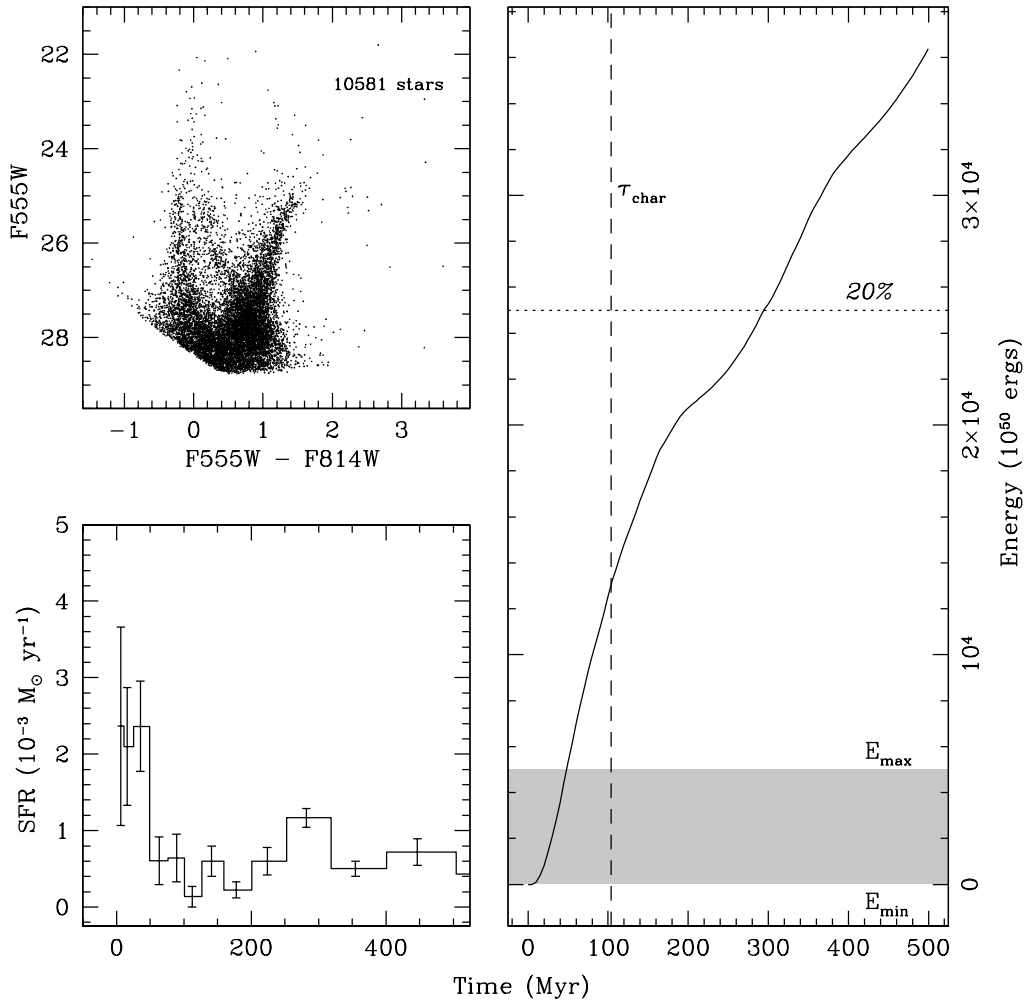

Figure 3.10 Same as Figure 3.8 except for M81 Dwarf A.

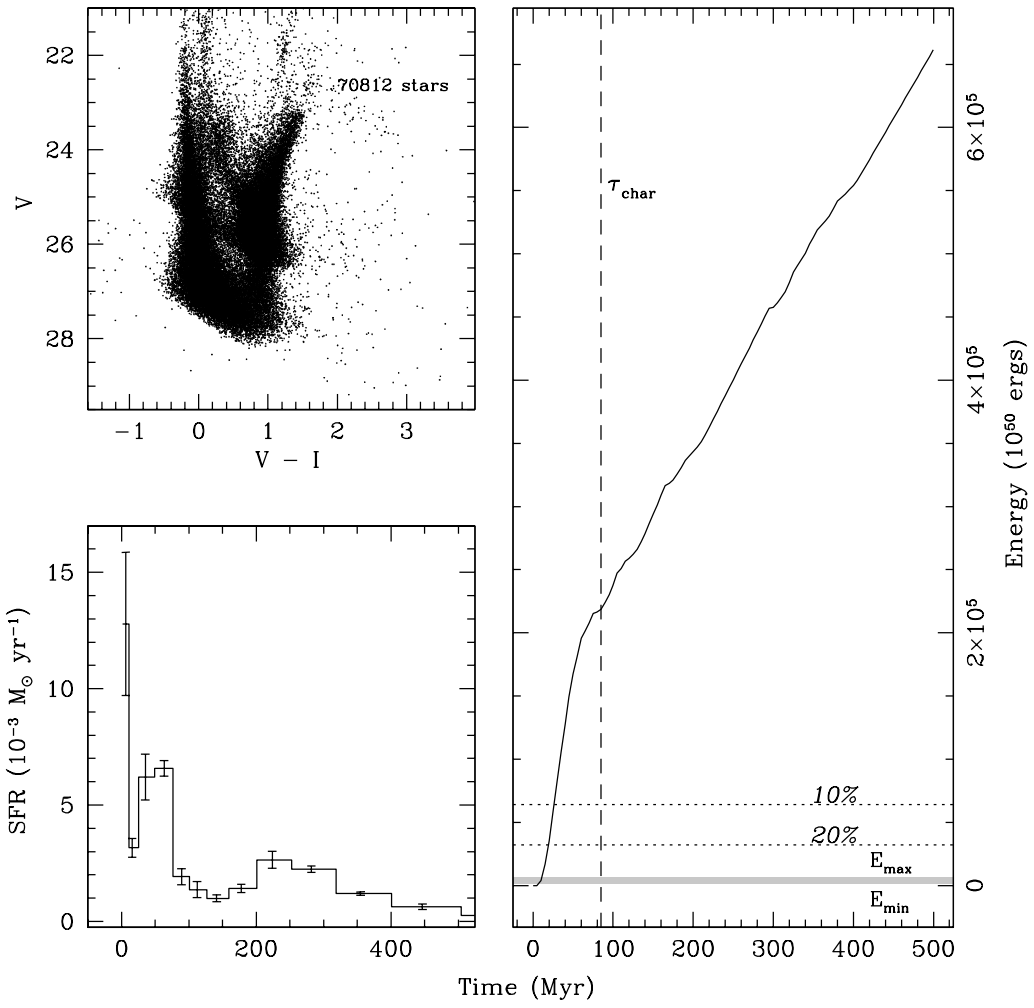

Figure 3.11 Same as Figure 3.8 except for Sextans A. The CMD is a combination of two different WFPC2 pointings of different integration times.

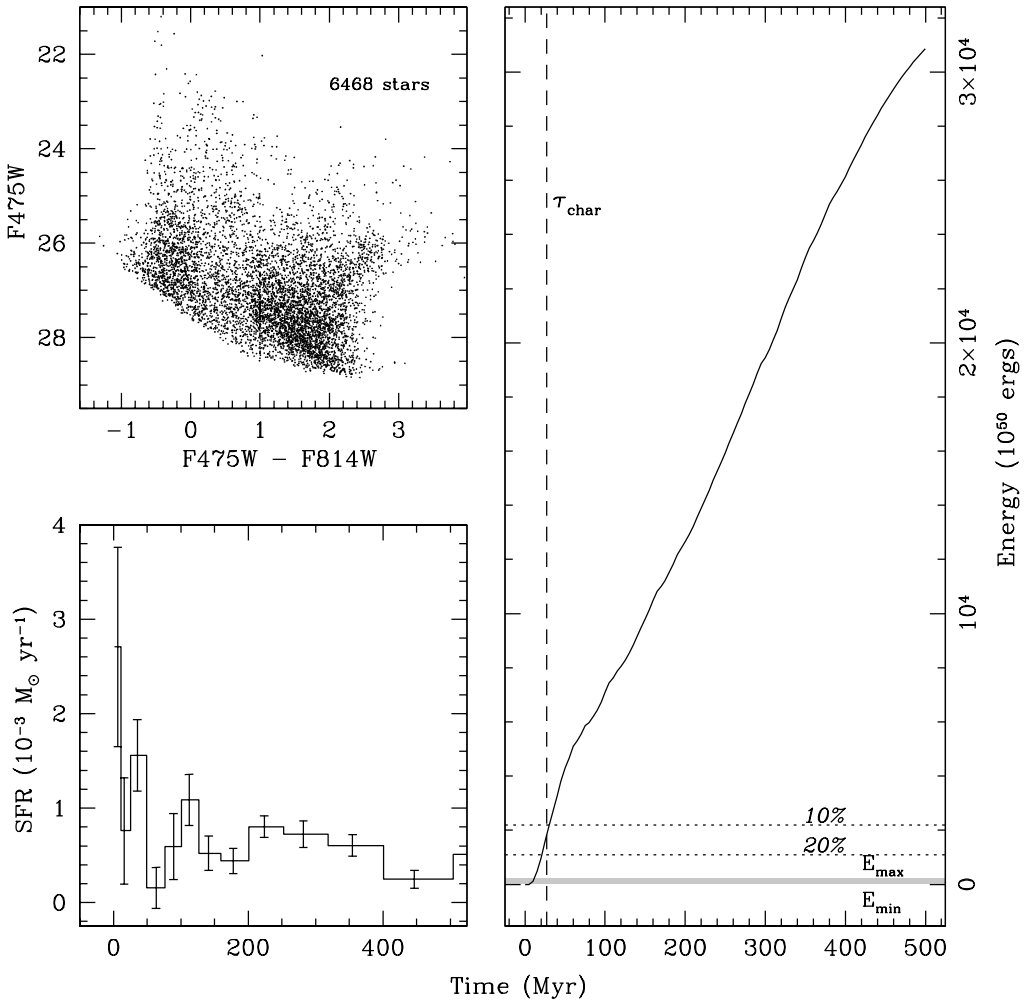

Figure 3.12 Same as Figure 3.8 except for UGC 8508.

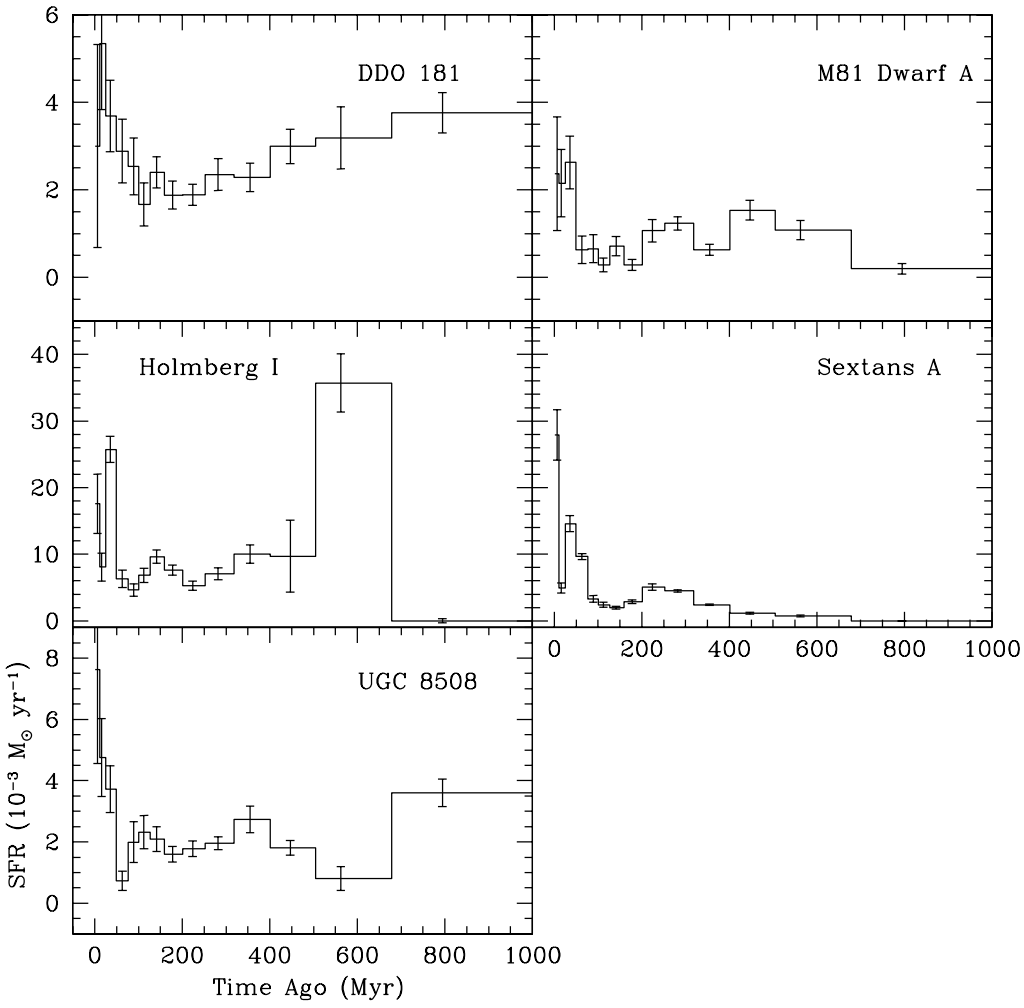

Figure 3.13 Global SFHs derived using all of the resolved stars observed for each galaxy in our centrally dominant hole sample. There is no common signature of a single, dominant hole creation event in the SFHs when compared to each other. When compared to the SFHs presented in Dohm-Palmer et al. (1998) and Weisz et al. (2008), the SFHs of this study do not distinguish themselves in any way.

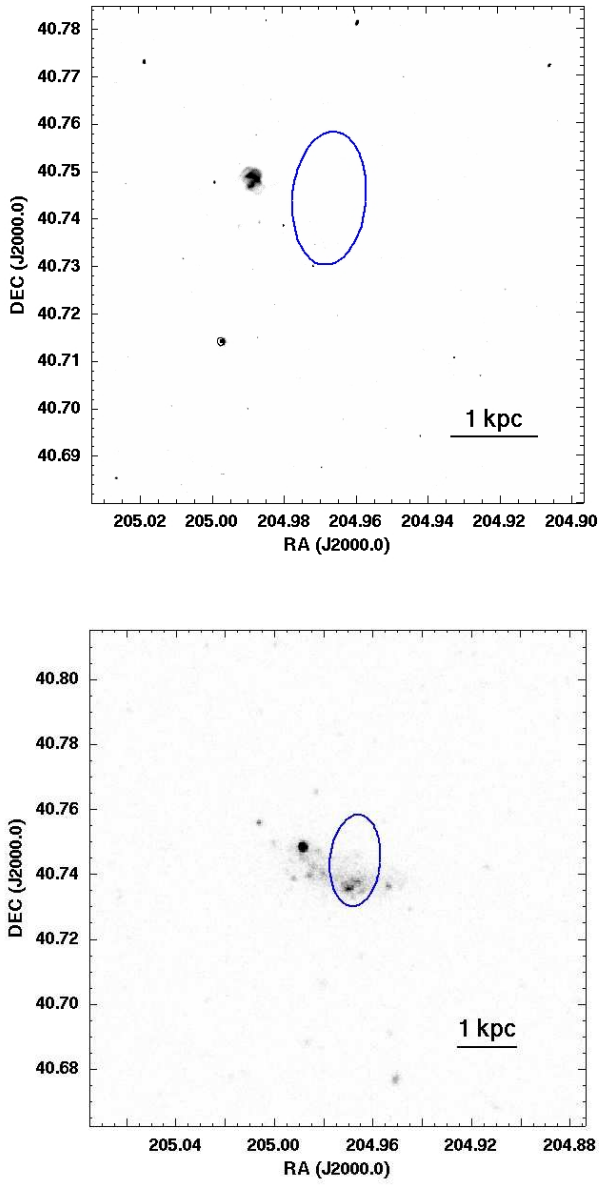

Figure 3.14 Ground based Hα (top) and GALEX FUV (bottom) image of DDO 181. The blue ellipses denote the area of the hole.

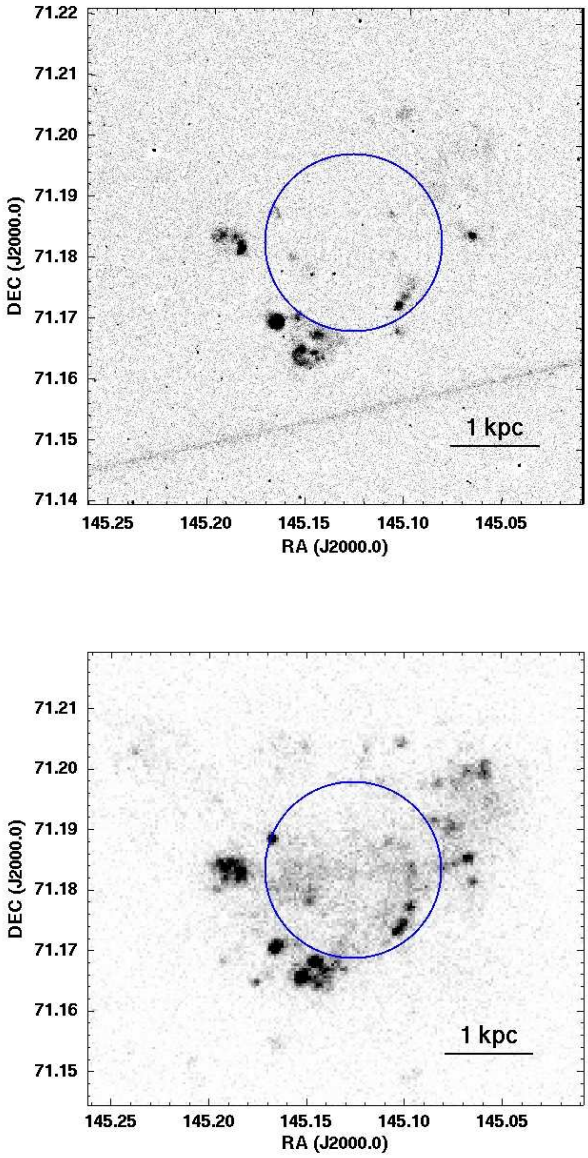

Figure 3.15 Ground based Hα (top) and GALEX FUV (bottom) image of Holmberg I. The blue circles denote the area of the hole.

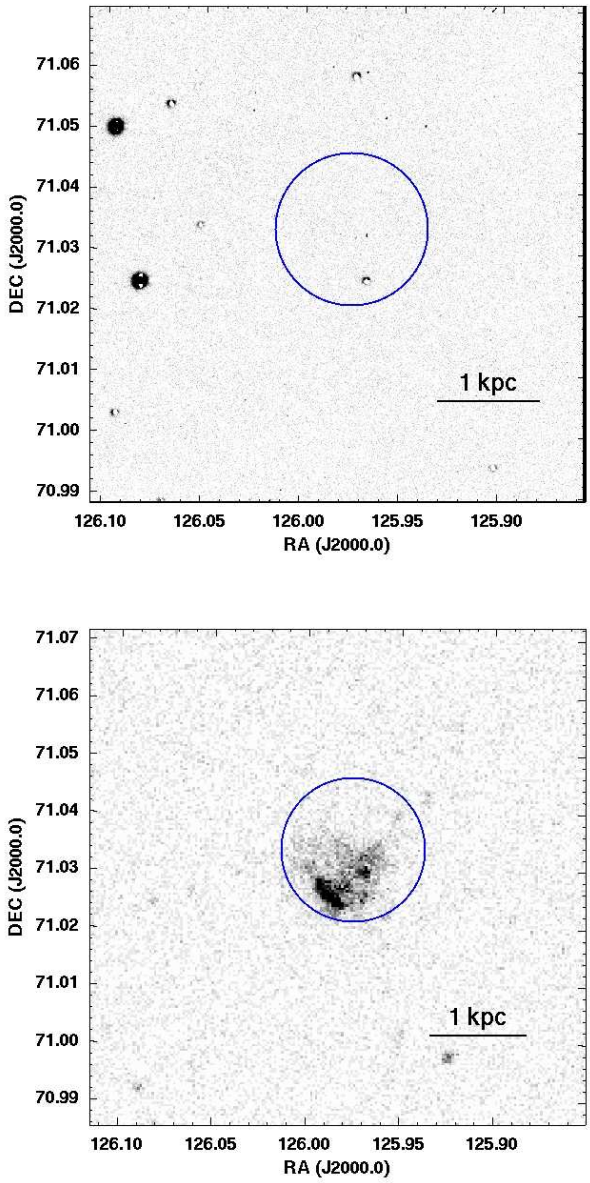

Figure 3.16 Ground based Hα (top) and GALEX FUV (bottom) image of M81 Dwarf A. The blue circles denote the area of the hole.

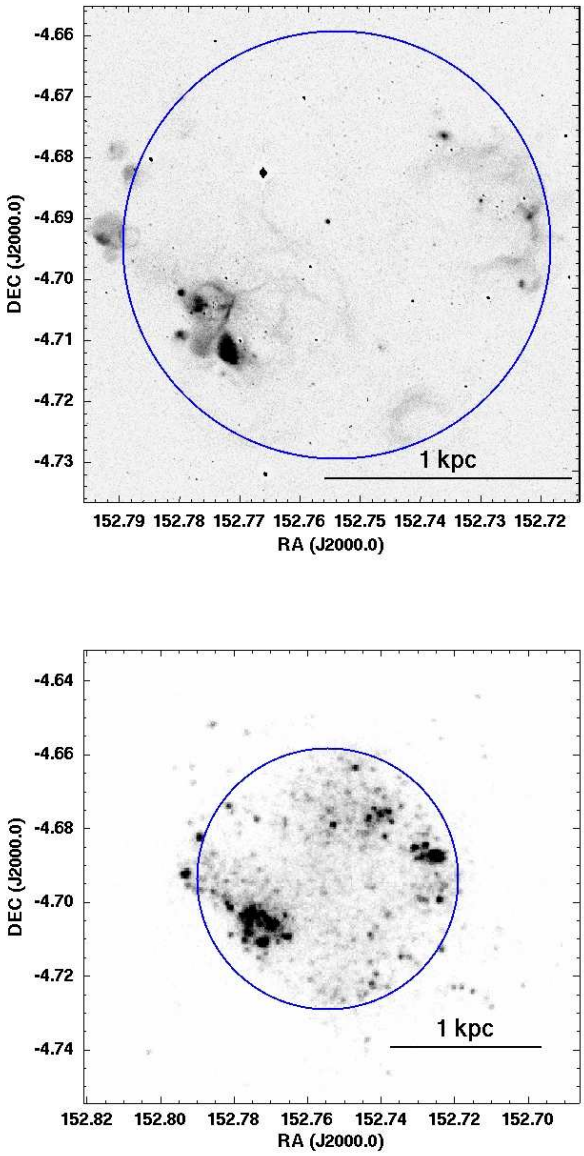

Figure 3.17 Ground based Hα (top) and GALEX FUV (bottom) image of Sextans A. The blue circles denote the area of the hole.

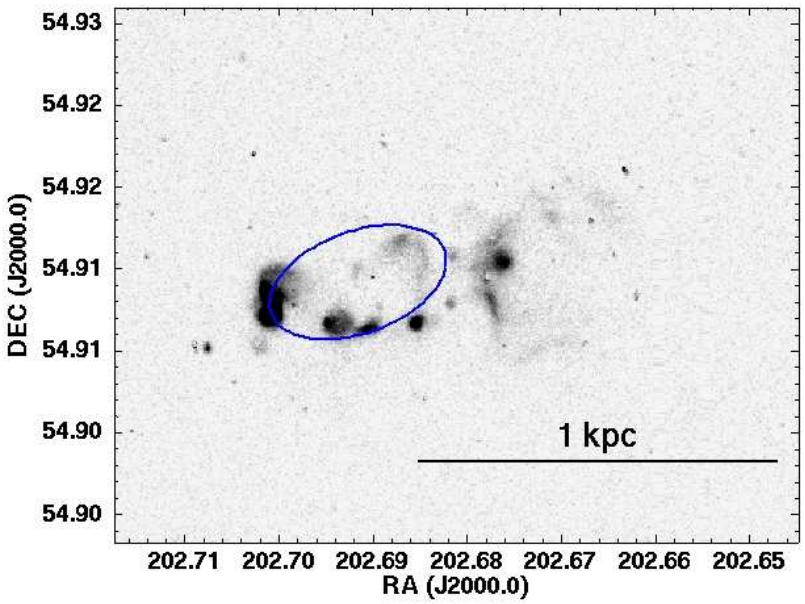

Figure 3.18 Ground based Hα image of UGC 8508. The blue ellipse denotes the area of the hole.

Table 3.1 Beam and Resolution of H I Images

Name	B_{maj} ($''$)	B_{min} ($''$)	BPA ($^{\circ}$)	Velocity Resolution (km s^{-1})
DDO 181	12.5	10.5	-80.4	0.63
Holmberg I	14.7	12.7	-41.6	2.5
M81 Dwarf A	15.9	14.2	10.2	2.5
Sextans A	11.6	10.9	47.6	0.63
UGC 8508	14.0	11.5	88.1	0.63

Table 3.2. General Galaxy Properties

1 Galaxy	2 RA (J2000.0)	3 DEC (J2000.0)	4 d (Mpc)	5 scale (pc/″)	6 m_B^a	7 M_B	8 L_B (10^7 $L_\odot$)	9 M_{HI} (10^7 $M_\odot$)	10 $N_{HI,Peak}$ (10^{21} cm^{-2})	11 $N_{HI,Ave}$ (10^{20} cm^{-2})	12 $<\sigma_v>$ (km s^{-1})
DDO 181	$13^h39^m53\overset{s}{.}8$	$+40°44'21''$	3.1	15.0	14.4	-13.0	1.12	2.60	1.77	3.12	8.2
Holmberg I	$09^h40^m32\overset{s}{.}3$	$+71°10'56''$	3.9	18.9	13.4	-14.5	4.45	14.6	2.26	2.78	7.9
M81 Dwarf A	$08^h23^m55\overset{s}{.}1$	$+71°01'56''$	3.4	16.5	16.3	-11.4	0.26	1.07	0.61	1.09	7.0
Sextans A	$10^h11^m00\overset{s}{.}8$	$-04°41'34''$	1.4	6.79	11.7	-14.0	2.81	6.80	5.98	5.16	9.8
UGC 8508	$13^h30^m44\overset{s}{.}4$	$+54°54'36''$	2.6	12.6	14.0	-13.1	1.22	2.20	2.98	2.42	10.3

Columns are: galaxy name, Right Ascension (RA), declination (DEC), distance (d), image scale, apparent B-band magnitude (m_B), absolute blue magnitude (M_B), blue luminosity (L_B), H I mass (M_{HI}), peak and average H I column density ($N_{HI,Peak}$, $N_{HI,Ave}$), and the average velocity dispersion measured in the second moment map ($<\sigma_v>$).

[a]Karachentsev et al. (2004), apparent magnitudes are corrected for Galactic foreground extinction.

Table 3.3. Hole Properties

1 Galaxy	2 RA (J2000.0)	3 DEC (J2000.0)	4 r_{hole} (pc)	5 P.A. (°)	6 τ_{char} (Myr)	7 E_{stars} (erg)	8 E_{max} (erg)	9 E_{min} (erg)	10 ϵ_{max}	11 ϵ_{min}	12 age_{alt} (Myr)
DDO 181	$13^h39^m52\overset{s}{.}1$	$+40°44'39\overset{''}{.}0$	755 (415)	85	90	1.1×10^{54}	5.3×10^{53}	3.9×10^{52}	48%	3.5%	>500, 240
Holmberg I	$09^h40^m30\overset{s}{.}$	$+71°11'01\overset{''}{.}8$	1000	0	124	3.4×10^{54}	1.2×10^{54}	6.7×10^{52}	35%	2.0%	395, 170
M81 Dwarf A	$08^h23^m54\overset{s}{.}1$	$+71°02'01\overset{''}{.}5$	745	0	104	1.4×10^{54}	5.0×10^{53}	3.5×10^{51}	35%	0.3%	>500, 390
Sextans A	$10^h11^m01\overset{s}{.}1$	$-04°41'37\overset{''}{.}0$	850	0	85	2.2×10^{55}	6.4×10^{53}	1.1×10^{53}	3%	0.5%	27, 19
UGC 8508	$13^h30^m45\overset{s}{.}9$	$+54°54'33\overset{''}{.}0$	285 (157)	20	27	1.8×10^{53}	2.2×10^{52}	9.2×10^{50}	12%	0.5%	30, 20

Columns are: galaxy name, Right Ascension (RA) and declination (DEC) of the center of the hole, the hole radius (semi-major axis length for DDO 181 and UGC 8508; semi-minor axis length is in parentheses), the position angle of the hole (P.A.), the characteristic age of the hole (τ_{char}), the cumulative stellar energy budget at the characteristic age of the hole (E_{stars}), the upper limit energy for creating the hole derived from Equation 3.1 (E_{max} is derived assuming $N_{HI} = 10^{21}$ cm^{-2}), the lower energy limit to create the hole (E_{min} is derived using the average observed N_{HI}), the upper and lower stellar feedback efficiencies (ϵ_{max} and ϵ_{min}), and alternative ages (age_{alt} are the age estimates for stellar feedback efficiencies of 10% and 20% using the upper limits of the hole creation energies (see §3.5)).

Chapter 4

Tracing Cold H I Gas in Nearby, Low-Mass Galaxies

A slightly modified version of this chapter has been published in The Astrophysical Journal with the following bibliographic reference: Warren, S. R., Skillman, E. D., Stilp, A. M. et al. 2012, ApJ, submitted

We analyze line-of-sight atomic hydrogen (H I) line profiles of 31 nearby, low-mass galaxies selected from the Very Large Array - ACS Nearby Galaxy Survey Treasury (VLA-ANGST) and The H I Nearby Galaxy Survey (THINGS) to trace regions containing cold (T $\lesssim$ 1400 K) H I from observations with a uniform linear scale of 200 pc beam^{-1}. Our galaxy sample spans four orders of magnitude in total H I mass and nine magnitudes in M_B. We fit single and multiple component functions to each spectrum to isolate the cold, neutral medium given by a low dispersion (<6 km s^{-1}) component of the spectrum. Most H I spectra are adequately fit by a single Gaussian with a dispersion of 8-12 km s^{-1}. Cold H I is found in 23 of 27 ($\sim$85%) galaxies after a reduction of the sample size due to quality control cuts. The cold H I contributes $\sim$20% of the total line-of-sight flux when found with warm H I. Spectra best fit by a single Gaussian, but dominated by cold H I emission (i.e., have velocity dispersions <6 km s^{-1}) are found primarily beyond the optical radius of the host galaxy. The cold H I is typically found in localized regions and is

generally not coincident with the very highest surface density peaks of the global H I distribution (which are usually areas of recent star formation). We find a lower limit for the mass fraction of cold-to-total H I gas of only a few percent in each galaxy.

4.1 Introduction

Dwarf irregular (dIrr) galaxies in the nearby universe are laboratories for studying the most fundamental properties of gas evolution and star formation. Large, multi-wavelength studies of these systems are only just beginning. However, recent, high resolution surveys of large, spiral galaxies in the ultraviolet (e.g., NGS - Gil de Paz et al. 2007), optical (e.g., NFGS - Jansen 2000; ANGST - Dalcanton et al. 2009), infrared (e.g., SINGS - Kennicutt et al. 2003), and radio (e.g., THINGS - Walter et al. 2008; HERACLES - Leroy et al. 2009) have given us insight into where and when stars form in a galaxy. They have also provided clues to the gas conditions surrounding sites of current star formation (Leroy et al. 2008; Bigiel et al. 2008). The conclusion is that stars form in regions rich in cold, dense, molecular material (Kennicutt, 1998a; Kennicutt & Evans, 2012). These studies mainly focus on high metallicity systems, however. How these results translate to low metallicity environments has not been fully explored, mainly due to the fact the most commonly observed tracer of molecular material, CO, is notoriously difficult to observe at low metallicity (e.g., Taylor et al. 1998; Barone et al. 2000; Leroy et al. 2005; Schruba et al. 2012).

Nearby dIrr galaxies offer the opportunity to study the star formation process in low metallicity systems at high spatial resolution. Studies of the star formation rates in dIrr galaxies defined from UV, 24μm, and/or Hα emission (e.g., Leroy et al. 2008; Bigiel et al. 2008; Roychowdhury et al. 2009) have found a non-linear correlation with the local atomic hydrogen (H I) distributions. However, the dependence of star formation on molecular gas content is apparent in the large spiral galaxies observed in Leroy et al. (2008) and Bigiel et al. (2008). The star formation rate surface density is shown to correlate linearly with the molecular gas surface density in these galaxies. These results can be understood if one assumes that efficient star formation requires molecular hydrogen (e.g., Krumholz et al. 2009 and references therein).

Based on theoretical studies, the very character of the interstellar medium (ISM) is likely to change at low metallicity (e.g., Spaans & Norman 1997). Glover & Mac Low (2011) modeled the so called X-factor which measures the relationship between amount of detected CO emission and the abundance of molecular hydrogen. They found that the amount of CO drops substantially at low metallicities, consistent with prior predictions (e.g., Maloney & Black 1988). This deficit of CO at low metallicities is supported by observations showing relatively low or no detections of CO emission in nearby dIrr galaxies (e.g., Taylor et al. 1998; Barone et al. 2000; Leroy et al. 2005; Schruba et al. 2012). Consequently, this lack of metals also results in lower amounts of polycyclic aromatic hydrocarbon (PAH) emission (e.g., Engelbracht et al. 2005; Jackson et al. 2006). The PAHs are important to the formation of the cold ISM since they are critical in the shielding of UV and soft X-ray photons.

The long standing problem of studying the molecular component in the low metallicity dwarfs continues. We expect dIrr galaxies to contain molecular hydrogen since they *are* forming stars. However, since direct observations of the molecular gas responsible for forming stars in large samples of dIrr galaxies via CO are currently not feasible, we must find a different tracer of star-forming gas.

One intriguing idea is to find the immediate precursors of the molecular gas. The assembly of star forming molecular clouds is generally believed to require cold H I (e.g., Wolfire et al. 2003; Krumholz et al. 2009). In our galaxy, cold H I clouds have been observed to surround and even intermix with molecular clouds (e.g., Krčo & Goldsmith 2010) through studies of H I narrow self absorption (HINSA; Li & Goldsmith 2003). One promising technique to find cold H I gas was pioneered by Young & Lo (1996, 1997) in a sample of nearby, star forming dIrr galaxies. These authors used high angular and spectral resolution H I data of two nearby dIrr galaxies to decompose line-of-sight spectra into narrow and broad Gaussian components. The narrow-lined gas ($\sigma \sim 4.5$ km s^{-1}) was found only in specific regions within the H I disk while the broad-lined gas ($\sigma \sim 10$ km s^{-1}) was found along every line-of-sight observed. The narrow Gaussian component was attributed to cold (T$\lesssim$1000 K) H I gas while the broad lined gas was assumed to be warm, neutral hydrogen (T$\gtrsim$5000 K). Young et al. (2003) studied three more dIrr galaxies, finding that they, too, contained evidence for cold H I gas. Other authors have used this technique to discover cold H I in a small number of other galaxies. de Blok &

Walter (2006) investigated the H I distribution in NGC 6822 and also found regions rich with cold H I gas. Recent work by Begum et al. (2006) found evidence of cold H I gas in six dIrr galaxies from the Faint Irregular Galaxies GMRT Survey (FIGGS; Begum et al. 2008). To date, cold H I in emission has been discovered in 10 nearby dIrr galaxies.

Within the limited data available, different measurements of the cold H I do appear to give comparable results. Two galaxies, DDO 210 and GR8, from the sample of Young et al. (2003) overlapped with that of Begum et al. (2006). Young et al. (2003) used the Very Large Array (VLA) at a linear scale of $\sim$200 pc beam^{-1} with a velocity resolution of 1.3 km s^{-1} while Begum et al. (2006) used the Giant Metrewave Radio Telescope (GMRT) at a linear resolution of $\sim$300 pc beam^{-1} with a velocity resolution of 1.65 km s^{-1}. Despite the use of different facilities and different spatial/spectral resolutions, both studies find similar results for both the spatial distributions and velocity dispersions of the narrow component. This agreement between the two studies suggests that the measurement of cold H I is generally robust, and not extremely sensitive to the exact observing parameters.

The technique of identifying a cold neutral medium has also been used in nearby, high metallicity spiral galaxies. Braun (1997) isolated cold H I gas using relatively low spectral resolution (6 km s^{-1}) imaging from the VLA for 11 of the closest spiral galaxies. He combined spectra from discrete radial bins and found that these combined spectra all had a narrow Gaussian core (FWHM $\lesssim$ 6 km s^{-1}) superposed onto broad (FWHM $\sim$ 30 km s^{-1}) Lorentzian wings. He also found that the cold H I gas is filamentary and is found in clumps, preferentially in the spiral arms. Since the majority of star formation in spiral galaxies occurs in molecular clouds within the spiral arms (e.g., Gordon et al. 2004), it is not surprising to find the bulk of the cold H I associated with these features.

The purpose of our study is to build upon the previous results of Young & Lo (1996, 1997), Young et al. (2003), Begum et al. (2006), and de Blok & Walter (2006) in order to provide limits to the locations and amount of cold H I gas in a large sample of 31 nearby, low-mass galaxies using a common spatial resolution. We describe our galaxy sample in §4.2 and our methods of signal extraction in §4.3. Our results are described in §4.4 and we end with a summary of our conclusions in §4.5.

4.2 Galaxy Sample, Observations, and Data Reduction

Galaxies for this work were taken from two major H I surveys of nearby galaxies: The H I Nearby Galaxy Survey (THINGS; AW0605; Walter et al. 2008) and the Very Large Array - Advanced Camera for Surveys Nearby Galaxy Survey Treasury (VLA-ANGST; AO0215; Ott et al. *in preparation*). Our sample consists of 24 galaxies from VLA-ANGST and 7 dwarf galaxies in the M81 Group from THINGS. The VLA-ANGST observations all have a high spectral resolution of 0.65 - 2.6 km s^{-1}. The 7 galaxies from the THINGS sample have velocity resolutions of 1.3 - 2.6 km s^{-1}. The high velocity resolution is crucial for detecting narrow velocity components. Other galaxies from the THINGS sample were not used because they had velocity resolutions of 5 km s^{-1}, too coarse for this type of analysis. Our final sample contains 31 galaxies with distances ranging from 1.3 - 5.3 Mpc (average 2.9 Mpc) and H I masses between 4×10^5 - 1×10^9 $M_\odot$.

All observations were made using the Very Large Array (VLA) observatory. We briefly outline the basic reduction procedure here, but note that both surveys followed similar recipes, described fully in Walter et al. (2008) and Ott et al. (*in preparation*). Standard AIPS processing of spectral line data was followed. Phase, bandpass, and flux corrections were made using typical VLA calibrators. Two sets of data cubes were produced: a natural weighted cube with a typical beam size of $\sim10''$ and a robust weighted cube with a beam size of $\sim7''$. Both sets of data have rms noise values of $\sim$1 mJy $beam^{-1}$ in a single line-free channel. We use the robust weighted cubes in this work, which allows us to use the smallest possible uniform linear scale. Further, robust weighting produces minimal side-lobes allowing for a clean-beam which better approximates the dirty beam structure than that of the more complex structure seen in the dirty-beam of natural weighting (Briggs, 1995). The better dirty-beam approximation of the robust weighting is ideal for the extended emission observed in H I data.

The main difference between the data for the two surveys is due to the inclusion of updated Expanded VLA (EVLA) antennas into the array for the VLA-ANGST survey

The VLA telescope of the National Radio Astronomy Observatory is operated by Associated Universities, Inc. under a cooperative agreement with the National Science Foundation.

The Astronomical Image Processing System (AIPS) has been developed by the NRAO.

(the EVLA has since been renamed the "Karl G. Janksy Very Large Array"). Unfortunately, the conversion of the digital EVLA signal to an analog signal (to be compatible with the VLA signal) aliased power into the first 0.5 MHz of the baseband. This only affected the EVLA-EVLA baselines and they were subsequently removed from the data (see Ott et al. *in preparation* for full details). Aliasing did not correlate into the mixed VLA-EVLA baselines and the VLA-VLA baselines were unaffected. To compensate for the loss of the EVLA-EVLA baselines, additional observation time was spent on each source. Table 4.6 gives an overview of the major observational properties of our galaxy sample. The table columns are: 1) galaxy name, 2,3) RA and DEC, 4) distance in Mpc (from TRGB measurements in Dalcanton et al. 2009 unless otherwise noted), 5) total H I mass, 6) absolute B-band magnitude, 7) the major-axis length in arcminutes at the $\sim$25 mag arcsec^{-2} level (except for KKH 98 and KK 230, which use the Holmberg system of $\sim$26.5 mag arcsec^{-2}; Karachentsev et al. 2004), 8) inclination (Karachentsev et al., 2004), 9) the 200 pc beam size (see §4.3.1), 10) the spectral resolution, and 11) the rms of the noise in the line-free channels of the data cube. While some metallicity estimates exist for the most massive galaxies in our sample, most do not have measured abundances. Using the relation in Lee et al. (2006) which relates M_B to the oxygen abundance (see also Berg et al. 2012), we expect a range of $7.0 \lesssim 12+\log(O/H) \lesssim 8.2$ with a median value of 7.7 for the low mass galaxies in our sample.

4.3 Identifying Narrow Spectral Components

4.3.1 Methodology

We analyze line-of-sight spectra following methods similar to those outlined in Young & Lo (1996, 1997) and Young et al. (2003). First, we smoothed each image cube with a Gaussian kernel to a common linear scale of 200 pc beam^{-1}. To do this we computed the angular size equivalent of 200 pc for each galaxy using the distances given in Table 4.6. We then used the CONVL task in AIPS which incorporates the initial beam size, beam position angle, and requested output beam size to compute the required convolving kernel. We note that our circular beam sizes can sample slightly larger linear scales depending on galaxy inclination. Spectra were then extracted through every 1.″5 pixel

(1″ pixels for NGC 247 and NGC 3109). Extracting spectra from every pixel oversamples the beam, but for our purposes, does not influence the results. Also, the beam sizes reported in Table 4.6 and the typical galaxy rotation speeds of 10-20 km s^{-1} are small enough that kinematic broadening is minimal, regardless of galaxy inclination. Note that spectral broadening would work to hide a narrow component, not create one.

Each extracted spectrum was successively fitted using our own routines with two different functional forms: a single Gaussian and a double Gaussian. We also attempted to fit the spectra with a fourth order Gauss-Hermite polynomial of the form

$$\phi(x) = ae^{-y^2/2}\left[1 + \frac{h_3}{\sqrt{6}}(2\sqrt{2}y^3 - 3\sqrt{2}y) + \frac{h_4}{\sqrt{24}}(4y^4 - 12y^2 + 3)\right] \tag{4.1}$$

where $y \equiv (x-b)/\sigma_{herm}$ (van der Marel & Franx, 1993), h_3 and h_4 measure the amplitudes of an asymmetric and a symmetric deviation from an underlying Gaussian profile with amplitude a, central velocity b, and standard deviation σ_{herm}. Gauss-Hermite polynomials offer useful characterizations of non-Gaussian line profiles, but as Young et al. (2003) point out, the direct relationship between the Gauss-Hermite variables and the physical conditions of the gas is not obvious. In general, the results of the double Gaussian and Gauss-Hermite polynomial fits were in excellent agreement, although the detection efficiency of the Gauss-Hermite polynomials is much lower. However, we expect the observed spectra to have a Gaussian profile if the gas has an isothermal density distribution (Merrifield, 1993). Since the relationship between the Gauss-Hermite polynomial parameters and the physical nature of the gas is not obvious, we only report the results of the single and double Gaussian fits.

A spectrum was identified as containing narrow-line H I only if multiple criteria were fulfilled. First, we only fit extracted spectra with a S/N greater than 10 (see §4.3.2). We define S/N in the same manner as Young & Lo (1996), that is, the peak in the spectrum divided by the rms noise in the line free channels of the data cube. We also required each individual component of the double Gaussian fit to have a minimum S/N of 3.1. This minimum S/N requirement was also used by Young & Lo (1996), Young & Lo (1997), and Young et al. (2003) and is motivated by our desire to obtain significant detections. Also, each spectrum (single or multiple component) was required to have a velocity dispersion greater than the velocity resolution of the data (0.65, 1.3, or 2.6 km

s^{-1}) beyond the 1σ errors in the fits. Requiring the velocity dispersion plus error to be greater than the velocity resolution ensures we are not fitting noise spikes in the data. Fortunately, none of the fitted spectra were affected by this criterion. Typical errors in the velocity dispersion of each single and double Gaussian component are roughly 0.7 km s^{-1}. We also do not enforce any restrictions on the central velocity offsets between individual components, leaving this as a free parameter.

To quantify which function best fitted each spectrum, we first computed the variance of the residuals for each fit. The ratio of the variances between the single and double Gaussian fits were then compared statistically via a single-tailed F-test. A double Gaussian fit was determined to be statistically significant if the probability of improvement over a single Gaussian fit was 95% or greater. We were as conservative with our approach as possible in order to provide secure lower limits to the total amount of narrow-line H I in each galaxy. Young & Lo (1996, 1997), Young et al. (2003), and Begum et al. (2006) were less conservative in their approach, requiring only a 90% significance of improvement over a single Gaussian profile. Because of our relatively high S/N cut-off, the results of our fitting are relatively independent of the F-test criterion that we use, as long as it is above roughly 70%. Since the number of detections of double Gaussian profiles increases very slowly as the cut-off is reduced from 95% down to 70%, we chose 95% confidence to establish a very firm lower limit on the total cold H I content. Establishing a realistic upper limit is more problematic and is highly dependent upon assumptions.

We further adopt the criteria of de Blok & Walter (2006) that cold H I has a velocity dispersion of less than 6 km s^{-1}. A velocity dispersion of 6 km s^{-1} results in an upper limit to the gas temperature of $\sim$1400 K (assuming $(3/2)kT = (1/2)m_p\sigma^2$). Thus, we did not ascribe a second component as cold H I when the fits detected multiple components with similar velocity dispersions between 6-10 km s^{-1} or one component with a velocity dispersion of 6-10 km s^{-1} and another component with a much higher dispersion. The vast majority of spectra that were best fit by double Gaussian profiles with both velocity dispersions greater than 6 km s^{-1} were double peaked (in both low and high inclination galaxies) which is normally associated with expanding structures (e.g., Brinks & Bajaja 1986). Furthermore, these higher velocity dispersions are not typical for the cold H I described in the literature with velocity dispersions of 2-6 km

s^{-1} (Young & Lo 1996; Braun 1997; Young & Lo 1997; Young et al. 2003; de Blok & Walter 2006; Begum et al. 2006); we therefore rejected these locations as having narrow line emission. de Blok & Walter (2006) also noted that the bulk of the spectra within this category for NGC 6822 were double-peaked, leading them to make a cut at 6 km s^{-1}. Thus, having a cut at 6 km s^{-1} ensures that we are both reporting cold gas and eliminating a large fraction of the double peaked spectra. The double-peaked spectra eliminated by this criteria represent less than 1% of the total spectra and are not included in any of the following analyses. We also identify spectra that were sufficiently fit by a single Gaussian profile with a velocity dispersion of less than 6 km s^{-1} as cold H I. Limiting our cold H I identifications to gas with velocity dispersions less than 6 km s^{-1} ensures we are not misidentifying warm H I as cold H I.

One possible scenario is that the broad component is the combination of multiple cold gas (narrow Gaussian) clouds. Given that the typical line-of-sight spectrum is best fit by a single Gaussian profile (see §4.4), the multiple cold H I clouds would have to conspire in such a way to maintain this Gaussianity. While this scenario is physically possible, it requires a large number of cold HI clouds with distributions in velocities and amplitudes that would systematically combine to maintain a total Gaussian velocity dispersion equal to the observed velocity dispersion for the warm HI phase. High resolution absorption line studies would be required to distinguish whether the broad component is truly broad or a composite of many narrow components. However, if we assume that the galaxies can be approximated by a thin disk we would expect that the line centroid of the cold H I to be at or very near the line centroid of the warm H I. Warm H I gas scale heights in dwarf galaxies tend to be a few hundred pc (e.g., Warren et al. 2011) compared to their few kpc diameters, so this is not a bad assumption. Offset velocity gas due to inclination effects would then contribute to the broadening of the warm (broad Gaussian) component and less so to the cold (narrow) component gas. Not surprisingly, the average central velocity offset between the components of the best fit double Gaussian profiles in our sample is 0.35 km s^{-1}, which is less than the velocity resolution of our data. Thus, the observations are most simply interpreted as a combination of cold gas near the central velocity (when observed) and nearly ubiquitous warm gas. We find it highly unlikely that the broad component is a combination of multiple narrow components. This leads us to the conclusion that the H I is dominated by the warm phase and that the cold

phase represents a much smaller fraction of the ISM in our sample of dwarf galaxies.

The top panel of Figure 4.1 shows an extracted spectrum (black) from the VLA-ANGST observations of Sextans A with single Gaussian profile (blue dashed), double Gaussian profile (solid red), and Gauss-Hermite polynomial fits (dotted magenta). The bottom panel shows the residual to the fit. This spectrum has a clear narrow peak that is not fit well by the single Gaussian profile. Both the double Gaussian profile and the Gauss-Hermite polynomial fit the spectrum statistically better than the single Gaussian profile at the 99.9% confidence level. Although the Gauss-Hermite polynomial is a better fit than the single Gaussian profile, the residuals clearly show that the double Gaussian profile is even better.

In summary, we identify cold H I by the following process: 1) only spectra with a S/N greater than 10 were fit, 2) each spectrum was successively fitted with a single and double Gaussian function, 3) each individual component of the double Gaussian fit was required to have a minimum S/N of 3.1, 4) the velocity dispersion plus error had to be greater than the velocity resolution of the data, 5) double Gaussian fits were accepted if they improved the fit over a single Gaussian profile at the 95% or greater confidence level in a single tailed F-test, and 6) cold H I can be described by single or double Gaussian profiles with velocity dispersions less than 6 km s^{-1}.

4.3.2 Simulations of Synthetic Spectra

There are two factors which could lead to non-detections of existing cold H I. Cold H I could be missed simply because the column density is too low to reach our S/N requirement, or it could be missed because a higher S/N is required to deblend the cold H I from the warm H I. As a test of our ability to extract multiple components from a given spectrum, we produced three sets of 50,000 uniformly distributed synthetic spectra that spanned the S/N of our sample ($10 \leq S/N \leq 60$; one set each at 0.65, 1.3, and 2.6 km s^{-1} velocity resolution). Each spectrum contained two Gaussian profiles that are representative of the warm and cold H I gas; a "broad" Gaussian with σ_{broad} between 8 and 12 km s^{-1} and a "narrow" Gaussian with σ_{narrow} between 3 and 6 km s^{-1}. We allowed for an offset of $\pm$2.5 km s^{-1} between the line centroids. Velocity offsets larger than 2.5 km s^{-1} allow for much higher detection fractions since the spectra become more asymmetric. The observed cold H I line centroids are also very similar to the warm

H I line centroids (as discussed in §4.3.1). For each S/N, we randomized the amplitude of the cold H I Gaussian. We then chose the warm H I Gaussian such that the S/N was conserved. As for the analysis with our observations, each individual component was required to have a S/N > 3.1. A new set of Gaussians was produced if each component did not have a S/N > 3.1. We next added random noise to each spectrum and then passed each randomly generated spectrum through our fitting routine to gauge our recovery rate.

The top row of Figure 4.2 shows histograms of the total number of synthetic spectra (solid black line) and the total number identified as requiring multiple components by a double Gaussian fit (solid red line) as a function of S/N. The red histograms also include the locations best fit by a single Gaussian with a velocity dispersion of less than 6 km s^{-1}. The bottom row shows the detection efficiency as a function of S/N for the double Gaussian fits (including the best fit single Gaussians with a velocity dispersion of less than 6 km s^{-1}). Figure 4.2 shows that we never identify all double Gaussian profiles within the range of S/N values scrutinized and our recovery efficiency worsens as the velocity resolution decreases. The differences in recovery efficiency between the 0.65 and 1.3 km s^{-1} simulations are less pronounced than from 1.3 to 2.6 km s^{-1}.

Table 4.2 shows the results of the simulations for each velocity resolution for the double Gaussian profiles that were identified. Column (1) is the velocity resolution, column (2) is the ratio between the input and extracted broad Gaussian amplitude ($A_{b,sim}/A_{b,extr}$), columns (3) and (4) are the average differences between the simulated and extracted broad Gaussian central velocities (Δv_{broad}) and velocity dispersions ($\Delta\sigma_{broad}$), column is the ratio between the input and extracted narrow Gaussian amplitude ($A_{n,sim}/A_{n,extr}$), and columns (6) and (7) are the average differences between the simulated and extracted narrow Gaussian central velocities (Δv_{nar}) and velocity dispersions ($\Delta\sigma_{nar}$), respectively. These results show that when we do recover two Gaussian profiles, our routines accurately reproduce the input Gaussian parameters.

In Figure 4.3 we plot the amplitude ratio of the broad and narrow Gaussian components ($A_{\rm broad}/A_{\rm narrow}$) versus the ratio of the velocity dispersions ($\sigma_{\rm broad}/\sigma_{\rm narrow}$) for the 1.3 km s^{-1} velocity resolution simulation. We show these ratios in four different S/N bins to understand where our fitting routines have trouble identifying the two Gaussian components. The grey points represent all of the simulated spectra, the red points are

those spectra identified as containing two Gaussian components, and the blue points are the simulated spectra best fit by a single Gaussian with a velocity dispersion of less than 6 km s^{-1} (even though the input spectra contains both a broad and narrow Gaussian as described above). As is shown in Figure 4.2, the recovery efficiency is dependent upon the S/N. The best fit single Gaussians are predominately in a regime where the narrow component dominates the spectra (amplitude ratios less than 1 and velocity dispersion ratios less than 2.5). We also have difficulty identifying the narrow component when the broad component dominates the spectra in all S/N bins. Lastly, our routines do not pick up multiple components when the velocity dispersions are similar. These plots show some of the complexities in simulating and recovering multiple Gaussian components. When we do identify the spectra as containing multiple components, however, our routines accurately reproduce the input parameters. The simulations indicate that we can be confident of our detections in the observed data. However, the simulations also show that we can only reliably compute lower limits to the cold H I content. A complete census of the cold H I would require both higher S/N spectra and a detailed knowledge of the intrinsic distributions in A_{broad}/A_{narrow} and $\sigma_{broad}/\sigma_{narrow}$ (in order to make incompleteness corrections).

We also produced 50,000 synthetic spectra of single Gaussian profiles to quantify our false positives. These spectra were generated using a velocity dispersion between 8 and 12 km s^{-1} with S/N values between 10 and 60. We used a velocity resolution of 2.6 km s^{-1} since this gives the worst recovery results. With our acceptance criteria, we failed to find a single false identification of multiple components in our synthetic spectra. We do not start to see the potential for false detections until the confidence level is lowered to $\sim$70%. These simulations give us confidence that our fitting results are robust to false detections.

4.4 Results

4.4.1 Cold H I Detections

Each galaxy in our sample varies in terms of the total number of spectra and observed minimum, maximum, and average S/N (and column density). In total, we have analyzed roughly 4,100 independent lines-of-sight. Table 4.3 summarizes the observed spectral

properties of each galaxy. The columns indicate 1) galaxy name, 2) total number of independent lines-of-sight scrutinized (N_t), 3) average S/N of the extracted spectra ($<S/N>_t$), 4) the approximate column density at a S/N of 10 ($N_{HI,min}$), 5) the peak column density ($N_{HI,peak}$), and 6) the average column density ($<N_{HI}>$). All of the H I spectra in DDO 82, KDG 73, KK 230, and KKH 98 have S/N values below our threshold and as a result had no spectra analyzed, reducing our final sample to 27 galaxies.

Table 4.4 summarizes the results of our fitting routine. The columns are described as follows: 1) galaxy name, 2) the average S/N of the spectra where cold H I is found ($<S/N>_c$), 3) the areal filling factor of the cold H I defined as the ratio of the number of cold H I detections and the total number of scrutinized spectra ($\mathcal{F}_{fill}$), 4) the cold-to-total H I mass fraction defined as the ratio of the total summed column densities of the cold H I Gaussian profiles and the total summed column densities in the areas scrutinized ($\mathcal{F}^{low}_{mass}$), 5) an estimate of the upper limit to the cold-to-total H I mass fraction assuming each line-of-sight contains cold H I ($\mathcal{F}^{up}_{mass}$; see §4.4.5), 6 & 7) the average velocity dispersion of the narrow and broad Gaussian components ($<\sigma_n>$ and $<\sigma_b>$), and 7) the average velocity dispersion of the locations where a single Gaussian profile was sufficient to describe the spectrum ($<\sigma_s>$). Column 5 also includes all of the best fit single Gaussian profiles with a velocity dispersion of less than 6 km s^{-1}, while column 7 excludes them.

We detected cold H I in 23 out of the 27 galaxies in our final sample. Figure 4.4 shows the spatial distribution of the cold H I for each galaxy. The left panels show the total integrated H I intensity maps with contours of 10^{20} and 10^{21} cm^{-2} overlaid. The right panels have the H I surface density contours overlaid on the locations of the cold H I emission. The majority of the cold H I is clumped in localized regions. Typically, the cold H I is not spatially coincident with the very highest peaks in the total H I distribution in a given galaxy, although it is mainly concentrated in locations where the total H I column density exceeds the canonical threshold for star formation of $\sim 10^{21}$ cm^{-2} (Skillman et al., 1987). Cold H I described in each of the previous studies also shows a preference for being located in regions of high column density, but not necessarily associated with the highest H I columns. The concentration of the cold H I in these regions is not unexpected given these location have the highest S/N values.

The four galaxies that we do not detect cold H I (DDO 99, MCG09-20-131, NGC 3741, and UGCA 292) show no distinguishing characteristics to give us insight as to why they are non-detections. Each of their total H I masses, M_B values, distances, stellar disk sizes, and star formation rates (see §4.4.7) are similar to other galaxies in our sample that do show cold H I detections.

4.4.2 Comparison with Previous Work

Fortunately, our sample of 27 galaxies had some overlap with previous studies using similar methods to detect cold H I. Young et al. (2003) detected cold H I in UGCA 292 and GR8 using the VLA while Begum et al. (2006) detected it in DDO 53, MCG09-20-131, GR8 and M81 Dwarf A using the GMRT. These five galaxies are amongst the faintest and smallest galaxies in our sample and as a result, we detected cold H I in only 3 of these 5 galaxies: DDO 53, GR8, and M81 Dwarf A. Our selection criteria failed to produce a cold H I signature in UGCA 292 or MCG09-20-131.

The three galaxies in which we did detect cold H I are included in Figure 4.4. For GR8, Young et al. (2003) and Begum et al. (2006) each found cold H I in both the northern and south-western portions of the galaxy while Young et al. (2003) also found some evidence in the eastern portion of the galaxy. In contrast, we only found cold H I in the northern region of GR8. For M81 Dwarf A we detect cold H I only in the eastern side of the galaxy while Begum et al. (2006) find a hint of cold H I in the western side of the galaxy as well. For DDO 53 we found good overall agreement with the previous study, although our total detection area is smaller.

The data quality between each survey is similar, yet they provide minor differences in their results. Our simulations suggest velocity resolution differences may play a role in the detection differences between the studies. The velocity resolutions in our sample for these galaxies are 0.65, 1.3, and 2.6 km s^{-1} for GR8, M81 Dwarf A, and DDO 53, respectively. The literature velocity resolutions are 1.3 and 1.65 km s^{-1} for GR8, 1.65 km s^{-1} for M81 Dwarf A, and 1.65 km s^{-1} for DDO 53. The galaxy with the most similar cold H I distribution, DDO 53, has the worst velocity resolution in our sample, 0.85 km s^{-1} worse than the literature value. GR8 has been analyzed with three different velocity resolutions and each study finds slightly different results. We reduced our velocity resolution to 1.3 km s^{-1} for GR8 to compare to the other studies and obtained no

difference in our results. M81 Dwarf A was analyzed with similar velocity resolutions, yet there still exists slight differences. Despite analyzing data from different observatories with different velocity resolutions, the general results are all similar. It seems likely that the differences in each galaxy arise from small differences in the selection criteria and beam shape. For example, both Young et al. (2003) and Begum et al. (2006) used naturally weighted data cubes which, on average, produce higher S/N spectra. However, as noted in §4.2, the robust weighting for combined array data is ideal for studying extended emission due to the better clean beam approximation of the dirty beam in the CLEAN algorithm. The previous studies also used a cutoff of 90% in the F-test statistic and also allow the narrow Gaussian component to be larger than 6 km s^{-1}, finding values up to $\sim$8 km s^{-1}.

4.4.3 Are the Cold H I Non-Detections Significant?

If each spectrum consisted of both a broad and narrow component and were not inherently a single Gaussian profile, we would expect to find far more locations with a narrow line signature than we actually do. The top panel of Figure 4.5 shows a histogram for every independent line-of-sight (black line), the expected number of identified narrow line detections (blue) (based upon our detection efficiency as calculated in §4.3.2 and the assumption that a narrow component exists at each location), and the actual number of narrow line detections (red) as a function of S/N. The bottom panel shows the detection fraction as a function of S/N. Figure 4.5 demonstrates the large gap between the number of spectra for which we are sensitive to the presence of narrow H I and the number of spectra for which there are detections. Our expected recovery fraction is insensitive to small changes in the reasonable ranges used for the parameters.

The lower S/N spectra have fewer fractional detections. As discussed in §4.3.2, the lower fractional detections at lower S/N values are due, in part, to our recovery efficiency but may also be due to a minimum total H I column density required for the appearance of cold H I. Kanekar et al. (2011) recently observed H I in the Milky Way and determined a minimum column density threshold of 2×10^{20} cm^{-2} for the formation of a cold phase of H I, which is just at the column density limit of where our sample begins. The top row of Figure 4.6 shows histograms of all of the observed column densities in our galaxy sample (black), and the column densities where we detect cold H I (red). The bottom

row shows our detection fraction as a function of column density.

The small fraction of narrow line detections at high S/N compared to what would be expected clearly shows that the cold H I that can be identified with this technique is inconsistent with a ubiquitous distribution. It should also be noted that there could exist cold H I at every line-of-sight below a S/N of 3.1 that we would be insensitive to. However, it would be unphysical for the presence of gas to be related to our S/N criterion and not to the H I column density. Furthermore, absorption line studies in the Milky way indicate that cold H I gas is not ubiquitous (e.g., Begum et al. 2010; Kanekar et al. 2011).

4.4.4 The Velocity Dispersions of Cold and Warm H I

The typical velocity dispersion for the cold H I is $\sim$4.5 km s^{-1}. The broad components and best-fit single Gaussian profiles vary by galaxy, but they generally have similar values. We expect the broad and best fit single components to be similar if they are both tracing the same warm H I. Figure 4.7 shows histograms of the narrow (red), broad (blue), and single (black) velocity dispersions for each galaxy. The dotted vertical line denotes our cold H I cutoff limit of 6 km s^{-1}. The single component histograms have been scaled in order to show the narrow and broad component histograms more clearly. Generally, the velocity dispersions of the broad components overlap with those of the single components. However, the peak in the broad component is offset from the peak in the single component towards higher values. This behavior is also seen for the majority of the cases in the literature, and is probably due to the fact that it is easier to identify a narrow component when the broad component has a much larger value.

In Figure 4.8, we plot the average velocity dispersion, $<\sigma>$, of the warm (black) and cold (red) H I gas as a function of radius for each of our different velocity resolutions. We have omitted the locations best fit by a single Gaussian with a velocity dispersion of less than 6 km s^{-1}. The average warm H I velocity dispersion declines with radius. This trend is similar to the total H I velocity dispersion versus radius seen by Tamburro et al. (2009). The decrease in the velocity dispersion with increasing radius may indicate a decrease in turbulent energy supplied by the underlying stellar population as the radius increases away from the center of the stellar disk.

4.4.5 The Areal and Mass Fractions of Cold H I

Recent work on galaxy simulations of spiral disks have put limits on the predicted volume filling factor of the different gas phases in the ISM (e.g., de Avillez & Breitschwerdt 2004). The cold (T < 1000 K) ISM occupies $\lesssim$20% of a galaxy's volume, depending upon the star formation (supernova) rate. The cold neutral medium, however, may occupy only a few percent of the volume (McKee & Ostriker, 1977). The actual value will vary by galaxy and must also be sensitive to the available ISM coolants (e.g., C+, CO, dust, etc.) and the global gravitational potential.

Without knowing the exact 3-dimensional structure of the galaxies in our sample, we cannot calculate the volume filling fractions. Instead, we calculate the areal filling fractions ($\mathcal{F}_{fill}$), i.e., the ratio of the number of lines-of-sight with detected cold H I and the total number of lines-of-sight with S/N > 10 (see Table 4.4, column 3). We derive an average $\mathcal{F}_{fill}$ value of 9%. The true volume filling fractions based upon our detections are most likely even lower than these values since the scale height of the warm H I will be larger than that of the cold H I. The low filling fractions we compute are consistent with the ISM model of McKee & Ostriker (1977).

We also computed a lower limit to the total mass (flux) contribution of the cold H I for each galaxy using the narrow component of the Gaussian fits ($\mathcal{F}^{low}_{mass}$; see Table 4.4, column 4). Young & Lo (1996, 1997) and de Blok & Walter (2006) found that roughly 20% of the total H I mass is in the cold H I, which is significantly higher than the $\sim$3% typical for our values of $\mathcal{F}^{low}_{mass}$. It is unclear as to the reason for this large discrepancy since the data are of similar quality. The biggest differences may lie in the higher S/N resulting from the natural weighting these other studies use as compared to the robust weighting we employ. Also, de Blok & Walter use a different statistical test in defining the acceptance of cold H I detections. These authors accept a double Gaussian fit as statistically better than a single Gaussian fit if the χ^2 value is improved by 10%. Furthermore, our values are lower limits given our selection criteria and sensitivities. Figure 4.9 plots $\mathcal{F}_{fill}$ and $\mathcal{F}^{low}_{mass}$ as a function of M_B (left) and M_{HI} (right). No obvious trends arise between the areal filling fraction and mass fraction with absolute B-band magnitude or total H I mass.

If we assume (as noted in §4.4.3) that each line of sight has cold H I just below our detection limits, we can estimate an upper limit to the amount of cold H I in each

galaxy. To do this we have used a representative cold H I Gaussian of amplitude 3.1σ and velocity dispersion of 4.5 km s^{-1} at each location where we do not detect cold H I. We then add this "extra" mass to our detected cold H I mass to produce an upper limit to the cold H I mass fraction ($\mathcal{F}^{up}_{mass}$; see column 5 in Table 4.4). These values of $\mathcal{F}^{up}_{mass}$ can range up to 50%. However, since the cold H I is most frequently associated with higher values of N_{HI} (see §4.4.1), it is unlikely that the true values of cold H I mass get as high as these upper limits.

Another, perhaps more reasonable way to calculate an upper limit to the cold-to-total H I mass fraction is to find the typical fractional flux contributed to the cold component along each line-of-sight and assume this fraction holds throughout the sample. For locations where we find both warm and cold H I components, the cold H I typically is not the dominant phase in the ISM. The top row of Figure 4.10 shows a normalized histogram of the flux ratio of cold and total H I defined as the ratio of the column density of the narrow Gaussian profile and the total column density along the line-of-sight. The cold H I constitutes ∼20% of the total line flux for any given line-of-sight. The bottom panels of Figure 4.10 show this same ratio as a function of S/N for each velocity resolution. If we assume that *every* line-of-sight contains cold H I, then an upper limit to the cold-to-total mass ratio for each galaxy is ∼20%. This value is what is reported by Young & Lo (1996, 1997) and de Blok & Walter (2006). However, this value is also likely too high since it requires the entire galaxy to contain cold H I gas. Dickey et al. (2000) observed the Small Magellanic Cloud in 21 cm absorption and found that the mass fraction of cold H I to be less than 15% of the total H I content. It seems likely that the true value of the cold H I mass fractions of the low mass galaxies in our sample are between our lower limits and ∼15%.

Begum et al. (2010) observed 21-cm Milky Way absorption towards 12 background radio continuum sources. They were able to determine the flux contribution of the cold H I along many of these sight lines. They find that the cold H I contributes from a low of ∼2% to as high as ∼69%, of the total flux determined in the same manner, with a median of ∼30%. While a direct comparison between the optically thick cold H I observed by Begum et al. (2010) and our optically thin emission is not obvious, we would not expect the fraction of cold H I in emission to be drastically different. Our result of ∼20% is slightly lower than their median value, but does not appear to be at

odds with their result.

4.4.6 Cold H I Locations that Lack a Warm Component

As discussed in §4.3.1, some lines-of-sight were best fit by a single Gaussian profile with a velocity dispersion of less than 6 km s^{-1}. These best fit single Gaussian profiles were found in 6 of the 23 galaxies with cold H I detections. Most of these six galaxies have a large fraction of their H I at galactocentric radii beyond the ∼25 mag $arcsec^{-2}$ optical level, and the majority of these single Gaussian fits are also located at larger radii. Figure 4.11 shows the radial distribution of the cold H I locations that lack a warm component. The galaxies have been ordered from low (M81 Dwarf A) to high (NGC 247) absolute *B*-band luminosity. Two of these galaxies, M81 Dwarf A and Holmberg I, have large central holes in their H I distributions (see Warren et al. 2011 and references therein) where much of their gas is pushed beyond the optical radius. Only NGC 247 has a majority of these locations within the optical radius.

Figure 4.12 shows an example of the difference between those areas that contain a warm component and those that lack one for NGC 4214. The left panel shows only those locations that contain both a warm and cold H I component while the right panel also includes the locations that lack a warm component. The contours correspond to the 10^{20} and 10^{21} cm^{-2} total H I column densities and the blue circle approximates the 25 mag $arcsec^{-2}$ level (uncorrected for inclination and position angle). It is immediately apparent that the majority of the best fit single Gaussian profiles fall well beyond the bulk of the stellar population and far from any heat sources. Tamburro et al. (2009) provides evidence that the warm H I velocity dispersions inside the optical radius of disk galaxies is driven by stellar processes, while areas beyond the optical radius may be driven by thermal broadening and/or magneto-rotational instabilities. These authors also point out that the velocity dispersions decline as a function of radius, falling below the typical 10 km s^{-1} beyond the optical radius. We also see this declining trend in the velocity dispersion with radius (see Figure 4.8). These results are suggestive that cold H I can be the dominant constituent of the ISM only in the lower UV radiation field beyond the ∼25 mag $arcsec^{-2}$ optical level.

4.4.7 Comparing the Cold H I Gas Mass with Molecular Gas Masses and Star Formation Rates

We next compare the cold H I gas masses to the molecular gas masses and star formation rates (SFRs) in each galaxy. To make these comparisons we compute the SFRs and estimate the amount of molecular hydrogen each galaxy contains. The relationship between the SFR and molecular hydrogen is discussed in detail in §4.1. We used the SFRs given by both FUV and Hα luminosities to estimate the amount of molecular hydrogen.

Table 4.6 lists the SFRs derived from FUV and Hα luminosities taken from the literature for each galaxy with a detected cold H I signature. The columns are: (1) galaxy name, (2) mass of the cold H I (M_{coldHI}) computed using the lower limit mass fraction from Table 4.4 multiplied by the total H I mass given in Table 4.6, (3) apparent FUV magnitude (m_{FUV}; Lee et al. 2011), (4) the logarithm of the FUV luminosity (L_{FUV}), (5) the FUV SFR (SFR_{FUV}) computed using the relation given in Salim et al. (2007), (6) the H_2 gas mass ($M_{H_2}^{FUV}$) computed from SFR_{FUV} assuming a 100 Myr timescale and a star formation efficiency of 10% ($M_{H_2}^{FUV} = SFR_{FUV} \times 100$ Myr / 0.1), (7) the approximate fraction of the cold ISM attributed to the cold H I ($\mathcal{M}_{FUV}$) defined as $M_{coldHI}/(M_{coldHI} + M_{H_2}^{FUV})$, (8) the logarithm of the Hα luminosity ($L_{H\alpha}$; Kennicutt et al. 2008), (9) the SFR derived from $L_{H\alpha}$ using the relation in Kennicutt (1998a), (10) the H_2 gas mass ($M_{H_2}^{H\alpha}$) computed from $SFR_{H\alpha}$ assuming a 5 Myr timescale and a star formation efficiency of 10% ($M_{H_2}^{H\alpha} = SFR_{FUV} \times 5$ Myr / 0.1), and (11) the approximate fraction of the cold ISM attributed to the cold H I ($\mathcal{M}_{H\alpha}$) defined as $M_{coldHI}/(M_{coldHI} + M_{H_2}^{H\alpha})$. Using our lower limit mass fraction from the spectra above S/N of 10 and extrapolating it over the entire galaxy provides a lower limit to the total cold H I mass.

The expected relationship between the currently observed cold H I and the computed molecular gas masses is not immediately clear. The mass fractions of the cold ISM attributed to the cold H I is lower for H_2 masses computed from the longer timescale SFR_{FUV} (Table 4.6, column 7) than they are for those computed from $SFR_{H\alpha}$ (Table 4.6, column 11). The time scale to convert the cold H I into molecular hydrogen is likely dependent upon the metallicity of the environment (a longer time scale is expected for lower metallicities) and local UV radiation field (a shorter time scale is expected for lower UV radiation). Since dwarf galaxies have both low metallicities and different ranges of

UV radiation strengths, it is not obvious which molecular gas mass estimate provides the best comparison. Unfortunately, our current data do not allow us to investigate these timescales further.

The top and bottom panels of Figure 4.13 show plots of the SFR_{FUV} (filled circles) and $SFR_{H\alpha}$ (open squares) as a function of the cold H I mass and total H I mass, respectively. If the cold H I is related to the star formation in any direct way, we would expect to find a trend in this relation. Indeed, the higher the cold H I gas mass, the higher the SFR, although this same trend is seen with the total H I gas mass and may just be a consequence of the more H I gas available, the higher the SFR. The middle panel shows the SFR efficiency (SFE_{HI}) defined as the SFR divided by the total H I gas mass as a function of the cold H I gas mass. The SFE_{HI} is roughly constant over our range of cold H I masses. The differences between the derived FUV and Hα star formation rates has been previously reported in Lee et al. (2009) and is due at least in part to the fact that the SFRs are averaged over different timescales. Environmental conditions may also influence $SFR_{H\alpha}$ by leakage of the ionizing photons from the star forming regions (see Relano et al. 2012 for details).

We can compare our molecular gas mass estimates derived from the SFRs to a direct observational estimate of the molecular gas in NGC 4214 (Walter et al., 2001) to see if our values are reasonable. These authors observed CO emission in the inner $\sim 1\farcm6 \times 1\farcm6$ of the star forming disk of NGC 4214 (an area much smaller than the H I disk, see §4.4.6) and derived a molecular gas mass of 5.1×10^6 $M_\odot$. This value is similar to the molecular gas mass estimate we get from $SFR_{H\alpha}$ of 6.1×10^6 $M_\odot$. The molecular gas mass value computed by Walter et al. was based on an assumed CO to H_2 conversion factor (the so called 'X-factor') derived from observations of Galactic environments (i.e., high metallicity). Recent work on the X-factor has shown that the relation changes with decreasing mean visual extinction (e.g., Leroy et al. 2009; Glover & Mac Low 2011; Schruba et al. 2012). The lower metallicity environment of dIrr galaxies results in lower visual extinction values and thus a different X-factor value. Depending upon the true mean visual extinction value of NGC 4214, the actual molecular gas mass could be higher by a factor of a few to an order of magnitude or more. Schruba et al. (2012) derive an X-factor value roughly 40 times higher than the Galactic value for NGC 4214. Using this value, the Walter et al. (2001) molecular gas mass increases to $\sim 2 \times 10^8$ $M_\odot$,

closer to our derived H_2 mass using SFR_{FUV} of $1{\times}10^8$ $M_\odot$. Schruba et al. (2012) also derive a molecular gas mass of $\sim 2{\times}10^8$ $M_\odot$ for NGC 4214. The factor of 2 difference between the values most likely arise from our basic assumptions of a timescale of 100 Myr for the FUV emission and/or the star formation efficiency of 10%. Unfortunately, the lack of CO detections for the few galaxies in our sample that have been observed for CO prohibit us from repeating this exercise for other galaxies in our sample (e.g., Israel et al. 1995; Verter & Hodge 1995; Leroy et al. 2009; Schruba et al. 2012). Nevertheless, our estimates of molecular gas masses, although uncertain, are not unreasonable. Direct comparisons between the CO detections in NGC 4214 and our cold H I detections is the focus of future work.

4.5 Conclusions

We have observed line-of-sight H I emission spectra in 31 nearby, low metallicity dIrr galaxies in order to search for cold H I defined by a velocity dispersion of less than 6 km s^{-1}. We have detected it in 23 of 27 galaxies after quality control cuts were applied. The cold H I may be the future sites of molecular cloud and star formation and to date, are the only way to potentially trace star forming gas at low metallicity. Based upon our observations, we find:

- The cold H I gas is found in localized regions and usually at total H I column densities above the canonical threshold of star formation of 10^{21} cm^{-2} (Skillman et al., 1987). The cold H I in a given galaxy is also not typically associated with the very highest surface density gas (see Figures 4.4 & 4.6).
- The cold H I has a typical velocity dispersion of $\sim$4.5 km s^{-1} ($T \lesssim 800$ K).
- We derive an average value to the volume filling fraction of the cold H I of 9% (assuming our lower limit detections).
- We find lower limits to the cold H I gas mass fractions of a few percent, consistent with some models of the multi-phase ISM (McKee & Ostriker, 1977).
- The SFE_{HI} is roughly constant as a function of the total cold H I mass over the observed gas mass ranges.

- The cold H I contributes ∼20% of the line-of-sight flux in locations where we detect both a cold and warm component.
- Cold H I gas that lacks a warm component is typically found at radii larger than the 25 mag arcsec^{-2} optical radius.

Future work will investigate the relationship between the cold H I, local ISM conditions, and tracers of current star formation.

4.6 Figures

We thank the anonymous referee for their many thoughtful comments and insightful suggestions which greatly improved the quality of this work. Support for this work was provided by the National Science Foundation collaborative research grant 'Star Formation, Feedback, and the ISM: Time Resolved Constraints from a Large VLA Survey of Nearby Galaxies,' grant number AST-0807710. SRW is grateful for support from a Penrose Fellowship, a University of Minnesota Degree Dissertation Fellowship, and a NRAO Research Fellowship number 807515. NRAO is operated by Associated Universities, Inc., under cooperative agreement with the National Science Foundation. This research has made use of NASA's Astrophysics Data System Bibliographic Services and the NASA/IPAC Extragalactic Database (NED), which is operated by the Jet Propulsion Laboratory, California Institute of Technology, under contract with the National Aeronautics and Space Administration.

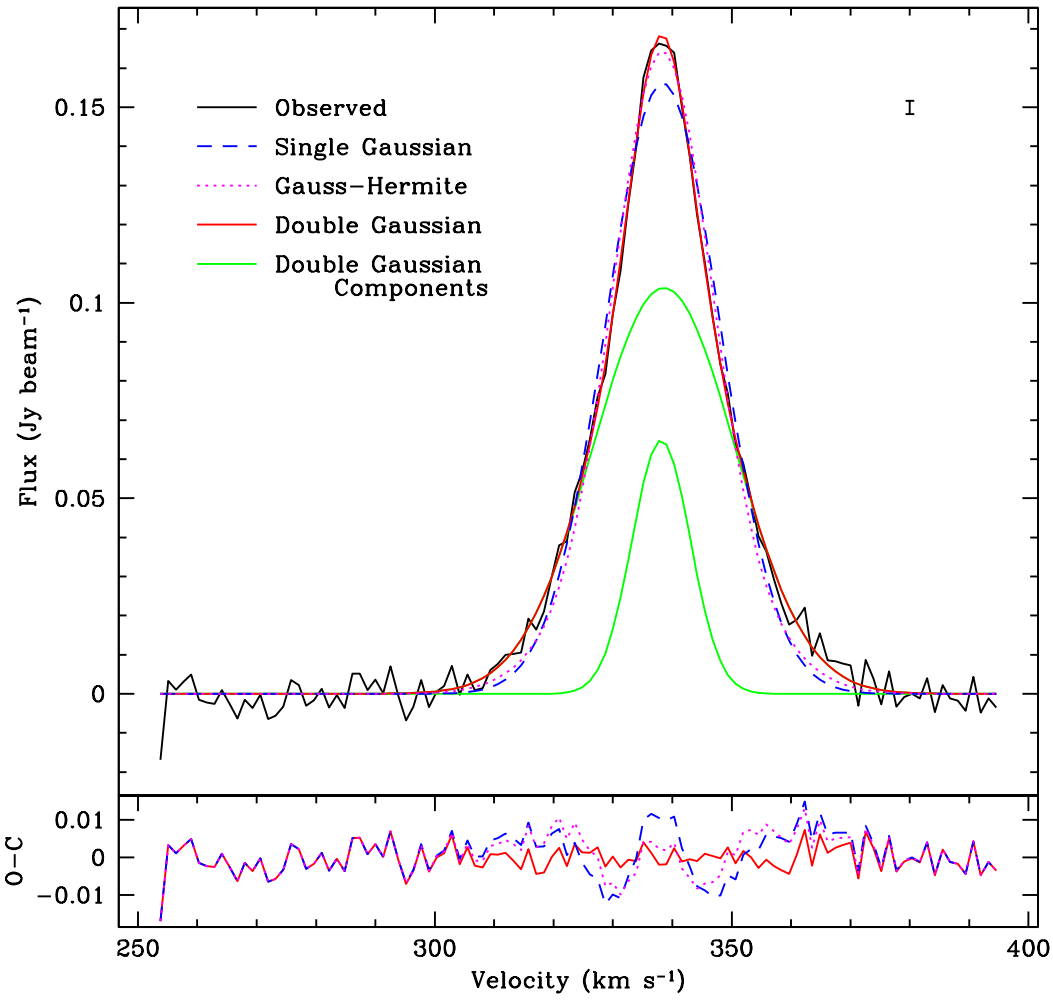

Figure 4.1 An example spectrum from Sextans A. The error on the points is shown in the upper right corner. This spectrum has a S/N of 37 and is clearly not fit well by a single Gaussian profile. The residuals to the fits are shown in the bottom panel. Both the double Gaussian profile and Gauss-Hermite polynomial statistically fit the observed spectrum better than the single Gaussian profile at the 99.9% confidence level in a single-tailed F-test.

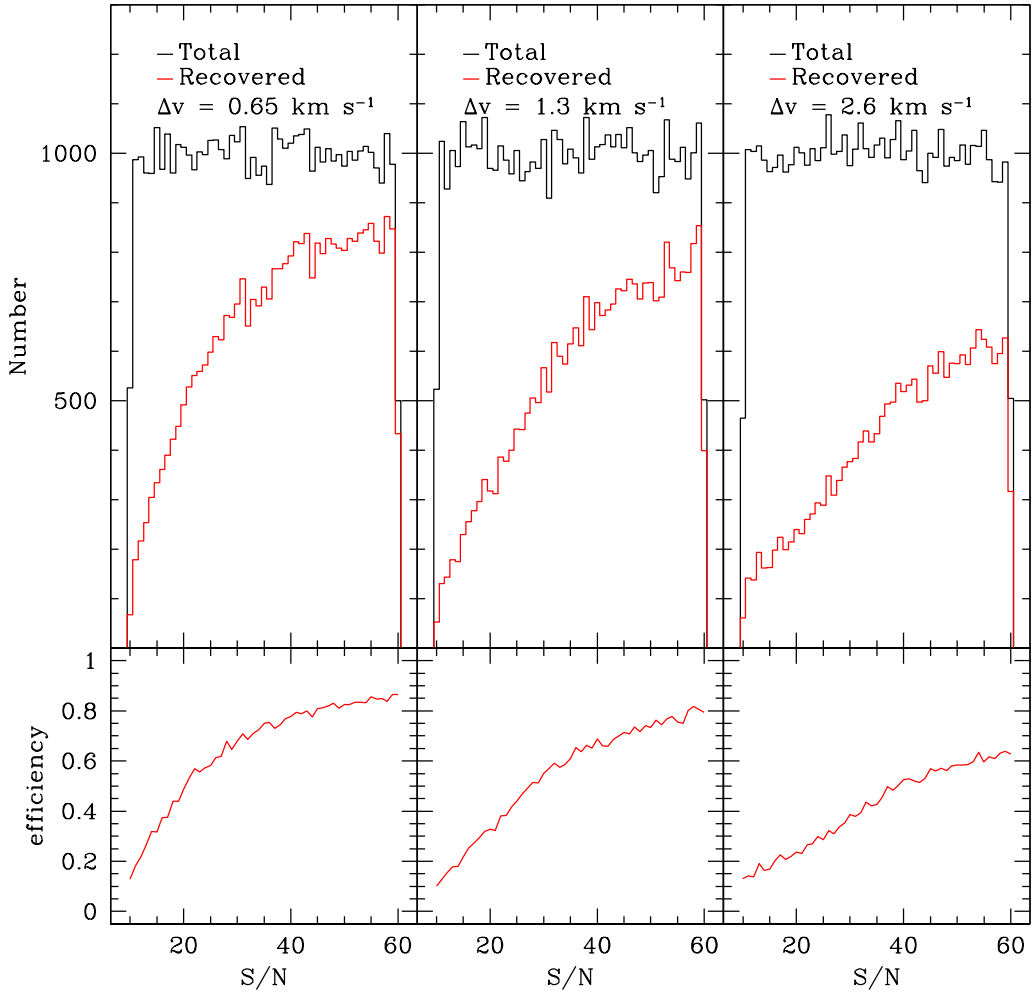

Figure 4.2 Results from the synthetic spectra containing two Gaussian components randomly generated and processed with our fitting routine. *Top Row:* The total sample (black) along with the recovered profiles (red; includes best-fit single Gaussian profiles with a velocity dispersion less than 6 km s^{-1} for the three different velocity resolutions (0.65, 1.3, and 2.6 km s^{-1}). *Bottom Row:* Our recovery efficiency versus S/N for the double Gaussian profiles.

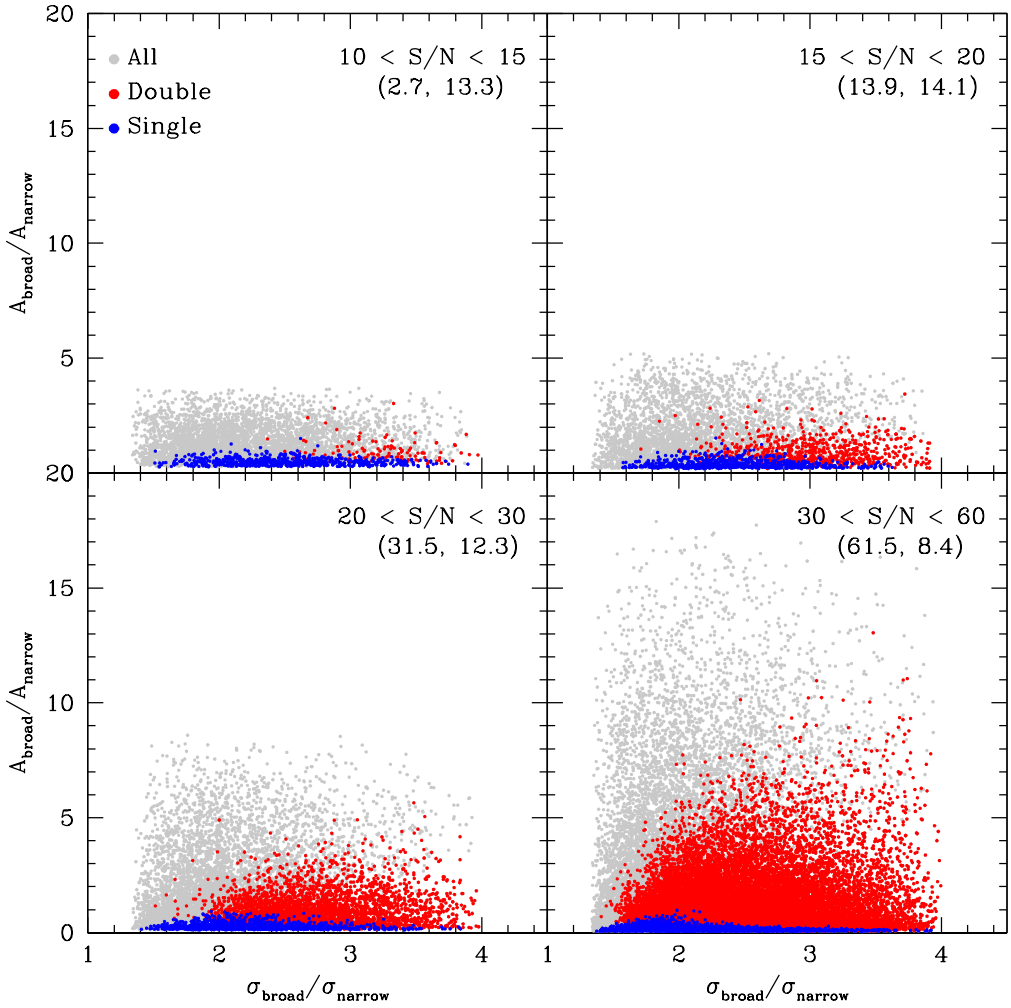

Figure 4.3 The ratio of the broad and narrow Gaussian amplitudes (A_{broad}/A_{narrow}) as a function of the ratio of the broad and narrow velocity dispersions ($\sigma_{broad}/\sigma_{narrow}$) for the 1.3 km s^{-1} velocity resolution simulation in four different S/N bins. The grey dots are all of the simulated spectra. The red dots are those spectra identified as containing two components by our fitting routines, and the blue dots are the simulated spectra that were identified only containing a single Gaussian component with a velocity dispersion of less than 6 km s^{-1}. The values in the parentheses are the recovery percentages for the best fit double (left) and single (right) Gaussians. We clearly identify more of the spectra at higher S/N values. Our routines have a harder time recovering the two Gaussian components when the velocity dispersions are similar.

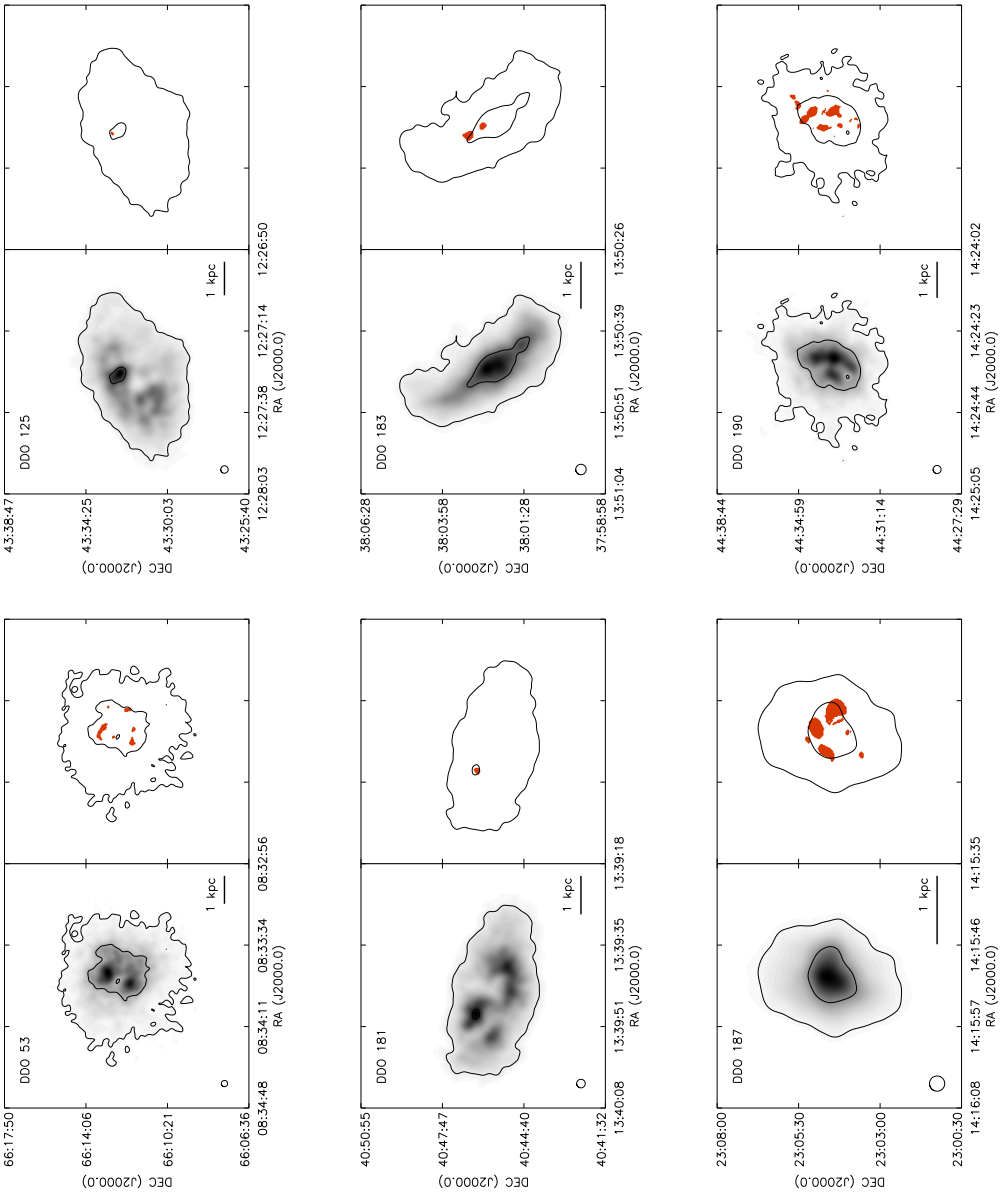

Figure 4.4 *Left:* The total H I integrated intensity map. *Right:* The cold H I locations best described by a double Gaussian (red) and single Gaussian (blue). The contours for all panels represent the 10^{20} and 10^{21} cm^{-2} column density levels. The scale bar at the bottom right denotes a linear size of 1 kpc. The 200 pc beam is shown at the lower left.

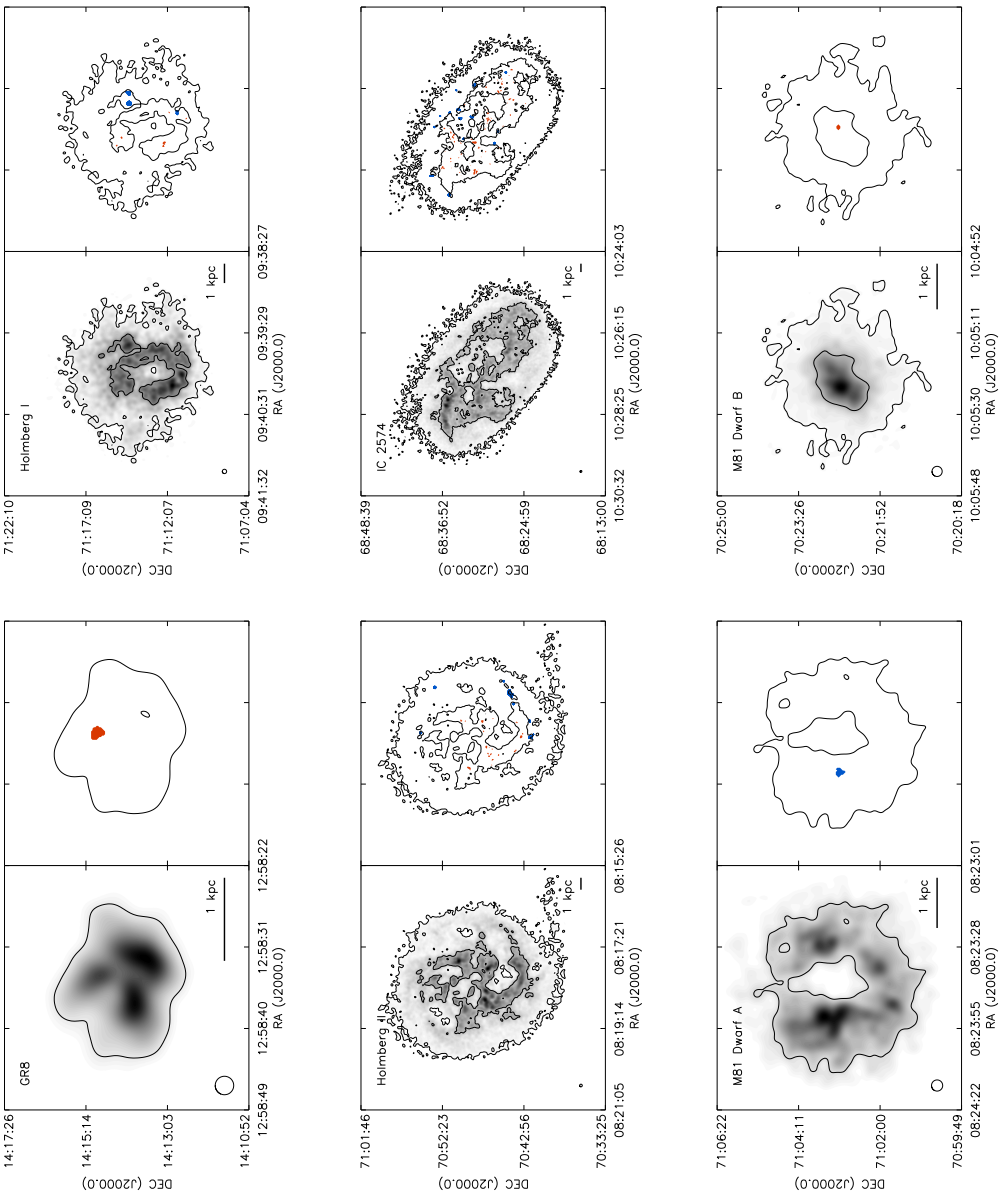

Figure 4.4 Continued...

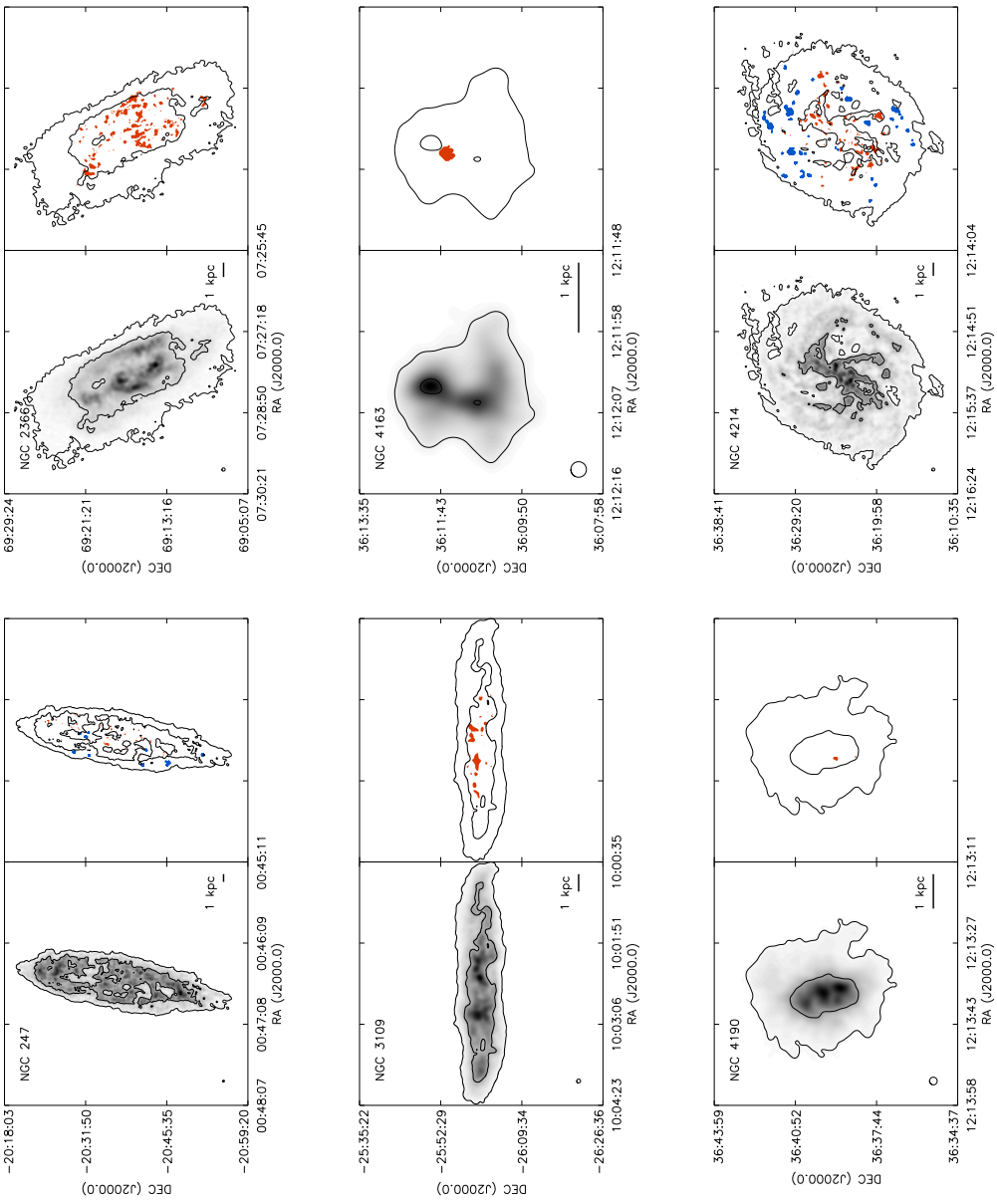

Figure 4.4 Continued...

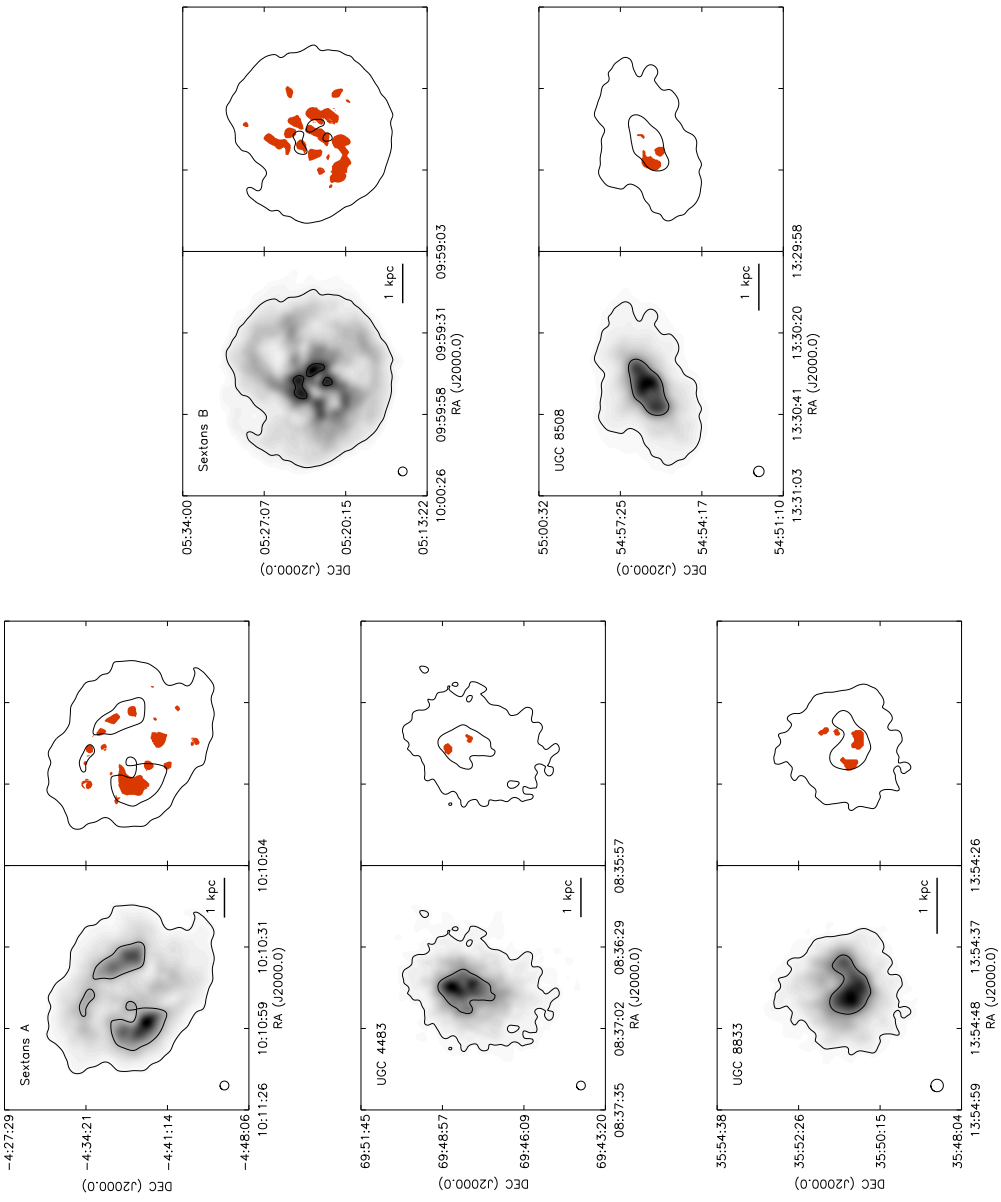

Figure 4.4 Continued...

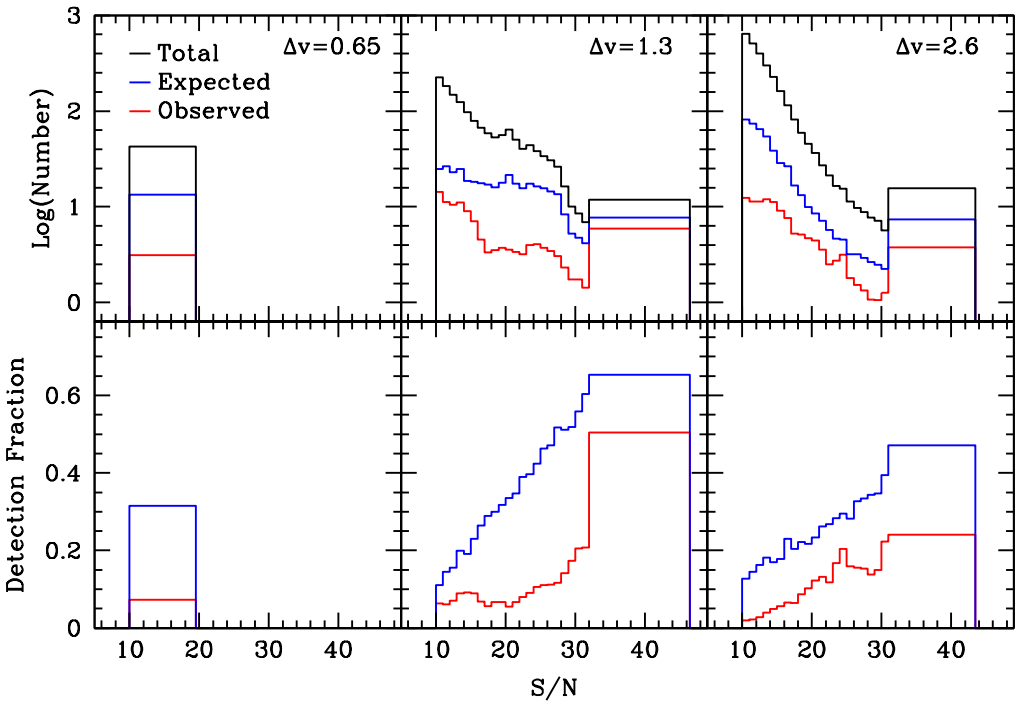

Figure 4.5 *Top:* Histograms of the total observed sample for all galaxies (black), the expected number of cold H I detections given our detection efficiency and assuming every line-of-sight contained multiple components (blue), and the actual number of cold H I detections (red) as a function of S/N for each velocity resolution. The histogram bins were chosen such that each contains at least one independent line-of-sight. The large gap between the blue and red histograms demonstrates the cold H I identified with this technique is not ubiquitous. *Bottom:* The detection fraction as a function of S/N.

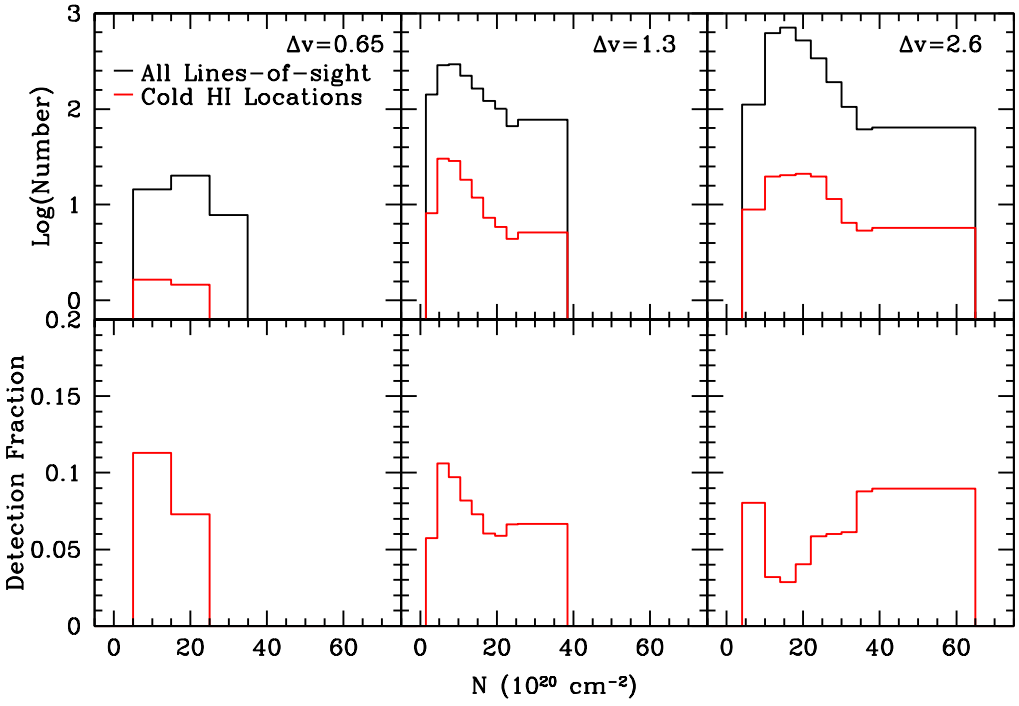

Figure 4.6 *Top:* Histograms of observed column densities of our entire sample (black) and where we find cold H I for each velocity resolution. *Bottom:* The detection fraction as a function of column density. Our detection fractions are relatively constant across all column densities observed.

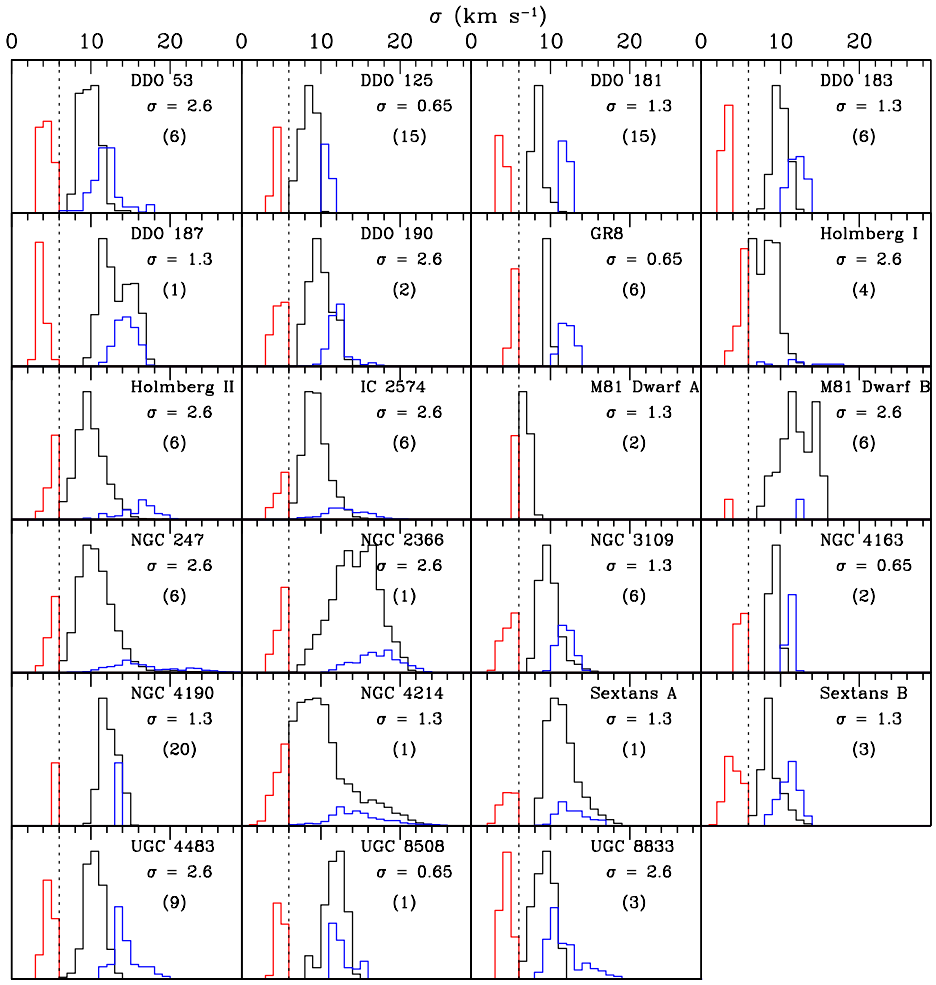

Figure 4.7 Histograms of the velocity dispersions of the best fit single Gaussian profiles (black), narrow component (red), and broad component (blue). The single Gaussian profile distributions have been scaled down by the number in the parentheses in order to discern the other two components. The dashed vertical line denotes our narrow-line cutoff of 6 km s^{-1}. The velocity resolution (σ) is listed below the galaxy names. Typically, the broad component velocity dispersions overlap with the single Gaussian profile velocity dispersions indicating they arise from the same gas phase.

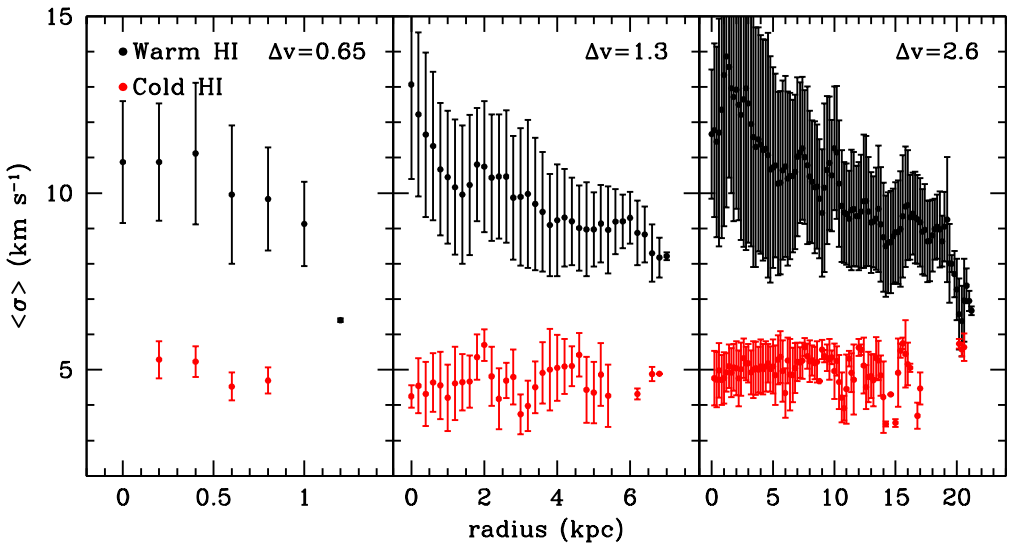

Figure 4.8 The average velocity dispersion, $<\sigma>$, as a function of radius for the warm (black) and cold (red) H I gas for each of our velocity resolutions. We have omitted the locations best fit by a single Gaussian with a velocity dispersion of less than 6 km s^{-1}. The averages are taken over 200 pc bins (the beam size). The error bars are the dispersions of the values in the bins. The velocity of the warm component decreases with radius indicating a possible decrease in turbulence as the radius increases from the main stellar body. Some of the errorbars at large radii for the 2.6 km s^{-1} velocity resolution overlap with values below our 6 km s^{-1} cutoff. This is due to the dispersions being affected by a few larger values in these bins.

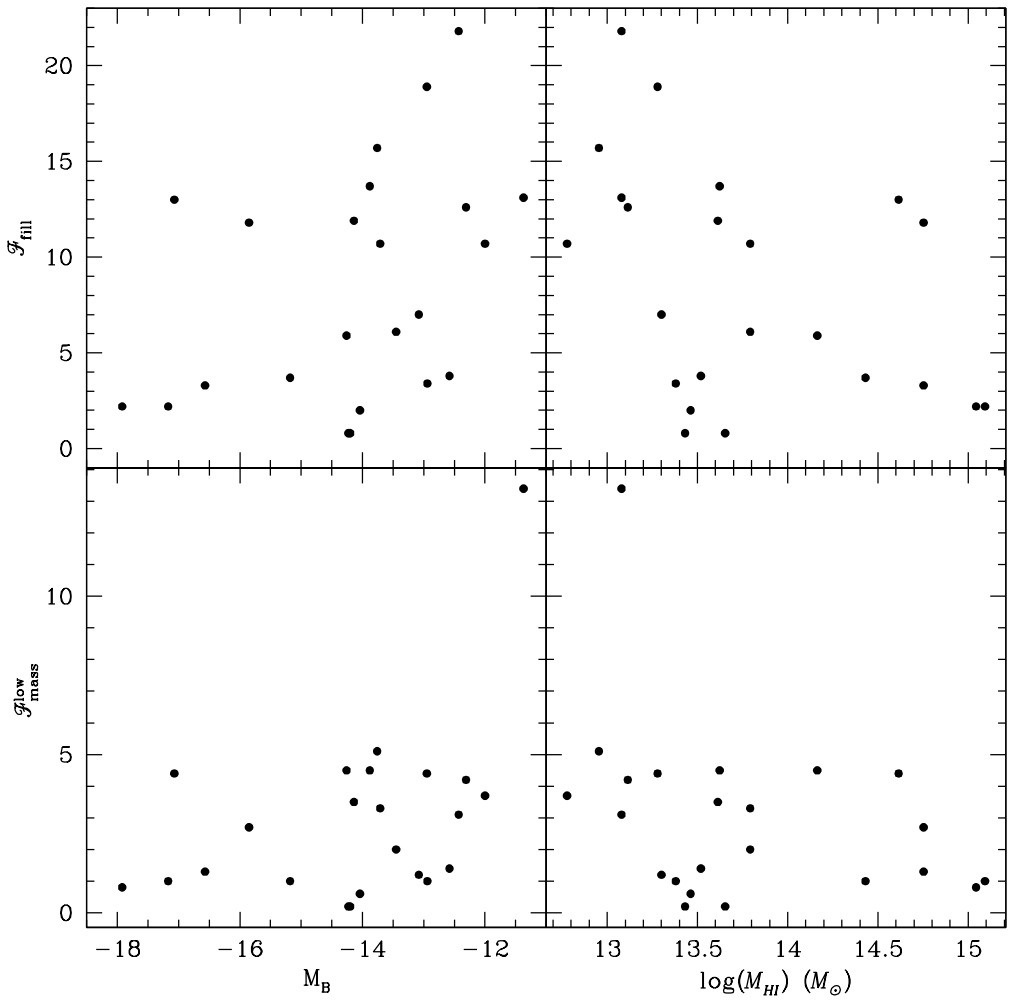

Figure 4.9 The areal fraction for the cold gas ($\mathcal{F}_{fill}$) and the lower limit to the fraction of H I gas in the cold phase ($\mathcal{F}^{low}_{mass}$) as a function M_B (left) and M_{HI} (right). The areal filling fraction and mass fractions do not correlate with M_B or M_{HI}.

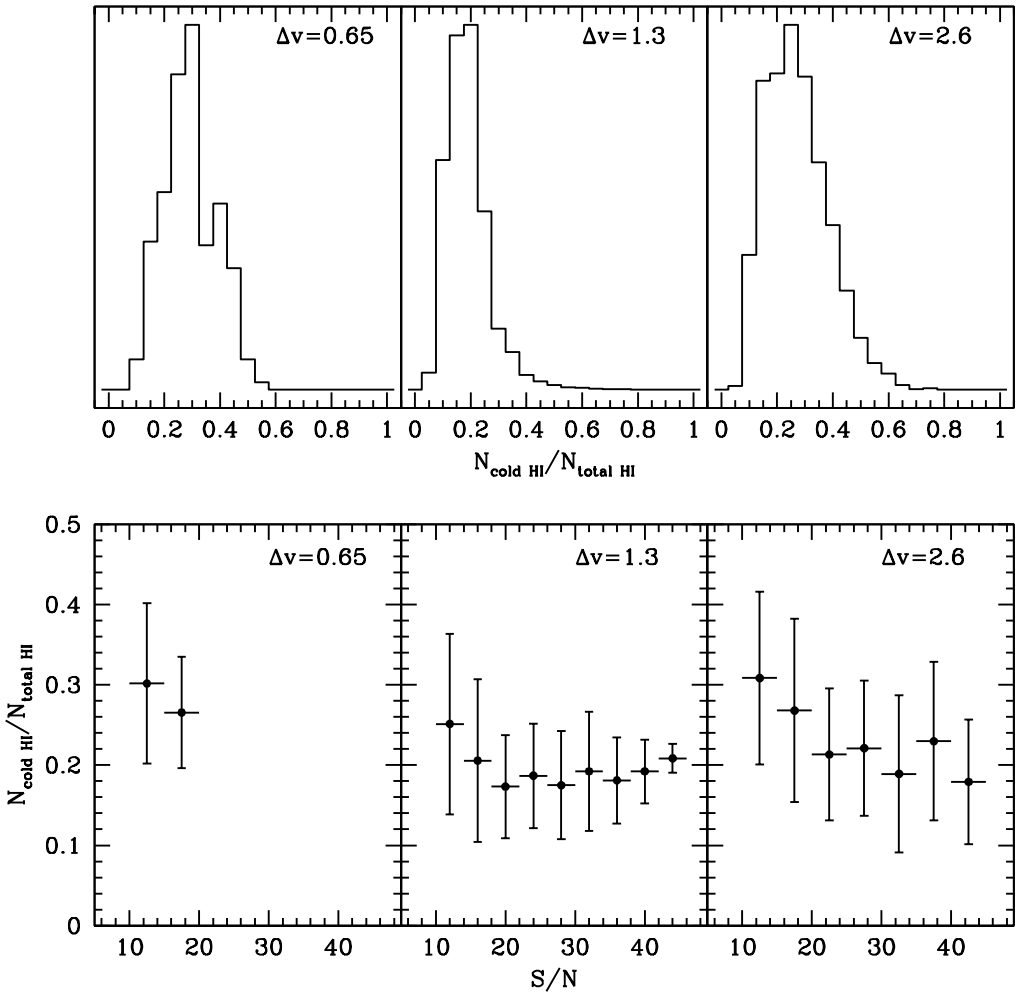

Figure 4.10 *Top:* Normalized histograms showing the contribution to the total line strength of the cold H I for each velocity resolution. *Bottom:* The average cold-to-total flux ratio as a function of S/N for each velocity resolution. The vertical error bars are the dispersions in the bins. The horizontal bar over each point shows the bin size from which the average was computed. For each panel we have omitted the locations where a single Gaussian profile with a velocity dispersion of less than 6 km s^{-1} best fit the data. The cold H I typically constitutes only 20% of the total line flux for locations which contain both cold and warm H I.

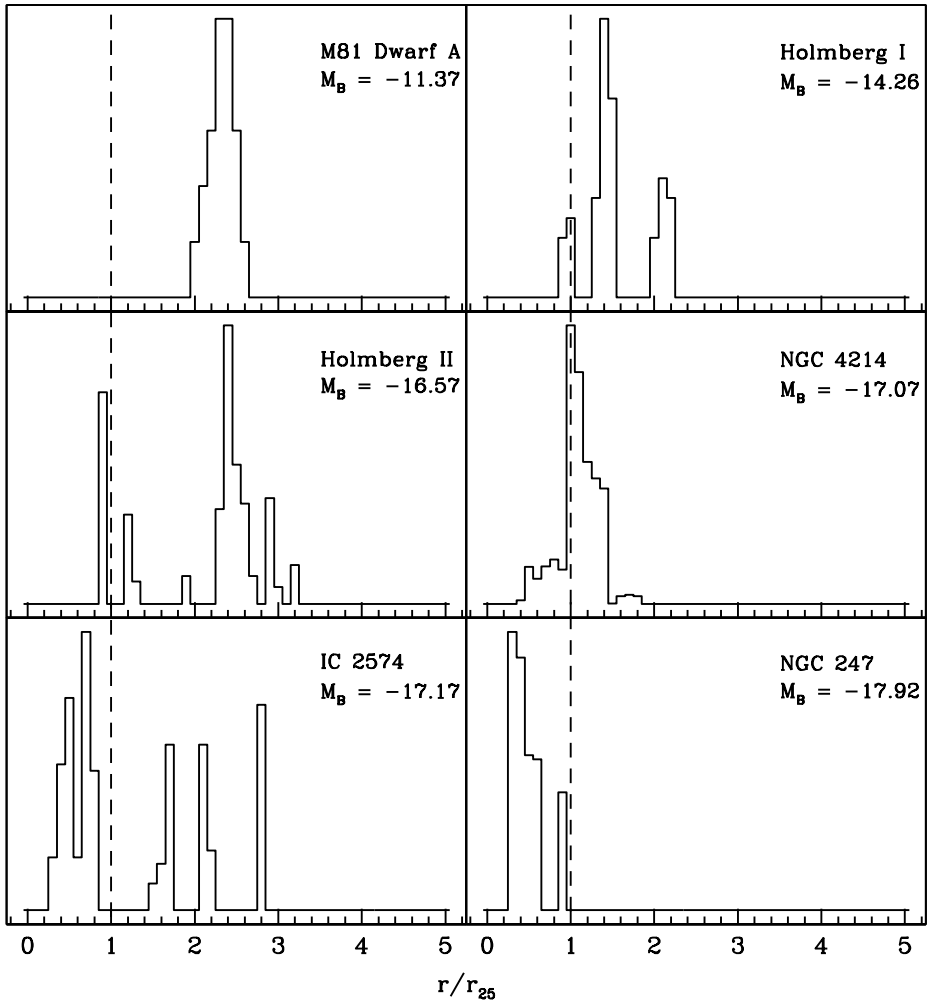

Figure 4.11 Radial distribution plots of the locations of the cold H I that lack a warm ($\sigma > 6$ km s^{-1}) component as a function of radius. The x-axis has been normalized by the 25 mag arcsec^{-2} radius (vertical dashed line). The galaxies have been ordered faint (M81 dwarf A) to bright (NGC 247) absolute B-band magnitude. A significant fraction of the cold H I is outside of the optical radius of each galaxy, except for NGC 247.

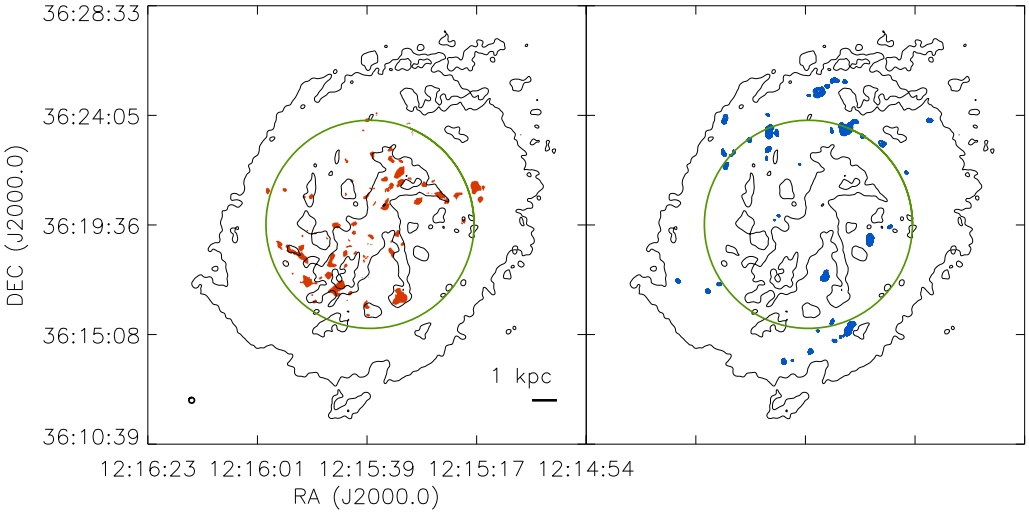

Figure 4.12 *Left:* The cold H I distribution (red) of NGC 4214 for those locations best fit by double Gaussians profiles only. *Right:* The cold H I distribution (blue) for those locations best fit by single Gaussian profiles with velocity dispersions less than 6 km s^{-1} only. The contours represent the 10^{20} and 10^{21} cm^{-2} total H I column densities. The green circle approximates the 25 mag $arcsec^{-2}$ optical level. The beam is shown at lower left. The majority of the cold H I detections described by a single Gaussian profile are outside of the bulk of the stellar distribution.

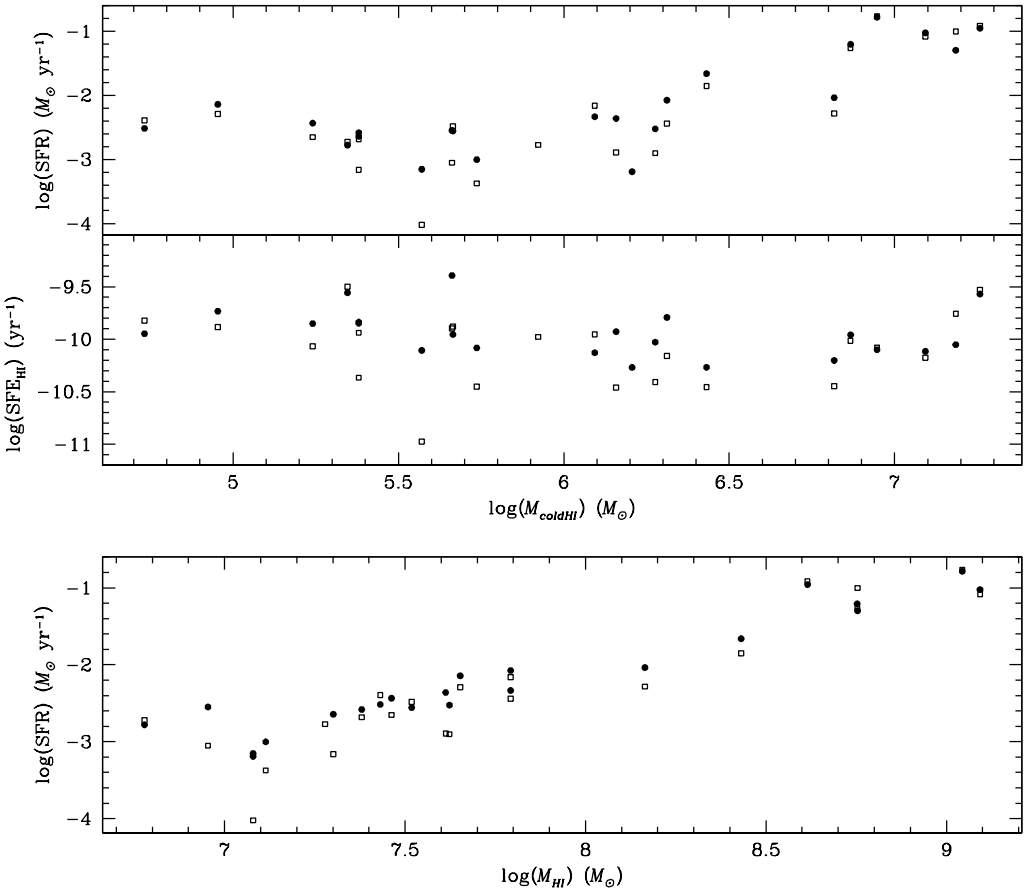

Figure 4.13 *Top:* SFR_{FUV} (filled circles) and $\mathrm{SFR}_{H\alpha}$ (open squares) as a function of the cold H I mass. *Middle:* The SFR efficiency (SFE_{HI}) defined as the SFR divided by the total H I gas mass as a function of the cold H I gas mass. *Bottom:* The SFR as a function of the total H I gas mass. The SFR shows a linear trend with both cold and total H I mass.

Table 4.1. Observed Galaxy Properties

1 Galaxy	2 RA (J2000.0)	3 DEC (J2000.0)	4 D[a] (Mpc)	5 $M_{\rm HI}$ (10^7 $M_\odot$)	6 M_B	7 a^b ($'$)	8 i[b] (deg)	9 Beam Size ($''$)	10 Δ V (km s^{-1})	11 rms$_{noise}$ (mJy beam^{-1})
DDO 53	$08^h34^m07\overset{s}{.}2$	$+66°10'54''$	3.61	6.2	-13.45	1.6	30	11.43	2.6	0.8
DDO 82	$10^h30^m35\overset{s}{.}0$	$+70°37'10''$	3.80	0.3	-14.44	3.4	55	10.86	1.3	1.7
DDO 99	$11^h50^m53\overset{s}{.}0$	$+38°52'50''$	2.59	4.7	-13.37	4.1	71	15.93	1.3	2.0
DDO 125	$12^h27^m41\overset{s}{.}8$	$+43°29'38''$	2.58	2.9	-14.04	4.3	58	15.99	0.65	3.0
DDO 181	$13^h39^m53\overset{s}{.}8$	$+40°44'21''$	3.14	2.4	-12.94	2.3	57	13.14	1.3	1.6
DDO 183	$13^h50^m51\overset{s}{.}1$	$+38°01'16''$	3.22	2.0	-13.08	2.2	75	12.81	1.3	1.5
DDO 187	$14^h15^m56\overset{s}{.}5$	$+23°03'19''$	2.21	1.2	-12.43	1.7	42	18.67	1.3	2.1
DDO 190	$14^h24^m43\overset{s}{.}5$	$+44°31'33''$	2.79	4.1	-14.14	1.8	28	14.78	2.6	0.7
GR8	$12^h58^m40\overset{s}{.}4$	$+14°13'03''$	2.08	0.6	-12.00	1.1	25	19.83	0.65	4.4
Holmberg I	$09^h40^m32\overset{s}{.}3$	$+71°10'56''$	3.90	14.6	-14.26	3.6	37	10.58	2.6	1.2
Holmberg II	$08^h19^m05\overset{s}{.}0$	$+70°43'12''$	3.38	56.6	-16.57	7.9	31	12.20	2.6	1.5
IC 2574	$10^h28^m27\overset{s}{.}7$	$+68°24'59''$	3.80	123.9	-17.17	13.2	68	10.86	2.6	0.9
KDG 73	$10^h52^m55\overset{s}{.}3$	$+69°32'45''$	4.03	0.05	-10.75	0.6	35	10.24	0.65	2.0
KK 230	$14^h07^m10\overset{s}{.}7$	$+35°03'37''$	1.97	0.07	-8.49	0.6	35	20.94	0.65	3.8
KKH 98	$23^h45^m34\overset{s}{.}0$	$+38°43'04''$	2.54	0.3	-10.29	1.1	58	16.24	0.65	2.8
M81 Dwarf A	$08^h23^m55\overset{s}{.}1$	$+71°01'56''$	3.44	1.2	-11.37	1.3	24	11.99	1.3	0.9
M81 Dwarf B	$10^h05^m30\overset{s}{.}6$	$+70°21'52''$	5.3[b]	2.7	-14.23	0.9	49	7.78	2.6	0.6
MCG09-20-131	$12^h15^m46\overset{s}{.}7$	$+52°23'15''$	1.6[c]	1.2	-12.36	1.2	77	25.78	1.3	3.3
NGC 247	$00^h47^m08\overset{s}{.}3$	$-20°45'36''$	3.52	110.6	-17.92	21.4	72	11.72	2.6	1.3
NGC 2366	$07^h28^m53\overset{s}{.}4$	$+69°12'51''$	3.21	56.7	-15.85	7.3	72	12.85	2.6	1.0
NGC 3109	$10^h03^m07\overset{s}{.}2$	$-26°09'36''$	1.27	27.0	-15.18	19.7	86	32.48	1.3	8.5
NGC 3741	$11^h36^m06\overset{s}{.}4$	$+45°17'07''$	3.24	8.1	-13.01	2.0	58	12.73	1.3	2.1
NGC 4163	$12^h12^m08\overset{s}{.}9$	$+36°10'10''$	2.87	0.9	-13.76	1.9	34	14.37	0.65	2.2
NGC 4190	$12^h13^m44\overset{s}{.}6$	$+36°38'00''$	3.5[b]	4.5	-14.20	1.7	29	11.79	1.3	1.5
NGC 4214	$12^h15^m39\overset{s}{.}2$	$+36°19'37''$	3.04	41.2	-17.07	8.5	40	13.57	1.3	1.1

Table 4.1 (cont'd)

1 Galaxy	2 RA (J2000.0)	3 DEC (J2000.0)	4 D[a] (Mpc)	5 $M_{\rm HI}$ (10^7 $M_\odot$)	6 M_B	7 a^b ($'$)	8 i[b] (deg)	9 Beam Size ($''$)	10 Δ V (km s^{-1})	11 rms$_{noise}$ (mJy beam^{-1})
Sextans A	$10^h11^m00\overset{s}{.}8$	$-04°41'34''$	1.38	6.2	-13.71	5.9	35	29.89	1.3	4.5
Sextans B	$10^h00^m00\overset{s}{.}1$	$+05°19'56''$	1.39	4.2	-13.88	5.1	48	29.68	1.3	2.0
UGCA 292	$12^h38^m40\overset{s}{.}0$	$+32°46'00''$	3.62	4.0	-11.36	1.0	47	11.40	0.65	2.1
UGC 4483	$08^h37^m03\overset{s}{.}0$	$+69°32'45''$	3.41	3.3	-12.58	1.2	56	12.10	2.6	0.8
UGC 8508	$13^h30^m44\overset{s}{.}4$	$+54°54'36''$	2.58	1.9	-12.95	1.7	55	15.99	0.65	2.3
UGC 8833	$13^h54^m48\overset{s}{.}7$	$+35°50'15''$	3.08	1.3	-12.31	0.9	28	13.39	2.6	0.6

[a]Dalcanton et al. (2009)

[b]Karachentsev et al. (2004)

[c]MCG09-20-131 may have a greater distance than indicated due to ambiguities in measuring the TRGB.

Table 4.2 Simulated Spectra Results

1	2	3	4	5	6	7
Velocity Resolution	$A_{b,sim}/A_{b,extr}$	Δv_{broad} (km/s)	$\Delta\sigma_{broad}$ (km/s)	$A_{n,sim}/A_{n,extr}$	Δv_{nar} (km/s)	$\Delta\sigma_{nar}$ (km/s)
0.65	1.0±0.1	0.0±0.3	0.0±0.6	1.0±0.1	0.0±0.2	0.0±0.3
1.30	1.0±0.2	0.0±0.5	0.0±0.7	1.0±0.1	0.1±0.2	0.1±0.3
2.60	1.0±0.2	-0.2±0.8	0.0±0.9	1.0±0.1	0.5±0.4	0.1±0.5

Table 4.3 Individual Galaxy Properties

1 Galaxy	2 N_t	3 $<S/N>_t$	4 $N_{HI,min}$ (10^{19} cm^{-2})	5 $N_{HI,peak}$ (10^{21} cm^{-2})	6 $<N_{HI}>$ (10^{20} cm^{-2})
DDO 53	48	14.8	6.76	3.19	16.0
DDO 82	0	···	19.20	···	···
DDO 99	19	12.7	14.28	2.38	13.0
DDO 125	6	10.8	14.07	1.62	11.3
DDO 181	9	11.2	13.69	1.53	11.3
DDO 183	11	11.9	11.78	1.97	14.1
DDO 187	13	14.8	7.78	2.59	14.0
DDO 190	46	20.6	3.86	3.55	15.8
GR8	3	10.7	12.97	1.06	9.23
Holmberg I	24	11.1	11.84	2.47	16.6
Holmberg II	207	12.0	11.11	3.82	18.1
IC 2574	1026	13.1	8.43	4.83	15.8
KDG 73	0	···	27.69	···	···
KK 230	0	···	10.77	···	···
KKH 98	0	···	15.55	···	···
M81 Dwarf A	3	10.7	6.91	0.64	5.67
M81 Dwarf B	9	11.8	10.93	3.53	22.9
MCG09-20-131	3	14.0	7.16	1.97	12.7
NGC 247	848	12.9	15.10	5.24	22.6
NGC 2366	511	16.2	6.54	6.83	21.0
NGC 3109	404	17.6	10.49	3.83	13.0
NGC 3741	9	11.0	17.62	3.07	22.0
NGC 4163	4	11.1	13.89	1.48	11.1
NGC 4190	20	12.0	14.63	3.32	22.6
NGC 4214	488	12.6	6.60	3.26	10.5
Sextans A	133	16.5	6.53	4.02	10.2
Sextans B	173	17.0	2.65	1.41	4.40
UGCA 292	20	12.0	24.97	3.55	23.6
UGC 4483	28	14.9	7.53	2.92	15.1
UGC 8508	12	13.1	11.42	2.47	16.8
UGC 8833	16	16.6	4.38	2.21	12.0

Table 4.4 Individual Galaxy Results

1 Galaxy	2 $<S/N>_c$	3 $\mathcal{F}_{fill}$ (%)	4 $\mathcal{F}^{low}_{mass}$ (%)	5 $\mathcal{F}^{up}_{mass}$ (%)	6 $<\sigma_n>$ (km s^{-1})	7 $<\sigma_b>$ (km s^{-1})	8 $<\sigma_s>$ (km s^{-1})
DDO 53	18.6	6.1	2.0	15.9	4.36	11.92	9.83
DDO 99	···	···	···	38.3	···	···	8.94
DDO 125	11.2	2.0	0.6	43.3	4.34	10.75	8.38
DDO 181	13.6	3.4	1.0	42.1	3.74	11.89	8.43
DDO 183	12.7	7.0	1.2	28.3	3.12	12.11	10.02
DDO 187	17.1	21.8	3.1	18.2	3.79	14.44	13.31
DDO 190	28.1	11.9	3.5	11.1	4.74	12.17	9.95
GR8	10.4	10.7	3.7	47.5	5.30	12.12	9.62
Holmberg I	11.8	5.9	4.5	30.0	5.20	12.60	8.27
Holmberg II	12.1	3.3	1.3	22.2	5.19	16.00	10.02
IC 2574	14.5	2.2	1.0	19.2	4.97	13.12	9.47
M81 Dwarf A	10.5	13.1	13.4	50.2	5.86	···	6.88
M81 Dwarf B	11.1	0.8	0.2	25.0	3.77	12.15	12.14
MCG09-20-131	···	···	···	3.6	···	···	11.99
NGC 247	12.5	2.2	0.8	23.7	5.15	17.10	10.81
NGC 2366	18.5	11.8	2.7	12.5	5.02	17.31	14.42
NGC 3109	23.6	3.7	1.0	28.2	4.69	11.88	9.85
NGC 3741	···	···	···	27.9	···	···	10.61
NGC 4163	11.4	15.7	5.1	41.8	5.12	11.27	9.27
NGC 4190	12.8	0.8	0.2	21.9	5.60	13.91	12.30
NGC 4214	13.0	13.0	4.4	23.5	4.77	14.90	10.72
Sextans A	25.0	10.7	3.3	23.2	4.60	12.71	11.52
Sextans B	25.1	13.7	4.5	22.8	4.10	11.13	8.89
UGCA 292	···	···	···	36.8	···	···	10.11
UGC 4483	20.7	3.8	1.4	18.2	4.77	14.30	10.43
UGC 8508	14.6	18.9	4.4	23.7	4.87	12.74	11.75
UGC 8833	21.6	12.6	4.2	14.2	4.39	11.75	9.12

Table 4.5. Star Formation Rates and Molecular Gas Masses

1 Galaxy	2 M_{coldHI} (10^5 $M_\odot$)	3 m_{FUV}[a] (mag)	4 $\log(L_{FUV})$ (erg/s/Hz)	5 SFR_{FUV} (10^{-3} $M_\odot$/yr)	6 $M_{H_2}^{FUV}$ (10^6 $M_\odot$)	7 $\mathcal{M}_{FUV}$	8 $\log(L_{H\alpha})$[b] (erg/s)	9 $SFR_{H\alpha}$ (10^{-3} $M_\odot$/yr)	10 $M_{H_2}^{H\alpha}$ (10^5 $M_\odot$)	11 $\mathcal{M}_{H\alpha}$
DDO 53	12.4	15.32	25.63	4.60	4.60	0.21	38.94	6.88	3.44	0.78
DDO 125	1.74	14.84	25.53	3.70	3.70	0.05	38.45	2.23	1.11	0.61
DDO 181	2.40	15.63	25.39	2.62	2.62	0.08	38.42	2.08	1.04	0.70
DDO 183	2.40	15.84	25.32	2.28	2.28	0.10	37.94	0.69	0.34	0.87
DDO 187	3.72	16.3	24.81	0.70	0.70	0.35	37.08	0.10	0.05	0.99
DDO 190	14.4	14.82	25.61	4.36	4.36	0.25	38.21	1.28	0.64	0.96
GR8	2.22	15.23	25.19	1.66	1.66	0.12	38.38	1.90	0.95	0.70
Holmberg I	65.7	14.74	25.93	9.18	9.18	0.42	38.82	5.22	2.61	0.96
Holmberg II	73.6	12.35	26.76	62.3	62.3	0.11	39.84	54.7	27.1	0.73
IC 2574	123.9	12.15	26.94	94.8	94.8	0.12	40.02	82.7	41.4	0.75
M81 Dwarf A	16.1	17.35	24.78	0.65	0.65	0.71	...	...	...	...
M81 Dwarf B	0.54	16.6	25.45	3.05	3.05	0.02	38.71	4.05	2.03	0.21
NGC 247	88.5	11.38	27.18	164.6	164.6	0.05	40.34	172.8	86.4	0.51
NGC 2366	153.1	12.47	26.67	50.3	50.3	0.23	40.1	99.5	49.7	0.75
NGC 3109	27.0	11.37	26.30	21.8	21.8	0.11	39.25	14.0	7.02	0.79
NGC 4163	4.59	15.35	25.42	2.84	2.84	0.14	38.05	0.89	0.44	0.91
NGC 4190	0.90	14.77	25.82	7.20	7.20	0.01	38.81	5.10	2.55	0.26
NGC 4214	181.3	11.5	27.01	110.7	110.7	0.14	40.19	122.4	61.2	0.75
Sextans A	20.5	12.58	25.89	8.41	8.41	0.20	38.66	3.61	1.81	0.92
Sextans B	18.9	13.72	25.44	2.99	2.99	0.39	38.2	1.25	0.63	0.97
UGC 4483	4.62	15.75	25.41	2.77	2.77	0.14	38.62	3.29	1.65	0.74
UGC 8508	8.36	...	...	...	...	...	38.33	1.69	0.85	0.91
UGC 8833	5.46	16.64	24.96	0.99	0.99	0.35	37.73	0.42	0.21	0.96

[a]Lee et al. (2011)

[b]Kennicutt et al. (2008)

Chapter 5

Direct H_2 Detections in the Low-Metallicity Galaxy NGC 4214[1]

To be submitted to the The Astrophysical Journal with the following bibliographic reference: Warren, S. R., Cannon, J., Skillman, E. D., et al.

We present Spitzer infrared spectrograph (IRS) observations of the nearby, low-metallicity galaxy, NGC 4214. We use the Short-High and Long-High modules to observe the 0-0 S(0), S(1), and S(2) (λ_{rest} = 28.221, 17.035, and 12.279 μm, respectively) pure rotational lines of molecular hydrogen (H_2) directed towards the known carbon-monoxide (CO) peaks. We detect the S(1) and S(2) H_2 lines at every observed location and we provide flux estimates for each transition. The S(0) line is undetected along each line-of-sight and we provide upper limits to the flux. We estimate a temperature for the ortho-to-para transitional pair S(1) - S(2) at each location of a few hundred K, which is similar to values described in the literature. The warm H_2 constitutes only a few times 10^{-5} of the total H_2 mass estimated from CO observations at each location given reasonable values of the α_{CO}. This

This work is based upon observations made with the *Spitzer Space Telescope*, which is operated by the Jet Propulsion Laboratory, California Institute of Technology, under contract with NASA.

suggests that the vast majority of the H_2 is well below our derived excitation temperatures. The strong S(1) and S(2) line detections and spatial coincidence with the known CO peaks in a low-metallicity galaxy make these transitions useful tracers of molecular gas locations in systems where CO is currently undetectable.

5.1 Introduction

Star formation is dependent upon the formation and shielding of molecular hydrogen (H_2) in dense gas regions of the interstellar medium (ISM). Both theoretical (e.g., Glover et al. 2010; Ostriker et al. 2010; Krumholz et al. 2011 and references within) and observational studies (e.g., Bigiel et al. 2008; Leroy et al. 2008; Bolatto et al. 2011 and references within) seem to confirm this hypothesis. Therefore, understanding the gas conditions where H_2 exists helps us to understand how star formation proceeds.

Typically, the observed luminosity of the carbon monoxide (CO) molecule is used as a proxy for the H_2 mass. The CO molecule is used for three main reasons: 1) the low-excitation states of the H_2 molecule are not easily observable from ground based observatories, 2) the CO molecule is typically the brightest molecular line in the dense ISM, and 3) the sizes of the CO emitting clouds have been shown to span the bulk of the dense H_2 regions of high metallicity gas (like that of the Milky Way) (references). However, recent studies have shown that the very nature of the ISM changes as the metallicity decreases to abundances significantly lower than Solar (e.g., Maloney & Black 1988). Mainly, as the metallicity decreases, the CO emitting regions become increasingly susceptible to photo-dissociation, reducing the sizes of the CO cores (see Bolatto et al. 2011 and references therein for more details). Therefore, once the metallicity dips below a certain value, CO is expected to disappear entirely or at least below currently detectable surface brightness levels. This observational limit occurs for metallicities below 12+Log[O/H] $\approx$ 8.0 (Taylor et al., 1998).

Low-metallicity dwarf irregular galaxies rich in atomic hydrogen are observed to be currently forming stars (Weisz et al., 2011) and sometimes even at very high rates (McQuinn et al., 2010). The vast majority of the these galaxies, however, either lack CO observations or are CO non-detections. Thus it is assumed that these galaxies are

rich in CO-dark H_2. This transitionary regime between CO-dark and CO-bright H_2 is not fully understood. An open question is to what extent do the CO clouds in a low-metallicity environment trace the H_2, if at all.

We aim to test the idea that the CO and H_2 co-exist in the ISM of a low-metallicity galaxy. We present results of a Spitzer infrared spectrograph (IRS) survey of the CO clouds in the low-metallicity (12+Log[O/H] = 8.25; Moustakas et al. 2010) galaxy NGC 4214 in search of the S(0), S(1) and S(2) pure rotational lines of the H_2 molecule. NGC 4214 is one of the few dwarf galaxies with detected CO emission (Walter et al. 2001; Leroy et al. 2009; Schruba et al. 2012). This unique characteristic combined with the close distance to NGC 4214 (D = 3.04 Mpc; Dalcanton et al. 2009) not only provides targets for H_2 observations, it also presents an opportunity to study the characteristics of the poorly understood ISM in a low-metallicity system in great detail. Our observational strategy and data reduction are presented in §5.2. Measurements of the H_2 rotational lines are discussed in §5.3 and we estimate properties of the H_2 gas in §5.4. We conclude our findings in §5.5.

5.2 Observations and Data Reduction

Observations were carried out under Program ID 3177 by Spitzer's IRS instrument (Houck et al., 2004) between 23 May - 06 June 2005. The Long-High (LH) and Short-High (SH) modules in spectral mapping mode were used to trace the S(0) (λ_{rest}=28.221 μm), S(1) (λ_{rest}=17.035 μm), and S(2) (λ_{rest}=12.279 μm) low-energy pure rotational lines of H_2. The high resolution ($\Delta\lambda/\lambda \approx 600$) SH and LH modules are sensitive to wavelengths between 9.9 - 19.6 μm and 19.1 - 37.2 μm, respectively. The observations were designed to obtain a 3σ detection of a H_2 cloud with a column density of 10^{20} cm^{-2} at an assumed temperature of 150 K.

Table 5.6 lists our observational parameters. The columns list 1) the Spitzer AOR file name, 2) the module used, 3) our adopted label name, 4 & 5) the Right ascention and Declination, 6) the starting date of the observations, 7 & 8) the starting and ending times of the observations, and 9) the total time on source. Figure 5.1 displays our slit positions overlayed on the Heracles integrated CO intensity map (Leroy et al., 2009). The SH observations are denoted by the red boxes, the LH by the blue boxes, and the

portions of the LH observations used in the comparisons with the SH coverages (see §5.3) are the green boxes. The green boxes do not match exactly with the SH red boxes due to the larger pixel sampling of the LH module. Our reference naming convention (R1-R4) is also displayed.

Initial data processing was performed with the Spitzer Science Center pipeline version S18.18. The spectra were then further reduced and calibrated using the CUbe Builder for IRS Spectra Maps (CUBISM; Smith et al. 2007). CUBISM takes the raw, basic calibrated data (BCD) spectral images as initial input. Bad spectral pixels are automatically detected and removed using a sigma-clipping method. While CUBISM has the ability to utilize background spectra to subtract from the source spectra, our observations lacked a dedicated background observation. This lack of a background observation limits our ability to compute absolute fluxes of the targeted lines, however, ratios between the lines do provide valuable insight into the ISM physics (see §5.4).

5.3 H_2 Line Detections and Measurements

Each of the observed regions show evidence of H_2. The S(1) and S(2) lines are both detected in each region with high confidence. The S(0) lines were not detected in any location. In order to compute the integrated line fluxes, the observed S(1) and S(2) lines were fitted with a Gaussian plus linear function. The linear function estimates the baseline level of the psuedo-continuum on either side of each line. The fitting was perform using the Peak Analysis (PAN) software available for use with the Interactive Data Language (IDL). PAN fits the 1-D spectra, including errors, using a Levenberg-Marquardt technique to solve the least-squares problem. Errors to the fit were estimated with a bootstrap Monte-Carlo method. Figure 5.2 shows the S(1) and S(2) lines (black) and our Gaussian (blue dotted) fits for each of our four pointings. The blue dotted lines also show the extent of each spectrum used to fit the lines. The vertical dashed lines denote the observed line centers of $\lambda = 12.29$ μm and $\lambda = 17.05$ μm for the S(2) and S(1) transitions, respectively.

We estimated upper limits to the S(0) flux at each position by selecting a region within the LH observations that best matched the coverages of the SH positions. The pixel sampling of the LH module is more coarse than that of the SH module within

CUBISM and thus an exact match to the SH area was unobtainable (see Figure 5.1). In order to estimate an upper limit to the S(0) line flux in each position, we fit the continuum level using PAN. The rms about this continuum level was then measured. We used an amplitude of 3 times the rms level at each location as the amplitude of a Gaussian. We defined the Gaussian sigma width for the S(0) line as the average of the Gaussian sigma widths of the S(1) and S(2) lines at each location. The upper limits to the S(0) lines were then computed as the integral of these Gaussians.

Table 5.2 details the results of our fitting. The columns are: (1) region name, (2), (3), & (4) are the integrated line fluxes in units of 10^{-18} W m^{-2} of the S(0), S(1), and S(2) lines, respectively. If we assume that the H_2 is confined within the boundaries of the observed CO clouds then our estimated line fluxes would require aperature correction factors of less than 2.5. It is likely that the warm H_2 occupies a much larger region than is traced by the dense CO. Our derived H_2 line fluxes are similar to those observed in a wider variety of galaxy morphologies observed in the Spitzer Infrared Nearby Galaxy Survey (SINGS; Roussel et al. 2007). In particular, the average S(1) and S(2) line fluxes for the 8 dwarf galaxies in their sample are 9.9 & 4.1×10^{-18} W m^{-2}, respectively. However, given the larger distances to these galaxies ($D_{ave} \sim 9$ Mpc) their observations represent averages over a much larger fraction of the galaxy. Their average linear scale covered by each pointing is ∼785 pc versus our ∼160 pc.

5.4 Estimates of Local ISM Conditions

We next look at properties of the H_2 gas that can be estimated from the observed line fluxes. The excitation temperature should only be derived between either ortho or para transition pairs since both collisional and radiative decay of H_2 changes the rotation number, J, by an even number. This J number change renders the ortho and para transitions largely independent of each other. However, low J transitions should remain in collisional equilibrium over a wide range of conditions given their low critical densities (Burton et al., 1992). Therefore we can use the observed S(1) and S(2) line fluxes to estimate the excitation temperatures (T_{exc}) needed to produce the observed line ratios.

Roussel et al. (2007) provide the equation

$$\mathrm{T}_{exc} = (\mathrm{E_{u2}/k} - \mathrm{E_{u1}/k})/\ln(\mathrm{N_{u1}/N_{u2}} \times g_{\mathrm{u2}}/g_{\mathrm{u1}})$$

where

$$\mathrm{N_{u1}/N_{u2}} = \mathrm{F_{u1}/F_{u2}} \times \mathrm{A_{u2}/A_{u1}} \times \lambda_{\mathrm{u1}}/\lambda_{\mathrm{u2}}$$

and

$$g_{\mathrm{u}} = (2\mathrm{I}+1)(2\mathrm{J}+1).$$

$\mathrm{E_u/k}$ is the upper level energy in Kelvin, k is the Boltzmann constant, $\mathrm{N_u}$ is the upper level column density, g_{u} is the statistical weight, F is the flux, A is the spontaneous emission coefficient, and λ is the observed central wavelength. For the statistical weight, g_{u}, I = 1 for odd J (ortho transitions) or I = 0 for even J (para transitions). Table 1 in Roussel et al. (2007) provides the values of $\mathrm{E_u/k}$ and A. In further analysis, we assume the excitation temperature derived from the S(1) and S(2) lines applies to the S(0) transition.

We can also estimate the column densities, $\mathrm{N_u}$, for each line transition with

$$\mathrm{N_u} = 4\pi\mathrm{F_u}/(\mathrm{h}\nu\mathrm{A}\Omega)$$

where h is the Planck constant, ν is the observed line frequency, and Ω is the solid angle observed (2.7×10^{-9} sr for the SH observations and 4.6 - 7.0×10^{-9} sr for the extracted LH observations).

Table 5.6 gives our estimates of the H_2 line properties. Column (1) gives the region name, (2) provides the estimated excitation temperature, T_{exc}, columns (3), (4), & (5) are our estimated column densities in the S(0) ($\mathrm{N_{S(0)}}$), S(1) ($\mathrm{N_{S(1)}}$), and S(2) ($\mathrm{N_{S(2)}}$) lines, respectively, and (6) is the total observed warm H_2 column density, $\mathrm{N_{warm}}$, defined as:

$$\mathrm{N}_{warm} \;=\; \mathrm{N}_u Z(\mathrm{T}_{exc}) \;/\; (\exp[-E_u/(k\mathrm{T}_{exc})] * g_u)$$

where the partition function

$$Z(\mathrm{T}) \;\sim\; 0.0247\mathrm{T}_{exc}/[1-\exp(-6000\ \mathrm{K}/\mathrm{T}_{exc})].$$

Column (7) is the estimated CO luminosity in our observed regions from the Heracles (Leroy et al., 2009) observations and column (8) is the ratio of the warm and cold H_2 column densities (N_{warm}/N_{cold}). The cold H_2 column densities are computed from the observed CO luminosities (see discussion below).

Using the CO (J=2-1) integrated intensity map of NGC 4214 from Heracles, we can estimate the total column density of the cold H_2, N_{cold}, expected at each location. Recent work by (Schruba et al., 2012) derived a conversion factor, α_{CO}, between the luminosity of CO (J=1-0), L_{CO}, and the total cold H_2 mass. For the metallicity of NGC 4214 $\alpha_{CO}\approx 50$ $M_\odot$ pc^{-2} (K km $s^{-1})^{-1}$. We assume, as did Schruba et al., that CO (J=2-1)/CO (J=1-0) = 0.7. Column (7) in Table 5.6 lists our estimated L_{CO} values for each region.

These values can then be converted into an estimate for N_{tot} by

$$N_{tot} = \alpha_{CO} \times L_{CO}/(m_{H_2} \times \Sigma)$$

where m_{H_2} is the mass of an H_2 molecule in solar masses and Σ is the observed surface area with units of cm^2. We next define the warm-to-cold H_2 fraction by comparing N_{warm} to N_{cold}. Column (8) in Table 5.6 lists the N_{warm}/N_{cold} fractions. The N_{warm}/N_{cold} ratios at each location are only $\sim 10^{-5}$. This suggests that the vast majority of the H_2 gas at each location within NGC 4214 has a lower temperature than our derived excitation temperatures.

5.5 Conclusions

We present results for our search of the low energy pure rotational lines of the H_2molecule in the nearby, low-mass galaxy NGC 4214. Our Spitzer observations target the known CO peaks (Walter et al. 2001; Leroy et al. 2009; Schruba et al. 2012). A summary of our results are:

- We detect the warm H_2 S(1) and S(2) transitions at each line-of-sight. The S(0) transition was undetected at the 3σ confidence level.
- Our direct detection of H_2 is among the first such detections in a low metallicity system.

- Flux estimates for the S(1) and S(2) lines at each location are consistent with literature values of low-mass systems.

- We estimate an excitation temperature at each location from the S(1) and S(2) transitions of a few hundred K. These temperatures are also consistent with literature values.

- Using our temperature estimate, we compute total warm H_2 column densities and compare them to the cold H_2 column densities inferred from CO observations. We find that the warm-to-cold H_2 column density ratio is only $\sim 10^{-5}$. This implies that the bulk of the H_2 is at temperatures much lower than those estimated for the warm H_2.

Given the spatial coincidence of the warm H_2 with the known CO clouds, the warm H_2 is a useful tracer of the molecular gas in low metallicity galaxies. Extending this work to more galaxies with and without CO detections will allow us to calibrate the warm H_2 detections with the presence of and local conditions of star formation.

5.6 Figures

SRW is grateful for support from a Penrose Fellowship and a University of Minnesota Degree Dissertation Fellowship. NRAO is operated by Associated Universities, Inc., under cooperative agreement with the National Science Foundation. This research has made use of NASA's Astrophysics Data System Bibliographic Services and the NASA/IPAC Extragalactic Database (NED), which is operated by the Jet Propulsion Laboratory, California Institute of Technology, under contract with the National Aeronautics and Space Administration.

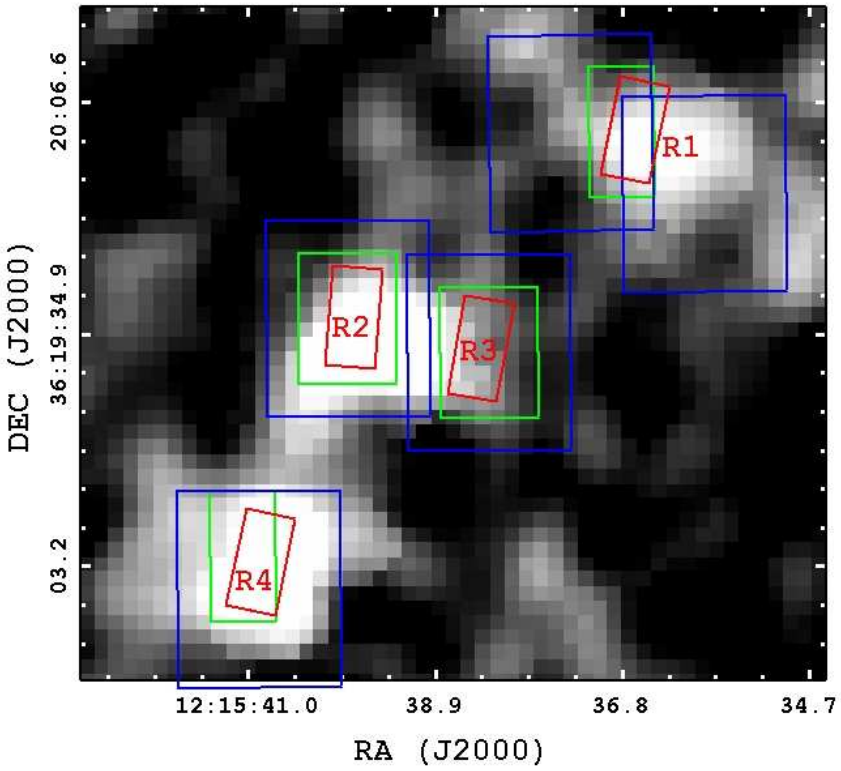

Figure 5.1 Spitzer IRS slit positions overlayed on the Heracles integrated CO intensity map. Our adopted position names are labeled R1-R4. The SH observations are defined by the red boxes, LH by the blue boxes, and the portions of the LH used in the comparisons with the SH are the green boxes. The green boxes do not match the red boxes exactly due to the larger pixel sampling of the LH module compared to the SH module.

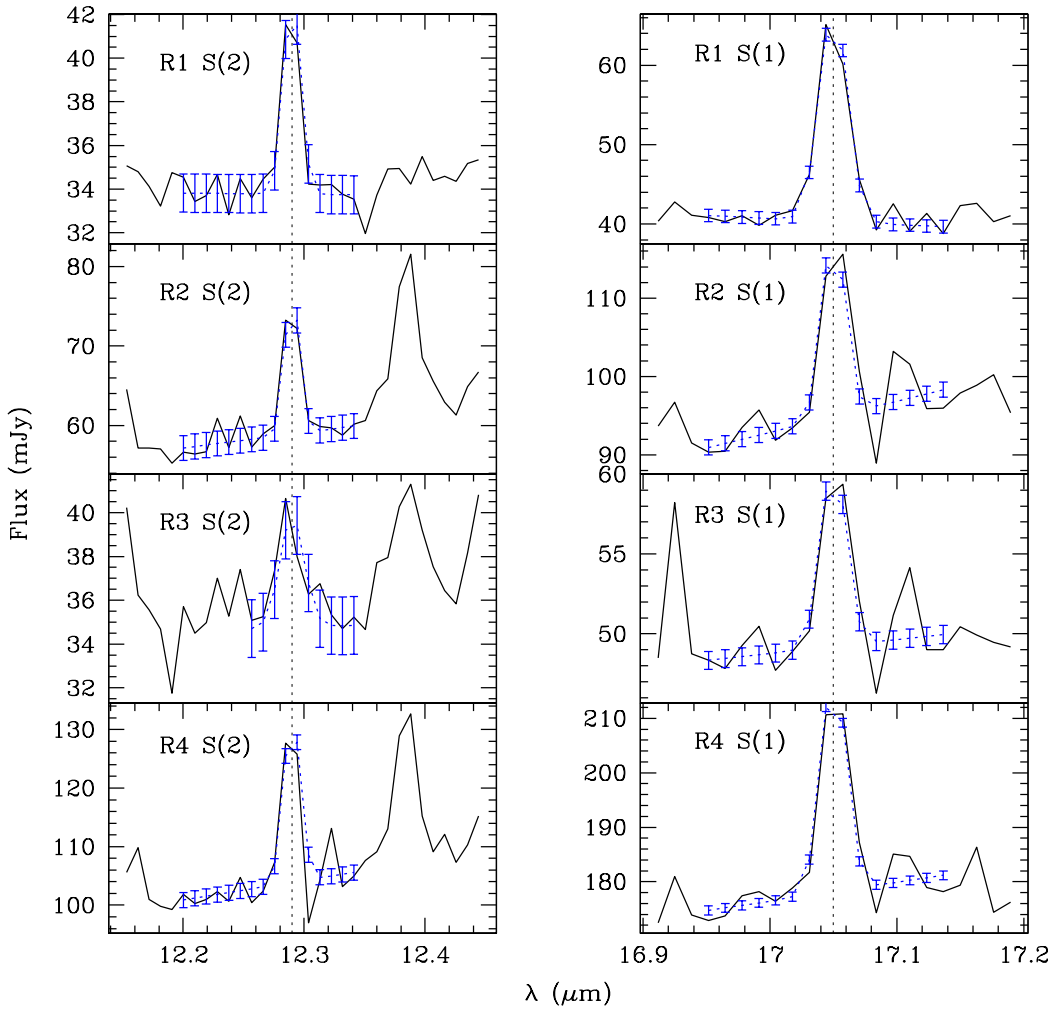

Figure 5.2 The S(2) (left) and S(1) (right) H_2 rotational lines for each pointing R1-R4. The dotted blue lines are our Gaussian plus continuum fits to the spectra. The blue lines span the portion of the spectra used to fit the lines. The vertical dotted lines denote the observed line centers of $\lambda = 12.29$ μm and $\lambda = 17.05$ μm for the S(2) and S(1) transitions, respectively.

Table 5.1. Observations of NGC 4212

1 AOR Name	2 Module	3 Label Name	4 RA (J2000.0)	5 DEC (J2000.0)	6 Obs. Date (YYYY-MM-DD)	7 t_{start} (hh:mm:ss)	8 t_{end} (hh:mm:ss)	9 t_{tot} (s)
IRSM-NGC4214-H1	SH	R1	12:15:36.65	+36:20:02.4	2005-06-05	23:28:41.6	01:30:07.5	7285.9
IRSM-NGC4214-L6	LH	R1	12:15:37.40	+36:20:14.0	2005-05-23	18:12:52.1	20:19:44.7	7612.6
IRSM-NGC4214-L5	LH	R1	12:15:35.90	+36:19:55.5	2005-05-24	07:05:59.9	09:12:52.7	7612.8
IRSM-NGC4214-H3	SH	R2	12:15:38.40	+36:19:32.9	2005-06-03	04:40:10.6	06:41:35.8	7285.2
IRSM-NGC4214-L2	LH	R2	12:15:39.90	+36:19:38.2	2005-05-24	13:34:32.0	15:41:24.1	7612.1
IRSM-NGC4214-H4	SH	R3	12:15:39.85	+36:19:36.9	2005-05-24	17:53:32.6	19:55:29.7	7317.1
IRSM-NGC4214-L1	LH	R3	12:15:38.30	+36:19:33.3	2005-05-24	15:44:02.1	17:50:54.3	7612.2
IRSM-NGC4214-H2	SH	R4	12:15:40.90	+36:19:03.4	2005-06-05	21:23:57.1	23:25:21.9	7284.8
IRSM-NGC4214-L4	LH	R4	12:15:40.90	+36:19:01.3	2005-05-24	11:25:02.3	13:31:54.2	7611.9

Table 5.2 Observed H_2 Line Properties

(1) Label Name	(2) S(0) (10^{-18} W m^{-2})	(3) S(1) (10^{-18} W m^{-2})	(4) S(2) (10^{-18} W m^{-2})
R1	$<1.30\pm0.09$	7.65 ± 0.90	3.02 ± 0.49
R2	$<4.58\pm0.32$	5.80 ± 0.68	5.53 ± 0.90
R3	$<5.32\pm0.38$	3.05 ± 0.36	2.43 ± 0.40
R4	$<89.32\pm6.33$	10.55 ± 1.24	9.91 ± 1.61

Table 5.3. Estimates of H_2 Properties

1 Label Name	2 T_{exc} (K)	3 $N_{S(0)}$ (10^{17} cm^{-2})	4 $N_{S(1)}$ (10^{17} cm^{-2})	5 $N_{S(2)}$ (10^{17} cm^{-2})	6 N_{warm} (10^{18} cm^{-2})	7 L_{CO} (10^6 K km s^{-1} pc^2)	8 N_{warm}/N_{cold} ($\times 10^{-5}$)
R1	308±29	<17.0±0.02	6.4±0.007	0.3±0.0003	6.3±0.006	1.52±0.02	3.3±0.20
R2	520±81	<39.8±0.04	4.9±0.005	0.6±0.0006	2.1±0.002	2.08±0.02	0.8±0.04
R3	455±62	<46.3±0.05	2.6±0.003	0.3±0.0003	1.3±0.001	1.06±0.01	1.0±0.07
R4	515±80	<1164.9±1.17	8.9±0.009	1.0±0.0011	3.9±0.004	2.56±0.02	1.2±0.06

Chapter 6

Conclusions

Throughout this dissertation, we have explored the ISM and star formation of nearby, low-mass galaxies. The work presented here represents much of the current understanding of the star formation processes in these systems. In this chapter, I summarize the main results of each of these studies.

6.1 Primary Results

6.1.1 The Very Large Array - ACS Nearby Galaxy Survey Treasury

In Chapter 2, I presented the VLA-ANGST survey. VLA-ANGST is a large, targeted H I emission line survey directed towards 35 low-mass galaxies selected from the ANGST galaxy sample. The VLA-ANGST project required ∼600 total hours of observing time, making it the largest survey of its kind. Beyond the work presented in this thesis, these high-quality H I data will be used for many years to come by the community at large. The final data products are made publicly available via a dedicated webpage consisting of both natural and robust weighted image cubes, integrated intensity maps, intensity-weighted velocity maps, and velocity dispersion maps.

6.1.2 The Formation of Kiloparsec-Scale H I Holes in Dwarf Galaxies

We investigated the role of multiple generations of star formation in the formation of large, kiloparsec scale cavities observed in the global H I distributions of five nearby, low

mass galaxies in Chapter 3. We estimated the amount of energy required to evacuate a cavity in the ISM based upon observed properties of the gas. We then compared this hole creation energy to an estimate of the amount of energy injected into the ISM by the underlying stellar distribution. We found that the underlying stellar processes produced ample energy (at least an order of magnitude or more) to have been the dominant creation source for the observed cavities. We showed the lack of evidence for a single stellar cluster creation source and suggested ways of improvement for future simulations.

6.1.3 Tracing Cold H I Gas in Nearby, Low-Mass Galaxies

Chapter 4 presented a new technique to trace cold H I gas, which may possibly be the immediate precursor to the molecular, star forming gas. We applied our technique to a large sample of 31 nearby, low-mass galaxies from the VLA-ANGST and THINGS surveys. Cold H I was discovered in ∼85% of the final sample (23/27) after quality control cuts were applied. The cold H I detections presented here represent a significant step forward in our ability to study the precursory gas to star formation where standard techniques fail. We found that the cold H I occupies only a small fraction of the total H I content in each galaxy, consistent with both theory and other observational techniques in the literature. The cold H I is typically found in higher density gas above the canonical threshold for star formation of 10^{21} cm^{-2}. However, the cold H I is markedly absent from the highest density peaks where current star formation is presumably heating the gas. The discovered regions rich in cold H I gas are the most promising targets for future observations addressing the star formation cycle.

6.1.4 Direct H_2 Detections in the Low-Metallicity Galaxy NGC 4214

Finally, in Chapter 5, we presented Spitzer IRS observations of the known CO clouds in NGC 4214. NGC 4214 is one of the only low-mass galaxies with detected CO emission. The goal of this work was to detect the presence of H_2 gas assumed to be spatially coincident with the CO. We detect H_2 at each location via the S(1) and S(2) pure rotational lines. The lower energy S(0) line went undetected. These detections confirm the association on the CO molecule with the H_2 molecule assumed in the literature. We

provided estimates of the excitation temperatures at each location of a few hundred K. These temperatures were then used to compute column densities of the warm H_2. We found that the bulk of the H_2 remains hidden at temperatures far below our estimates.

6.2 Potential for Future Work

The overwhelming wealth of high quality, multi-wavelength information available for every galaxy presented in this dissertation begs for follow up studies. Some of the following ideas are currently being planned.

The detection of cold H I in low-mass galaxies in Chapter 4 is just the beginning of this work. To truly understand the role that the cold H I plays in the star formation process you must compare it to the many other tracers of star formation and dense gas. It will be useful to first compare the cold H I to the resolved stars in the ANGST HST data. The ages of the stars can help determine the time scale needed to form the cold H I gas. A direct spatial correlation study between the cold H I and the GALEX FUV and/or Hα emissions can be used to understand how the physics in the surrounding gas is affecting the rate at which the stars form.

The most promising observations to compare to the cold H I may come from ALMA. ALMA's resolving power and sensitivity allows for spatially resolved studies of the dust continuum and molecules in low mass galaxies. It will be interesting to see if the regions rich with cold dust are also filled by cold H I emission. These two ingredients are the most important in forming H_2. The opacity of the dust can be used to estimate the H_2 mass (e.g., Bolatto et al. 2011). Piecing together the cycle of star formation in these important systems can be done by comparing the warm/cold H I, the H_2, the dust, and the star formation rates and histories.

References

Allen, R. J., Ivette Rodríguez, M., Black, J. H., & Booth, R. S. 2012, AJ, 143, 97

Baars, J. W. M., & Wendker, H. J. 1976, A&A, 48, 405

Bagetakos, I., Brinks, E., Walter, F., de Blok, W. J. G., Usero, A., Leroy, A. K., Rich, J. W., & Kennicutt, R. C. 2011, AJ, 141, 23

Banerjee, A., Jog, C. J., Brinks, E., & Bagetakos, I. 2011, arXiv:1103.4494

Barnes, D. G., & de Blok, W. J. G. 2001,AJ, 122, 825

Barnes, D. G., & de Blok, W. J. G. 2004, MNRAS, 351, 333

Barone, L. T., Heithausen, A., Hüttemeister, S., Fritz, T., & Klein, U. 2000, MNRAS, 317, 649

Bastian, N., et al. 2011, MNRAS, 412, 1539

Begum, A., Chengalur, J. N., Karachentsev, I. D., Kaisin, S. S., & Sharina, M. E. 2006, MNRAS, 365, 1220

Begum, A., Chengalur, J. N., Karachentsev, I. D., Sharina, M. E., & Kaisin, S. S. 2008, MNRAS, 386, 1667

Begum, A., Stanimirović, S., Goss, W. M., et al. 2010, ApJ, 725, 1779

Berg, D. A., Skillman, E. D., Marble, A. R., et al. 2012, arXiv:1205.6782

Bigiel, F., Leroy, A., Walter, F., Brinks, E., de Blok, W. J. G., Madore, B., & Thornley, M. D. 2008, AJ, 136, 2846

Bolatto, A. D., Leroy, A. K., Jameson, K., et al. 2011, ApJ, 741, 12

Borissova, J., Kurtev, R., Georgiev, L., & Rosado, M. 2004, A&A, 413, 889

Braun, R. 1997, ApJ, 484, 637

Briggs, D. S. 1995, Ph.D. Thesis, New Mexico Institute of Mining and Tchnology

Brinks, E., & Bajaja, E. 1986, A&A, 169, 14

Bureau, M., & Carignan, C. 2002, AJ, 123, 1316

Burton, M. G., Hollenbach, D. J., & Tielens, A. G. G. 1992, ApJ, 399, 563

Cannon, J. M., Dohm-Palmer, R. C., Skillman, E. D., Bomans, D. J., Côté, S., & Miller, B. W. 2003, AJ, 126, 2806

Cannon, J. M., Giovanelli, R., Haynes, M. P., et al. 2011, ApJ, 739, L22

Cash, W., Charles, P., Bowyer, S., Walter, F., Garmire, G., & Riegler, G. 1980, ApJ, 238, L71

Chakraborti, S., & Ray, A. 2011, ApJ, 728, 24

Chevalier, R. A. 1974, ApJ, 188, 501

Chu, Y.-H. 2008, IAU Symposium, 250, Massive Stars as Cosmic Engines, ed. F. Bresolin, P. A. Crowther, & J. Puls (Cambridge: Cambridge University Press), 341

Clark, B. G. 1980, A&A, 89, 377

Cole, S., Aragon-Salamanca, A., Frenk, C. S., Navarro, J. F., & Zepf, S. E. 1994, MNRAS, 271, 781

Daigle, A., Joncas, G., Parizeau, M., & Miville-Deschênes, M.-A. 2003, PASP, 115, 662

Dalcanton, J. J., et al. 2009, ApJS, 183, 67

Dale, D. A., et al. 2009, ApJ, 703, 517

de Avillez, M. A., & Breitschwerdt, D. 2004, A&A, 425, 899

de Blok, W. J. G., & Walter, F. 2006, AJ, 131, 363

de Vaucouleurs, G., de Vaucouleurs, A., Corwin, H. G., Jr., Buta, R. J., Paturel, G., & Fouqué, P. 1991, Third Reference Catalogue of Bright Galaxies (New York: Springer)

Dib, S., & Burkert, A. 2005, ApJ, 630, 238

Dickey, J. M., & Lockman, F. J. 1990, ARA&A, 28, 215

Dickey, J. M., Brinks, E., & Puche, D. 1992, ApJ, 385, 501

Dickey, J. M., Mebold, U., Stanimirovic, S., & Staveley-Smith, L. 2000, ApJ, 536, 756

Dohm-Palmer, R. C., et al. 1997, AJ, 114, 2527

Dohm-Palmer, R. C., et al. 1998, AJ, 116, 1227

Dohm-Palmer, R. C., Skillman, E. D., Mateo, M., Saha, A., Dolphin, A., Tolstoy, E., Gallagher, J. S., & Cole, A. A. 2002, AJ, 123, 813

Dolphin, A. E. 2000, PASP, 112, 1383

Dolphin, A. E. 2002, MNRAS, 332, 91

Efremov, Y. N., Elmegreen, B. G., & Hodge, P. W. 1998, ApJ, 501, L163

Ehlerová, S., & Palouš, J. 2005, A&A, 437, 101

Elmegreen, B. G. 1997, ApJ, 477, 196

Elmegreen, B. G., Kim, S., & Staveley-Smith, L. 2001, ApJ, 548, 749

Engelbracht, C. W., Gordon, K. D., Rieke, G. H., et al. 2005, ApJ, 628, L29

Ferrara, A., & Tolstoy, E. 2000, MNRAS, 313, 291

Fragile, P. C., Murray, S. D., Anninos, P., & Lin, D. N. C. 2003, ApJ, 590, 778

Fukui, Y., & Kawamura, A. 2010, ARA&A, 48, 547

Gallart, C., Zoccali, M., & Aparicio, A. 2005, ARA&A, 43, 387

Gerola, H., & Seiden, P. E. 1978, ApJ, 223, 129

Gil de Paz, A., et al. 2007, ApJS, 173, 185

Glover, S. C. O., Federrath, C., Mac Low, M.-M., & Klessen, R. S. 2010, MNRAS, 404, 2

Glover, S. C. O., & Mac Low, M.-M. 2011, MNRAS, 412, 337

Gordon, K. D., Pérez-González, P. G., Misselt, K. A., et al. 2004, ApJS, 154, 215

Hatzidimitriou, D., Stanimirovic, S., Maragoudaki, F., Staveley-Smith, L., Dapergolas, A., & Bratsolis, E. 2005, MNRAS, 360, 1171

Heiles, C. 1979, ApJ, 229, 533

Heiles, C. 1984, ApJS, 55, 585

Helfer, T. T., Thornley, M. D., Regan, M. W., et al. 2003, ApJS, 145, 259

Holmberg, E. 1950, Meddelanden fran Lunds Astronomiska Observatorium Serie II, 128, 1

Holtzman, J. A., Afonso, C., & Dolphin, A. 2006, ApJS, 166, 534

Houck, J. R., Roellig, T. L., Van Cleve, J., et al. 2004, Proc. SPIE, 5487, 62

Huchtmeier, W. K., & Richter, O.-G. 1989, A General Catalog of HI Observations of Galaxies. The Reference Catalog. Huchtmeier, W.K., Richter, O.-G., pp. 350. ISBN 0-387-96997-7. Springer-Verlag Berlin Heidelberg 1989

Huchtmeier, W. K., Karachentsev, I. D.,Karachentseva, V. E., & Ehle, M. 2000, A&AS, 141, 469

Huchtmeier, W. K., Karachentsev, I. D., & Karachentseva, V. E. 2000, A&AS, 147, 187

Huchtmeier, W. K., Karachentsev, I. D., & Karachentseva, V. E. 2003, A&A, 401, 483

Hunter, D. A., Brinks, E., Elmegreen, B., Rupen, M., Simpson, C., Walter, F., Westpfahl, D., & Young, L. 2007, Bulletin of the American Astronomical Society, 38, 895

Israel, F. P., Tacconi, L. J., & Baas, F. 1995, A&A, 295, 599

Jackson, D. C., Cannon, J. M., Skillman, E. D., et al. 2006, ApJ, 646, 192

Jansen, R. A. 2000, Ph.D. Thesis, Kapteyn Astronomical Institute, Univ. Groningen

Jörsäter, S., & van Moorsel, G. A. 1995, AJ, 110, 2037

Kanekar, N., Braun, R., & Roy, N. 2011, arXiv:1107.0744

Karachentsev, I. D., Karachentseva, V. E., &

Karachentsev, I. D., Karachentseva, V. E., Huchtmeier, W. K., & Makarov, D. I. 2004, AJ, 127, 2031

Karachentseva, V. E. 1968, Soobshcheniya Byurakanskoj Observatorii Akademiya Nauk Armyanskoj SSR Erevan, 39, 61

Kennicutt, R. C., Jr. 1998, ApJ, 498, 541

Kennicutt, R. C., Jr. 1998, ARA&A, 36, 189

Kennicutt, R. C., Jr., et al. 2003, PASP, 115, 928

Kennicutt, R. C., Jr., Lee, J. C., Funes, S. J., José G., Sakai, S., & Akiyama, S. 2008, ApJS, 178, 247

Kennicutt, R. C., Calzetti, D., Aniano, G., et al. 2011, PASP, 123, 1347

Kennicutt, R. C., Jr., & Evans, N. J., II 2012, arXiv:1204.3552

Kim, S., Dopita, M. A., Staveley-Smith, L., & Bessell, M. S. 1999, AJ, 118, 2797

Krčo, M., & Goldsmith, P. F. 2010, ApJ, 724, 1402

Krumholz, M. R., McKee, C. F., & Tumlinson, J. 2009, ApJ, 693, 216

Krumholz, M. R., Leroy, A. K., & McKee, C. F. 2011, ApJ, 731, 25

Koribalski, B. S., Staveley-Smith, L., Kilborn, V. A., et al. 2004, AJ, 128, 16

Koribalski, B. S. 2008, Galaxies in the Local Volume, 41

Lee, H., Skillman, E. D., Cannon, J. M., et al. 2006, ApJ, 647, 970

Lee, J. C., Kennicutt, R. C., Funes, J. G., Sakai, S., Tremonti, C. A., & van Zee, L. 2004, Bulletin of the American Astronomical Society,36, 1442

Lee, J. C., Gil de Paz, A., Tremonti, C., et al. 2009, ApJ, 706, 599

Lee, J. C., et al. 2011, ApJS, 192, 6

Leitherer, C., et al. 1999, ApJS, 123, 3

Leroy, A., Bolatto, A. D., Simon, J. D., & Blitz, L. 2005, ApJ, 625, 763

Leroy, A. K., Walter, F., Brinks, E., Bigiel, F., de Blok, W. J. G., Madore, B., & Thornley, M. D. 2008, AJ, 136, 2782

Leroy, A. K., et al. 2009, AJ, 137, 4670

Li, D., & Goldsmith, P. F. 2003, ApJ, 585, 823

Lo, K. Y., & Sargent, W. L. W. 1979, ApJ, 227, 756

Loeb, A., & Perna, R. 1998, ApJ, 503, L35

Mac Low, M.-M., & Ferrara, A. 1998, IAU Colloq. 166: The Local Bubble and Beyond, 506, 559

Mac Low, M.-M., & Ferrara, A. 1999, ApJ, 513, 142

Maloney, P., & Black, J. H. 1988, ApJ, 325, 389

Marigo, P., Girardi, L., Bressan, A., Groenewegen, M. A. T., Silva, L., & Granato, G. L. 2008, A&A, 482, 883

Mashchenko, S. Y., Thilker, D. A., & Braun, R. 1999, A&A, 343, 352

Mateo, M. L. 1998, ARA&A, 36, 435

McCray, R., & Kafatos, M. 1987, ApJ, 317, 190

McKee, C. F., & Ostriker, J. P. 1977, ApJ, 218, 148

McKee, C. F., & Ostriker, E. C. 2007, ARA&A, 45, 565

McQuinn, K. B. W., Skillman, E. D., Cannon, J. M., et al. 2010, ApJ, 721, 297

Merrifield, M. R. 1993, MNRAS, 261, 233

Meyer, M. J., Zwaan, M. A., Webster, R. L., et al. 2004, MNRAS, 350, 1195

Momany, Y., et al. 2005, A&A, 439, 111

Morrissey, P., et al. 2007, ApJS, 173, 682

Mould, J. R., Schneider, D. P., Harding, P., & Bothun, G. D. 1986, PASP, 98, 732

Moustakas, J., Kennicutt, R. C., Jr., Tremonti, C. A., et al. 2010, ApJS, 190, 233

Muller, E., Staveley-Smith, L., Zealey, W., & Stanimirović, S. 2003, MNRAS, 339, 105

Oey, M. S., & Massey, P. 1995, ApJ, 452, 210

Oh, S.-H., de Blok, W. J. G., Walter, F., Brinks, E., & Kennicutt, R. C. 2008, AJ, 136, 2761

Ostriker, E. C., McKee, C. F., & Leroy, A. K. 2010, ApJ, 721, 975

Ott, J., Walter, F., Brinks, E., Van Dyk, S. D., Dirsch, B., & Klein, U. 2001, AJ, 122, 3070

Ott, J., Skillman, E., Dalcanton, J., Walter, F., West, A., & Koribalski, B. 2008, Frontiers of Astrophysics: A Celebration of NRAO's 50th Anniversary, 395, 376

Padoan, P., Jimenez, R., & Jones, B. 1997, MNRAS, 285, 711

Padoan, P., Kim, S., Goodman, A., & Staveley-Smith, L. 2001, ApJ, 555, L33

Perna, R., & Gaensler, B. M. 2004, ApJ, 606, 326

Persic, M., Salucci, P., & Stel, F. 1996, MNRAS, 281, 27

Puche, D., Westpfahl, D., Brinks, E., & Roy, J.-R. 1992, AJ, 103, 1841

Puche, D., & Westpfahl, D. 1994, European Southern Observatory Conference and Workshop Proceedings, 49, 273

Pustilnik, S. A., & Martin, J.-M. 2007, A&A, 464, 859

Rahman, N., Bolatto, A. D., Xue, R., et al. 2012, ApJ, 745, 183

Recchi, S., & Hensler, G. 2006, A&A, 445, L39

Relaño, M., Beckman, J. E., Daigle, O., & Carignan, C. 2007, A&A, 467, 1117

Relano, M., Kennicutt, R. C., Jr., Eldridge, J. J., Lee, J. C., & Verley, S. 2012, arXiv:1204.4502

Rhoads, J. E. 1997, ApJ, 487, L1

Rhode, K. L., Salzer, J. J., Westpfahl, D. J., & Radice, L. A. 1999, AJ, 118, 323

Rohlfs, K., & Wilson, T. L. 2004, Tools of radio astronomy, 4th rev. and enl. ed., by K. Rohlfs and T.L. Wilson. Berlin: Springer, 2004

Roussel, H., Helou, G., Hollenbach, D. J., et al. 2007, ApJ, 669, 959

Roychowdhury, S., Chengalur, J. N., Begum, A., & Karachentsev, I. D. 2009, MNRAS, 397, 1435

Sargent, W. L. W., Sancisi, R., & Lo, K. Y. 1983, ApJ, 265, 711

Salim, S., Rich, R. M., Charlot, S., et al. 2007, ApJS, 173, 267

Schlegel, D. J., Finkbeiner, D. P., & Davis, M. 1998, ApJ, 500, 525

Schneider, S. E., Thuan, T. X., Magri, C., & Wadiak, J. E. 1990, ApJS, 72, 245

Schruba, A., Leroy, A. K., Walter, F., et al. 2012, arXiv:1203.4231

Silich, S., Lozinskaya, T., Moiseev, A., Podorvanuk, N., Rosado, M., Borissova, J., & Valdez-Gutierrez, M. 2006, A&A, 448, 123

Simpson, C. E., Hunter, D. A., & Knezek, P. M. 2005, AJ, 129, 160

Skillman, E. D., Bothun, G. D., Murray, M. A., & Warmels, R. H. 1987, A&A, 185, 61

Skillman, E. D., Terlevich, R., Teuben, P. J., & van Woerden, H. 1988, A&A, 198, 33

Skillman, E. D. 1996, The Minnesota Lectures on Extragalactic Neutral Hydrogen, 106, 208

Smith, J. D. T., Armus, L., Dale, D. A., et al. 2007, PASP, 119, 1133

Spaans, M., & Norman, C. A. 1997, ApJ, 483, 87

Springob, C. M., Haynes, M. P., Giovanelli, R., & Kent, B. R. 2005, ApJS, 160, 149

Stewart, S. G., & Walter, F. 2000, AJ, 120, 1794

Stilp, A. M., et al. 2012, in preparation

Stinson, G. S., Dalcanton, J. J., Quinn, T., Kaufmann, T., & Wadsley, J. 2007, ApJ, 667, 170

Tamburro, D., Rix, H.-W., Leroy, A. K., et al. 2009, AJ, 137, 4424

Taylor, C. L., Kobulnicky, H. A., & Skillman, E. D. 1998, AJ, 116, 2746

Tenorio-Tagle, G. 1981, A&A, 94, 338

Tenorio-Tagle, G., & Bodenheimer, P. 1988, ARA&A, 26, 145

Theis, C., Burkert, A., & Hensler, G. 1992, A&A, 265, 465

Thilker, D. A., Braun, R., & Walterbos, R. M. 1998, A&A, 332, 429

Thornton, K., Gaudlitz, M., Janka, H.-T., & Steinmetz, M. 1998, ApJ, 500, 95

Tolstoy, E., Hill, V., & Tosi, M. 2009, ARA&A, 47, 371

Úbeda, L., Maíz-Apellániz, J., & MacKenty, J. W. 2007, AJ, 133, 932

van den Bergh, S. 1959, Publications of the David Dunlap Observatory, 2, 147

van der Kruit, P. C. 1981, A&A, 99, 298

van der Marel, R. P., & Franx, M. 1993, ApJ, 407, 525

van Driel, W., Kraan-Korteweg, R. C., Binggeli, B., & Huchtmeier, W. K. 1998, A&AS, 127, 397

van Dyk, S. D., Puche, D., & Wong, T. 1998, AJ, 116, 2341

Verter, F., & Hodge, P. 1995, ApJ, 446, 616

Vorobyov, E. I., & Shchekinov, Y. A. 2004, A&A, 416, 499

Vorobyov, E. I., Klein, U., Shchekinov, Y. A., & Ott, J. 2004, A&A, 413, 939

Vorobyov, E. I., & Basu, S. 2005, A&A, 431, 451

Vorontsov-Velyaminov 1962, *Morphological Catalog of Galaxies* (Moscow: Moscow State University).

Wada, K., Spaans, M., & Kim, S. 2000, ApJ, 540, 797

Walter, F., & Brinks, E. 1999, AJ, 118, 273

Walter, F., Taylor, C. L., Hüttemeister, S., Scoville, N., & McIntyre, V. 2001, AJ, 121, 727

Walter, F., & Brinks, E. 2001, AJ, 121, 3026

Walter, F., Brinks, E., de Blok, W. J. G., Bigiel, F., Kennicutt, R. C., Thornley, M. D., & Leroy, A. 2008, AJ, 136, 2563

Warren, S. R., Weisz, D. R., Skillman, E. D., et al. 2011, ApJ, 738, 10

Warren, S. R., Skillman, E. D., Stilp, A. M., et al. 2012, ApJ, submitted

Weaver, R., McCray, R., Castor, J., Shapiro, P., & Moore, R. 1977, ApJ, 218, 377

Weisz, D. R., Skillman, E. D., Cannon, J. M., Dolphin, A. E., Kennicutt, R. C., Jr., Lee, J.C., & Walter, F. 2008, ApJ, 689,160

Weisz, D. R., Skillman, E. D., Cannon, J. M., Dolphin, A. E., Kennicutt, R. C., Lee, J., & Walter, F. 2009, ApJ, 704, 1538

Weisz, D. R., Dalcanton, J. J., Williams, B. F., et al. 2011, ApJ, 739, 5

Wolfire, M. G., McKee, C. F., Hollenbach, D., & Tielens, A. G. G. M. 2003, ApJ, 587, 278

Young, L. M., & Lo, K. Y. 1996, ApJ, 462, 203

Young, L. M., & Lo, K. Y. 1997, ApJ, 490, 710

Young, L. M., van Zee, L., Lo, K. Y., Dohm-Palmer, R. C., & Beierle, M. E. 2003, ApJ, 592, 111